The Propagation of Electromagnetic Waves in Laboratory Plasmas

L.B. Whitbourn
Ph.D. Thesis
May 1973

Summary

This thesis describes the initial stages of a program in the Wills Plasma Physics Department within the University of Sydney for developing far-infrared diagnostics of plasmas. The author is concerned with far-infrared hydrogen cyanide (HCN) gas lasers, wave interactions with the laser plasma, and the use of the HCN laser radiation for interferometric measurements of electron densities in transient laboratory plasmas.

A pulsed 337 μm wavelength HCN laser is studied experimentally and various plasma refractive effects occurring within the laser resonator are investigated. In particular, the production of "spiking" output pulses by the pulsed laser is observed, and a theoretical explanation of the plasma-origin of these pulses is given.

Ways in which a continuous 337 μm HCN laser may be used for plasma electron density measurements are

investigated and the self-modulating laser-interferometer (or "laser interferometer") principle is studied in detail. A simple theory of loss modulation of a laser is presented. Predictions about laser interferometer fringe shapes, fringe size and frequency response are then compared with experimental results.

Experiments are described which demonstrate the use of an HCN laser interferometer for electron density measurements in a decaying helium plasma immersed in a large magnetic field. The performance of the laser interferometer is compared theoretically and experimentally with that of conventional interferometers using the HCN laser as a source. In the course of these studies interactions such as plasma beam bending and focusing, and Faraday rotation of the 337 μm beam probing the decaying helium plasma are observed and investigated.

Finally, there is a study of the decay process of the initially highly-ionized, magnetically-confined helium plasma to which 337 μm diagnostics have been applied. The experimental decay rate is found to agree with the predictions of collisional-radiative recombination theory and the dominant energy loss mechanism of the plasma is shown to be thermal conduction by the background neutral gas.

THE PROPAGATION OF ELECTROMAGNETIC WAVES IN LABORATORY PLASMAS

by

L.B. Whitbourn B.Sc. (Hons).

A Thesis Submitted for the Degree of Doctor of Philosophy in the Faculty of Science of the University of Sydney.

May 1973

CONTENTS

PREFACE

Summary

This thesis describes the initial stages of a program in the Wills Plasma Physics Department within the University of Sydney for developing far-infrared diagnostics of plasmas. The author is concerned with far-infrared hydrogen cyanide (HCN) gas lasers and their use for interferometric measurements of electron densities in transient laboratory plasmas. Experimental results are obtained with two HCN gas lasers; one pulsed and one continuous, as well as the Sydney University Plasma Physics Experimental Rig - No. I, hereafter referred to as SUPPER I.

Our pulsed 337 μm HCN laser is studied experimentally and various plasma effects occurring within the laser resonator are investigated. In particular the production of "spiking" output pulses by the pulsed laser is observed and a theoretical explanation of the plasma-origin of these pulses is given.

Ways in which a continuous HCN laser may be used for plasma electron density measurements are investigated and the self-modulating laser-interferometer (or "laser interferometer") principle is studied in detail.

Experiments are described which demonstrate the use of an HCN laser-interferometer for electron density measurements in a decaying helium plasma ("the SUPPER I helium plasma") in a large magnetic field. The performance of the laser-interferometer is compared theoretically and experimentally with that of conventional interferometers using the HCN laser as source. In the course of these studies interactions such as plasma beam bending and focusing, and Faraday rotation of the 337 μm beam probing the SUPPER I helium plasma are observed and investigated.

Finally, the decay processes of the highly-ionized, magnetically-confined SUPPER I helium plasma are also studied and the experimental decay rate is compared with the predictions of collisional-radiative recombination theory.

Arrangement of Material

Chapter 1 gives the general background to the author's research topic; reasons for our interest in HCN lasers in the plasma physics laboratory are indicated, and we briefly discuss the occurrence of interesting plasma effects within the HCN laser itself.

Chapter 2 describes the design of our pulsed and continuous HCN lasers and, for the pulsed laser, an experimental investigation of the dependence of pulse energy on various parameters.

Chapter 3 starts by deriving the refractive index of an unmagnetized plasma as a function of its electron density. This serves as a theoretical background for Chapters 4 to 7. Microwave interferometric measurements of electron densities in the pulsed laser are presented as an introduction to Chapters 4 and 5.

Chapters 4 and 5 then deal with plasma effects in the pulsed HCN laser. This concludes the work with the pulsed laser and attention is turned to the CW HCN laser.

Chapter 6 describes a simple theory of operation of a self-modulating laser interferometer based on a CW HCN laser and compares the theory with experimental observations.

Chapter 7 describes electron density measurements with the HCN laser interferometer system and interactions of the 337 μm beam propagating through a decaying helium plasma.

Chapter 8 is devoted to the study of the decay processes of the highly-ionized, magnetically-confined helium plasma used in Chapter 7.

Author's Contributions

The pulsed HCN laser described in this thesis (Ch. 2) was designed by the author in collaboration with Dr. L.C. Robinson. The experimental investigation of this source was devised and executed by the author with assistance in the gathering of data from Dr. Robinson and Mr. G.D. Tait.

The investigation of plasma effects in the pulsed HCN laser was stimulated by the ideas of Dr. Robinson but the experimental procedures were the responsibility of the author. Both Dr. Robinson and G.D. Tait assisted with the experimental observations. However the analysis of the results (Chs. 3,4, and 5) and the theory of Ch. 5 are the sole responsibility of the author.

The continuous HCN laser (Ch. 2) was designed by the author. The interferometer configurations using this source (Ch. 6) were developed by the author in collaboration with Mr. N.R. Heckenberg. The theory of the self-modulating laser interferometer was developed by N.R. Heckenberg and G.D. Tait with contributions from the author. The extension of this theory which makes various predictions about the frequency response of a loss-modulated laser is due to G.D. Tait with some contributions from N.R. Heckenberg.

All of the experimental results described in Chs. 6 and 7 were obtained by the author in collaboration with N.R. Heckenberg and G.D. Tait. The analysis in Ch. 7 was divided equally between the author and N.R. Heckenberg.

The electron density (Ch. 7) and temperature (Ch. 8) profiles of the SUPPER I helium plasma are, with the exception of the 337 μm measurements, entirely the work of N.R. Heckenberg. However the analysis of the plasma decay was performed by the author in collaboration with N.R. Heckenberg.

In the course of this work the author was involved in the construction of both HCN lasers as well as various ancillary equipment for the far-infrared detection systems. Such items as electrical discharge circuitry, gas-inlet systems and vacuum systems were constructed by the author. The author has used extensively, and is completely familiar with, the cryogenic techniques involved in operating a liquid helium cooled far-infrared detector (Putley detector), the microwave techniques used for plasma electron density measurements, and the operation of the SUPPER I plasma source.

Acknowledgements

It has often been said that far-infrared techniques embrace more and diverse branches of physics than most other areas of current research. It is perhaps for this reason that the author finds himself indebted to a great many people who have helped him in the course of his Ph.D. project.

I am grateful to Professor C.N. Watson-Munro and Dr. L.C. Robinson for their guidance throughout the course of these studies. I am particularly indebted to Dr. Robinson for stimulating my interest in far-infrared physics and for a great deal of practical help throughout the course of my work.

I have enjoyed discussions with all of the members of staff, and students, of the Wills Plasma Physics Department particularly Associate Professor D.D. Millar, Drs. L.C. Robinson and W.I.B. Smith and fellow students David Blatt, Norman Heckenberg and Graeme Tait. It has been my good fortune to collaborate with the latter two colleagues and I have learnt a great deal from both of them.

Graeme Tait deserves special thanks for his continual moral and material support, including many voluntary all-night stints in the Wills Plasma Physics Department. Without Graeme's willing help and clear

physical insights I would have achieved less than I have.

Many people have given me practical assistance with laboratory equipment. Messrs. Neville Lowe, John Pigott, Emeric Peklo and Sergie Romashenko are thanked for their efforts in the fields of laser construction, vacuum and cryogenic engineering and electronic design and construction. My thanks also go to Stephen Simpson for his assistance in aspects of the early laser construction and to Michael Bell who commissioned the Putley detector.

It is a pleasure to acknowledge Dr. G.F. Brand for his assistance with microwave techniques, Mr. R. Kemp of the National Standards Laboratory (C.S.I.R.O.) for arranging many leak tests of liquid helium transfer siphons and Dr. A.R. Lacey and Mr. R. Burrows of the School of Chemistry, University of Sydney, for liquefying much of the helium which was used in the Putley detector.

My thanks also go to Mr. Steve King of Pennicook-Davison Pty. Ltd. for somehow obtaining what must have been the first sample of sheet T.P.X. in Australia. From this our first T.P.X. lenses were made.

I am very grateful to Elaine Rodgers and Bill Green for their craftsmanship in the typing, and photography, involved in the production of this thesis.

To my parents, Marge and Barney, thank you for your patience.

Last but not least, it is a pleasure to acknowledge Professor H. Messel and the Science Foundation within the School of Physics for the provision of research facilities, and the Australian Institute of Nuclear Science and Engineering and the Australian Research Grants Committee for financial assistance for the purchase of laboratory equipment.

Author's Publications

Experimental Investigation of a Pulsed 337 μm HCN Gas Laser.

L.C. Robinson and L.B. Whitbourn (1971), Proc.IREE Aust. 32, p.355.

The Origin of Spiking Pulses in HCN Gas Lasers.

L.B. Whitbourn, L.C. Robinson and G.D. Tait (1972), Phys. Lett. 38A, p.315.

Quantum Mechanical Description and Noise Analysis of the Cyclotron Resonance Spectrometer-Detector.

L.C. Robinson and L.B. Whitbourn (1972), J.Phys.A: Gen Phys. 5, p.263.

A 337 μm HCN Laser Interferometer for Plasma Diagnostics.

N.R. Heckenberg, G.D. Tait and L.B. Whitbourn (1973), J.Appl.Phys. (accepted for publication).

Also available as Wills Plasma Physics Department Experimental Report: ER.67; June, 1972.

Chapter 1

GENERAL BACKGROUND TO THE SELECTED RESEARCH TOPIC

1.1 Introduction

The work described in this thesis was carried out in the Wills Plasma Physics Department within the University of Sydney. Very broadly, the author's project was to develop far-infrared gas-laser diagnostics for measuring electron densities in transient laboratory plasmas and to study the interactions of far-infrared radiation propagating in laboratory plasmas. More particularly, the gas-laser itself was to be regarded as a laboratory plasma - a specially useful one - and worthy of study in its own right.

Such a project naturally involves several branches of far-infrared physics which may be conveniently summarized as:

(a) Gas-laser generation of far-infrared radiation,

(b) Far-infrared optics,

(c) Detection of far-infrared radiation, and

(d) Far-infrared wavelength measurements. At the time of commencement of the author's candidature fields (c) and (d) were already quite well developed by spectro-

scopists, who have traditionally used black-body sources in the far-infrared. However fields (a) and (b) were rather less well developed.

The approach adopted was as follows. Since development work could not be undertaken simultaneously in all four of the fields outlined above it was decided that the author should concentrate mainly on the generation problem and,to a lesser extent, on far-infrared optics. Accordingly, commercial detectors and interferometers were purchased essentially complete and used throughout the course of this work. Two 337 μm HCN lasers were built in the Wills Plasma Physics Department; the first was a pulsed source and the second was continuous. Since the physical processes which occur within HCN lasers were far from being well understood the pulsed laser was studied experimentally. This led to the discovery of a strong interaction between the laser radiation and the laser discharge plasma. The first half of this thesis is devoted mainly to the pulsed laser and the study of effects resulting from this interaction. The second half deals with the continuous laser and its use for plasma electron density measurements, concluding with the study of a decaying helium plasma to which 337 μm diagnostics have been applied.

Evidently, we are to be particularly concerned with plasma interaction with far-infrared waves throughout most of this thesis. In the next section therefore, let us briefly consider this interaction.

1.2 Interaction of Far-Infrared Waves with Laboratory Plasmas

The convenience and reliability of interferometric measurements of plasma electron densities have been accepted by plasma physicists for some time, but in the past most such measurements have utilized microwave radiation (Heald and Wharton, 1965). The technique involves the interferometric measurement of the refractive index of the plasma under study and this is quite simply related to its electron density. For instance, in the case of a collisionless unmagnetized plasma, the refractive index μ is related to the electron density by $\mu = (1 - n/n_c)^{\frac{1}{2}}$, where n_c is the plasma resonance density corresponding to the frequency of radiation being used. When n is greater than n_c the radiation is reflected by the plasma.

Clearly a fundamental limitation arises because electron densities above the plasma resonance density (or cutoff density) n_c cannot be measured. The radiation frequency f and the cutoff density are related by $f[\mathrm{Hz}] = 2\pi(n_c e^2/m_e \varepsilon_o)^{\frac{1}{2}} = 8979\ (n_c[\mathrm{cm}^{-3}])^{\frac{1}{2}}$. When microwave techniques are extended to their practical limit ($f \simeq 120$ GHz) n_c is only of the order of 10^{14} cm^{-3}; the interferometric measurement of higher densities requires

a higher radiation frequency. However the minimum detectable density, corresponding to the smallest phase-shift which may be measured by a given interferometer, is simply proportional to the radiation frequency f. The result is that the use of optical or infrared radiation does not generally give satisfactory sensitivity.

Thus it is apparent that the radiation chosen to probe a plasma should not have its cutoff density very much higher than the largest densities of interest. The 337 μm (f = 890 GHz) HCN line with its cutoff density near 10^{16} cm^{-3} is particularly favourably placed in this regard; it considerably extends the range of densities accessible to microwave interferometry but overlaps part of this range. Furthermore, since the maximum density which may be measured is proportional to f^2 and the minimum density is proportional to f the dynamic range of a far-infrared interferometer is somewhat better than that of its microwave counterpart. We have already seen that in principle the 337 μm line allows electron density measurements up to its cutoff density of 10^{16} cm^{-3}; on the other hand, we shall show in Ch. 7 that under suitable conditions densities as low as 2×10^{12} cm^{-3} may be measured. This wide potential range makes 337 μm interferometry a very attractive diagnostic technique. Further advantages are discussed in Chs. 6 and 7, where we have

exploited not only the 337 μm wavelength but also the advantages of the self-modulating laser interferometer principle.

But the foregoing discussion leads us to an interesting observation. Since electron densities as low as 2×10^{12} cm^{-3} can cause measurable phaseshift of 337 μm radiation and since the discharge of the HCN laser itself has densities of 2×10^{12} cm^{-3} and larger (see Ch. 3) then the laser plasma must significantly change the phase of the radiation propagating through it. In a continuous laser this is of little consequence but in the pulsed laser, where the electron density is actually decaying during the period of laser emission it is very important. We may view the laser discharge as having a time-varying effective length (through the refractive index of its plasma electrons). Resulting from this, any particular laser cavity mode has a time-varying resonant frequency. Now the beat frequency between adjacent low-loss cavity modes is generally greater than the linewidth of the laser transition in HCN lasers so that under suitable conditions laser action may only occur when the frequency of one or more low loss modes is swept through the spontaneous emission line. Under such conditions the laser output pulse shape, as well as its delay and duration, will be determined by this cavity mode sweeping

effect; multiple mode sweeping will produce "spiking" output.

These are the plasma effects which we mentioned in Sec. 1.1 and they are studied in detail in Chs. 3, 4 and 5. Firstly however, we shall examine in Ch. 2 the generation of far-infrared radiation with HCN gas lasers.

Chapter 2

FAR-INFRARED WAVE GENERATION WITH HCN LASERS

2.1 Introduction

Since the initial observations in 1964 of far-infrared lasing in cyanide compounds (Gebbie et al, 1964) many groups have studied the radiation generated by both pulsed and continuous electrical discharges through a variety of gas mixtures and organic vapours containing the elements carbon, nitrogen and hydrogen. These studies have clarified many features of the laser action, but the mechanisms of the gas discharge which produce emissive molecules in inverted population states are very complex and are in need of more detailed investigation.

The work that has been done can be divided into four categories: (a) spectroscopic studies of the line emissions and the consequent identification of the HCN molecule as the source of the 337 μm line and other lines, (b) studies of modes of excitation of the resonator, (c) observations of the output power, pulse shapes, etc., under a variety of discharge conditions, and (d) studies of chemical and physical properties of the active emissive medium itself. Topics (a) and (b) have been investigated

in considerable detail. The frequencies of the various emission lines have been carefully measured (Hocker et al, 1967; Hocker and Javan, 1967; Mathias et al, 1968), and the precise vibrational-rotational transitions of the HCN molecule involved in the generation of the 337 μm line and associated lines established (Lide and Maki, 1967; Maki, 1968). Theoretical and experimental studies (Kneubühl and Steffen, 1967; Steffen and Kneubühl, 1968; Schwaller et al, 1967) of the resonances in Fabry-Perot resonators with plane and concave mirrors have enabled the identification of the modes of excitation. The literature shows that topics (c) and (d) have been less thoroughly investigated. There is a need for a study of the dependence of laser output power on a full range of discharge parameters covering and extending the previous partial investigations, and there is a need also for study of the plasma properties of the discharge for these have hitherto been almost totally ignored.

It should be stated at the outset that our principal interest in this chapter is in the pulsed HCN laser. We first describe the design of a pulsed HCN laser which was built specifically to allow study of topics (c) and (d) mentioned above. We then describe an experimental investigation of laser operation at 337 μm, leaving the study of plasma effects in the pulsed HCN laser until

Chs. 3, 4 and 5. We then describe a continuous HCN laser which was built for use as a source for 337 μm interferometry. The performance of this laser is not studied in detail; we merely present operating characteristics which are important in our studies of laser interferometry (Chs. 6 and 7).

The present state of understanding of HCN lasers is dispersed in a literature of about one hundred papers. It is desirable therefore, as a background to our studies of HCN lasers, to summarize some of the most significant relevant features of this level of understanding. This is done in the next section.

2.1.1 Background to HCN Lasers

Consider the situation of a low pressure (1 torr) mixture of gases containing the elements carbon, nitrogen and hydrogen which fills a Fabry-Perot resonator designed to have low losses at far-infrared wavelengths. If a pulsed electrical discharge suddenly delivers approximately 1 eV per molecule to this gas mixture it becomes partially ionized ($\lesssim$ .1%) and in the subsequent decay many chemical reactions take place. Among the reaction products the formation of hydrogen cyanide is highly favoured but even so, not very much of it is formed (estimated partial pressure $\approx$ 1 mtorr; Chantry, 1971). If the gas mixture is flowing through the resonator at a constant rate, and if it is pulsed repetitively, an equilibrium concentration of HCN will be maintained. Now each discharge pulse excites the hydrogen cyanide molecules into various modes of vibration and rotation. If conditions are favourable, some of the vibration-rotation levels will have higher populations than levels slightly lower in energy. For hydrogen cyanide this state of population inversion is readily achieved for a number of pairs of energy levels whose separations are so small that downward transitions between them cause the emission of far-infrared photons. If the resonator is tuned to the wavelength of one of these transitions laser

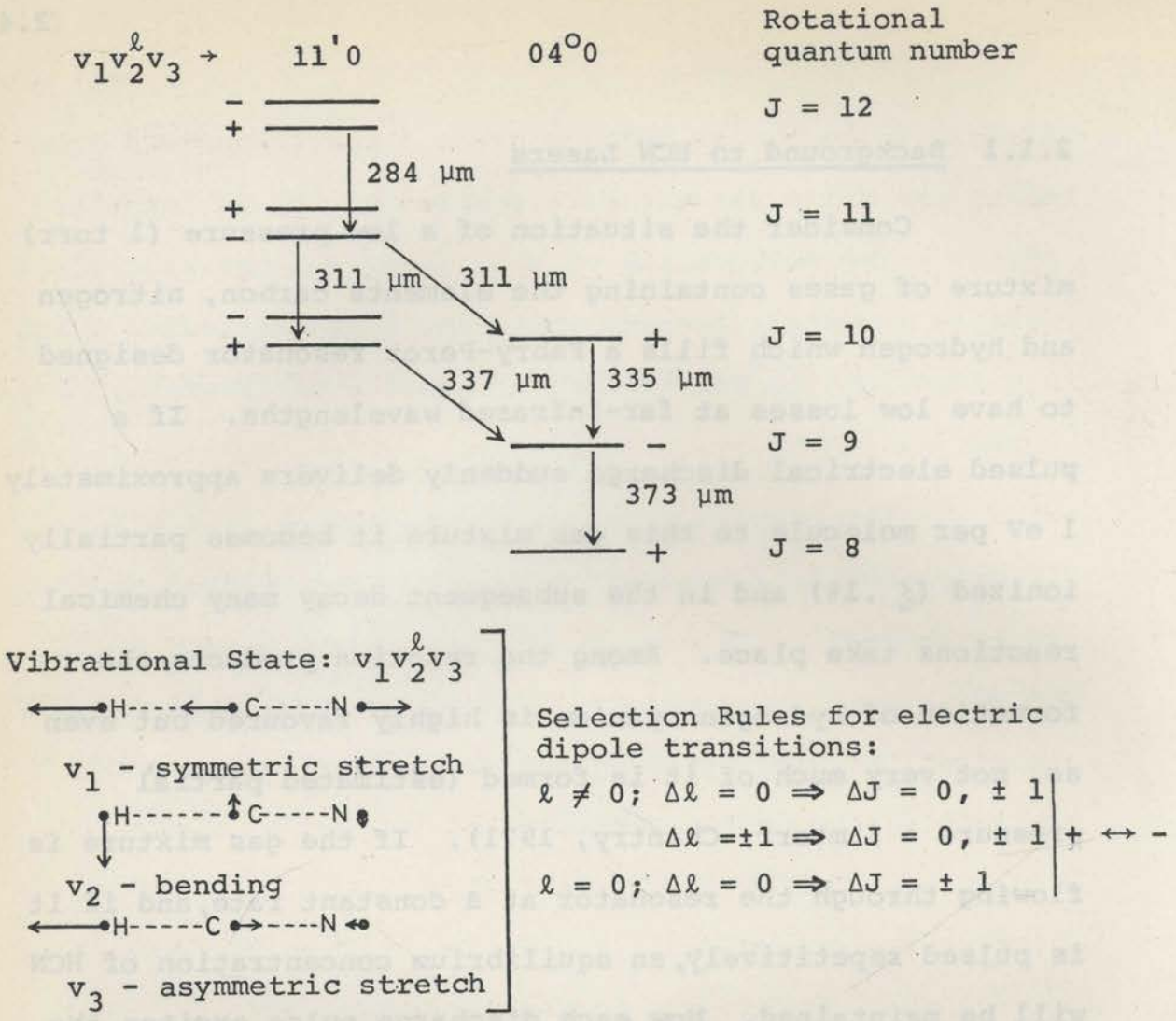

Fig. 2.1. Energy Level Scheme for the Observed Transitions of HCN near 300 μm.

For a molecule which is not rotating the v_2 bending mode is a degenerate pair because vibrations in the plane of the page and perpendicular to it are indistinguishable. However, certain combinations of these two vibrations give rise to rotation of the molecule about its axis with angular momemtum component $\pm \ell h$. The quantum number $|\ell|$ is written as a superscript after v_2. In the case of a rotating molecule the two possible values $\pm \ell h$ of vibrational angular momentum split the rotational levels into pairs when $|\ell| \neq 0$. This splitting, known as ℓ-type doubling, accounts for the pairs of rotational levels of the 11'0 vibrational state. The alternate plus and minus signs refer to the symmetry of the wavefunctions of the rotational states. For further explanation see Townes and Schawlow (1955).

action will be observed and a small amount of coherent far-infrared radiation may be coupled out of the cavity.

Stimulated emission by hydrogen cyanide molecules has been observed at more than a dozen wavelengths throughout the far-infrared. About one half of them are pure rotational transitions; the rest are vibrational-rotational, as is the strongest line which occurs at a wavelength of 337 μm. Figure 2.1 shows the energy level scheme (Lide and Maki, 1967) for the family of HCN lines near 300 μm. The energies of the vibration-rotation levels, all of which are about 2800 cm^{-1} above the ground state, are known quite accurately from infrared studies of HCN. The calculated frequencies of the far-infrared lines agree with the observed frequencies within 0.01 cm^{-1}. Precise frequency measurements (Hocker and Javan, 1967) have verified that the parallelogram formed by the 310 μm, 311 μm, 335 μm and 337 μm lines in Fig. 2.1 closes to 1 part in 10^6. Thus there is little doubt about the validity of this assignment. All of the other HCN lines lie between 110 μm and 165 μm. In the discussion which follows however, attention is restricted to the 337 μm transition and the 337 μm HCN laser. Reference to Fig. 2.1 shows that the 337 μm transition occurs between the $11^{1}0$ and $04^{0}0$ vibrational states, and involves a simultaneous change from the J = 10

to the J = 9 rotational state. Such a transition would not normally be very probable but the near degeneracy of the $11^{1}0$ and $04^{0}0$ states at J = 10 causes Coriolis coupling and significant mixing (or overlapping) of the wave-functions of the two states. This allows a much higher transition probability.

Hydrogen cyanide lasers are typically several metres long and 10 cm in diameter, and because far-infrared window materials tend to be lossy they usually employ internal mirrors. Metallic reflectors with output coupling apertures are commonly used because partially transmitting reflectors are virtually non-existent in the far-infrared; notable exceptions are metal grid reflectors which have been used with a fair degree of success (Yamanaka et al, 1968).

Both hole-output and grid reflectors seriously perturb the mode structure of the laser. Alternative forms of output coupling use a beamsplitter mounted inside the laser resonator or an annular transmitting region around the edge of a laser mirror. This latter method merely couples out the diffraction losses of the Fabry-Perot resonator. The optimum output coupling for pulsed HCN lasers is of the order of 10% per pass.

The emissive material or fuel used in HCN lasers

can be almost any organic vapour (e.g. CH_3CN) or mixture of gases (e.g. methane and nitrogen) containing the elements carbon, nitrogen and hydrogen. In a 2 m long discharge tube, a pulsed electrical discharge delivering of the order of 10 Joules (ten times per second) to 10 litres of such a fuel at a pressure between 0.1 and 1 torr gives a pulsed gain of up to 0.7 per metre (Jones et al, 1969) while a D.C. discharge (e.g. 1 kV at 1 A) gives a continuous gain in the vicinity of 0.1 per metre (Jones et al, 1969). However, in a repetitively pulsed laser or in a D.C. laser the fuel is quite rapidly used up and a flowing gas mixture is required. In fact, the flow rate is as important as any other of the abovementioned parameters and the performance quoted would only be obtained at the optimum flow rate which is of the order of 1 litre/sec.

With continued use HCN lasers build up a deposit of brown polymer film on their walls and it seems that the formation of this is associated with the removal of HCN from the discharge. Murai (1969) has observed spectroscopically that a discharge through nitrogen in a vessel contaminated by the brown wall deposit results in the formation of cyanide (CN^-) ions and that this production is enhanced by the addition of bromine to the discharge. He suggests that the cyanide ions thus formed in a laser

discharge may react with hydrogen ions to form HCN. In support of this he finds that a given static filling of gas will lase for hours if bromine is included in the gas mixture but only for minutes if it is not.

When excited by short current pulses ($\lesssim$ 10 μsec duration) HCN lasers produce a single output pulse in the afterglow of the discharge (Fig. 2.5). Peak powers of 1 to 10 W are common for the 337 μm line and pulse durations of 10 to 50 μsec are typical. With long current pulses of lower amplitude lasing can occur during the period of active excitation but under these conditions the output radiation occurs as a succession of short ($\sim$ 1 μsec) spikes followed by the usual pulse in the afterglow which is longer in duration (Fig. 5.1). The origin of this spiking is discussed in Ch. 5.

With one kilowatt of excitation continuous HCN lasers produce milliwatts of power at 337 μm while the figures in the previous paragraph imply that a pulsed laser working at 10 pulses per second delivers an average power of 0.1 to 1 mW. Assuming 10 J per electrical discharge pulse the average excitation of the latter is 100 watts. Thus the efficiencies of the pulsed and continuous HCN lasers are about the same; they are about 10^{-3} to 10^{-4} %. It is interesting to compare this with

the maximum possible efficiency which may be achieved by pumping the upper laser level from the ground state of the HCN molecule. The ground state is about 2800 cm^{-1} below the $11^{1}0$ and $04^{0}0$ vibrational states and their separation is about 30 cm^{-1} (Lide and Maki, 1967). The maximum efficiency, taken as the ratio of these figures, is about 1%. Thus in principle, a considerable improvement in the efficiency of HCN lasers is possible.

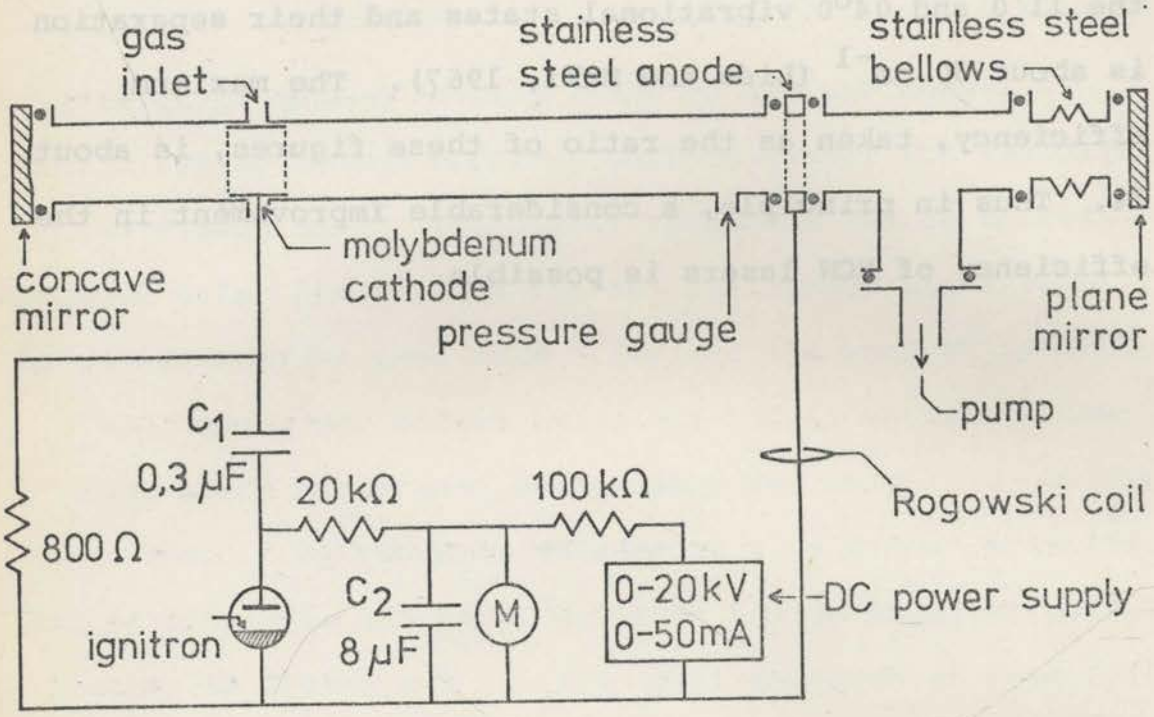

Figure 2.2. Diagram of the pulsed HCN gas laser.

The laser vessel has a length of 2.2 m between mirrors, a diameter of 7.6 cm and discharge electrodes 1.5 m apart. The peak discharge voltage was measured with the meter M and the pulsed current was observed by integrating (τ = 1 mS) the output of the Rogowski coil and displaying it on an oscilloscope.

2.2 A Pulsed HCN Gas Laser

2.2.1 Mechanical Design

The pulsed laser (Fig. 2.2) is constructed from 7.6 cm I.D. pyrex pipe sections, joined by means of annular stainless-steel flanges with O-rings in grooves and sealed at its ends by the resonator mirrors. A stainless steel flange near one end of the laser is used as the positive discharge electrode; the other electrode is a 5 cm x 24 cm strip of thin molybdenum wrapped inside the pyrex pipe to form a short tube. The electrodes are 1.5 m apart and positioned symmetrically with respect to the laser mirrors which are 2.2 m apart. The mirror at the high voltage end of the laser is clamped directly to the end of the vessel. At the earth end the mirror is mounted on a flexible bellows and its tilt and axial position are adjusted by three micrometers. Adequate vacuum is provided by a single stage mechanical pump connected to a sidearm in the discharge tube near the earth end of the laser. Base pressures in the vicinity of 20 mtorr are readily achieved even in the presence of the brown deposit which builds up on the walls of the discharge tube in normal operation.

The pressure in the laser was measured by means of a Pirani gauge which was calibrated against a mercury

McLeod gauge. No precautions were taken to prevent mercury vapour from entering the laser vacuum system although the McLeod gauge was isolated when not in use. No adverse effects on laser operation were observed, even when the McLeod gauge was used while the laser was running.

2.2.2 Gas Inlet and Monitoring System

The gas used in the laser consists of a mixture of approximately equal quantities of methane and nitrogen, flowing at about 1 litre/second at a total pressure near 1 torr. The flow rates of the gases are individually controlled by needle-valves and measured upstream of the needle-valves at a pressure of approximately 100 cm Hg. Commercial flowmeters consisting of a sapphire ball in a vertical tapered capillary tube were used. The operation of the flowmeters is not viscosity dominated so that their calibrations are not strongly temperature sensitive. Temperature variations are quite validly ignored as the laser is housed in an airconditioned laboratory (T = 22 ± 3C). The flowmeters were calibrated by timing the displacement of a known volume of (saturated) water at atmospheric pressure for each individual flow rate which was used. As the flow rates were very small the accuracy of this procedure was limited only by the accuracy of the volume measurement. It was estimated to be 10%. Pressure

measurements were made with aneroid-type pressure gauges to an accuracy of a few percent. In practice the gas inlet system operated with sufficient precision to ensure very reproducible laser performance (e.g. see Fig. 2.7).

2.2.3 The Laser Resonator

In the study described in Sec. 2.3.3 the laser resonator consisted of an 8 m radius spherical mirror at the high voltage end of the laser and a plane mirror at the earth end. The concave mirror was aluminized to a diameter of 5.1 cm but the plane mirror had an aperture of only 3.8 cm on a fused quartz plate. Laser output was extracted through the quartz plate from the annular region bounded by the aluminizing of the plane mirror and the inside diameter of the bellows on which it was mounted (5.1 cm). As this resonator configuration was used quite extensively it is worthy of some discussion.

Firstly, the aperture of the resonator is restricted to a maximum of only 5.1 cm while the diameter of the discharge tube is 7.6 cm. Murai (1969) has shown that wall chemistry can play an important role in HCN lasers using a static filling of gas but it is probable that wall chemistry also plays a role when a flowing gas is used. Restricting the aperture of our resonator does tend to be wasteful of active medium but has the advantage

of confining the region of laser amplification to the vicinity of the centre of the discharge. It follows that the continuous buildup of brown wall deposit with use of the laser will be less likely to cause a long term variation in its performance. This is highly desirable for the experimental investigation presented in Sec. 2.3.3. Another advantage of the small aperture resonator is that excitation of "tube modes" (Steffen and Kneubühl, 1968) which depend on reflection of radiation by the inside wall of the discharge tube will be much less likely. Tube modes are undesirable in our mode studies in connection with the observations of spiking output (Ch. 5) because they are far more complicated than the modes of an open resonator. They are also undesirable because the buildup of brown deposit on the tube wall will cause long-term variation in its reflection coefficient.

Secondly, the choice of annular output coupling has the advantage that it perturbs the modes of the resonator and their relative losses far less seriously than the very popular hole-type output coupling. Hole-output coupling preferentially loads axial modes and may prevent them from oscillating at all (McCumber, 1969). Nevertheless hole-output coupling was used for some observations of spiking (Ch. 5) and exclusively for

experiments with continuous HCN lasers. Beamsplitter output coupling was not used because of the difficulty of mounting a beamsplitter in the laser vacuum system and providing suitable output windows.

The diffraction loss of the resonator described above is obtained as follows. One first uses the equivalence relations given by Kogelnik and Li (1966) to find an equivalent plane-concave resonator with mirrors of equal apertures. It is then straightforward to use the numerical results of Li (1965) for the diffraction losses of the TEM_{00} and TEM_{01} modes for such resonators. This procedure gives a value of 22% loss per pass for the TEM_{00} mode and 60% per pass for the TEM_{01} mode. Of course, one would expect the latter mode to oscillate only under very high gain conditions. However, it is worth noting that Li's theory does not take into account the possibility of internal wall reflections. Steffen and Kneubühl (1968) have calculated the effect of the glass walls on the modes of a plane-parallel resonator and found that their losses are much lower than for the modes of an open resonator. They have also verified this result experimentally. However, we do not expect wall reflections to play an important role in our small-aperture resonator.

The rather high value of 22% for the loss per pass of the TEM_{00} mode is not surprising when one realizes

that the spot diameters (calculated on the basis of infinite mirror apertures (Kogelnik and Li, 1966)) on the two mirrors are both of the order of 4 cm. According to Gordon and Kogelnik (1964) the ratio of the spot size w to aperture a may be taken as a measure of the loss at a mirror. It follows that if the subscripts 1 and 2 refer to the two mirrors of a resonator then the quantity $w_1 a_2 / w_2 a_1$ is a measure of the relative magnitudes of the diffraction losses occurring at the two mirrors. For the present resonator this ratio has a value of 1.1 when subscript 1 refers to the plane mirror. Thus slightly more than half of the diffraction loss of the resonator appears as output.

Finally, it is interesting to calculate the Q of the resonator for the TEM_{00} mode. If the steady radiation intensity in the cavity corresponds to N photons then 0.22 N are lost per (one-way) transit. Thus the Q is approximately $2\pi \times 1/0.22 \times d/\lambda$ where d is the length of the resonator and λ is the wavelength. Assuming λ = 337 μm which corresponds to the strongest of the HCN lines, gives a value of 2×10^5 for Q. The e-folding time for decay of photons in the resonator is Q/ω (Garrett, 1967) or approximately 0.03 μsec. This is significantly shorter than the decay times of 337 μm pulses normally observed.

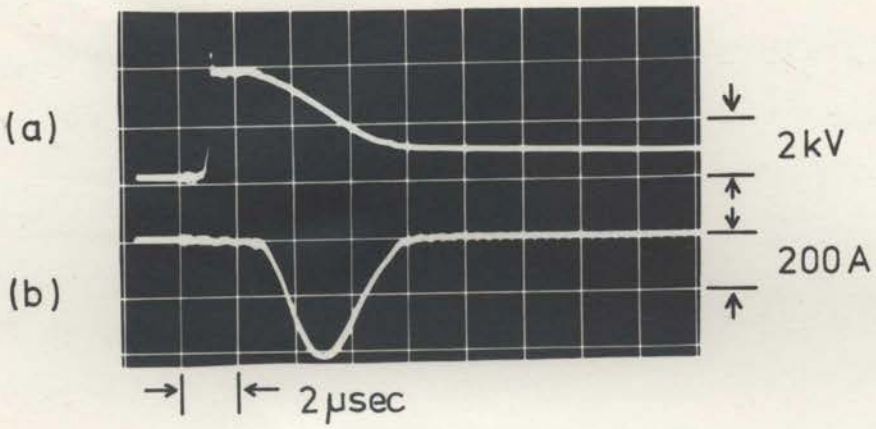

Fig. 2.3. Typical voltage (a) and current (b) waveforms for the laser discharge. There is a delay of ∿ 2 μsec between triggering the ignitron and the commencement of gas breakdown. This delay decreases slightly at higher discharge voltages but at any particular discharge voltage it is quite reproducible. Although the discharge extinguishes before the voltage across it falls to zero the 800 Ω dump resistor (Fig. 2.2) ensures that the energy storage capacitor is fully discharged before the next pulse. This is important in reducing pulse to pulse variations in laser excitation.

2.3 Empirical Study of the Performance of the Pulsed Laser

2.3.1 Electrical Properties of the Gas Discharge

In normal operation, with a mixture of roughly equal proportions of methane and nitrogen at a total pressure of about 1 torr, the laser requires a discharge voltage in the range 4 to 10 kV for maximum output pulse energy. This produces a current pulse of duration 3 to 4 μsec and peak amplitude 400 to 2000 A in the discharge circuit of Fig. 2.2. Typical voltage and current waveforms are shown in Fig. 2.3. The discharge voltage is not measured from a waveform such as that shown in Fig. 2.3(a) however but from the meter M across capacitor C_2 in Fig. 2.2. This capacitor is necessary to allow rapid recharging of the discharge capacitor C_1 (Fig. 2.2) between pulses when repetition rates up to 20 per second are used. C_2 also has the desirable effect of reducing pulse to pulse variations in the discharge current. The pulsed current is measured by means of a Rogowski coil which is conveniently calibrated by comparing the steady current which charges C_2 with the integral of the current waveform (Fig. 2.3(b)) multiplied by the pulse repetition rate.

In addition to the discharge capacitor C_1, and the impedance of the gas discharge which is largely

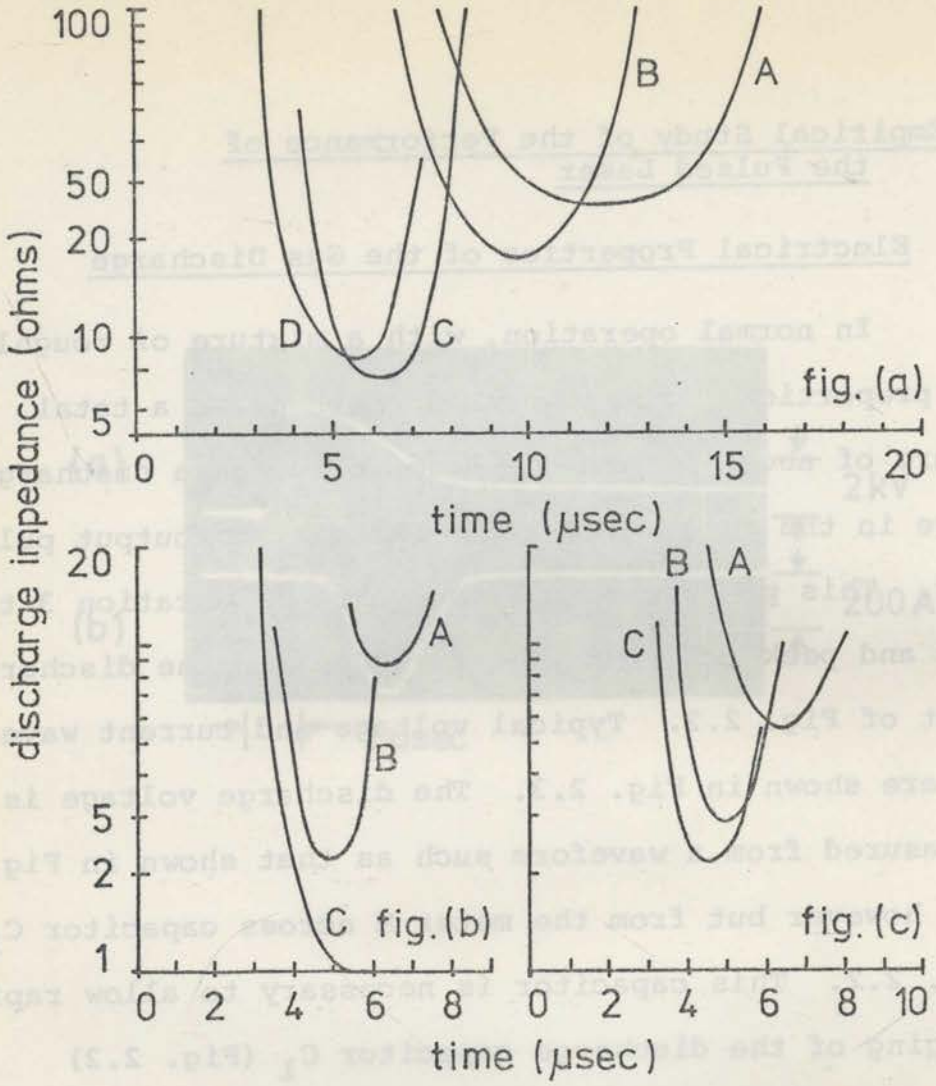

					V			
fig	n	p	f	R	A	B	C	D
(a)	10	.65	.9	1	5.0	5.5	6.5	7.0
(b)	10	.73	.5	1/2	5.1	6.6	8.0	-
(c)	10	.63	.8	2/9	5.2	6.9	7.9	-
Units	p.p.s.	torr	ℓs^{-1}	-	kV	kV	kV	kV

Fig. 2.4. Impedance of the HCN laser discharge as a function of time. The symbols used are:

n - pulse repetition rate (pulses per sec).
p - total pressure (torr).
f - total flowrate (litres sec^{-1}).
R - ratio of nitrogen flowrate to methane flowrate.
V - discharge voltage (kilovolts).

resistive, the discharge circuit of Fig. 2.2 includes about 4 μH of series inductance. Thus when the ignitron is triggered there is a tendency for the circuit to ring unless it is critically damped or overdamped. This is undesirable as the ignitron is erratic in its conduction of reverse currents and this results in large fluctuations in laser output power. For C_1 = 0.3 μF the circuit is critically damped when the discharge resistance is about 7 Ω but reverse current does not flow if the discharge resistance is greater than about 1 Ω. Figure 2.4 shows the discharge impedance as a function of time for a range of operating conditions. It is greater than 1Ω for most conditions and no ringing is observed. If C_1 is reduced to 0.2 μF however, the discharge current does ring under some conditions.

Kon et al (1967) have observed that, if all other parameters are kept constant, the performance of a pulsed HCN gas laser depends only on the input pulse energy. In view of this there is no reason why C_1 should not be quite large (so long as the appropriate discharge voltage remains high enough to produce breakdown); a lower discharge voltage is safer to use and reduces noise pickup in sensitive detection circuits. In the present laser however, a value much larger than 0.3 μF is not convenient because of the limited current available from the D.C.

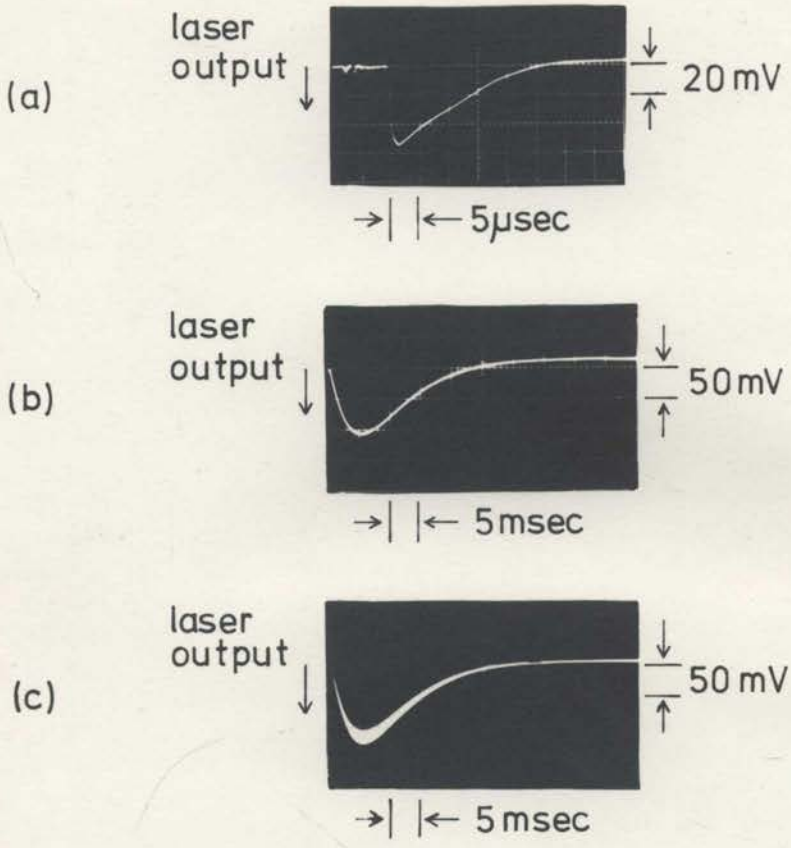

Fig. 2.5. Records of the 337 μm Output of the Pulsed Laser

(a) Shows the time resolved 337 μm output observed with a Putley Detector.

(b) Shows the response of a Golay cell to a pulse like that in (a).

(c) Shows a superposition of fifty Golay cell records indicating the normal fluctuations in laser output pulse energy.

power supply (Fig. 2.2). In any case, the laser produced more power with C_1 = 0.3 μF than with C_1 = 0.4 μF in contradiction to the results of Kon et al (1967) (Sec. 2.3.3.1).

2.3.2 The Laser Output

Wavelength measurements with a far-infrared Michelson (N.P.L. cube) interferometer and a mesh-type Fabry-Perot interferometer (Advanced Kinetics, FIR 1) indicated that the laser output always consisted entirely of 337 μm radiation. No other wavelengths were observed. With the pulsed discharge described in Sec. 2.3.1 the output of the laser occurs as a single pulse of 337 μm radiation in the afterglow of the discharge. It is delayed 0 to 10 μsec with respect to current extinction and its duration is 10 to 50 μsec. Figure 2.5(a) shows such a pulse, observed with a liquid helium cooled Putley detector (t_r = 0.2 μsec; see Appendix 1) working at 4.2 K with a 25 kG magnetic field. The exact values of the delay and duration of the laser output pulse (as well as its shape) change as the length of the laser resonator is altered. The explanation is that laser emission occurs as the time-varying refractive index of the plasma electrons sweeps the effective length of the cavity through a resonant length. This effect is studied and

discussed in detail in Ch. 4. However, the pulse shown in Fig. 2.5(a) is representative of the output obtained when the resonator length is tuned to give maximum output pulse energy.

Because of the variability of laser pulse shape, output pulse energy is a more suitable measure of laser performance than peak output power. Thus, in a study of laser performance over a wide range of operating conditions it is appropriate to integrate the detector output or alternatively, to use a slow detector. Figure 2.5(b) shows the response of a Golay cell (t_r = 25 mS; see Appendix 1) to a laser pulse like that of Fig. 2.5(a). This detector effectively integrates the laser output pulse giving a pulse whose peak amplitude is simply proportional to pulse energy. The Golay cell is a room temperature detector and therefore much more convenient to use than a Putley detector. Because its use is entirely appropriate anyway, the whole study of laser performance presented in Sec. 2.3.3 was carried out using a Golay cell. The method of recording pulse energy is shown in Fig. 2.5(c) which is a superposition of fifty laser output pulses observed with the Golay cell. This method has the advantage of simultaneously recording fluctuations in pulse energy. These fluctuations are attributed to discharge inhomogeneity, perhaps arising

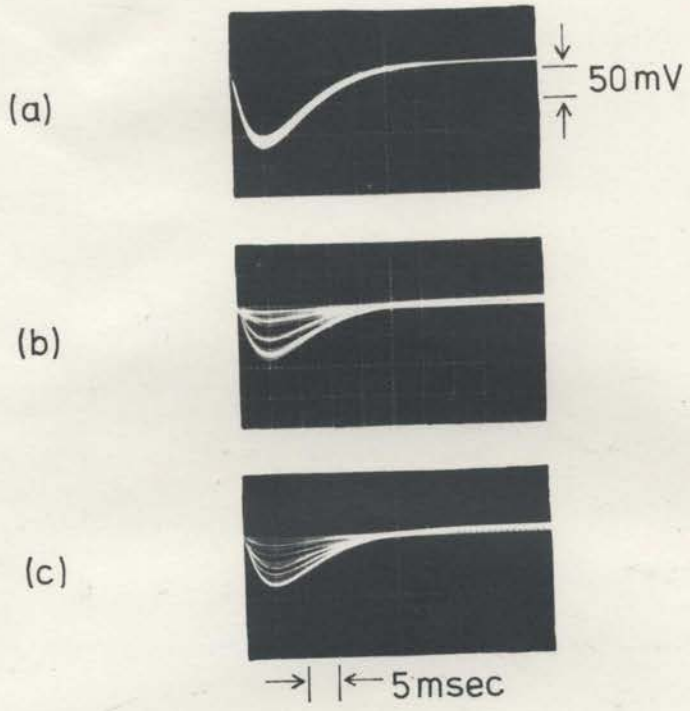

Fig. 2.6. Polarization Characteristics of the 337 μm Pulsed Output.

(a) Shows a superposition of fifty Golay cell traces for the laser working under normal conditions.

(b) Shows the same output as (a) when a polarizer is placed between the laser output window and the Golay cell.

(c) Shows the same output again, this time with the polarizer rotated 90° with respect to its orientation in (b).

The reduced amplitude in (b) and (c) is due to attenuation by the polarizer.

from the fact that the discharge always emanates from one or two of a number of preferred points on the surfaces of the annular electrodes. These inhomogeneities apparently play an important role in determining the polarization of the laser output, as much larger fluctuations in output power are observed when only one component of polarization reaches the detector. Figures 2.6(a), (b) and (c) show this effect.

The peak output power of the laser was estimated by comparing Golay cell and Putley Detector records of the laser output. The Golay cell was assumed to have its nominal responsivity (Appendix 1). Our measurements indicate that the maximum peak output power of the laser was of the order of 100 mW.

2.3.3 Dependence of Laser Pulse Energy on Various Parameters

2.3.3.1 Continuous Gas Flow

The power generated by the pulsed laser is a function of many variables; the most important of these are the gas mixture, pressure and volumetric flowrate, as well as the discharge voltage and pulse repetition frequency. In this study the effect of varying each of these variables while keeping all of the others constant is determined. This leads to a phenomenological under-

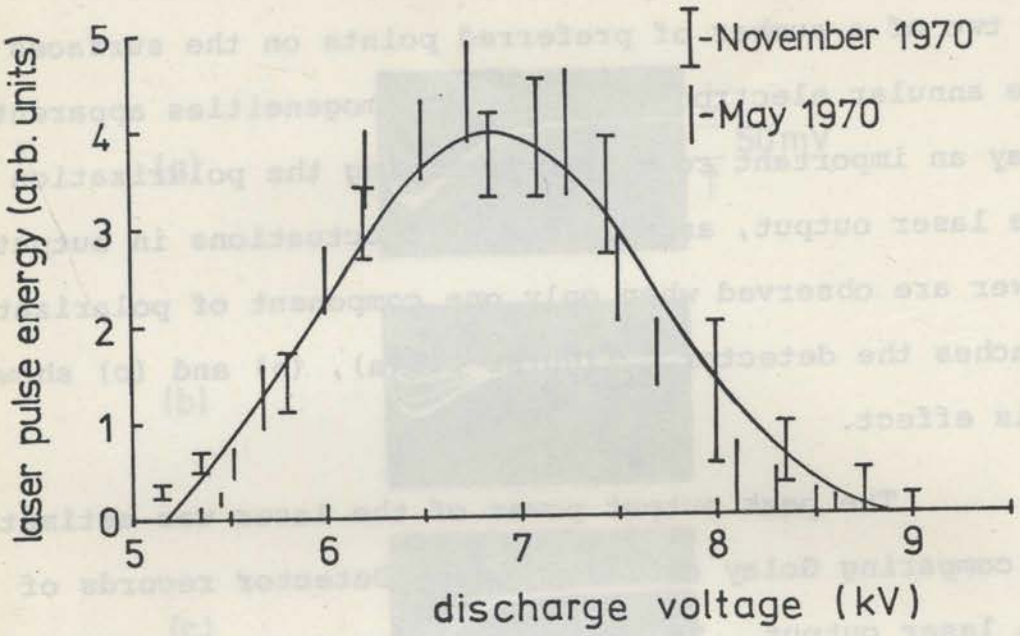

parameter	n	p	f	R
value	10	.74	.7	$^1/_2$
units	p.p.s.	torr	ℓs^{-1}	-

Fig. 2.7. Reproducibility of Results: The two sets of error bars show results obtained in May 1970 and again in November 1970 for the dependence of laser output pulse energy on discharge voltage. All other parameters were the same on both occasions. The smooth curve is an estimate of the laser behaviour based on both sets of results.

standing of what happens in a pulsed HCN laser. In addition, an optimum set of operating conditions is evolved.

In view of the fact that this is an empirical study; that there is no theory to compare the results with, it is natural to enquire about their reproducibility. Figure 2.7 shows the variation of laser output pulse energy with discharge voltage for gas conditions similar to those which produce maximum pulse energy. There are two sets of error bars on this curve, one set corresponding to experimental results obtained early in the course of the empirical study and a second set for results obtained five months later, when this study was completed. The error bars indicate the spread in pulse energies obtained from superpositions of fifty Golay cell traces as shown in Fig. 2.5(c). This comparison gives a measure of the reproducibility of the laser behaviour as well as the accuracy with which the gas conditions and discharge conditions could be reproduced and the extent to which the responsivity of the Golay cell may have deteriorated in the intervening period. Taking all these possible variables into account, the agreement between the two sets of results is good. It indicates that there were no serious omissions from the set of laser parameters which were controlled and monitored.

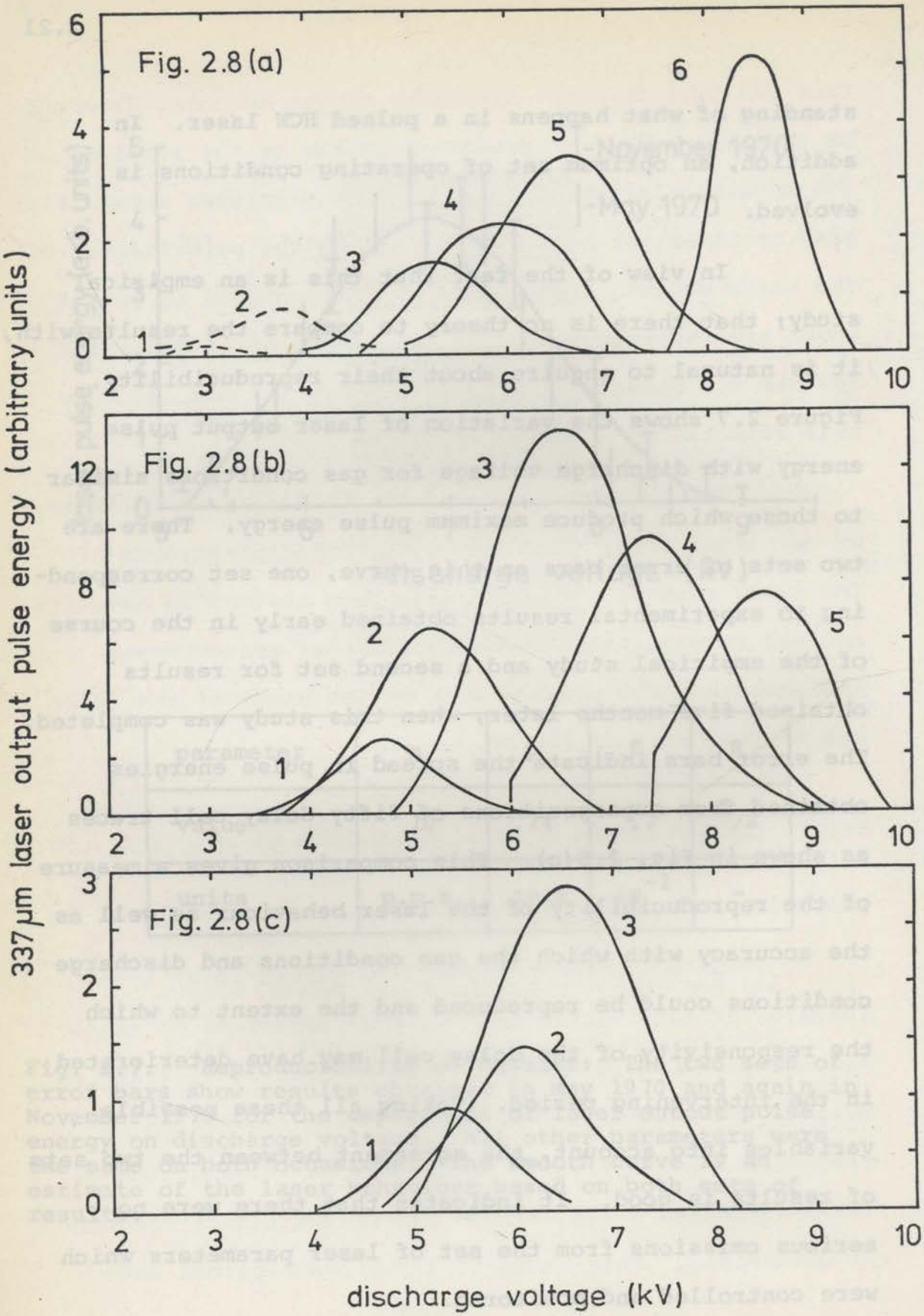
Fig. 2.8(a)
Fig. 2.8(b)
Fig. 2.8(c)
337 μm laser output pulse energy (arbitrary units)
discharge voltage (kV)

Fig. 2.8. Laser Pulse Energy as a Function of Discharge Voltage

The three sets of curves (a), (b) and (c) correspond to different mixing ratios of the nitrogen-methane gas mixture (R). The units on the three ordinates are the same, so it is clear that the R = $^{1}/_{2}$ gas mixture is optimum. Stoechiometrically, this mixture is best for the production of hydrogen cyanide from nitrogen and methane. The dashed curves in (a) are five times actual size.

			Curve						
Fig. 2.8	R	Parameter	1	2	3	4	5	6	Units
(a)	1	p	.24	.32	.45	.60	.65	1.1	torr
		f	.5	.5	.8	.7	.9	.5	ℓs^{-1}
(b)	$^{1}/_{2}$	p	.37	.55	.73	.80	.96		torr
		f	.5	.5	.5	.5	.5		ℓs^{-1}
(c)	$^{2}/_{9}$	p	.5	.55	.65				torr
		f	.7	.7	.4				ℓs^{-1}

Pulse repetition rate (n) = 10 p.p.s.
p = Total pressure (torr).
f = Total flowrate (litres sec^{-1}).
R = Ratio of nitrogen to methane.

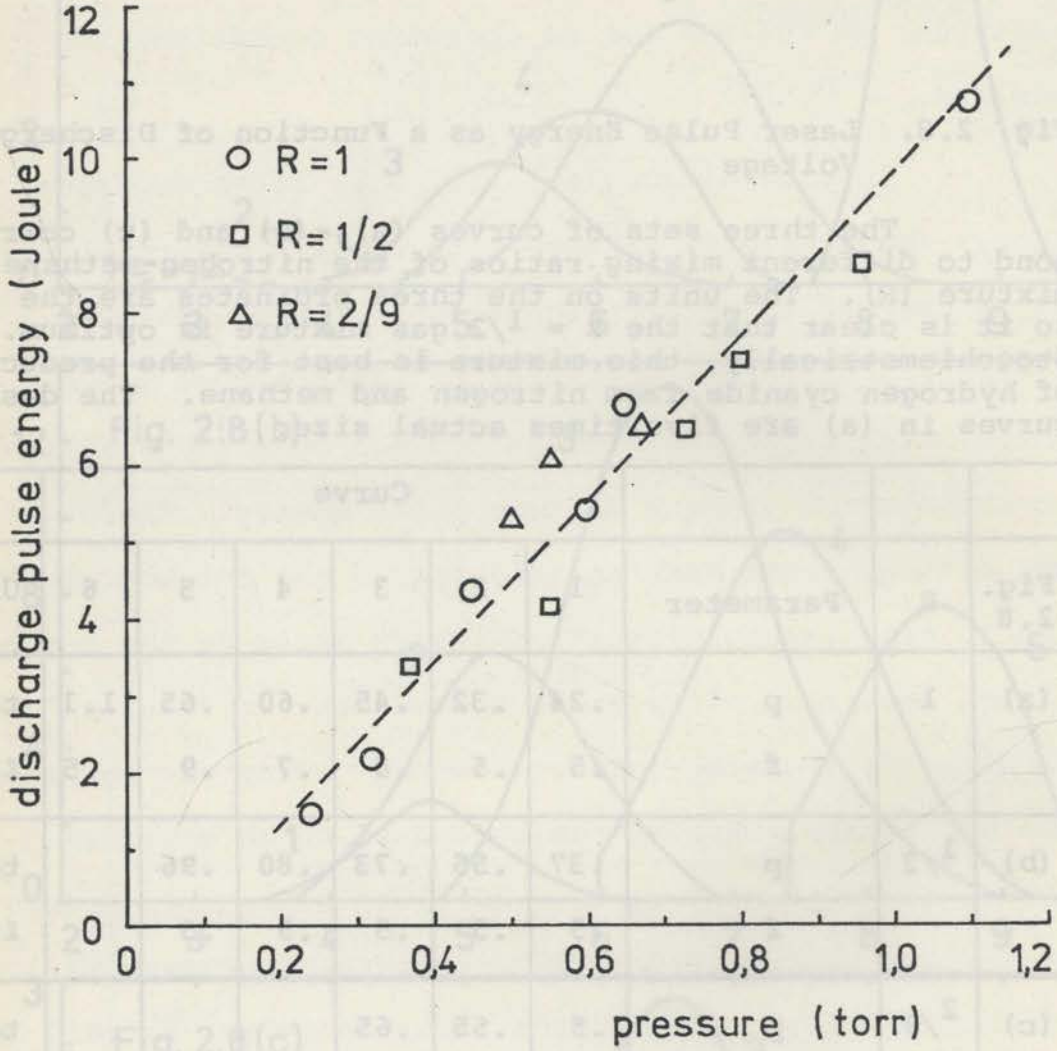

Fig. 2.9. Dependence on gas pressure of the electrical discharge pulse energy required to produce maximum laser output pulse energy. The points plotted are obtained from the maxima of the curves plotted in Fig. 2.8.

The strong variation of laser pulse energy with discharge voltage apparent in Fig. 2.7 was observed with all of the gas conditions which were investigated. In fact, the nature of this variation was always the same, as can be seen in Fig. 2.8 which shows pulse energy as a function of discharge voltage for a wide range of gas conditions. At any particular pressure there is a voltage which produces maximum laser output pulse energy. The laser pulse energy falls off almost symmetrically for voltages above and below the value for maximum output. The reason for fall-off with increasing voltage is not fully understood but is discussed in Sec. 2.3.3.4. The units of energy in Figs. 2.8(a), (b) and (c) are the same, indicating clearly that the gas mixture which produces maximum output power is that used in (b) where the ratio R of nitrogen to methane is ½. It may be significant that this mixture has the highest potential hydrogen cyanide yield. As shown in Fig. 2.8(a) the maximum pulse energy is less when R = 1 although curves are not shown beyond that for maximum output. Methane-rich gas mixtures produce even less laser pulse energy, as can be seen in Fig. 2.8(c) which is for R = $^{2}/_{9}$.

As might be expected, the electrical pulse energy required to produce maximum laser pulse energy at any pressure is approximately proportional to the pressure.

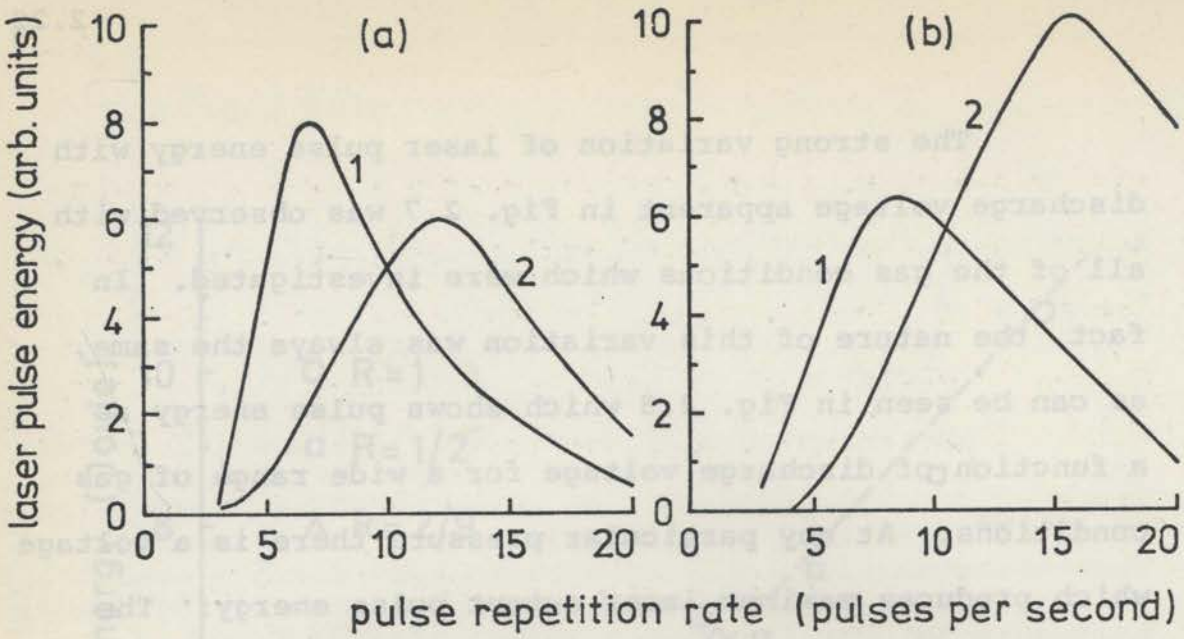

fig.	p	f	R	V
(a): 1	0.58	0.5	1	6.0
2	0.58	0.75	1	6.0
(b): 1	0.37	0.68	1/2	5.0
2	0.68	0.68	1/2	6.5
Units	torr	ℓs^{-1}	-	kV

Fig. 2.10. Variation of laser output pulse energy with discharge repetition rate.

(a) Shows the variation with repetition rate for two different gas flowrates. Evidently, the repetition rate which causes the laser to produce maximum output pulse energy is approximately proportional to the flowrate.

(b) Shows the variation with repetition rate for two different gas pressures. Here the repetition rate which causes the laser to produce maximum output pulse energy is approximately proportional to the pressure. The discharge voltages used in obtaining curves 1 and 2 are close to those corresponding to maximum output for their respective gas pressures (c.f. Fig. 2.8(b)).

Figure 2.9 shows the electrical energy $\frac{1}{2} C_1 V^2$ for maximum laser pulse energy, plotted against pressure, for each of the three gas mixtures. It is most interesting that the proportionality constant between electrical pulse energy and pressure is the same regardless of gas mixture or flowrate.

For constant voltage, pressure, and flowrate there is an optimum pulse repetition frequency which produces maximum energy per laser pulse. Figure 2.10(a) shows this effect for two flowrates and Fig. 2.10(b) for two pressures. It is clear that the optimum pulse repetition frequency increases approximately linearly with both gas pressure and flowrate. The latter effect suggests that at any given pressure there is an optimum number of pulses for a volume element of gas mixture entering the laser to experience while flowing through the discharge region. This optimum number is proportional to the pressure and for the present laser it lies between 100 and 200 pulses. It is natural to interpret this effect as being due to a balance between the rate of hydrogen cyanide production and the rate at which it is subsequently deactivated. Deactivation probably results from some chemical action at the walls of the discharge tube where a brown deposit is formed.

It is not surprising that for constant voltage, pressure and pulse repetition rate, there is a flowrate which produces maximum laser output pulse energy. This can be inferred from Fig. 2.10(a) but is more strikingly illustrated by comparison of Fig. 2.7 and curve 3 of Fig. 2.8(b). Both of these curves show the dependence of laser pulse energy on discharge voltage under identical conditions except for the flowrates. The flowrate for the latter is two thirds of that for the former. As a result the power levels of Fig. 2.8(b) are three times greater than those of Fig. 2.7 but the form of the dependence of output pulse energy on discharge voltage is quite similar. On the basis of these observations and those of the previous paragraph, one might expect the flowrate and pulse repetition frequency to vary in approximate proportion for the maintenance of maximum output pulse energy. That is

$$\left.\frac{\partial n}{\partial f}\right]_{\text{maximum pulse energy}} = \text{constant}. \qquad 2.1$$

Yamanaka et al (1968) have found such a relationship to exist but they give no supporting data. For the wide range of operating conditions investigated with the present laser it is only roughly satisfied.

The dependence of laser output pulse energy on input pulse energy for a number of values of the discharge

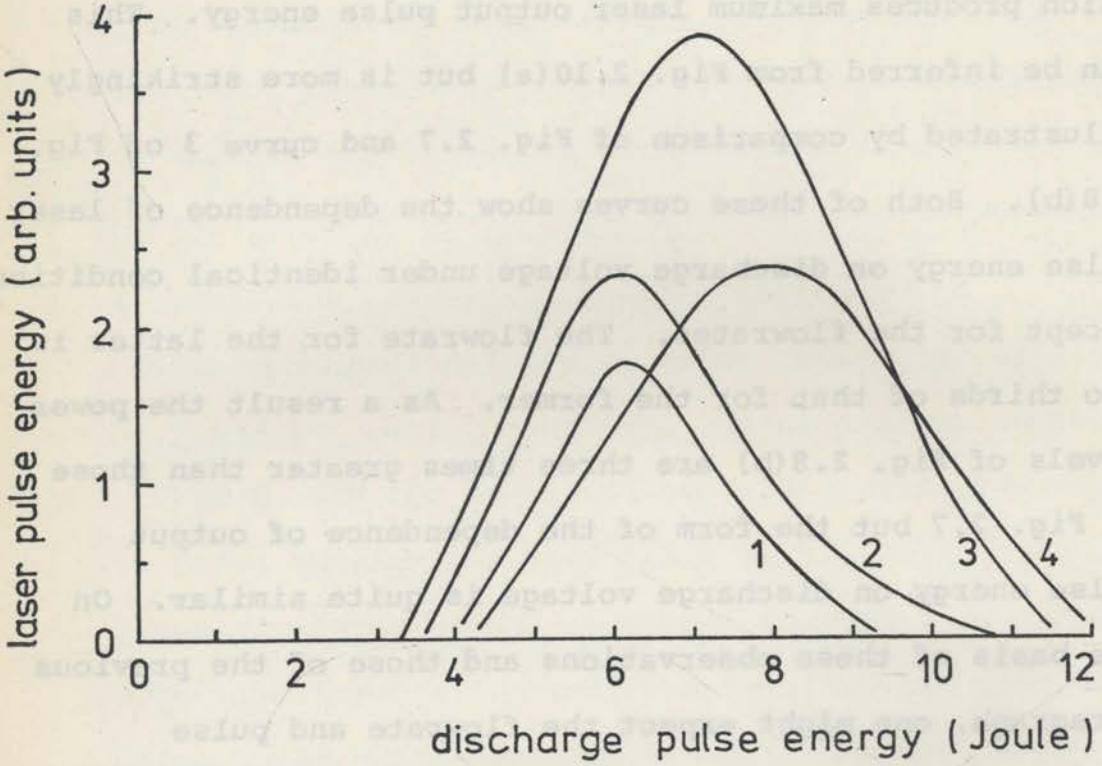

Parameter	n	p	f	R
Value	10	.73	.7	$^1/_2$
Units	p.p.s.	torr	ℓs^{-1}	-

Fig. 2.11. Laser output pulse energy as a function of the electrical energy input to the gas discharge for different values of the discharge capacitor C_1 (Fig. 2.2). Curves 1, 2, 3 and 4 are for C_1 = 0.4, 0.3, 0.2, and 0.1 μF respectively.

capacitor C_1 of Fig. 2.2 is shown in Fig. 2.11. Kon et al (1967) have presented results showing that the laser output energy depends only on the value of the electrical energy input to a static filling of C_2H_5CN pulsed once per second. The results of Fig. 2.11 indicate that this is not the case for a flowing mixture of nitrogen and methane; changing C_1 does make some difference to the laser output energy. Although increased laser output is available when C_1 = 0.2 μF the discharge circuit is subject to ringing (see Sec. 2.3.1) under some circumstances. For this reason a value of C_1 = 0.3 μF was used for studying the performance of the laser over a broad range of the variables which affect it.

2.3.3.2 Static Filling

With a static filling of gas, lasing starts only after several discharge pulses; the pulse power then rises to a maximum after a definite number of discharge pulses, and falls gradually to zero by the time approximately twice this number of pulses has elapsed. This behaviour is consistent with the observation in the previous section that maximum power output occurs under continuous flow conditions for particular combinations of flow rate and pulse repetition frequency which subject an element of the gas to an optimum number of discharge pulses.

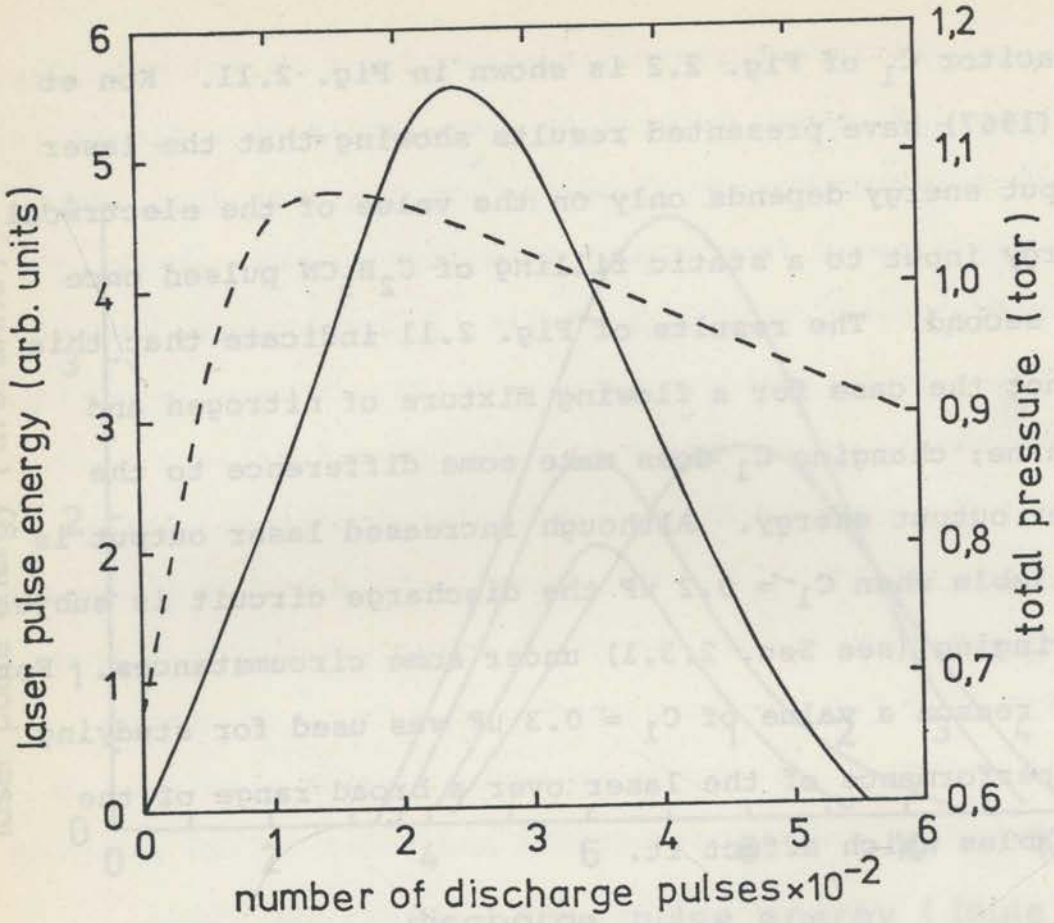

Parameter	n	f	R	V
Value	1	0	1/2	7.0
Units	p.p.s.	-	-	kV

Fig. 2.12. The dependence of laser output pulse energy (full curve) and gas pressure (dashed curve) on the number of discharge pulses in a static filling of gas.

The results of a static filling experiment plotted in Fig. 2.12 show not only that the power rises to a maximum and subsequently decays but that the pressure in the discharge vessel behaves similarly. It increases rapidly with the early discharge pulses and rises to a maximum somewhat before maximum laser output is reached. Beyond this there is a steady fall in pressure. The initial pressure rise is a natural consequence of the dissociation of the molecules in the gas mixture and the formation of new molecules such as HCN. It seems likely that the pressure drop is due to the formation of the brown wall deposit mentioned earlier and the associated removal of HCN from the gas mixture.

2.3.3.3 Optimum Operating Conditions

It will be useful for future reference to define the "optimum operating conditions" for our pulsed HCN laser. Study of the results presented in Sec. 2.3.3.1 shows that the laser produces maximum pulse energy when the gas conditions correspond to those for curve 3 of Fig. 2.8(b) and the discharge voltage is 6.5 kV. This assumes a pulse repetition frequency of 10 pulses per second. Accordingly we define the optimum operating conditions of the laser to be :

Discharge Capacitor :	0.3 μF
Discharge Voltage :	6.5 kV
Pulse Repetition Frequency :	10 p.p.s.
Gas - Mixture :	1:2 (nitrogen:methane)
- Pressure :	0.7 torr
- Flowrate :	0.5 litre sec^{-1}

The last three quantities in this list shall be taken to define the "optimum gas conditions" for the pulsed laser.

2.3.3.4 Discussion

In optimizing the performance of a pulsed HCN laser a compromise is made between the chemical processes which form HCN molecules in a pulsed discharge through an appropriate gas mixture, and the physical processes which subsequently produce an inverted population of these molecules. Certainly it is clear from the static filling experiment and from the investigation of power variation with pulse repetition rate that the two roles of the discharge are distinct. For the laser will not operate on the first few pulses in the former experiment, nor will it work at all when low repetition rates are used in the latter. In both cases it can only be because insufficient HCN is formed. However, distinct as the two roles of the discharge might be they are not completely independent,

because if they were equation 2.1 would have been satisfied more accurately.

The static filling experiment has another message. Not only does a pulsed discharge through nitrogen and methane produce HCN molecules, but it has the capacity to remove them as well. There may be circumstances where this is the dominant effect. So now there are three processes to balance, but how do they compete?

To restate the problem; one has to optimize the *average* quantity of HCN molecules maintained in the repetitively pulsed, flowing gas mixture while optimizing the excitation mechanism responsible for producing excess molecules in the $11^{o}0$ vibrational state. It has been suggested by Chantry (1971) that the optimum quantity of HCN molecules in the discharge is very small. Otherwise, self collisions of HCN would rapidly restore thermal equilibrium between the almost coincident (in energy) $11^{l}0$ and $04^{o}0$ levels which are responsible for the 337 μm line. In the light of this, the fall-off in laser pulse energy at high discharge voltages (Fig. 2.8) is not surprising. It may be that high discharge voltages produce too much HCN. Or perhaps at high voltages HCN is removed more effectively than it is produced. The latter possibility is quite real as HCN is unstable to electron

impact (Chantry, 1971). In any case it is certainly true that there is so little HCN in the HCN laser that it is extremely difficult to detect (Chantry, 1971; Gehre, 1972).

There is one other important complication which arises from the refractive effect (Heald and Wharton, 1965) of the electrons in the laser plasma, an effect which is quite significant for the 337 μm wavelength radiation. Because the refractive index of these electrons is less than unity and decreases with increasing density it follows that in most lasers, where the electron density is greatest at the centre of the discharge, the electrons will constitute a diverging element which becomes less diverging as the plasma decays. McCaul (1970) has shown that this effect can prevent stable resonator modes until some time in the afterglow of his laser discharge (but see Sec. 4.4.2). It seems likely that this process could sometimes be responsible for the delay which is generally observed between the extinction of the current pulse and the onset of laser action. This mechanism may be the clue to understanding the fall-off of laser output with increasing discharge voltage. It is possible for example, that the laser resonator cannot sustain any stable modes during the period when a population inversion exists. In addition the author has shown (Ch. 4) that the direct cavity mode

sweeping effect of the laser plasma electrons contributes to the form of the fall-off of laser output power at high discharge voltages. Chapters 4 and 5 of this thesis are devoted to the study of plasma effects in our pulsed HCN laser.

It is possible that several of the factors outlined above play a role in the decrease in laser output pulse energy at high discharge voltages. There may be other factors which are not known to us. The study presented in this chapter contributes to our understanding of how these factors may interact and our study of plasma effects (Chs. 3, 4 and 5) makes an additional contribution to this level of understanding.

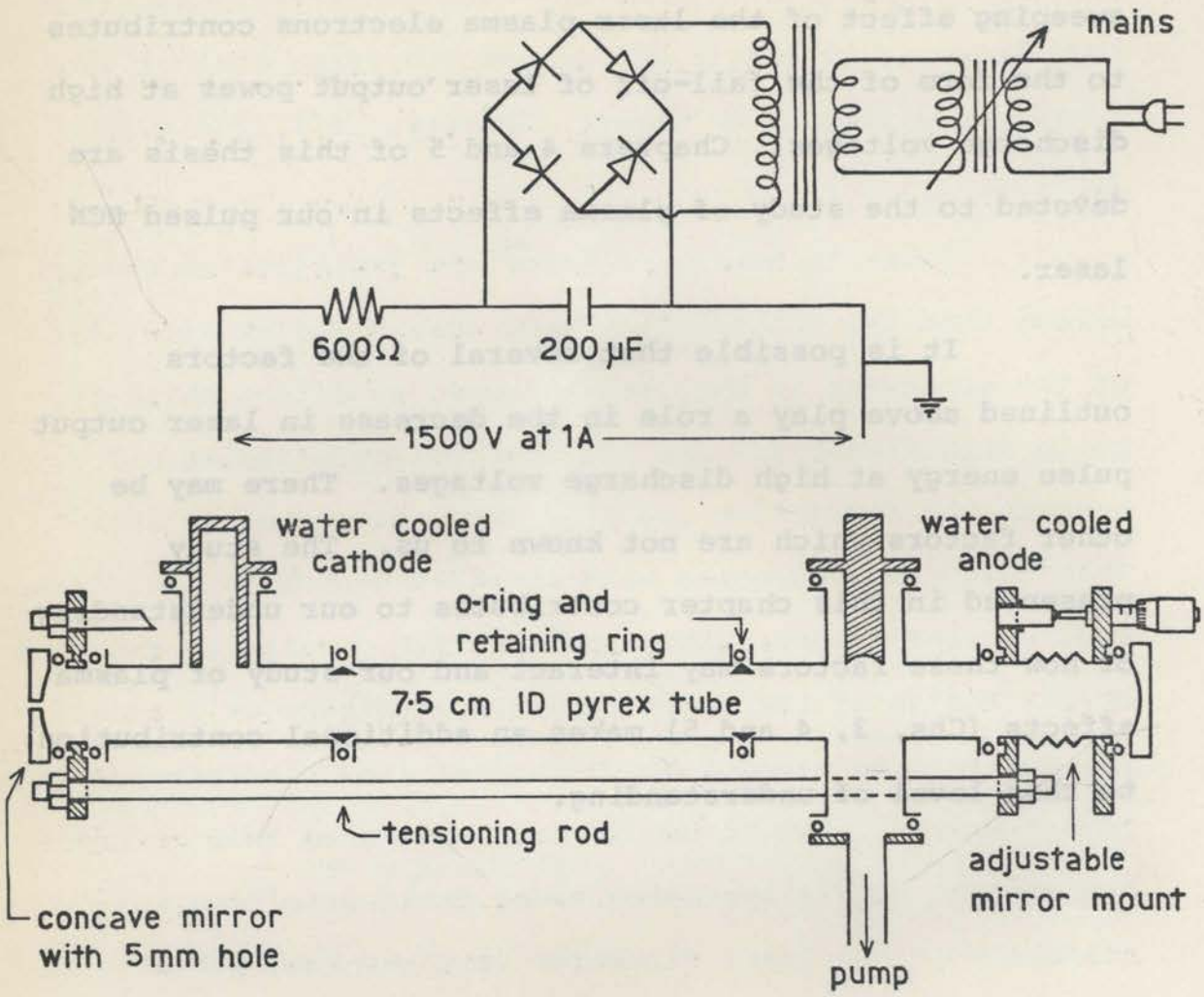

Fig. 2.13. Mechanical design of the CW HCN gas laser. The separation of the laser mirrors is maintained by four steel tensioning rods, thermal expansion of the pyrex tube being taken up by the O-rings. The right hand mirror is adjusted by three symmetrically placed micrometers and alignment of the other mirror is effected by altering the compression of its O-ring seal.

2.4 A Continuous HCN Laser

Following the pulsed HCN gas laser, a CW laser which was required as a source for 337 μm interferometry was designed and constructed. Its dimensions are similar to those of the pulsed laser, and its gas inlet and vacuum systems are identical. In the description of the CW laser which follows it is implicit where details are omitted, that it is essentially the same as the pulsed laser.

2.4.1 Mechanical Design and Assembly

The mechanical design of the laser, shown in Fig. 2.13, maintains a constant distance between its (internal) mirrors despite thermal expansion of the 1.8 m long discharge tube. The tube is fabricated from standard 7.6 cm I.D. pyrex pipe sections which are sealed by O-rings and the whole assembly is held in compression by four steel rods connecting (but suitably insulated from) two stainless steel end flanges. The laser tube is air-cooled by means of a high capacity blower and the discharge electrodes are water cooled. The cathode consists of a deep ($\sim$ 15 cm) brass cylinder closed at one end. It is similar to the hollow brass cathode described by Yamanaka et al (1968). The gas mixture is admitted into the laser through a small hole in the cathode.

The mirrors of the CW laser are mounted similarly to those of the pulsed laser, the important difference being that they are both aluminized to a diameter of 7.6 cm. Thus the diffraction losses in the CW laser are much lower than those in the pulsed laser; in the latter however these losses actually produce the output. In the CW laser, 337 μm output is extracted through central holes in one or both of the mirrors which are sealed by 25 μm mylar films.

2.4.2 Resonator Configurations

Two resonator configurations were used. In both, the mirror at the cathode end of the laser had a 2.8 m radius of curvature and a 5 mm diameter output coupling hole. Hole-output coupling yields a divergent, diffraction limited beam but avoids the problems associated with mounting a beamsplitter in the discharge tube. The mirror normally used at the anode end had a 3.7 m radius of curvature. Alternatively a plane mirror with a 5 mm diameter hole could be used to provide double-ended output. All of the mirrors are aluminized to a diameter of 7.6 cm giving a Fresnel number of 2.4 for the 1.8 m mirror spacing of the laser. For an axial mode in either resonator the spot sizes and waist diameters (calculated on the basis of infinite apertures; Kogelnik and Li, 1966) are of the

order of 3 cm. In the absence of holes these resonators would have very low diffraction losses. However the presence of coupling apertures in one or both of the mirrors introduces high losses in the axial and low order transverse modes. Meanwhile, the possibility of internal wall reflections will allow very low losses for the higher order transverse modes. Thus in our resonators it is difficult to estimate which will be the lowest loss (or operating) mode. It will depend strongly on resonator imperfections such as the non-unity reflection coefficient of the discharge tube wall material and losses occurring at side ports etc. However, assuming that the laser has a gain of about 10% per metre (Jones et al, 1969) we infer that the operating mode can have losses of no more than about 15% per pass (for a 1.5 m discharge column).

The double-ended output configuration was tried because it allowed easy alignment of the external cavity of a self modulating laser interferometer analogous to the He-Ne laser interferometer developed by Ashby et al (1965) (see Sec. 6.4 and Fig. 6.6). However in this case the alignment of the laser resonator was far more critical. Even when the laser resonator was well aligned the output power levels were about an order of magnitude smaller than those obtained with single-ended output. Furthermore, the 337 μm output was extremely noisy, to the extent of

being quite unusable.

2.4.3 Operating Conditions

The gas mixture used in the laser consisted of methane (0.9 torr) and nitrogen (0.3 torr) flowing at 0.5 litre-torr/sec. A discharge current of 1A through this mixture produced a bright central column of plasma 3-4 cm in diameter with a voltage drop of 1500 volts, causing the pressure to rise to approximately 1.5 torr. Under these conditions the discharge had a negative dynamic resistance so that a 600 Ω ballast resistor was required to stabilize the discharge current. These conditions were found to give the highest output power, consistent with the limitations imposed by the pumping ability of the mechanical vacuum pump. However the laser was not very stable in operation as its output power decreased rapidly after about 2 minutes of continuous operation. In spite of the air-cooling the hottest point on the outside of the pyrex tube reached 100 C in this short time. It seems likely that the rise in temperature is directly responsible for the rapid deterioration of laser performance (Frayne, 1969).

With single-ended output the laser resonator was very easy to align. After a preliminary procedure

utilizing a He-Ne laser beam, adjustment of one of the micrometers of the mirror mount was always sufficient to produce 337 μm output. [The wavelength was measured with a mesh-type Fabry-Perot interferometer. Only the 337 μm line was observed, at average power levels up to 1 mW.] As the micrometer was adjusted continuously through several wavelengths many resonances were encountered. For a large number of these the laser output had a large wideband noise content like the output obtained with the double-ended system (coupling holes in both mirrors). However, several modes were noise-free and suitable for interferometry. The interesting aspect of this behaviour is that while turning one micrometer alters the length of the resonator, thereby tuning it through the resonant lengths of successive modes, it also changes the tilt of the adjustable mirror by a large amount. Some of the modes observed lased quite strongly with the mirror tilted as much as 50' off axis. These may correspond to the "tube-modes" described by Steffen and Kneubühl (1968), some of which have enhanced output with an end mirror misaligned. A plausible explanation of the noisy modes is that they were probably those tube-modes which had a large proportion of their field distribution in areas outside of the central plasma column of the gas discharge. In these areas fluctuations in light intensity emitted by the plasma were

clearly visible and would certainly have been associated with fluctuations in the gain of the laser discharge. Such an explanation is consistent with the observation that the double-ended output configuration always yielded noisy output. With this configuration the high losses of the axial and low order transverse modes caused by having holes in both mirrors (McCumber, 1965) may have left only the higher order tube-modes (Steffen and Kneubühl, 1968) with low enough losses to sustain laser action. It does not follow that all the tube modes observed were noisy. In fact, many of the quiet modes corresponded to large off-axis tilts of the adjustable mirror. A consequence of the laser's operation in tube modes, particularly when the mirrors were not strictly parallel, was that the output was not always directed along the axis of the discharge tube. Measurements of the angular position of the peak of the diffraction limited output beam were made by scanning with a Golay cell. These measurements indicated that misalignments of the order of 3^{o} were quite common.

Further measurements of the variation of laser output in any one mode with mirror displacement indicated a gainwidth for the 337 μm (891 GHz) transition of about 13 MHz. As the laser was not highly excited (337 μm was

the only wavelength at which output was ever observed) the linewidth should not be less than the gainwidth. We infer that the total linewidth (full-width at half power) of the transition was of the order of 13 MHz. It is important to know the relative contributions of Doppler and collision (pressure) broadening to this figure in order to determine the appropriate form of the saturation formula; eq. 6.3 used in Ch. 6. To place an upper limit on the contribution due to the Doppler effect which varies as the square root of the temperature, we estimate the maximum neutral gas temperature in the discharge as follows. We assume that the 1500 watts dissipated in the tube maintains a 3 cm diameter central column of plasma at a uniform temperature. Heat is lost from this column by thermal conduction through the surrounding gas to the tube walls (at temperature 400 K). The thermal conduction calculation indicates a value of 2600 K for the temperature of the central column. A column narrower than 3 cm would imply a higher temperature but visual observations indicated that the bright central column was at least 3 cm in diameter. The inside wall temperature of 400 K is also an upper limit, based on estimates of the temperature gradient in the wall of the pyrex tube. The Doppler linewidth (Townes and Schawlow, 1955) for an HCN molecule at 2600 K and radiating at 891 GHz is about 6 MHz which is

to be compared with our estimate of 13 MHz for the total linewidth. Since tht total linewidth is approximately equal to the square root of the sum of the squares (Townes and Schawlow, 1955) of the contributions from the two sources the contribution from pressure broadening must be considerably greater than 6 MHz. We conclude that the 337 μm transition in our laser is essentially homogeneously broadened. This is consistent with the fact that no published continuous 337 μm laser resonator interferogram shows the Lamb-dip (Sinclair and Bell, 1969) even though most of the lasers involved use lower working pressures than the present laser so that the collision linewidths were proportionally smaller (see Appendix 2). Yamanaka et al (1968) mention observing a Lamb-dip of 2% in a CW HCN laser operating at 0.2 torr where the collision linewidth would be an order of magnitude less than in our laser (p = 1.5 torr). For further discussion of line broadening processes in far-infrared lasers see Appendix 2.

2.5 Summary

In this chapter we have described two 337 μm HCN lasers; one pulsed and one continuous. The pulsed laser was designed and constructed for the purpose of investigating physical processes occurring within the laser; the continuous laser was for use merely as a source for 337 μm interferometry.

We have presented a detailed empirical study of the dependence of the output pulse energy of the pulsed laser on all of the parameters which affect it. For a nitrogen-methane gas mixture we have investigated the effect on laser output pulse energy of discharge voltage, pulse repetition frequency, gas mixture, pressure and flow-rate. This study represents the major original contribution of this work. In addition we have evolved a set of optimum operating conditions; conditions which produce maximum 337 μm output pulse energy from our laser (Sec. 2.3.3.3). These operating conditions were used as a basis throughout subsequent investigations of the physical processes occurring within the laser (Chs. 3, 4 and 5).

In the case of the continuous laser we have described a set of operating conditions which produce about 1 mW of continuous 337 μm output. These operating conditions were used exclusively in subsequent experiments.

In addition we have described aspects of the operation of the laser which are of importance in relation to its use in a self-modulating laser interferometer configuration (Chs. 6 and 7).

Chapter 3

ELECTRON DENSITIES IN THE PULSED HCN LASER

3.1 Introduction

In this chapter we describe measurements of the time varying electron density in our pulsed laser plasma for several different discharge conditions. Much of the importance of this data lies in its use in Chapters 4 and 5. But because electron density effects are central to the theme of this thesis they must be carried out with techniques that we understand well and can use reliably. See Section 4.4.2 as an illustration of the results of insufficient care or experience in work of this type. Accordingly in this chapter we describe the techniques of microwave interferometry that we use, we present records of interferograms as well as plots of the data they yield. Since we interpret out experimental records in terms of well known plasma dispersion equations let us start with a summary of some useful plasma equations. These equations are also fundamental to our studies of far-infrared electromagnetic waves in the laser cavity and are the basis of our far-infrared diagnostic work (Ch. 7).

We first derive the equation relating the plasma refractive index to its electron density, establish that

collisional attenuation is unimportant, and obtain equations which are of use in microwave and far-infrared diagnostics. Following this we present the results of electron density measurements in our pulsed HCN laser for the optimum set of operating conditions evolved in Ch. 2. These densities were so high that we were immediately able to predict strong plasma effects on the 337 μm radiation in the laser cavity. Subsequent investigations of plasma effects in the pulsed HCN laser required further electron density measurements. These measurements are also presented in this chapter and will be referred to in Chapters 4 and 5.

3.2 Propagation of Electromagnetic Waves in Plasmas with no Magnetic Field

An electromagnetic wave propagating through a plasma interacts with the charged particles through its oscillating electric field, the interaction with its magnetic field being negligible by comparison. Because the ions are so much more massive than the electrons they may be regarded, with the neutrals, as a stationary background through which the electrons move with viscous damping. It is apparent that an electron displaced from its equilibrium position will experience a restoring force due to space charge effects and an elementary analysis (Heald and Wharton, 1955; hereafter referred to as H and W; p.2) reveals that this force is proportional to displacement. Thus there is a natural frequency of oscillation ω_p (radians/sec.) for electrons in a plasma given by (H and W, p.2),

$$\omega_p^2 = \frac{ne^2}{m\varepsilon_o} \qquad 3.1$$

where m and e are the mass and charge of an electron, n is the electron density and ε_o is the permittivity of free-space. This frequency is of considerable practical importance. If a wave of angular frequency less than ω_p impinges on a plasma boundary the electrons respond at

the wave frequency and set up a conduction current which is much larger than the displacement current. Consequently the wave is reflected. For wave frequencies greater than the plasma frequency electron inertia reduces the electron response considerably and the wave can propagate, the principal effect of the electrons being a reduction of the dielectric constant below its free-space value and a corresponding increase in the phase velocity of the wave.

A model of a plasma which is appropriate for the present purpose is the so called "cold plasma" in which the electron thermal velocity is much less than the wave phase velocity. This assumption is readily verified for the plasmas encountered in this thesis, where electron energies are no greater than about 1 eV. In addition we assume that the collective properties of the plasma electrons can be inferred from the motion of one electron. Accordingly, we start with the equation of motion for a single electron,

$$m\ddot{x} = - eE - \nu m\dot{x} . \qquad 3.2$$

E is the electric field which results from the wave field and space charge effects and ν is a phenomenological damping constant; the collision frequency for momentum transfer. In assuming a "cold plasma" we have eliminated

all dissipative effects other than collisions. For a steady state solution ($\propto \exp(j\omega t)$) and a current density $J = -ne\dot{x}$ eq. 3.2 gives the complex conductivity,

$$\bar{\sigma} = \frac{ne^2}{m} \cdot \frac{1}{\nu + j\omega} = \frac{\varepsilon_o \omega_p^2}{\nu + j\omega} \quad . \qquad 3.3$$

We now consider Maxwell's fourth equation for a steady state solution at frequency ω in a conducting medium;

$$\underset{\sim}{\nabla} \times \underset{\sim}{H} = \underset{\sim}{J} + \varepsilon_o \frac{\partial \underset{\sim}{E}}{\partial t}$$

$$= \left(\bar{\sigma} + \varepsilon_o \frac{\partial}{\partial t}\right) \underset{\sim}{E}$$

$$= \left(\bar{\sigma} + j\omega\varepsilon_o\right) \underset{\sim}{E} \quad . \qquad 3.4$$

We see that it takes on the form which it has in free-space ($\sigma = 0$) if we define a complex permittivity

$$\bar{\varepsilon} = \varepsilon_o + \frac{\bar{\sigma}}{j\omega} \quad , \qquad 3.5$$

which automatically defines a complex dielectric constant,

$$\bar{K} = 1 + \frac{\bar{\sigma}}{j\omega\varepsilon_o} \quad . \qquad 3.6$$

Indeed, it can be shown rigorously (H and W, p.6, p.396) that propagation of electromagnetic waves in such a conducting medium is described in terms of a complex refractive index $\bar{\mu}$ which is simply the square root of this complex dielectric constant. For the plasma under discussion we obtain, on substituting eq. 3.3 into eq. 3.6,

$$\bar{K} = \left(1 - \frac{\omega_p^2}{\omega^2 + \nu^2}\right) - \frac{j\nu}{\omega}\left(\frac{\omega_p^2}{\omega^2 + \nu^2}\right) . \qquad 3.7$$

Taking the square root of this expression (H and W, p.7) we find the complex refractive index,

$$\bar{\mu} = \mu - j\chi \qquad 3.8$$

is given by;

$$\mu = \left\{\frac{1}{2}\left(1 - \frac{\omega_p^2}{\omega^2+\nu^2}\right) + \frac{1}{2}\left[\left(1 - \frac{\omega_p^2}{\omega^2+\nu^2}\right)^2 + \left(\frac{\omega_p^2}{\omega^2+\nu^2}\cdot\frac{\nu}{\omega}\right)^2\right]^{\frac{1}{2}}\right\}^{\frac{1}{2}},$$

$$\chi = \left\{-\frac{1}{2}\left(1 - \frac{\omega_p^2}{\omega^2+\nu^2}\right) + \frac{1}{2}\left[\left(1 - \frac{\omega_p^2}{\omega^2+\nu^2}\right)^2 + \left(\frac{\omega_p^2}{\omega^2+\nu^2}\cdot\frac{\nu}{\omega}\right)^2\right]^{\frac{1}{2}}\right\}^{\frac{1}{2}}. \qquad 3.9$$

μ is the real refractive index and χ is the attenuation index. It follows that a plane wave propagating through a uniform plasma has fields proportional to,

$$\exp\left[j\omega\left(t - \frac{\bar{\mu}x}{c}\right)\right] = \exp\left[j\omega\left(t - \frac{\mu x}{c}\right)\right] \cdot \exp\left[-\frac{\omega\chi x}{c}\right] . \qquad 3.10$$

3.2.1 Effect of Collisions

It is clear that eqs. 3.9, which determine the behaviour of a wave propagating through a plasma, can be simplified in various limits. In the present instance we are interested in propagation, which only occurs when $\omega > \omega_p$ and we are interested in knowing where ν lies in relation to ω and ω_p. Generally, ν is equal to the sum of the respective collision frequencies for momentum transfer for electron-ion collisions (ν_{ei}) and electron-neutral collisions (ν_{en}).

The electron-ion collision frequency (assuming singly charged ions) is given by (Banks, 1966a)

$$\nu_{ei} = \frac{3.6\ n[cm^{-3}]\ell n\ \Lambda}{(T[K])^{3/2}} \qquad 3.11$$

where n and T are the electron density and temperature and Λ is the ratio of the cutoff-radii in the integral for the total Coulomb scattering cross-section. $\ell n\ \Lambda$ is a slowly varying function of n and T and for our laboratory plasmas it is appropriate to let $\ell n\ \Lambda = 6$ (Spitzer, 1962; p.128).

The electron-neutral collision frequency is related simply to the electron temperature T and the appropriate collision cross-section σ by the expression

$$\nu_{en} = n_n \sigma v_t \quad , \qquad 3.12$$

where n_n is the neutral density and v_t is the average electron thermal speed, given by

$$v_t = \sqrt{\frac{8kT}{\pi m}} \quad . \qquad 3.13$$

Here m is the mass of an electron and k is Boltzmann's constant.

For the SUPPER I helium plasma (Chs. 7 and 8) we have electron density (Fig. 7.3, p.7.9) and temperature (Fig. 8.3, p.8.11) measurements and the cross-section σ to be used in eq. 3.12 is 7.5×10^{-16} cm^2 for electron temperatures up to about 1 eV (Banks, 1966a). Thus we may readily calculate ν_{ei} and ν_{en} for the SUPPER I helium plasma; representative values are shown in Table 3.1. As would be expected for this highly ionized plasma electron-ion collisions dominate.

In the case of the pulsed HCN laser we do not have electron temperature measurements. However we do have electron density measurements (see Sec. 3.3.1) and we expect that, during excitation, the electron tempera-

ture may be as high as a few eV (Garrett, 1967, p.52; Smith and Sorokin, 1966; p.229). For this slightly ionized plasma such temperatures would cause electron-neutral collisions to dominate (see eqs. 3.11 to 3.13).

Under conditions of peak excitation we may estimate the total collision frequency for momentum transfer from the measured electrical conductivity of the laser plasma using eq. 3.3 with $\omega = 0$. Taking the plasma resistance to be 10 Ω (see Fig. 2.4, p.2.17) when $n = 10^{13}$ cm^{-3} and assuming a uniform plasma column (length 1.5 m) 10 cm^2 in area we obtain a conductivity of $\sigma = 150\ \Omega^{-1}\ m^{-1}$. This leads to a total collision frequency of about 2×10^9 sec^{-1}.

We may now work backwards (using eqs. 3.11 to 3.13) to estimate the electron temperature and ν_{ei}. Assuming that electron-neutral collisions do dominate and using a value of σ of 10×10^{-16} cm^2 which seems appropriate for our methane-nitrogen gas mixture and electron temperatures up to a few eV (Brown, 1959; Shkarofsky et al, 1966; p.178; Banks, 1966a) eqs. 3.12 and 3.13 indicate that the electron temperature is about 10^4 K. Equation 3.12 then gives $\nu_{ei} = 2 \times 10^8$ sec^{-1}, justifying our initial assumption that $\nu_{ei} << \nu_{en}$.

Table 3.1

	Frequencies of Interest								
Plasma	f	ω	n_n	σ	n	T	ν_{ei}	ν_{en}	ω_p
SUPPER I	35	2.2×10^{11}			10^{15}	10^4	2×10^{10}	1×10^8	1.8×10^{12}
	120	7.5×10^{11}	3×10^{15}	7.5	10^{12}	10^3	7×10^8	4×10^7	5.6×10^{10}
helium	890	5.6×10^{12}							
Pulsed	10	6.3×10^{10}			10^{13}	$\sim10^4$	2×10^8	2×10^9	1.8×10^{11}
HCN laser	35	2.2×10^{11}	3×10^{16}	$\simeq 10$	10^{11}	300	4×10^8	3×10^8	1.8×10^{10}
$CH_4 + N_2$	890	5.6×10^{12}							
Continuous HCN laser $CH_4 + N_2$	890	5.6×10^{12}	3×10^{16}	-	$<10^{12}$	-	$\nu_{cond} < 3\times10^{10}$		$<5.6\times10^{10}$
Units	GH_z	rad sec^{-1}	cm^{-3}	$10^{-16} cm^2$	cm^{-3}	K	sec^{-1}	sec^{-1}	rad sec^{-1}

Late in the decay of the laser plasma this situation may change as the electron temperature falls. We shall not be interested in times when the electron density is less than 10^{11} cm^{-3} and can obtain an upper limit to ν_{ei} at such times by assuming an electron temperature of 300 K. For these conditions ν_{ei} is slightly larger than ν_{en}, as shown in Table 3.1.

For the continuous HCN laser we have neither electron density nor electron temperature measurements but on the basis of our experience with the pulsed laser we estimate that the electron density is not as large as 10^{12} cm^{-3}. The conductivity of the DC discharge of the laser is about 1 Ω^{-1} m^{-1} so again using eq. 3.3 (with $\omega = 0$) we find that ν is less than 3×10^{10} sec^{-1}.

All of the collision frequencies calculated above are shown in Table 3.1, which also shows electron plasma frequencies and the wave angular frequencies of interest. Inspection of these data leads to the conclusion that for *all* of the wave propagation experiments which are described in this thesis,

$$\nu << \omega_p < \omega \quad , \qquad 3.14$$

and in this limit eqs. 3.9 become (H and W, p.9),

$$\mu \simeq \left(1 - \frac{\omega_p^2}{\omega^2}\right)^{\frac{1}{2}} \qquad 3.15$$

and

$$\chi \simeq \frac{\nu}{2\omega} \cdot \frac{\omega_p^2}{\omega^2} \cdot \left(1 - \frac{\omega_p^2}{\omega^2}\right)^{-\frac{1}{2}} . \qquad 3.16$$

Thus the refractive effects of our plasmas are not affected by electron collisions at all and there is negligible attenuation except near microwave cutoff, where it causes the pinching-off of interferograms which is often observed (e.g. Figs. 3.7 and 3.10).

3.2.2 Interferometric Measurements of Electron Densities in Decaying Plasmas

It is evident from eq. 3.15 that an electromagnetic wave propagating through a uniform plasma will suffer a phase-shift with respect to free-space propagation which depends only on its instantaneous electron density. We may use this fact to measure electron densities. The experimental situation in which we are interested is that of a cylindrical plasma which we probe along a diameter with a narrow beam of radiation of frequency ω. This defines a cutoff density n_c given by (see eq. 3.1)

$$\omega^2 = \frac{n_c e^2}{m\varepsilon_o} \quad , \qquad 3.17$$

and using eqs. 3.1 and 3.17 we may rewrite the refractive index (eq. 3.15) in the more useful form,

$$\mu = \left(1 - \frac{n}{n_c}\right)^{\frac{1}{2}} \quad . \qquad 3.18$$

If the diameter of the plasma column is d and n(x) is its *radial electron density profile* then the phase shift of the radiation beam with respect to free space propagation is given by

$$\Delta\Phi = 2 \cdot \frac{2\pi}{\lambda} \int_o^{d/2} \left[1 - \left(1 - \frac{n(x)}{n}\right)^{\frac{1}{2}}\right] dx \quad , \qquad 3.19$$

where λ is the free-space wavelength. Thus measurement of the phaseshift $\Delta\Phi$ as a function of time allows the electron density to be calculated, provided that the functional form of the profile n(x) is known. Of course, in order to avoid diffraction effects, we require that the radiation wavelength and the width of the probing beam be somewhat less than the diameter of the plasma column.

Equation 3.19 simplifies in two useful limits. Firstly, if $n(x) << n_c$ for all x the integrand may be approximated by the bionomial expansion

to give

$$\Delta\Phi \simeq \frac{4\pi}{\lambda} \int_{o}^{d/2} \frac{n(x)}{2n_c}\, dx \quad . \qquad 3.20$$

Secondly, when the density profile is uniform ($n(x) = n$ for all x) we have,

$$\Delta\Phi = \frac{2\pi d}{\lambda} \cdot \left[1 - \left(1 - \frac{n}{n_c} \right)^{\frac{1}{2}} \right] \quad .$$

When $n << n_c$ as well this reduces to

$$\Delta\Phi \simeq \frac{\pi d}{\lambda} \cdot \frac{n}{n_c} \quad . \qquad 3.21$$

Equations 3.19 to 3.21 are used extensively in the microwave and 337 μm diagnostics discussed later. Equation 3.21 is also used to estimate plasma effects in the pulsed HCN laser where n is always much less than n_c for 337 μm radiation.

There is a variety of techniques for measuring the phaseshift of an electromagnetic wave propagating through a plasma. The specific technique depends on the frequency of the probing beam, which is chosen so that the appropriate critical density n_c (eq. 3.17) is larger than the electron density in the plasma. However the critical density must not be too much larger than the electron

densities of interest otherwise there is insufficient interaction between the plasma electrons and the probing beam to cause useful phaseshifts. To measure electron densities in our pulsed HCN laser 3.2 cm and 8.8 mm microwave interferometry is appropriate. For measuring the higher electron densities in the SUPPER I Helium plasma (Ch. 7) 2.5 mm microwave and 337 μm far-infrared interferometry are more suitable.

However all these interferometric techniques are based on the same principles. Coherent monochromatic radiation from a suitable source (e.g. a klystron or a laser) is divided into two beams; the probing beam and the reference beam. After passage through the plasma the phase-shifted probing beam is mixed with the reference beam in a square-law detector. The phase shift of the reference beam is adjusted for $\pi/2$ phase difference in the absence of plasma. Under these circumstances the detected signal is proportional to,

$$\overline{(A \cos(\omega t + \pi/2 + \Delta\Phi) + B \cos \omega t)^2}$$

where A and B are the amplitudes of the signal and reference beams respectively and $\Delta\Phi$ is the plasma phase-shift. The bar denotes a time average over the radiation period $T = 2\pi/\omega$. Taking the time average we find that the

detected signal, V, varies as,

$$V = A^2 + B^2 - 2AB \sin \Delta\Phi \qquad 3.22$$

and the phase shift can be measured in multiples of 2π by counting fringes. The electron density can then be calculated by using one of eqs. 3.19 to 3.21. In practice it is possible to estimate phase shifts as small as $\pi/2$ or less, depending on the noise level in the detector system. For a given path length, the minimum detectable phase determines the lowest density which may be measured. The maximum density is near the cutoff density determined by the frequency of the probing beam. Table 3.2 summarizes the cutoff densities and densities for $\pi/2$ phase-shift for the far-infrared and microwave diagnostics over the pathlengths encountered in this thesis.

Table 3.2

Plasma	f	path length	n ($\pi/2$)	n_c
Pulsed HCN	35	3	2.2×10^{12}	1.5×10^{13}
Laser	10	6 (double pass)	2.8×10^{11}	1.1×10^{12}
SUPPER I	120	15	1.5×10^{12}	1.7×10^{14}
Helium	890	150 (double pass)	1.1×10^{12}	9.8×10^{15}
Units	GHz	cm	cm^{-3}	cm^{-3}

3.3 Electron Density Measurements in the Pulsed HCN Laser

In this section we describe our measurements of the time-varying electron density in the pulsed HCN laser under a variety of operating conditions. The measurements presented in Sec. 3.3.1 were originally made as a part of the study of the pulsed laser which was described in Sec. 2.3. However the magnitude of the densities measured lead to the prediction of strong plasma effects on the 337 μm radiation in the laser resonator. As a result more electron density measurements were required. The measurements presented in Sec. 3.3.2 are required for the analysis of plasma effects appearing in Sec. 4.2 and the measurements presented in Sec. 3.3.3 are required for our study of pulse spiking phenomena in the pulsed HCN laser (Ch. 5).

The electron density measurements presented in this section were obtained by interferometry using 8.8 mm and 3.2 cm wavelength microwaves. These wavelengths are ideal for measuring the range of electron densities encountered in our pulsed laser, but as we shall see shortly, the plasma column in the laser has a width which is of the order of the larger wavelength. Thus diffraction effects must occur to some extent. However the diverging effect of the cylindrical plasma column in our laser

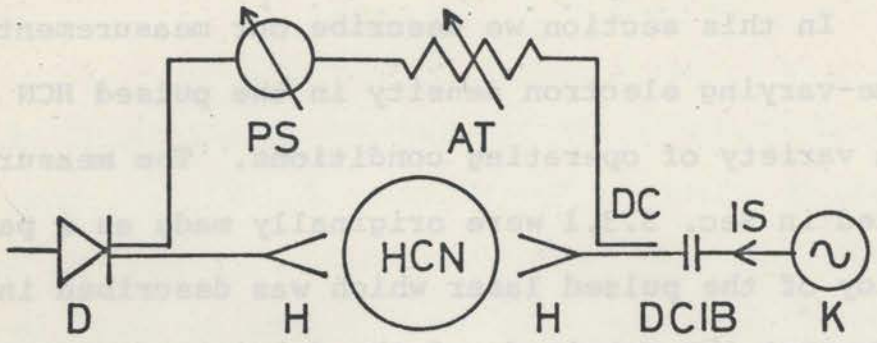

K - 8.8 mm klystron
IS - isolator
DCIB - DC isolating break
DC - directional coupler
AT - attenuator
PS - phase shifter
D - crystal detector
H - horn antenna

Fig. 3.1 Microwave Interferometer.

does cause the region nearest the line joining the two microwave antennae (Fig. 3.1) to be more effectively probed than areas further away and our experimental apparatus is designed to take maximum advantage of this fact.

Experimentally, our microwave interferograms show little evidence of diffraction effects. Of course, the 3.2 cm measurements would be expected to be more seriously affected by diffraction than the 8.8 mm measurements. But the good agreement which we obtain where the 8.8 mm and 3.2 cm measurements overlap leads us to believe that both microwave interferometers operate in the desired manner. Furthermore, the agreement obtained between the predictions of our electron density measurements and our cavity mode sweeping observations (Chs. 4 and 5), over the *entire range* of comparison, lends support to the validity of the present measurements.

3.3.1 8.8 mm Microwave Interferometric Electron Density Measurements in the Pulsed HCN Laser

A convenient method for measuring electron densities in the range from 10^{12} cm^{-3} to 1.5×10^{13} cm^{-3} in our pulsed HCN laser is the microwave interferometer shown in Fig. 3.1. In this system horn antennae, whose dimensions are greater than the (microwave) wavelength, are used to launch and collect plane waves which

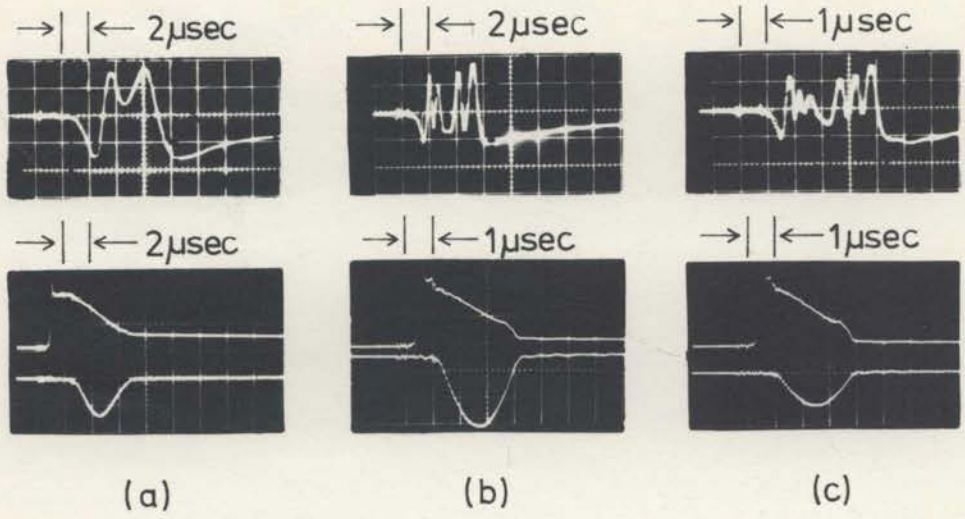

	a	b	c	
V_{peak}	5	6.6	7.3	kV
I_{peak}	460	1120	1300	A

Fig. 3.2. Microwave interferograms (upper trace) and corresponding voltage (middle trace) and current waveforms for the pulsed HCN laser, operating under optimum conditions (curve 3, Fig. 2.8(b)). The interferograms (a) and (b) show very clearly, the symmetry with respect to rising and falling densities mentioned in the text. Trace (c) shows about 3¼ fringes to cutoff at 4.3 μsec and a similar number in the decay which starts at about 4.7 μsec. Diffraction around the plasma column gives a slowly varying signal for the 0.4 μsec cut-off interval.

probe the plasma. The phase shifted probing beam is recombined in a crystal detector (Fig. 3.1) with a reference beam which passes through an attenuator and phase shifter as shown in Fig. 3.1.

Under optimum operating conditions (Sec. 2.3.3.3) the pulsed laser produces 8.8 mm microwave interferograms like those shown in Fig. 3.2 for three discharge voltages. These show both the initial rise and the subsequent decay of the "average" electron density, the turning point quite often appearing as a small fractional fringe which always has equal numbers of fringes before and after it. This indicates that the width of the electron density profile must be essentially the same for both rising and falling densities. The interferogram in Fig. 3.2(c) shows what happens when the electron density at the centre of the discharge just reaches cutoff (1.5×10^{13} cm^{-3}) for 8.8 mm radiation. Cutoff occurs after 3¼ fringes at approximately 4.3 μsec and there is a slowly varying diffraction signal until 4.7 μsec followed by another 3¼ fringes in the plasma decay. At still higher discharge voltages than those corresponding to the interferograms in Fig. 3.2 the cutoff interval becomes longer and more clearly observable. Thus we were always able to positively identify the cutoff interval by briefly operating the

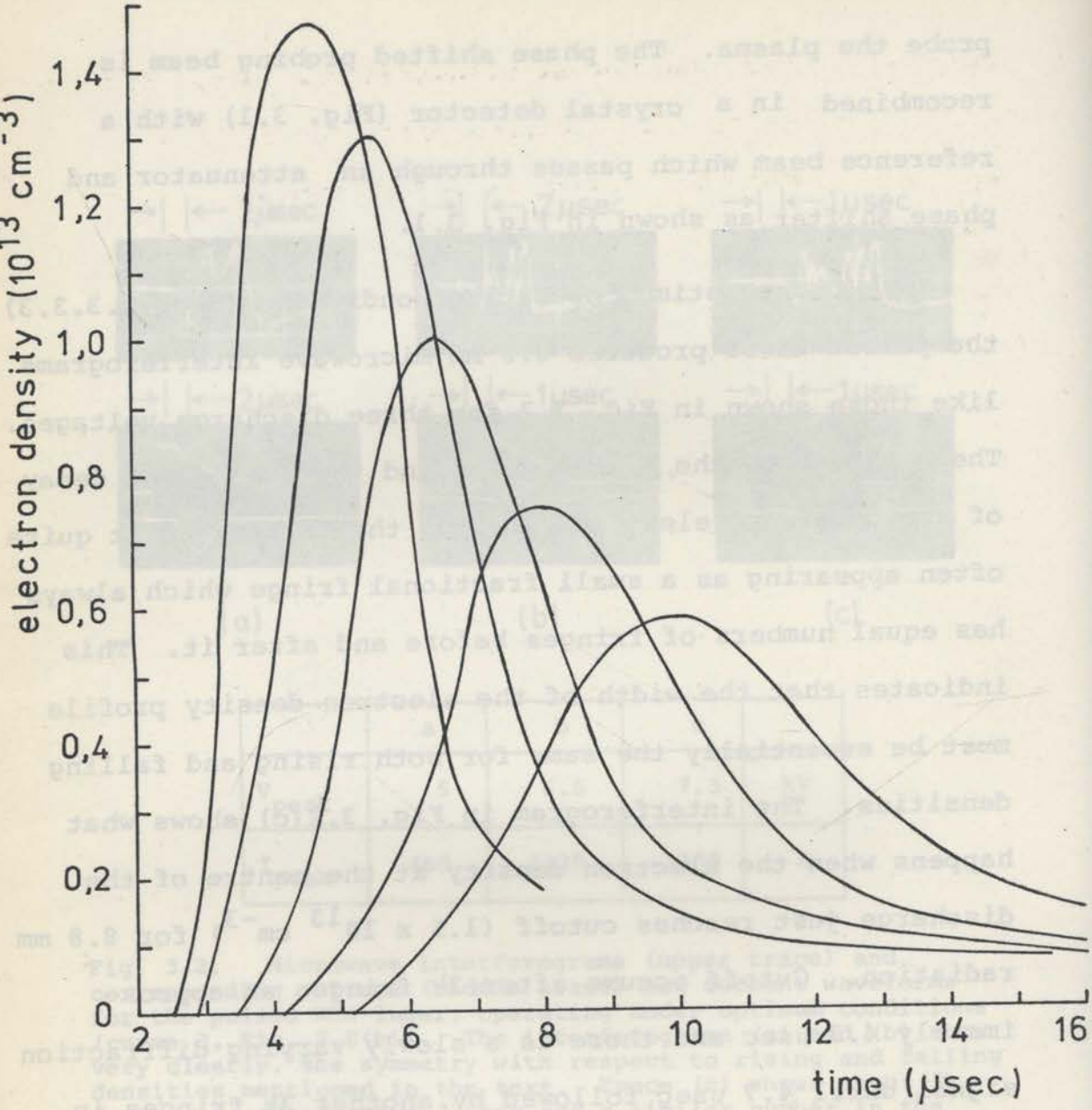

Fig. 3.3. Time dependent electron density on axis of the pulsed HCN laser. These curves correspond to a sequence of voltages on the optimum power curve 3 of Fig. 2.8(b). The voltages are 4.3, 4.9, 5.4, 6.5 and 7.4 kV, the peak density increasing with discharge voltage.

laser at higher than normal discharge voltages. For the range of experimental conditions encountered in Sec. 2.3.3.1 we observed between 3¼ and 4¼ fringes to cutoff, the number being generally closer to 3½. For the present operating conditions however there were 3¼ fringes to cutoff. In view of the fact that a 7.6 cm ID tube filled uniformly with plasma above cutoff density would produce 8.6 fringes (7.6/0.88) we infer that the effective width of the plasma column is much less than the tube diameter. If we assume a uniform electron density profile its width must be only 2.9 cm (3.25 x 0.88). Such a narrow column is consistent with the observation of a diffraction signal during cutoff.

Assuming a uniform profile 2.9 cm wide the variation of electron density with time is easily calculated from interferograms like those in Fig. 3.2. It is shown in Sec. 3.3.1.1 that the choice of a uniform profile is a good one. Figure 3.3 shows the time-dependent electron density obtained in this manner for a series of laser operating voltages on the optimum power curve 3 of Fig. 2.8(b). It will be seen that at the higher discharge voltages a peak density of the order of 10^{13} cm^{-3} is achieved and this decays to about 10^{12} cm^{-3} in a few microseconds. Using eq. 3.21 we find that the phase

shifts expected for 337 μm radiation after passage through 1.5 metres of such a medium are 5 π and 0.5 π for densities of 10^{13} cm^{-3} and 10^{12} cm^{-3} respectively. Such phase-shifts would be expected to have profound effects on laser operation. It is shown in later sections that they do. Before proceeding to study these effects however, we must justify our choice of electron density profile and investigate the uniformity of the laser's axial electron density distribution.

3.3.1.1 Radial Profile of Electron Density

It was shown in Sec. 3.2.2 that the electron density of a plasma could be readily inferred from measurements of microwave phase shift provided that the radial profile of electron density n(x) is known. In the present instance this profile is not known. However, in the study of plasma effects in the HCN laser we are principally concerned with the electron density along the axis of the discharge vessel. It is this density which causes first order changes in the effective length of our laser resonator, and plasma tuning effects. Of course the density must be less at positions nearer to the walls of the laser discharge tube. This has a lensing effect which may alter the mode spacings of the laser resonator

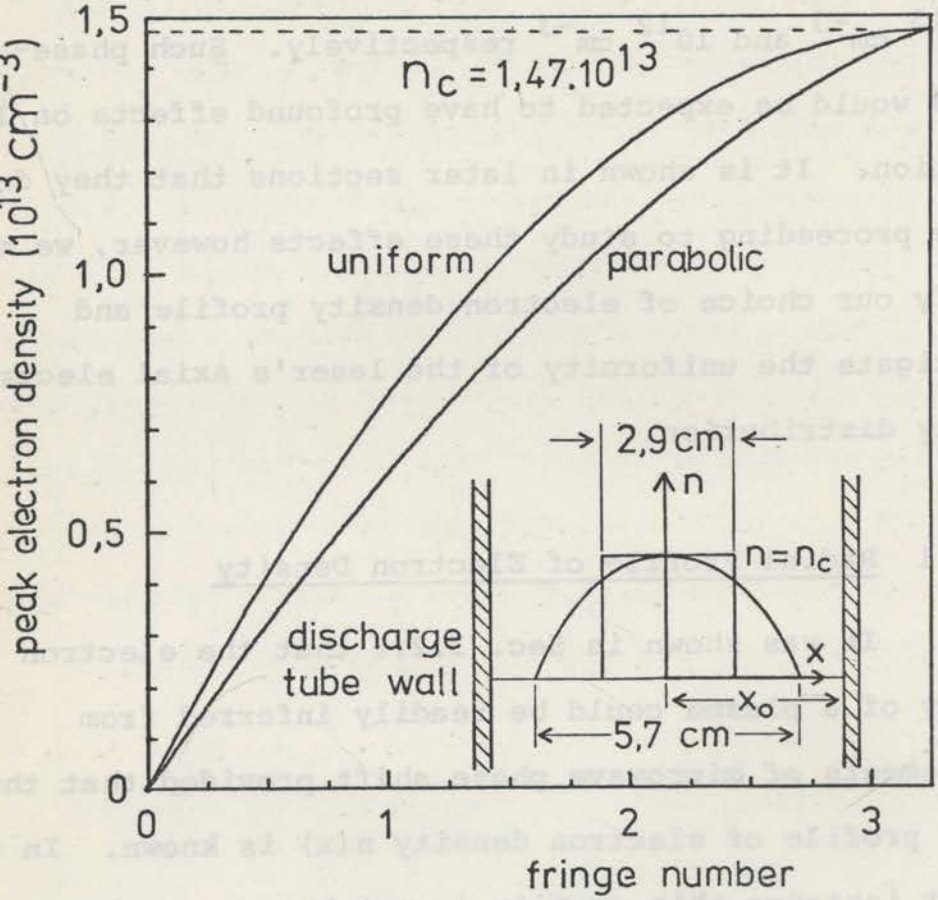

Fig. 3.4. Comparison of electron density obtained from 8.8 mm microwave fringe number assuming (a) uniform, and (b) parabolic electron density profiles of appropriate widths. The uniform profile always gives a higher estimate of the electron density at tube centre. The overestimate is zero at cutoff (1.47×10^{13} cm^{-3}), about 10% at 1.3×10^{13} cm^{-3} and rises to about 25% for $n \leqslant 0.4 \times 10^{13}$ cm^{-3}.

but we expect this to be a second order tuning effect. Our observations in Ch. 5 indicate that this is indeed so as the mode separations of our laser resonator are not changed measurably by plasma effects.

Fortunately, we find that if an arbitrary profile is assumed, the peak density inferred from phase-shift measurements is not strongly dependent on the form of the profile, provided that it has the correct effective width. That is, the width of the profile chosen must give the correct number of fringes to cutoff. To illustrate this point, we show in Fig. 3.4, curves of central density as a function of fringe number for two cases:

(a) A uniform profile of width 2.9 cm (corresponding to 3¼ 8 mm fringes to cutoff). Here,

$$n = n_c \left(\frac{2r}{k} - \frac{r^2}{k^2} \right) \qquad 3.23$$

where r = fringe number,

and k = number of fringes to cutoff.

Equation 3.23 is obtained from eq. 3.19 by putting

$$\Delta\Phi = 2\pi r,$$

$$d = k\lambda,$$

and $n(x) = n$.

(b) A parabolic profile

$$n(x) = n\left[1 - \beta\left(\frac{x}{x_o}\right)^2\right] \quad . \qquad 3.24$$

Here x_o is the tube radius and β is chosen to give the correct number of fringes to cutoff ($\beta > 1$ in cases of interest). If eq. 3.24 is substituted into the integral 3.19 we obtain (true only for $\beta \gtrsim 1$)

$$r = \frac{x_o}{\lambda\sqrt{\beta}}\left[1-\left(1 - \frac{n}{n_c}\right)\left(\frac{n_c}{n}\right)^{\frac{1}{2}} \ell n\left(\frac{1}{\left(1 - \frac{n}{n_c}\right)^{\frac{1}{2}}} + \frac{1}{\left(\frac{n_c}{n} - 1\right)^{\frac{1}{2}}}\right)\right] , \qquad 3.25$$

where r is the fringe number corresponding to the electron density n at tube centre and the maximum number of fringes to cutoff is given by $k = x_o/\lambda\sqrt{\beta}$.

Equations 3.23 and 3.25 are plotted in Fig. 3.4 for $k = 3\frac{1}{4}$. The relative widths of the uniform (width 2.9 cm) and parabolic profiles ($\beta \simeq 1.8$; width 5.7 cm) are also shown. It is evident that to give the same number of fringes to cutoff the parabolic profile must be wider than the uniform profile. It follows that the use of a uniform profile to analyse microwave interferograms when a parabolic profile really exists leads to an overestimate of the peak electron density. However

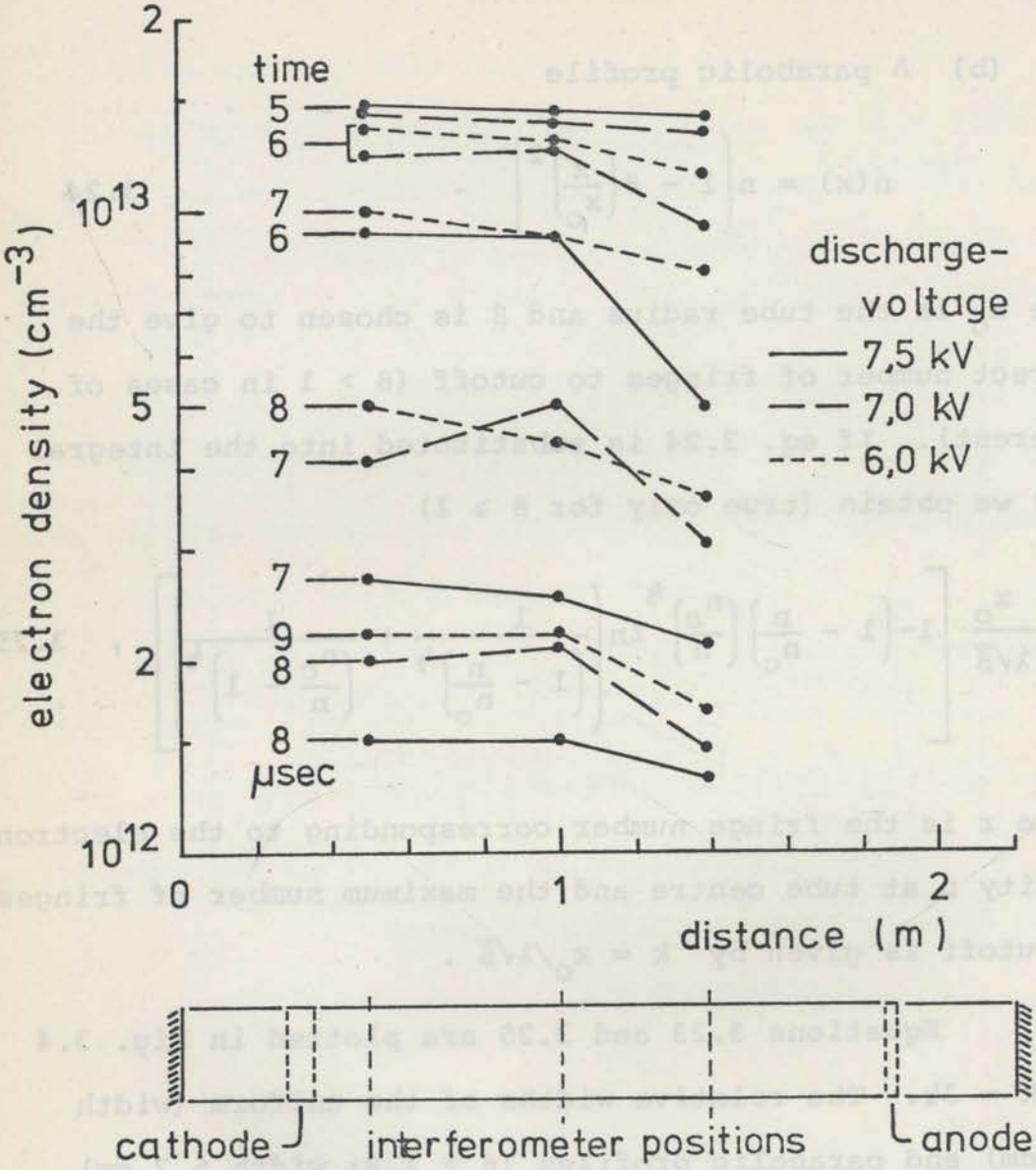

Fig. 3.5. Axial profiles of electron density in the HCN laser plasma for several discharge voltages on the optimum power curve 3 of Fig. 2.8(b). The time in microseconds for each profile is indicated at its left hand end. The length of the laser resonator and the relative positions of the 8.8 mm interferometer and discharge electrodes are shown to scale underneath the figure.

reference to Fig. 3.4 indicates that this overestimate is only about 10% at high densities and no more than about 25% at low densities. These are not serious errors. Because of this, and the fact that the uniform profile is simpler, it is used extensively in the analysis of microwave interferograms in this chapter.

3.3.1.2 Axial Uniformity of Laser Plasma

It is reasonable to expect a roughly uniform axial distribution of electron density in the laser plasma. However, before making quantitative estimates of plasma refractive effects, it was necessary to check this distribution experimentally. Accordingly, the 8.8 mm interferometer shown in Fig. 3.1 was set up at three positions along the axis of the laser vessel and used to measure electron densities under as nearly identical operating conditions as possible. Figure 3.5 shows the results of these measurements for three discharge voltages in the range of interest. Inspection of these results indicates that the laser plasma is reasonably uniform. The density for the position of the interferometer nearest the anode is always lowest. The very large deviations which occur at 6 μs (7.5 kV) and 7 μs (7 kV) are probably due to shot to shot variations in the laser plasma.

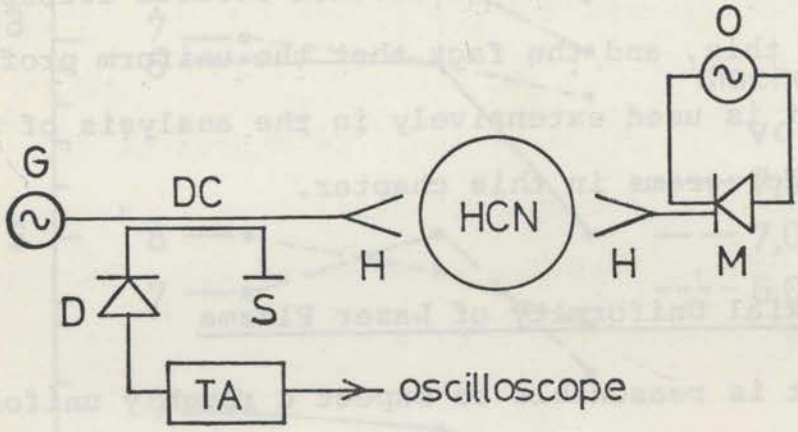

G	3.2 cm Gunn-effect oscillator
DC	directional coupler
S	short circuit
D	crystal detector
H	horn antenna
O	30 Mhz. oscillator
M	modulated crystal
TA	30 Mhz. tuned amplifer

Fig. 3.6 . Modulated Reflection Interferometer

It should be noted that the middle position of the interferometer (Fig. 3.5) was used for all other electron density measurements. This may lead to an overestimate of plasma refractive effects when a uniform axial profile is assumed. Allowing for the possibility that the electron density may fall at positions closer to the anode than those at which measurements were taken, we estimate that this error could be as large as 30%.

3.3.2 3.2 cm Microwave Interferometric Electron Density Measurements

We saw in Sec. 3.3.1 that during active excitation the peak electron density in the HCN laser reaches 10^{13} cm^{-3} and decays to 10^{12} cm^{-3} in a few microseconds. The 8.8 mm interferometer is not capable of measuring electron densities much below 10^{12} cm^{-3} (see Table 3.2). However comparison of the times of onset of typical laser output pulses (Fig. 2.5) with the electron density decay curves in Fig. 3.3 indicates that lasing takes place when the electron density is less than or of the order of 10^{12} cm^{-3}. Thus electron density measurements below 10^{12} cm^{-3} are required.

For measuring electron densities in the range from 10^{12} cm^{-3} down to 3×10^{11} cm^{-3} a 3.2 cm (9.38 GHz)

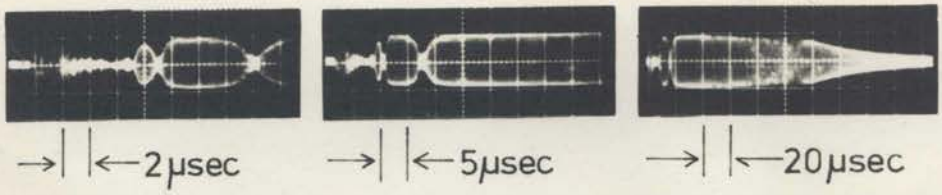

Double Pass Phaseshift	Time	Single Pass Fringe No. (r)	n
4π	8.2	1	1.09
3π	9.1	$^3/_4$	1.02
2π	11.0	$^1/_2$	0.82
π	18.2	$^1/_4$	0.48
radians	μsec	-	10^{12} cm^{-3}

Fig. 3.7. 3.2 cm interferogram for the pulsed HCN laser plasma, for operating conditions corresponding to Fig. 4.1. Cuton occurs at about 8.2 μsec and is followed by one highly attenuated quarter fringe and three normal quarter fringes. Large attenuation is expected near cutoff because the electron collision frequency is not much less than the 3.2 cm wave angular frequency (Table 3.1).

modulated reflection interferometer (Robinson, 1964) was used (Fig. 3.6). In this instrument radiation which has made a single pass through the plasma is reflected by a crystal diode which is driven by a 30 MHz sinewave generator. Under these circumstances the crystal has a time varying reflection coefficient. Thus radiation carrying a 30 MHz "label" is returned to the plasma. Radiation which has made two passes through the plasma is then mixed with a reference signal by means of the simple directional coupler and short circuit configuration shown in Fig. 3.6. A transient plasma produces a signal consisting of a 30 MHz signal amplitude modulated by the plasma fringes.

Figure 3.7 shows a 3.2 cm interferogram obtained under typical lasing conditions. The laser operating conditions were optimum (Sec. 2.3.3.3) except that the flowrate was higher by a factor of about two and the discharge voltage was 7.0 kV. These conditions correspond exactly to the investigation of cavity mode sweeping presented in Sec. 4.2.1. Referring to the interferogram, we see that a noise signal starts about 2 μsec after the beginning of the trace. This signal originates in the laser discharge triggering electronics and actually starts about 1 μsec before the laser current pulse. This disguises

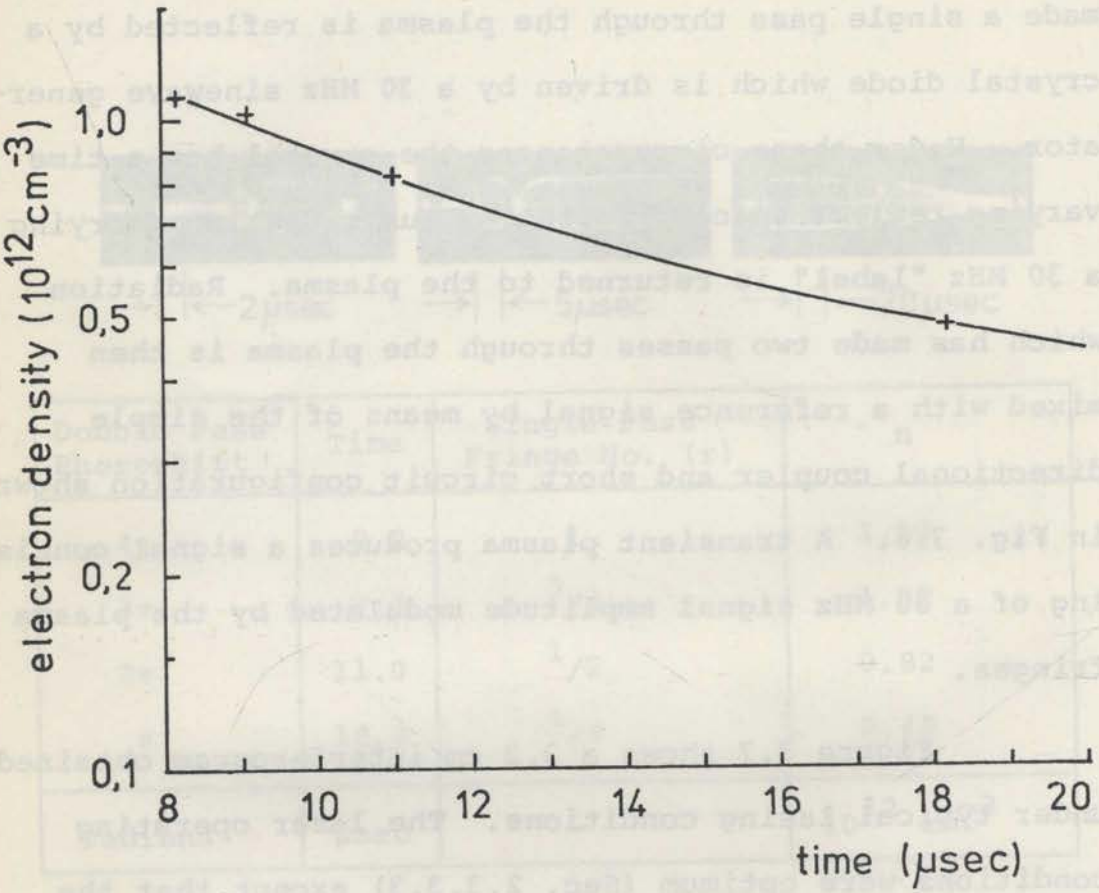

Fig. 3.8. Time dependent electron density along the axis of the pulsed HCN laser discharge. The operating conditions were optimum (Sec. 2.3.3.3) except that the discharge voltage was 7.0 kV and the flowrate was higher by a factor of about two. The points for this curve are obtained from analysis of the interferogram shown in Fig. 3.7.

the plasma preparation fringes which should occur in the first 0.4 μsec or so. The noise continues long after this but ceases before 3.2 cm cuton (1.09×10^{12} cm^{-3}) which occurs at about 8.2 μsec. By this time the laser discharge current has ceased flowing (Fig. 3.2). After cuton, there are four fringe maxima in the subsequent decay of the plasma. Thus we infer that there is a total phaseshift of 4π to cutoff, for a double pass through the laser plasma. Analysis of the interferograms on the basis of a uniform profile 3.2 cm ($\equiv \lambda$) wide (e.g. 3.23 with $k = 1$) gives the electron densities tabulated under Fig. 3.7. The resulting time-variation of electron density is plotted in Fig. 3.8. This curve is used in the analysis of cavity mode sweeping presented in Sec. 4.2.1.

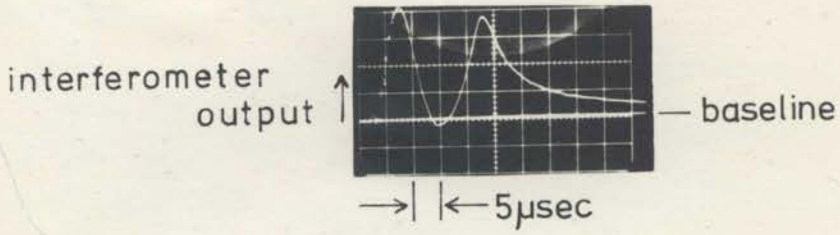

Phaseshift	0	90	135	180	135	degrees
Time	2.5	7.5	10.7	15	20.3	μsec
Electron Density	0	1.5	2.2	3.0	2.2	10^{12}cm^{-3}
± Error	-	0.2	0.2	0.2	0.2	10^{12}cm^{-3}
Phaseshift	90	67	30	14.5		degrees
Time	23	24	28	34		μsec
Electron Density	1.5	1.1	0.50	0.24		10^{12}cm^{-3}
± Error	0.1	0.05	0.05	0.05		10^{12}cm^{-3}

↑
3 cm cuton

Fig. 3.9. 8.8 mm microwave interferogram obtained under the laser discharge conditions (Table 5.1) which produced the spiking output shown in Fig. 5.1. A baseline, which corresponds to zero plasma phaseshift is superimposed on the photo. Because of the symmetry with respect to rising and falling densities which we always observed with 8.8 mm interferograms (Sec. 3.3.1) we know that the electron density turning point occurs at about 15 μsec, near where the interferogram crosses the baseline for the second time. The total plasma phaseshift at 15 μsec is close to 180°. The table underneath the interferogram shows the phaseshift and electron density variation with time which the former implies.

3.3.3 Electron Densities for Discharge Conditions Which Produce Spiking Output

In this section we present measurements of the time-varying electron density along the axis of the pulsed HCN laser for discharge conditions under which it produces spiking output. This is an essential part of the study of spiking output in Ch. 5. For two reasons these measurements are presented in rather more detail than those of the previous sections. Firstly, the densities are in a range which requires the use of both 3.2 cm and 8.8 mm interferometry. Secondly, the measurements are required for a careful comparison of theory and experiment. Because of the lengthy discussion involved in presenting these measurements they would distract from the central theme if they were presented in Ch. 5. It is better than they be given here and used later.

The laser operating conditions in which we are presently interested are summarized in Table 5.1. Figure 3.9 shows an 8.8 mm microwave interferogram obtained under these conditions. As the maximum phaseshift observed is only π radians we infer that the peak electron density is well below cutoff density ($n_c \simeq 1.5 \times 10^{13}$ cm^{-3}), so to a very good approximation the plasma refractive index is related linearly to the electron density by (eq. 3.18),

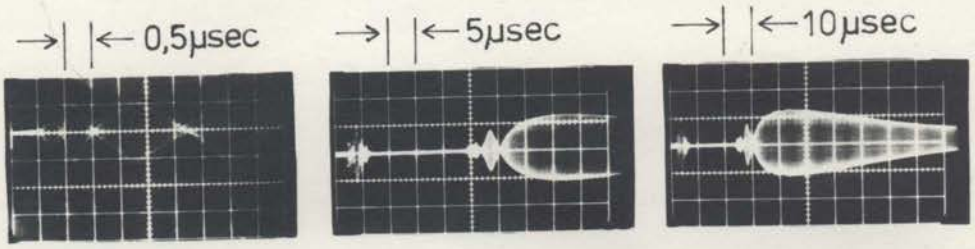

$\Delta\Phi$	5π	4π	3π	$5\pi/2$	2π	$3\pi/2$	π	$\pi/2$	rad.
t	24	24.4	25	25.8	26.6	28.5	30.3	44	μsec
n	1.09	1.05	0.92	0.82	0.70	0.56	0.39	0.21	10^{12} cm^{-3}

$\Delta\Phi$ = Double pass phaseshift

t = Time

n = Electron Density at tube centre

Fig. 3.10. 3.2 cm modulated reflection interferogram for the laser discharge conditions which produced the spiking output shown in Fig. 5.1 and the 8.8 mm interferogram shown in Fig. 3.9. Trace (a) is triggered approximately 0.5 μsec before 3 cm cuton while traces (b) and (c) are triggered at our normal time zero. The electron densities given in the table are calculated from the total phaseshift assuming a uniform profile 4.0 cm wide (eq. 3.23 with k = $5/4$).

$$\mu = \left(1 - \frac{n}{n_c}\right)^{\frac{1}{2}} \simeq 1 - \frac{n}{2n_c} \quad . \qquad 3.26$$

[Use of this approximation causes an error of only 2% in our electron density measurement at its maximum (at 15 μsec) and less at all other times.] This has the fortunate consequence that the total microwave phaseshift is simply proportional to the electron density at tube centre at any instant of time, regardless of the form of the electron density profile. We can readily take advantage of this fact because we know the electron density at tube centre precisely at the instant of 3.2 cm cuton. It will be seen (Fig. 3.10) that this occurs at 24 ± 0.3 μsec. It should be noted that this procedure is correct provided that the electron density profile does not change markedly with time. We are normally constrained to make this assumption anyway.

The table in Fig. 3.9 shows the 8.8 mm phase-shift implied by the interferogram as a function of time. Electron densities obtained using the procedure described above, and errors based on the uncertainty in estimating the time at which a certain phaseshift occurred are also shown. The resulting time-varying electron density is plotted with error bars in Fig. 3.11.

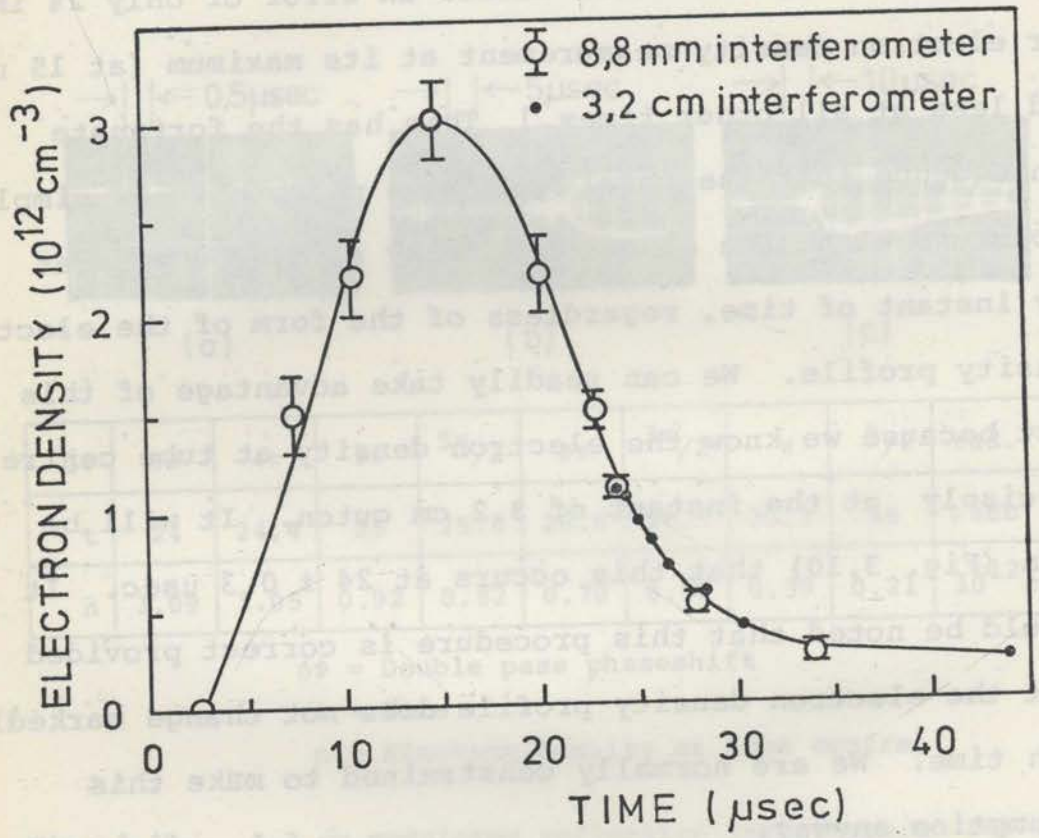

Fig. 3.11. Time dependent electron density, along the axis of the pulsed HCN laser plasma (length 1.8 m), for the discharge conditions (Table 5.1) corresponding to the spiking output records shown in Fig. 5.1.

Figure 3.10 shows a 3.2 cm interferogram obtained under the same operating conditions as the 8.8 mm interferogram in Fig. 3.9. Underneath the interferogram, which is shown on three timebases, is a table of the resulting 3.2 cm phaseshift as a function of time. As the interferograms show five distinct fringe maxima to cutoff we infer that the effective width of the electron density profile is 3.2 x 5/4 cm = 4.0 cm. Analysing the phaseshifts on the basis of a uniform profile (eq. 3.23 with $k = 5/4$) we obtain the electron densities which are also shown in the table under Fig. 3.10. The principal source of error in these measurements is the uncertainty in the choice of electron density profile; our choice of a uniform profile may cause a slight density overestimate.

Figure 3.11 shows the results of the 8.8 mm and 3.2 cm electron density measurements. It is clear that the two sets of results are in good agreement where they overlap, and this leads us to be confident about their validity elsewhere. There are two comments which should be made in regard to errors. Firstly, it should be recognised that the curve in Fig. 3.11 gives the electron density at tube centre at one axial position along the laser discharge (middle position in Fig. 3.5) and does not take axial nonuniformity into account. Referring to

Fig. 3.5 we see that the density measured at this position could be higher than the average along the tube axis by as much as 30%. This uncertainty should be remembered when Fig. 3.11 is used to estimate plasma refractive effects. Secondly, the reader may notice that the peak electron density shown in Fig. 3.11 is some 7% greater than a previously published result (Whitbourn et al, 1972). The present result represents an improvement in the analysis of our data.

3.4 Summary

In this chapter we have derived equations describing electromagnetic wave propagation in laboratory plasmas. These equations are fundamental to our studies of plasma effects in HCN lasers (Chs. 4 and 5) and 337 μm diagnostics of laboratory plasmas (Ch. 7). An important conclusion is that we will never observe significant collisional attenuation of 337 μm radiation in our present studies.

Measurements of electron densities in the pulsed HCN laser plasma have also been presented. Our preliminary measurements (Sec. 3.3.1) indicated that the densities are sufficiently large to cause plasma tuning effects in the cavity of the pulsed laser. We have described additional electron density measurements which are required for our studies of these plasma effects in Chapters 4 and 5.

Chapter 4

PLASMA EFFECTS IN THE PULSED 337 μm HCN LASER

4.1 Introduction

In Chapter 2 of this thesis we described an empirical study of our pulsed HCN laser. As a part of this study we originally measured the time-varying electron density in the laser discharge (Ch. 3), and this led to the prediction of strong plasma effects on pulsed HCN laser behaviour. In the present chapter and Chapter 5 we look more deeply into these effects. We base this study on the electron density measurements presented in Chapter 3.

Chapter 4 deals with "typical" laser operating conditions. The observations described are for conditions very similar to the optimum set evolved in Ch. 2 (Sec. 2.3.3.3), under which the laser produces a single pulse of 337 μm radiation in the afterglow of the (short-duration) discharge current pulse. We shall see that this pulse arises as the time-varying refractive index of the laser plasma electrons sweeps a cavity resonance through the 337 μm emission line. Our present observations indicate that multiple mode sweeping can produce spiking output from pulsed HCN lasers. In Chapter 5 we show that

spiking output is produced when we excite the laser with a low-amplitude long-duration current pulse and use a more stable resonator configuration. The long current pulse establishes a population inversion while current is still flowing and the electron density is sufficiently high to cause multiple mode sweeping. A more stable resonator is required because, as we shall see later in Chapter 4, high electron densities can cause our resonator to become unstable.

For the present however we restrict our attention to typical operating conditions, when a large-amplitude short-duration current pulse is used to excite the laser. Under these conditions laser action is only observed in the afterglow of the discharge when the electron density is generally too low to cause multiple mode sweeping. Laser action does not occur during the current pulse because either pumping of the upper laser level does not occur until later *or* the high electron density at early times precludes stable resonator modes. Thus the laser output consists of a single pulse of 337 μm radiation in the afterglow of the discharge. In the sections which follow, we study plasma effects involved in the production of this output pulse, the plasma contribution to the form of the variation of laser output pulse energy with

discharge voltage observed in sec. 2.3.3.1, and electron density effects on the stability of laser resonators.

4.2 Plasma Sweeping Through Laser Cavity Modes

On the basis of the electron density measurements presented so far we may make definite assertions about the delay and duration of HCN laser pulses. Firstly however, it is necessary to summarize some of the relevant properties of cavity modes in far-infrared lasers, especially in relation to the gainwidth for laser emission.

It is well known (Schwaller et al, 1967; Steffen and Kneubühl, 1968) that the gainwidth for laser emission for the 337 μm HCN line is much less than the spacing between the nearest pairs of low loss resonator modes. For this reason "laser resonator interferometry", which describes the process of observing the variation in laser output while translating one of its mirrors axially through several wavelengths, yields output only at specific lengths. As the total linewidth of the 337 μm (890 GHz) line is of the order of 10 MHz (Appendix 2; Steffen and Kneubühl, 1968) a fractional change in cavity length of $10^7/0.89 \times 10^{12}$ is sufficient to tune a cavity resonance through the width of the emission line. For a 2 meter laser resonator this implies a length change of 20 μm whereas axial cavity modes are 168 μm ($\lambda/2$) apart. A cavity using spherical mirrors has transverse modes $TEM_{p\ell q}$ for lengths lying between integer multiples of $\lambda/2$ but their losses increase quite

rapidly with the transverse (i.e. radial and azimuthal) quantum numbers p and ℓ and only a few of them have losses low enough to sustain laser action (Appendix 3).

It was shown in Sec. 3.3.1 that under typical operating conditions the electron density on the axis of the pulsed HCN laser falls from 10^{13} cm^{-3} to 10^{12} cm^{-3} in a few μsec, and that these two densities cause 337 μm phaseshifts of 5π and 0.5π per pass respectively. Alternatively, we may say that the electron density changes the effective length of the laser cavity. If the length of the laser discharge column is L its effective length is μL, where μ is the plasma refractive index given by eq. 3.18. μ can be approximated, for electron densities much lower than n_c ($n_c = 0.98 \times 10^{16}$ cm^{-3} for 337 μm radiation) by,

$$\mu = 1 - \frac{n}{2n_c} \quad . \qquad 4.1$$

Thus the change in effective cavity length caused by electron density n is,

$$\Delta L_{plasma} = - \frac{Ln}{2n_c} \quad . \qquad 4.2$$

Using eq. 4.2 we find that electron densities of 10^{13} cm^{-3} and 10^{12} cm^{-3} cause length changes to our 1.5 m discharge column of -760 μm and -76 μm respectively.

However, we saw above that a 20 μm length change is sufficient to tune through a single cavity resonance. Also, successive low loss cavity resonances do not overlap. We are led to hypothesise that laser emission occurs as the time-varying effective length of the laser resonator is swept through the resonant length of a low loss cavity mode. This is our cavity mode sweeping hypothesis. This hypothesis leads us to make two assertions; the first is related to the delay and duration of the pulsed laser output and the second is related to the spiking output which is sometimes produced by pulsed HCN lasers. We deal with these assertions in order.

Firstly, by altering the length of an HCN laser resonator we should change the delay and duration of the (delayed) output pulse. Lengthening the resonator should reduce the pulse delay because the effective length is least when the electron density is greatest (eq. 4.2). The duration of the pulsed output will be determined by the rate of plasma tuning through the laser transition. In view of the form of the plasma decay (Fig. 3.3; the rate of change of electron density decreases with time) later pulses should be longer than early ones. These effects have been observed by other experimenters (Steffen et al,1967a; Steffen and Kneubühl, 1968; Jones et al, 1969)

but they did not measure electron densities and therefore they were not in a position to establish the cause of the phenomena. Our discovery and explanation of these effects was completely independent. More recently, we have become aware of the work at Stanford University by McCaul (1969) who did measure electron densities. However his measurements are incorrect (see Sec. 4.4.2). Nevertheless it is clear that a good deal of parallel thinking developed in our laboratory and at Stanford, the essential difference being that the bias of McCaul's investigation was towards the diverging effect of the discharge plasma within the laser cavity. His theoretical results in this respect are valuable and will be considered and applied to our laser in the present chapter (Sec. 4.4.3).

Our second assertion following from the cavity mode sweeping hypothesis is related to the production of spiking output from pulsed HCN lasers. Under circumstances when laser emission occurs at early times the electron density will be high enough to sweep the effective cavity length through the resonant lengths of several low loss cavity modes. This would give rise to spiking output. We have observed such spiking output and it is studied in detail in Ch. 5.

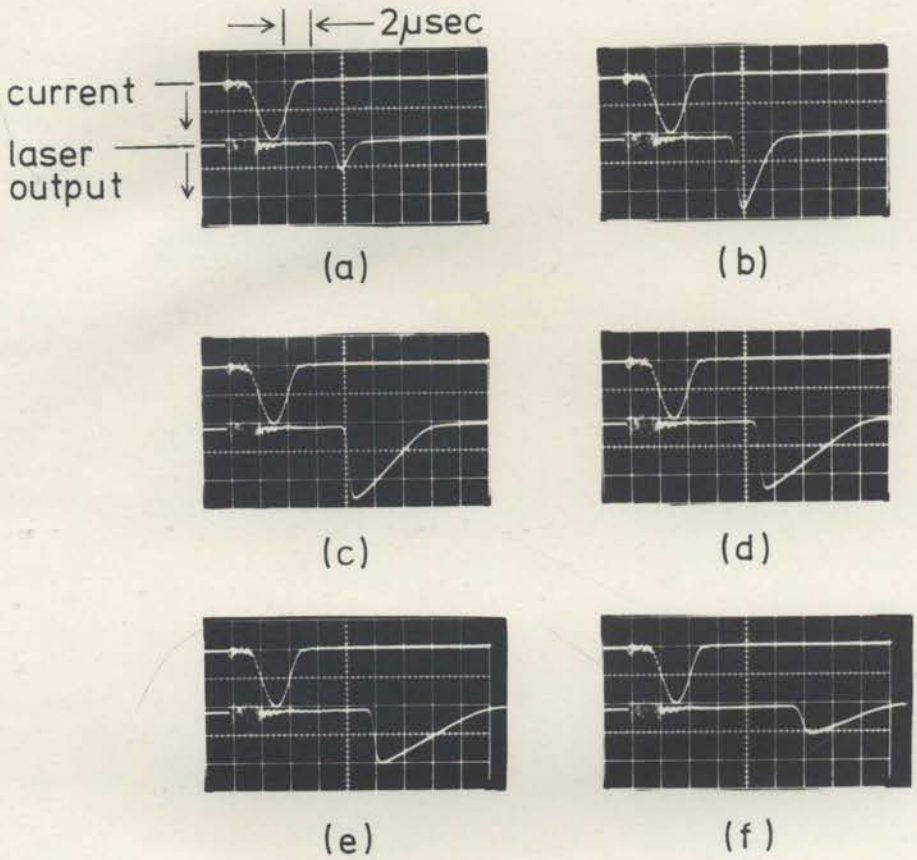

Fig. 4.1. Oscilloscope traces showing the variation of laser output pulse delay and duration with cavity length. Traces (a) to (f) are for successive decreases of 6.3 μm in cavity length. The upper trace in each photo is the laser discharge current (800 A; peak) and the time-base is 2 μsec per large scale division.

4.2.1 Observations of Cavity Mode Sweeping

We return now to our first assertion, that of variation of pulse delay and duration with laser cavity length. Figure 4.1 shows laser output pulses observed when the laser operating conditions were optimum (Sec. 2.3.3.3) except that the flowrate was higher by a factor of about two and the discharge voltage was 7.0 kV. The laser resonator was the same as in Ch. 2 (Sec. 2.2.3). Traces (a) to (f) correspond to successive decreases of 6.3 μm in cavity length, which were effected by displacing just one of the three micrometers on the mirror mount in 12.5 μm steps. The alignment of the resonator was approximately optimum for pulses (c) and (d) and distinctly inferior for pulses (a) and (f), which explains their low output powers. Pulses (a) and (f) are shorter than they would be if the cavity was optimally aligned. Study of the sequence of oscilloscope traces in Fig. 4.1 shows that the rising edge of the laser pulses occurs at successively later times. For example, from (a) to (f) there is an increase in pulse delay of about 4 μsec. In order to compare these results with our theory the time-varying electron density in the laser discharge was measured. The details of this measurement have already been presented in Sec. 3.3.2 and the time varying electron density is plotted in Fig. 3.8.

Table 4.1

	Measured			Predicted*	
Pulse	Delay	Duration	Cavity Length d	ΔL_{plasma} during pulse	ΔL_{plasma} between pulses
a	9.1	1.9	d_o	-	
					-
b	9.3	5.6	d_o -6.3	32	
					5.0
c	9.9	6.0	d_o -12.7	30	
					5.0
d	10.6	7.6	d_o -19.0	30	
					6.3
e	11.5	8.5	d_o -25.4	28	
					-
f	13	6.7	d_o -31.7	-	
Units	μsec	μsec	μm	μm	μm

* Changes in effective cavity length are predicted from the electron density decay shown in Fig. 3.8, using eq. 4.2.

Table 4.1 shows the delays and durations of the pulses shown in Fig. 4.1 and compares these with the predictions of our cavity mode sweeping hypothesis. Using eq. 4.2 we have calculated the change in effective length of the plasma column during each pulse, predicted by the electron density decay shown in Fig. 3.8. We have also calculated the change in effective cavity length occurring between the successive pulses shown in Fig. 4.1. Pulses (a) and (f) have been ignored in this analysis because they are significantly shortened by mirror misalignment.

These results show that decreasing the length of the laser resonator by 6.3 μm causes the pulse delay to increase just sufficiently for the effective length of the plasma column to increase by about the same amount; experimentally 5 to 6 μm. In addition we see that during each of pulses (b), (c), (d) and (e) the time-varying electron density sweeps the effective length of the laser resonator (length d) by an amount $\Delta d \simeq 30$ μm. Assuming that the observed pulses correspond to single mode sweeping Δd is related to the "effective gainwidth", Δf, of the 337 μm (f = 890 GHz) transition by, $\Delta d/d = \Delta f/f$. The present results (d = 2.2 m, $\Delta d \simeq 30$ μm) indicate an effective gainwidth of about 12 MHz. We shall see in Sec. 5.1.1 that the effective gainwidth should be of the order of the

sum of the width of the 337 μm spontaneous emission line and the width of the laser cavity resonance; for our laser this is about 10 MHz. Our observation of an effective gainwidth of 12 MHz is in good agreement with this. Thus our observations of the variation of pulse delay and duration with laser cavity length are in good agreement with our cavity mode sweeping hypothesis.

The measurements presented so far, are based on a small number of observations. Very good order of magnitude agreement between the predictions of the cavity mode sweeping hypothesis and experimental observations has been obtained. Nevertheless it is desirable that further comparison of theory and experiment be performed. This should be based on a much larger set of experimental observations. The experiment described above does not lend itself to a rigorous experimental treatment as well as the observations of spiking pulses presented in Sec. 5.2. Accordingly we defer a more detailed comparison of theory and experiment until then.

The foregoing experimental analysis relates to typical HCN laser operating conditions; the conditions described above lie in a range covered by the study in Ch. 2. With our present level of understanding of plasma effects in the pulsed HCN laser we are in a position to consider their contribution to some aspects of the laser

behaviour observed in Ch. 2. In particular we now turn our attention to the variation of laser output pulse energy with discharge voltage.

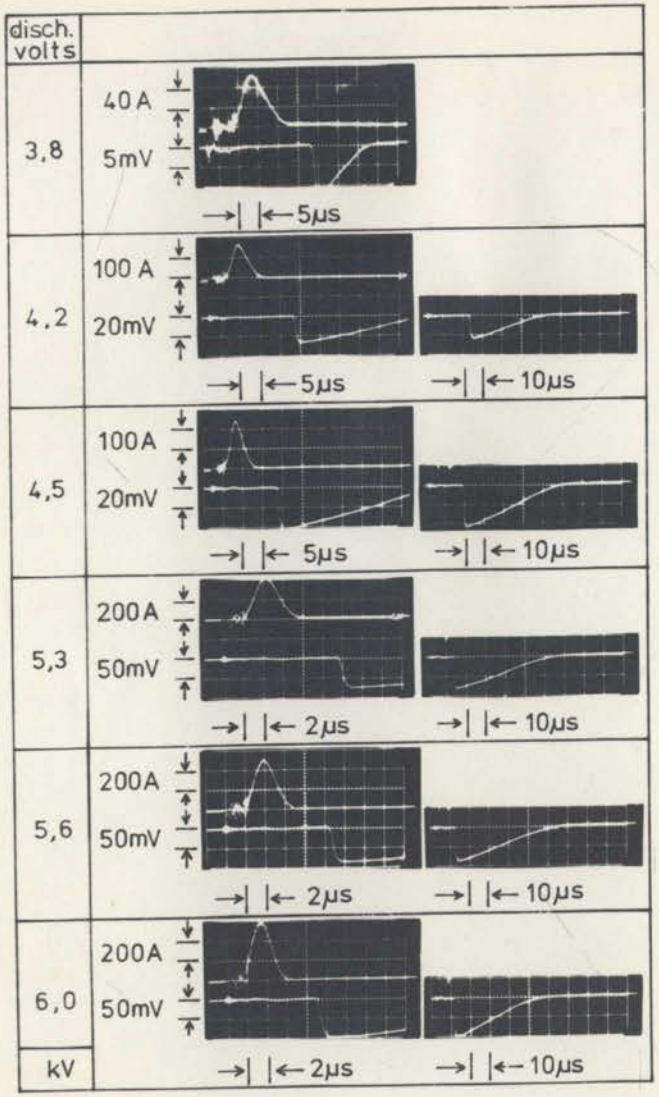

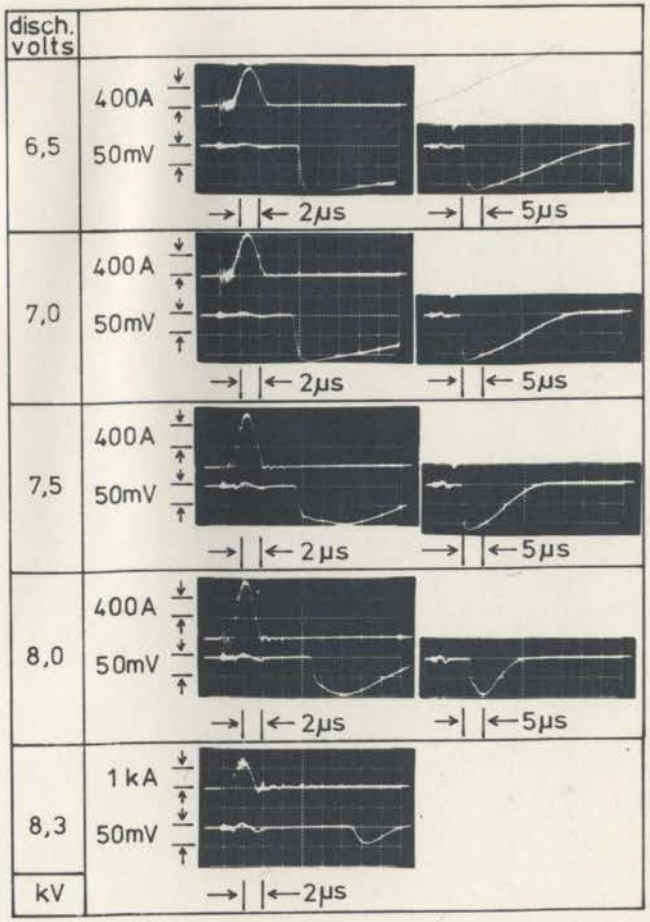

Fig. 4.2. Time resolved laser output pulses (lower and side traces) for a sequence of discharge voltages. The discharge current pulse (upper trace) is shown as a time reference for pulse delay measurements.

4.3 Contribution of Plasma Effects to the Variation of Laser Output Pulse Energy with Discharge Voltage

The reader will recall that in the study of Ch. 2 we observed that there was always an optimum discharge voltage for the production of maximum laser pulse energy. This was so for any particular set of gas conditions. We suggested (Sec. 2.3.3.4) that the refractive effect of the laser plasma electrons contributes to the decrease in laser plasma energy at higher than optimum discharge voltages. We now investigate this plasma effect.

Figure 4.2 shows photographs of the time resolved laser output power for a sequence of discharge voltages. All other conditions were optimum (Sec. 2.3.3.3) and the alignment and length of the laser resonator (as in Sec. 2.2.3) was kept constant throughout these observations. The pulses in Fig. 4.2 show considerable variation in both delay and duration with discharge voltage. We now check to see if the changing form of the electron density decay with discharge voltage (Fig. 3.3) is responsible for these variations. Measurements made with the 3.2 cm interferometer (Fig. 3.6) indicated that laser action only occurs when the electron density along the axis of the laser discharge is less than about 10^{12} cm^{-3} (i.e. after 3.2 cm cuton; 1.1×10^{12} cm^{-3}). Accordingly, electron densities

Table 4.2

	Observed (from Fig. 4.2)			Predicted* ΔL_{plasma}	
Discharge Voltage	† Pulse Delay	Pulse Duration	Pulse Amplitude	Onset of Lasing	Pulse Extinction
3.8	6	15	11	-51	-37
4.2	9	36	24	-51	-19
4.5	6	41	38	-51	-19
5.3	4	51	70	-57	-16
5.6	4	53	85	-60	-16
6.0	3	50	100	-72	-19
6.5	3	38	115	-72	-19
7.0	3	28	115	-72	-23
7.5	3	20	115	-72	-28
8.0	5	14	90	-60	-30
8.3	10	5	95	-51	-37
kV	μsec	μsec	mV	μm	μm

* The predicted plasma contributions ΔL_{plasma} to the laser cavity length are obtained from 3.2 cm microwave interferometric density measurements using eq. 4.2.

† The pulse delay is measured from the extinction of the discharge current pulse.

at times of interest are obtained entirely from 3.2 cm interferograms, in exactly the same manner as described in Sec. 3.3.2.

Table 4.2 summarizes the delays, durations and amplitudes of the pulses shown in Fig. 4.2 and the plasma contribution to the effective length of the laser resonator at times corresponding to the onset and extinction of each laser pulse. These lengths are calculated from the 3.2 cm interferometric electron density measurements (eq. 4.2) assuming the length of the plasma column to be 1.5 m.

Using the data in Table 4.2 we can plot the range in effective length of the laser resonator, swept by the time-varying electron density during the period of lasing, as a function of discharge voltage. This is shown in Fig. 4.3. It is clear that although the range in effective length swept during laser action varies considerably with discharge excitation, the centre of the range remains approximately fixed; 42 μm shorter than the free-space length of the laser resonator. This suggests that at line centre (890 GHz) the cavity is 42 μm shorter than the resonant length for the mode being excited. The fact that laser emission is observed over effective length changes of up to 53 μm indicates that the effective gainwidth for laser emission is as high as 21 MHz if a single mode is

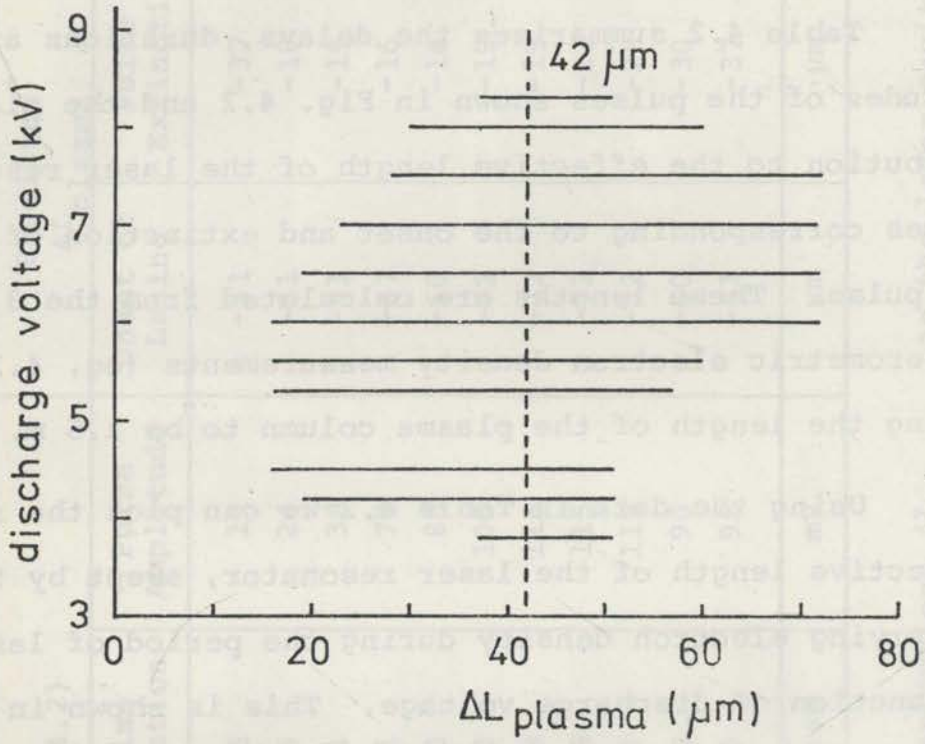

Fig. 4.3. Range in effective length of the laser resonator, swept by the time-varying plasma refractive index during the period of laser emission, as a function of discharge voltage. Although the range swept varies considerably with discharge excitation the centre of the range remains approximately fixed, at about 47 μm less than the free-space distance between the laser mirrors.

swept. This is much larger than the figure of 10 MHz suggested in Sec. 4.2; it is clearly much too large. However the separation of the two lowest loss modes (TEM_{00} and TEM_{01}) of the resonator used in this present study (one plane mirror and one with an 8 m radius of curvature) is only 30 μm (Appendix 3). It is shown in Sec. 5.1.1 that under high gain conditions these two modes will overlap to produce pulses spanning about 50 μm of effective cavity length when the gainwidth of an axial cavity mode is about 14 MHz. Since the present observations correspond to optimum operating conditions (Sec. 2.3.3.3), when the gain of the laser is undoubtedly quite high, this explanation seems quite likely.

It is now clear how the variations in pulse energy with discharge voltage observed in Ch. 2 are affected by plasma refraction. Referring to Fig. 4.2 we see that as the discharge voltage is raised from 6.0 to 6.5 and then 7.0 kV the peak laser output power remains essentially the same. The range of effective cavity length over which laser action is observed (Fig. 4.3) also remains about the same. However, the rate of electron density tuning during the lasing period increases with discharge voltage in this range (compare the range of cavity length swept during laser emission (Fig. 4.3) with the duration

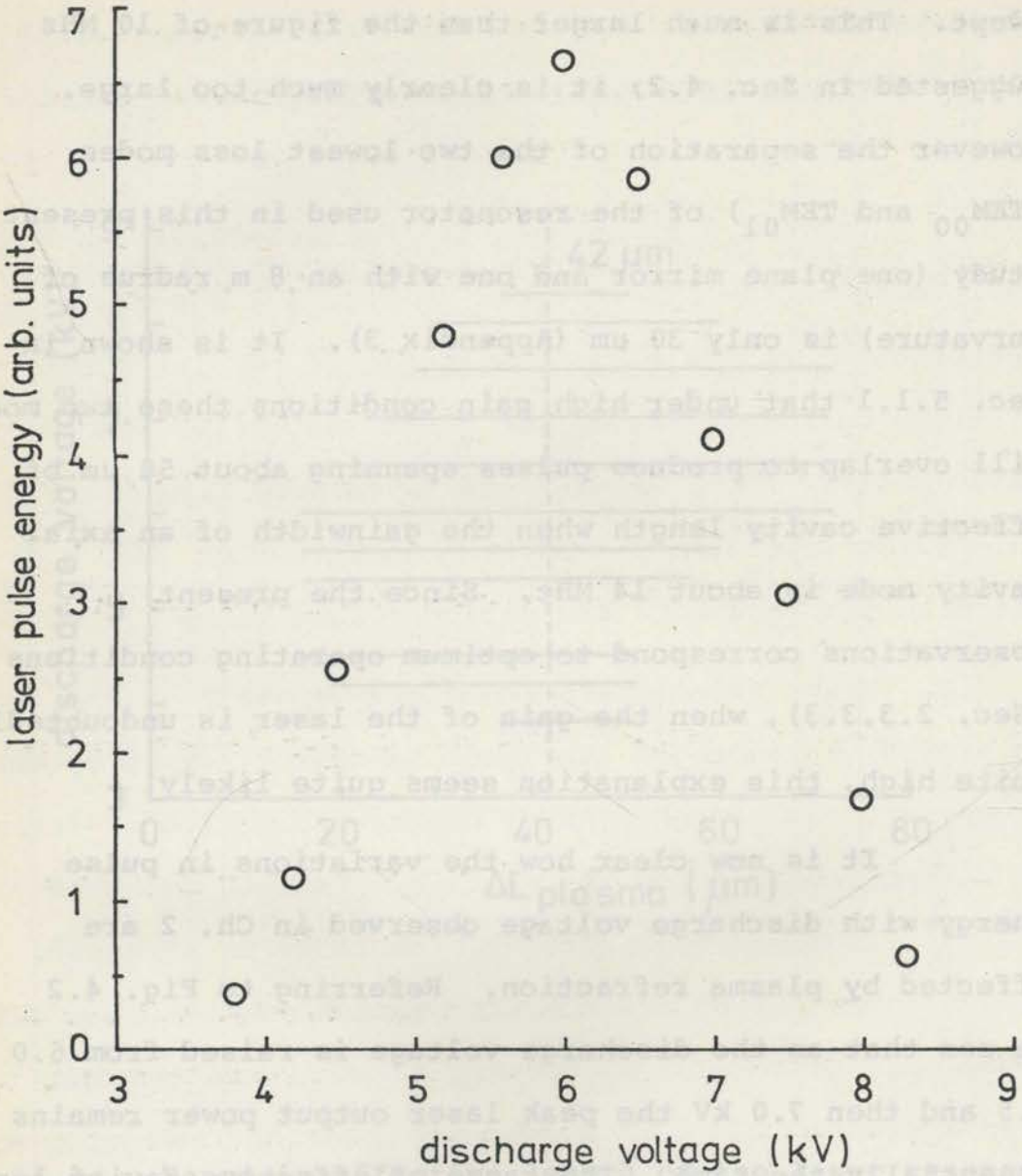

Fig. 4.4. Laser output pulse energy as a function of discharge voltage for optimum gas conditions (Sec. 2.3.3.3). The points plotted are energy estimates obtained by multiplying the pulse height by pulse duration as observed with the Putley detector (Fig. 4.2). The form of the curve is very similar to that obtained when the Golay cell was used to measure pulse energy directly (Fig. 2.8).

of laser emission (column 3; Table 4.2)); the pulses become shorter in duration and the pulse energy drops. This trend continues to higher voltages but eventually the range of cavity length swept during the period of laser output decreases. This indicates that the gain of the discharge does fall off for large input pulse energies. Thus the characteristic nature of the variation of laser pulse energy with discharge voltage depends on both plasma effects *and* the efficiency of the discharge excitation. It is also apparent that the pulse delay and duration are determined by :

(a) The existence of a state of population inversion, and

(b) The time and rate at which a low loss cavity resonance is tuned through the laser line.

Clearly, the behaviour shown in Fig. 4.2 would be modified in detail if the laser cavity length were set to a different value. This length was adjusted initially to give maximum pulse energy at the optimum operating voltage ($\simeq$ 6 kV) so the pulses shown in Fig. 4.2 should correspond well to the cavity conditions used in Ch. 2. As a check on this, the laser pulse energy; crudely estimated by multiplying pulse height by pulse amplitude, is plotted as a function of discharge voltage in Fig. 4.4. It is clear

that the *form* of the variation of output pulse energy with discharge voltage is the same as that observed when the Golay cell is used to measure 337 μm pulse energy directly (Fig. 2.8). But now the origin of this form is a little clearer.

4.4 Plasma Effects on Cavity Stability

In addition to the plasma effects already discussed, the electrons in the HCN laser will constitute a diverging element because their density is greatest at the centre of the discharge vessel and falls to zero at its walls. It is possible, for a sufficiently large radial electron density gradient, that this electron lens effect will preclude stable resonator modes. McCaul (1969; 1970 ; McCaul and Schawlow, 1970) has measured electron densities in a pulsed HCN laser quite similar in dimensions to the pulsed laser constructed by the author. By choosing a suitable parabolic electron density profile McCaul calculated stable resonator configurations as a function of the electron density at the discharge tube centre. Then, using a variable curvature laser mirror he measured the range of curvatures which would support laser action for the (small) range of electron densities in which laser action was observed. McCaul found reasonable agreement between his theory and his experimental findings provided that he suppressed tube-modes (i.e. those which depend on internal wall reflections) by placing annuli of "eccosorb" (a commercial microwave absorber) inside the discharge vessel. However, McCaul made several errors in the analysis of his experimental data and his results

need to be re-interpreted (Sec. 4.4.2).

In addition to these measurements McCaul observed the variation in pulse delay with mirror position described and discussed in Sec. 4.2.1 and proposed the cavity mode sweeping mechanism and the possibility of producing multiple output pulses if the effective length of an HCN laser resonator is swept through successive cavity resonances. He did not give any quantitative verification of the first effect, nor did he indicate that he had observed the second effect at all.

We are interested in the implications of McCaul's diverging lens effect in relation to our pulsed laser but we cannot apply his theory and results directly. As we pointed out above there are several errors in his experimental analysis. In addition McCaul's laser discharge extended over the full length of the laser resonator but ours does not. His theory must be extended to cover the more general situation. It is appropriate therefore to present a brief summary of McCaul's theory before examining his experimental results. We then extend his theory to cover our experimental situation and see what effect the diverging lens effect has in our pulsed laser.

4.4.1 McCaul's Theory

McCaul's treatment starts with the paraxial analysis for light rays travelling through a medium with a refractive index gradient (Born and Wolf, 1965). The differential equation describing propagation of a ray in the z direction, at a distance r from the principal axis of a system is,

$$\frac{d^2r}{dz^2} = \frac{1}{\mu}\frac{d\mu}{dr} \quad , \qquad 4.3$$

where μ is the refractive index.

Then approximating eq. 3.18 for the refractive index of a medium of electrons we have

$$\mu = 1 - \frac{n}{2n_c} \quad , \qquad 4.4$$

which is valid when $n << n_c$.

Combining eqs. 4.3 and 4.4 we find (to first order),

$$\frac{d^2r}{dz^2} = -\frac{1}{2n_c}\cdot\frac{dn}{dr} \quad . \qquad 4.5$$

Thus for propagation through the parabolic distribution

$$n(r) = n_o\left[1 - \beta\left(\frac{r}{r_o}\right)^2\right] \quad , \qquad 4.6$$

where r_o is the tube radius, the ray differential equation is,

$$\frac{d^2r}{dz^2} = \frac{\beta n_o}{r_o^2 n_c} \cdot r \quad , \tag{4.7}$$

to first order. The general solution of this equation is

$$r(z) = A \text{ Cosh } \alpha z + B \text{ Sinh } \alpha z \quad , \tag{4.8}$$

where

$$\alpha^2 = \frac{\beta n_o}{r_o^2 n_c} \quad . \tag{4.9}$$

It may be readily verified that,

$$r(z + L) = r(z) \text{ Cosh } \alpha L + r'(z) \overline{\text{Sinh } \alpha L}/\alpha$$

and $\tag{4.10}$

$$r'(z + L) = r(z) \, \alpha \text{ Sinh } \alpha L + r'(z) \text{ Cosh } \alpha L \quad ,$$

where $r' = \frac{dr}{dz}$.

Thus in matrix form we may write

$$\begin{bmatrix} r(z + L) \\ r'(z + L) \end{bmatrix} = \begin{bmatrix} \text{Cosh } \alpha L & \overline{\text{Sinh } \alpha L}/\alpha \\ \alpha \text{ Sinh } \alpha L & \text{Cosh } \alpha L \end{bmatrix} \begin{bmatrix} r(z) \\ r'(z) \end{bmatrix} \quad , \tag{4.11}$$

and we may describe propagation through a distance L of this medium by the ray transfer matrix (Kogelnik and Li, 1966),

$$\begin{bmatrix} a & b \\ c & d \end{bmatrix} \equiv \begin{bmatrix} \text{Cosh } \alpha L & \overline{\text{Sinh } \alpha L}/\alpha \\ \alpha \text{ Sinh } \alpha L & \text{Cosh } \alpha L \end{bmatrix} . \qquad 4.12$$

Now the ray transfer matrix for reflection from a mirror with radius of curvature R is (Kogelnik and Li, 1966),

$$\begin{bmatrix} 1 & 0 \\ -2/R & 1 \end{bmatrix} ,$$

so that the round trip matrix for a laser resonator of length L, containing the parabolic distribution of electrons described by eq. 4.6 is,

$$\begin{bmatrix} A & B \\ C & D \end{bmatrix} \equiv \begin{bmatrix} 1 & 0 \\ -2/R_1 & 1 \end{bmatrix} \begin{bmatrix} a & b \\ c & d \end{bmatrix} \begin{bmatrix} 1 & 0 \\ -2/R_2 & 1 \end{bmatrix} \begin{bmatrix} a & b \\ c & d \end{bmatrix} \qquad 4.13$$

where R_1 and R_2 are the radii of curvature of the two laser mirrors.

Now, for any infinite sequence of identical elements, each described by the ray transfer matrix

$$\begin{bmatrix} A & B \\ C & D \end{bmatrix} ,$$

it may be shown (Kogelnik and Li, 1966) that the system is stable only if

$$-1 \leqslant \frac{A + D}{2} \leqslant 1 \quad . \qquad 4.14$$

Thus the stability condition for our laser resonator, containing the parabolic distribution of electrons, is obtained by substituting A and D from eq. 4.13 into eq. 4.14. After a little algebra we arrive at the condition,

$$0 \leqslant \left(a - \frac{b}{R_1}\right)\left(a - \frac{b}{R_2}\right) \leqslant 1 \quad , \qquad 4.15$$

where a and b are determined by eq. 4.12. Using these values of a and b we find,

$$0 \leqslant \text{Cosh}^2 \alpha L - \frac{\text{Cosh } \alpha L \text{ Sinh } \alpha L}{\alpha}\left(\frac{1}{R_1} + \frac{1}{R_2}\right)$$

$$+ \frac{\text{Sinh}^2 \alpha L}{\alpha^2} \cdot \frac{1}{R_1 R_2} \leqslant 1 \quad , \qquad 4.16$$

is the required stability condition. Since $\alpha^2 = \beta n_o / r_o{}^2 n_c$ we may plot, for given values of $\beta n_o / n_c$, a stability

diagram with coordinates $1/R_1$ and $1/R_2$ (or L/R_1 and L/R_2), determined by eq. 4.16. McCaul (1970; figs. 2 and 3) did this but it should be noted that he lost β somewhere in his algebra and the curves plotted in his paper for particular values of n_o/n_c (N_O/N_P in McCaul's notation) really apply to those values of $\beta n_o/n_c$. Alternatively his stability diagrams may be considered to apply when $\beta = 1$. In this connection it is worth noting that his definition of M (McCaul, 1970; p.655) lacks a factor β in the denominator.

The stability condition may be viewed in a different way. If one laser mirror is fixed (e.g. R_1 fixed) then for any particular value of $\beta n_o/n_c$ there is a range of values of R_2 which satisfy the stability condition eq. 4.16. McCaul (1970) has plotted, for $g_1 (\equiv 1 - L/R_1) = 0.28$ (the value corresponding to his fixed mirror) the range of stable values of $g_2 (\equiv 1 - L/R_2)$ for a few values of β. (McCaul's fig. 10 is for $\beta = 0.65$; fig. 11 is for $\beta = 0.65$, 1.0 and 1.44). Experimentally, he measured the electron density and the range of stable mirror curvatures simultaneously and compared these results with the range predicted by eq. 4.16. In the next section we discuss McCaul's results in detail.

4.4.2 McCaul's Results

There are several anomalies in McCaul's results. They follow from two errors in his interpretation of microwave interferograms and lead him to overestimate the electron densities in his pulsed laser by a factor of about two at early times and by about an order of magnitude at later times. For the purpose of discussing McCaul's results we shall confine our attention to his paper published in Applied Optics (McCaul, 1970). There is very little additional information in his thesis (McCaul, 1969) or the third reference (McCaul and Schawlow, 1970) - both contain the same errors.

Referring first to McCaul's fig. 12, which shows the experimental variation of pulse delay with cavity length, and referring to his electron density decay curve (fig. 9) we find that the smallest change in electron density (at tube centre) during a laser pulse is 2×10^{12} cm^{-3}. Assuming a 1.5 m discharge column (an underestimate) this implies a change Δd_1 in effective cavity length d due to plasma tuning (eq. 4.2) of 150 μm during the period of laser emission. But since the effective gainwidth Δf is of the order of 10 MHz (Sec. 5.1.1) laser action should only occur over a range Δd_2 of cavity length d given by

$$\Delta d_2 = d \cdot \frac{\Delta f}{f} = \frac{1.6 \times 10^6 \times 10^7}{890 \times 10^9}$$

$$= 18 \ \mu m \ .$$

The change in effective cavity length during laser emission Δd_1 should not be much greater than this figure. Ideally Δd_1 and Δd_2 should be equal. McCaul did this calculation in a rather more roundabout way. He concluded that since Δd_1 is not much greater than the axial mode separation ($\equiv \lambda/2 = 168 \ \mu m$) then he should not have observed multiple mode sweeping. He was aware that Δd_1 was anomalously large but proposed that this could be due to a detector effect (quite unlikely) or a large cavity mode linewidth caused by the electron lens effect. In the light of our own cavity mode sweeping observations (Secs. 4.2.1 and 5.2) the latter explanation is highly unlikely. In fact, if the electron density was as large as McCaul believed, then multiple mode sweeping should have occurred because his resonator would be likely to have at least one low loss transverse mode between successive axial modes. There is also the possibility that the gainwidths of two nearby modes could overlap, giving rise to an anomalously wide apparent gainwidth. This too, is unlikely to cause the very large gainwidth which McCaul observed.

These considerations lead us to believe that McCaul's electron density measurements are far too high. We could check this directly if McCaul had supplied with fig. 12, the axial mirror displacements giving rise to the observed changes in pulse delay. It is ironic that he did not attempt to correlate this information because it gives a direct measure of the average electron density along the laser axis. It would have revealed his error immediately.

Referring now to McCaul's microwave interferograms (fig. 6) we see that they are not unlike those shown in Fig. 3.2 except that the last quarter fringe ($\pi/2$ phase shift occurs at $\sim$ 7.6 μsec) decays much more quickly than ours and is followed by two very small amplitude "wiggles" (zero crossings at 13 μsec and 30 μsec). McCaul has erroneously includes these wiggles in his fringe count and has made the additional error of ascribing 2π phase shift to successive zero crossings instead of π. Thus all his phase-shift measurements are too high by a factor exceeding two.

It is our experience with microwave measurements of electron densities in decaying plasmas that small amplitude wiggles sometimes occur in the afterglow of the plasma. Their origin is unclear but they are never plasma

fringes. We can show that the last two wiggles which McCaul counts could not possibly be half-fringes because their amplitude is far too small. An upper limit to the electron-ion collision frequency (Sec. 3.2.1) assuming T_e = 300 K (the worst possible case) still gives $\nu/\omega < 0.1$. This agrees with the figure quoted in McCaul's thesis. Substitution into eq. 3.16, using McCaul's electron densities as an upper limit gives an attenuation length of about 10 cm (equal to his vessel diameter). But the last two wiggles are about 8 db and 15 db down with respect to the last unmistakable plasma fringe. It is clear that plasma fringes could not suffer so much collisional attenuation.

It is hard to explain McCaul's interferograms. The last quarter fringe does decay exceptionally fast and the sudden change in gradient at 13 μs is very strange. Without having access to McCaul's equipment it is hard for us to diagnose the cause of the small wiggles which lead him into trouble. The fact that he borrowed his interferometer and his error in assigning 2π phase shift to successive zero crossings suggest that he was insufficiently experienced with microwave interferometry to be able to recognise the peculiarities of his interferograms.

In view of these errors it is clear that McCaul's conclusions, for instance about the choice of β may be incorrect. In order to make a new comparison of his theory with his experimental results we need to re-analyse his microwave interferograms. However it should be pointed out that his use of the *same* parabolic profile to calculate the electron density at tube centre *and* the divergent lens effect may not be appropriate. When a parabolic profile is used for estimating the electron lens effect the essential function of the parameter β (see eq. 4.6) is to give the right radial electron density gradient at tube centre. However if the parabolic profile is used to estimate the electron density in the laser discharge β should be chosen to give the correct effective width for the electron density profile (see Sec. 3.3.1.1). The same value of β is unlikely to be appropriate for both purposes unless the electron density profile in the laser is exactly parabolic; this is highly unlikely. McCaul plotted a family of curves (fig. 11) showing stable mirror curvatures as a function of electron density for various values of β. He then compared this family with the range of stable mirror curvatures which sustained laser action for the range of measured electron densities during laser emission. However for each comparison (i.e. each value

of β) he re-analysed his microwave interferograms for the corresponding value of β. The danger of this procedure is obvious. The value of β which McCaul favoured was β = 0.65 which implies a very wide electron density profile; our observations (Sec. 3.3.1.1) of 3¼ to 4¼ 8.8 mm microwave interferometer fringes to cutoff indicates that β lies between about 1.8 and 1, suggesting a much narrower profile. But a broad profile requires a lower peak electron density to produce a given total microwave phase-shift than a narrow one. Thus analysis of McCaul's interferograms assuming a parabolic profile with β = 0.65 may underestimate the electron density in his laser. [Of course McCaul's errors in interpreting his microwave interferograms caused him to overestimate his microwave phase shifts - the magnitude of this overestimate far outweighed the compensating effect of using a wide electron density profile.]

Instead of following McCaul's procedure it is better to make the best possible estimate of the time-varying electron density in his laser resonator. Then by comparing our electron density estimates and the range of stable cavity curvatures observed with McCaul's cavity stability diagrams we can select the best value of β for describing the diverging electron lens effect. Because

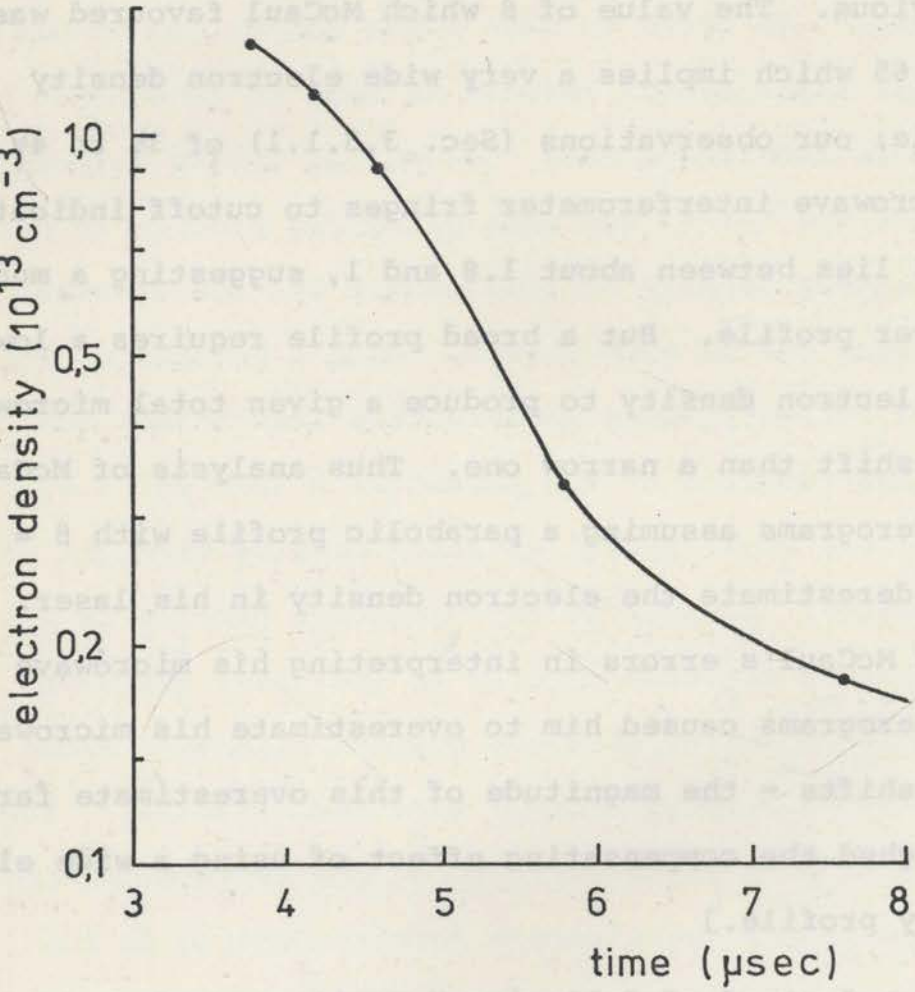

Fig. 4.5. Estimate of the time-dependent electron density along the axis of McCaul's laser resonator. 8.0 mm phase-shifts were inferred from McCaul's interferograms (McCaul, 1970; fig. 6) and analysed assuming a uniform profile 4.0 cm wide (i.e. using eq. 3.23 with k = 5). McCaul's time zero is at the switch-on of the laser discharge current pulse.

McCaul's laser and operating conditions were so similar to ours we estimate his electron densities assuming a uniform plasma column 4 cm in diameter (eq. 3.23 with $k = 3\frac{1}{4}$). This is close to our value of 2.9 cm (Sec. 3.3.1) scaled in the ratio of the respective tube diameters. This gives the electron density decay shown in Fig. 4.5. Because of the strange behaviour of McCaul's interferograms we have not estimated phase shifts less than $\pi/2$ which means that we cannot measure densities later than about 7.6 μsec.

We can infer from McCaul's figs. 9 and 10 that laser action was observed at times between 5.5 and 21 μsec so we can only estimate the electron density at the early end of the lasing range. At 5.5 μsec we obtain from Fig. 4.5, $n_e = 4.3 \times 10^{12}$ cm^{-3}, which if plotted on fig. 11 of McCaul's paper, indicates that $\beta \simeq 1$ is the best choice for fitting his theory to his experimental results. However the first conclusion below has some bearing on the value of this choice.

McCaul's work leads us to the following conclusions:

1. By altering the curvature of one of his laser mirrors McCaul was able to scan the range of stable resonators in the presence of the diverging electron lens effect.

However he did not observe laser emission earlier than about 5.5 μsec under any circumstances. This was so, despite the fact that he was able to produce resonator configurations which would have been stable at times earlier than 5.5 μsec. Equally well, it appears that scanning the laser cavity length did not cause laser emission earlier than 5.5 μsec either. The design of McCaul's variable curvature mirror ensured that this scanning would have occurred whenever he altered its curvature. Thus the minimum delay of 5.5 μsec (measured from the beginning of McCaul's 5 μsec current pulse) must have been determined by lack of population inversion at early times rather than either the diverging or longitudinal refractive self-Q-switching effect.

Of course, it is quite common for the delay to be increased by the electronic changes in effective cavity length (see Sec. 4.2) and it is possible that in some HCN lasers the pulse delay may be affected in the same way by the diverging electron lens effect. Nevertheless, the fact remains that McCaul's results do not demonstrate refractive self-Q-switching by the effect which he proposes. It follows that our estimate of $\beta \simeq 1$ is made only on the basis that it makes the predictions of McCaul's diverging lens theory consistent with his experimental results.

2. McCaul calculated the effects of gain focusing, and focusing due to the anomalous dispersion of the laser medium, assuming a parabolic gain profile with $\beta = 1$ and compared the results with those of the electron lens effect. He found that for the gain measured in his laser ($\simeq$ 26% per pass) the "focal lengths" associated with these effects were at least an order of magnitude greater than the focal length due to the electron lens. This would also apply to the lasers described in this thesis.

Footnote. We stated earlier that McCaul did not attempt to correlate his measured electron densities with the observed pulse-delay versus cavity-length data; in fact, where he presented pulse delay data he did not provide the values of the corresponding cavity length changes. However, he has presented in his thesis (McCaul, 1969; fig. 16) a graph of experimental pulse-delay versus cavity-length for discharge conditions *similar* to those for which he has given electron density measurements. On the basis that only single mode sweeping is responsible for the laser output in this case the data in McCaul's fig. 16 imply peak electron densities of only about 2×10^{11} cm^{-3} whereas his measurements (even after our revised analysis earlier in this section) indicate peak densities greater than 10^{13} cm^{-3}. The most probable explanation of this

anomally is that the excitation of tube-modes in McCaul's laser (a complication which we have avoided in our pulsed laser; see Sec. 2.2.3) has prevented him from observing plasma sweeping of a *single* cavity mode in the instance quoted. In support of this, we note that McCaul says that for some laser operating conditions the delay of the output pulse was essentially independent of the laser cavity length. In this case his laser must have had many overlapping low-loss tube-modes. Under these circumstances we cannot hope to infer meaningful electron density values from pulse-delay versus cavity-length information.

4.4.3 Comparison with Present Laser

It is of interest to know whether the diverging effect of the plasma electrons can be a significant effect in the pulsed laser described in Ch. 2. The round trip matrix for this laser is more complicated than McCaul's

because the discharge does not extend to the laser mirrors. Figure 4.6 shows the relevant dimensions of the laser and the ray transfer matrices for its various elements, where a, b, c and d are still defined by eq. 4.12.

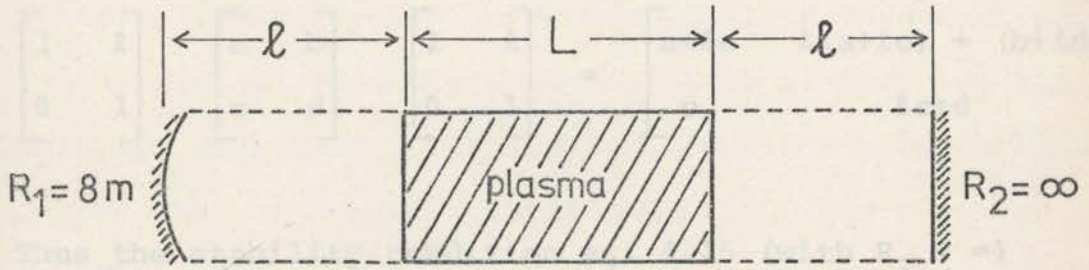

$$\begin{bmatrix} 1 & 0 \\ -2/R_1 & 1 \end{bmatrix} \quad \begin{bmatrix} 1 & \ell \\ 0 & 1 \end{bmatrix} \quad \begin{bmatrix} a & b \\ c & d \end{bmatrix} \quad \begin{bmatrix} 1 & \ell \\ 0 & 1 \end{bmatrix} \quad \begin{bmatrix} 1 & 0 \\ -2/R_2 & 1 \end{bmatrix}$$

Fig. 4.6 Ray transfer matrices for the elements of the pulsed HCN laser

Thus the round trip matrix is,

$$\begin{bmatrix} A & B \\ C & D \end{bmatrix} = \begin{bmatrix} 1 & 0 \\ -2/R_1 & 1 \end{bmatrix} \begin{bmatrix} 1 & \ell \\ 0 & 1 \end{bmatrix} \begin{bmatrix} a & b \\ c & d \end{bmatrix} \begin{bmatrix} 1 & \ell \\ 0 & 1 \end{bmatrix}$$

$$\times \begin{bmatrix} 1 & 0 \\ -2/R_2 & 1 \end{bmatrix} \begin{bmatrix} 1 & \ell \\ 0 & 1 \end{bmatrix} \begin{bmatrix} a & b \\ c & d \end{bmatrix} \begin{bmatrix} 1 & \ell \\ 0 & 1 \end{bmatrix}$$

which is equivalent to eq. 4.13 if

$$\begin{bmatrix} a & b \\ c & d \end{bmatrix}$$

is replaced by,

$$\begin{bmatrix} 1 & \ell \\ 0 & 1 \end{bmatrix} \begin{bmatrix} a & b \\ c & d \end{bmatrix} \begin{bmatrix} 1 & \ell \\ 0 & 1 \end{bmatrix} = \begin{bmatrix} a+\ell c & \ell(a+\ell c) + (b+\ell d) \\ c & \ell c+d \end{bmatrix}.$$

Thus the stability condition eq. 4.15 (with $R_2 = \infty$) becomes,

$$0 \leqslant \left[(a+\ell c) - \frac{\ell(a+\ell c) + (b+\ell d)}{R_1} \right] (a+\ell c) \leqslant 1 \qquad 4.17$$

The expression in eq. 4.17 is a function of a, b, c and d which are all explicit functions of L (the length of the discharge column) and (eq. 4.9),

$$\alpha = \left(\frac{\beta\, n_o}{r_o^{\,2} n_c} \right)^{\frac{1}{2}} .$$

For a resonator which is stable in the absence of plasma the lower inequality is satisfied for all $\alpha \geqslant 0$. The maximum value of α which satisfies the upper inequality in eq. 4.17 is readily calculated for any particular

plasma length L and resonator configuration.

We now investigate the stability condition eq. 4.17 in two cases. Firstly, we consider the resonator and discharge conditions described earlier (Sec. 4.2.1) where the laser was excited by a large-amplitude short-duration current pulse and produced a single output pulse in the afterglow of the decaying laser plasma. We then turn our attention to the conditions which produce spiking output (Ch. 5). Here a small-amplitude long-duration current pulse is used to excite the laser and pumping of the upper laser level occurs as early as the time of maximum current. At these early times the electron density is high enough to cause multiple mode sweeping of cavity resonances and spiking output is produced.

For the cavity mode sweeping observations described in Sec. 4.2.1 laser action was not observed for peak electron densities (n_o) greater than about 10^{12} cm^{-3}. Calculation of the maximum allowable α for the appropriate conditions (L = 1.5 m, ℓ = 0.35 m, R_1 = 8 m) leads to a value of 0.31 m^{-1}. This places an upper limit of 1.4×10^{12} cm^{-3} on βn_o. Thus if the electron lens effect does preclude stable resonator modes then the effective value of β must be as large as 1.4. Alternatively it may be that laser action does not occur at early times because

population inversion is not established when $n_o > 10^{12}$ cm^{-3} (just by coincidence).

We arrive at two conclusions:

(a) Regardless of the explanation of why laser emission was not observed at early times we can easily understand why multiple mode sweeping was not observed with the pulsed laser as described in Ch. 2. A peak electron density of only 10^{12} cm^{-3} changes the effective cavity length of the laser by 80 μm. This is insufficient to sweep the effective length of the laser resonator through the resonant lengths of several modes.

(b) The diverging lens effect *may* be responsible for the minimum delay between extinction of our laser current pulse and the onset of 337 μm emission. However it does not affect our cavity mode sweeping observations at later times (Secs. 4.2 and 4.3).

Let us now consider the resonator and discharge conditions under which our pulsed laser produces spiking output. They are summarized in Table 5.1. Under these conditions laser emission is observed as early as 16 μsec (Figs. 5.2 and 5.3) (about the time of peak discharge current Fig. 5.1) when the peak electron density (n_o) in the laser discharge is about 3×10^{12} cm^{-3}. Calculation of the maximum allowable α which satisfies the stability

condition eq. 4.17 for the new set of conditions ($L = 1.8$ m, $\ell = 0.2$ m, $R_1 = 3.7$ m) leads to a value of $0.43\ m^{-1}$. This places an upper limit of $2.6 \times 10^{12}\ cm^{-3}$ on βn_o and if the electron lens effect is responsible for preventing laser emission before 16 μsec then β must be 0.9. This is very close to our estimate of $\beta \simeq 1$ for McCaul's results. Thus it seems quite likely that the diverging lens effect is responsible for the minimum pulse delay of 16 μsec. If this is so, it is apparent that replacing the 8 metre radius mirror with a 3.7 metre radius mirror (see Sec. 5.2 and Table 5.1) is equally important for the production of spiking output as the small-amplitude long-duration current pulse. For if the 8 metre radius mirror had been used the resonator would have become unstable for peak electron densities greater than $1.2 \times 10^{12}\ cm^{-3}$ (calculated from the stability condition eq. 4.17 with $L = 1.8$ m, $\ell = 0.2$ m, $R = 8$ m, $\beta = 0.9$) instead of $3 \times 10^{12}\ cm^{-3}$ when the 3.7 metre radius mirror is used. A density of $1.2 \times 10^{12}\ cm^{-3}$ changes the effective length of the laser resonator by only 100 μm. This is barely enough to cause multiple mode sweeping.

We also conclude from these calculations that β is probably not as large as 1.4 for normal laser operating

conditions. Thus it appears that under normal operating conditions when the pulsed laser is excited by a large-amplitude short-duration current pulse it is lack of pumping rather than the diverging lens effect which prevents laser action at early times.

4.5 Summary

The important features of the work described in this chapter are listed below:

1. We have presented experimental observations of 337 μm laser output pulses which show increasing pulse delay and duration with decreasing cavity length. By measuring the time-varying electron density in our laser discharge we have compared these observations with the predictions of our cavity mode sweeping theory. Good agreement was obtained. The observed pulse durations were consistent with an effective gainwidth for laser emission of the order of 10 to 15 MHz for the conditions under study.

2. We have observed widely varying 337 μm pulse delays and durations from our pulsed HCN laser as a result of changing only the discharge conditions. These variations have been shown to be entirely consistent with our cavity mode sweeping theory. This study has shown in one instance, how plasma effects contribute to the laser behaviour which was studied in Ch. 2.

3. Examination of McCaul's theory of the possible diverging effect of the laser plasma electrons leads us to believe that this effect can preclude stable resonator modes. However we found that McCaul's results do not

indicate that this effect was responsible for the minimum pulse delay of the output of his pulsed laser. Nevertheless, under some circumstances the diverging effect of the laser plasma electrons could be responsible for the minimum delay which usually occurs between extinction of the excitation current pulse and the onset of laser action. In practice the delay will be further increased by the direct cavity mode sweeping effect of the discharge plasma.

4. We have calculated the possible diverging effect of the plasma electrons in our pulsed laser under two sets of conditions.

(a) Under normal operating conditions the laser is excited by a large-amplitude short-duration current pulse and the output consists of a single delayed 337 μm pulse in the afterglow of the discharge. Here we have seen that the diverging lens effect could prevent laser emission at early times if the radial electron density gradient at tube centre is quite large ($\beta = 1.4$). It seems more likely that laser emission is not observed at early times because short current pulses do not cause pumping of the upper laser level at early times.

(b) When the laser is excited by a low-amplitude long-duration current pulse laser emission commences during the

current pulse when the electron density at tube centre is quite high. Multiple mode sweeping then causes the output to occur as a series of spikes during the current pulse as well as the normal delayed pulse in the afterglow of the gas discharge (Sec. 5.2). We have shown that the diverging lens effect is probably responsible for the minimum pulse delay in this case. If this is so then our use of a more stable resonator for the spiking observations in Ch. 5 is an essential requirement for producing spiking output. [We will see in Ch. 5 that the electron lens does not alter the mode separations of our resonator during the period of laser emission.]

Chapter 5

SPIKING EFFECTS IN THE PULSED HCN LASER

5.1 Introduction

In Chapter 4 we studied plasma sweeping of a single cavity resonance through the 337 μm HCN emission line. We now turn our attention to circumstances where plasma effects sweep several distinct resonances through the emission line in quick succession. This produces "spiking" output. For the resonator and discharge conditions described in Ch. 4 multiple mode sweeping did not occur. We saw that the reason for this was that either the resonator was not sufficiently stable at high electron densities or there was not an inverted population of HCN molecules at earlier times.

By using a low-amplitude, long-duration current pulse it is possible to establish population inversion during excitation, under conditions where the density of electrons at tube centre is quite high. In addition we can employ a more stable resonator configuration to ensure laser action at these higher electron densities. In this situation multiple mode sweeping is observed.

Until now the laser has been exactly as described in Ch. 2. In this chapter we describe discharge and resonator alterations which cause our pulsed laser to produce spiking output. We then present our observations of spiking output under two sets of operating conditions and compare them with the predictions of our cavity mode sweeping theory. As a background to this study we first repeat and extend some of the relevant theory.

5.1.1 Theory

In Chapter 4 we saw that the 337 μm output of the pulsed HCN laser occurs as plasma effects sweep the resonant frequency of its cavity through the "effective gainwidth" of the laser transition. It was stated that the effective gainwidth depends on the width of the 337 μm emission line, the natural width of the laser cavity resonance, and the degree of excitation of the laser. We shall now elaborate on this dependence in some detail.

The effective gainwidth Δf (which is a "full-width") is related to the range Δd of cavity length d for which laser emission (in any particular mode) is observed, by the expression

$$\frac{\Delta f}{f} = \frac{\Delta d}{d} \quad , \qquad 5.1$$

where f is the centre frequency of the laser transition. Equation 5.1 may be taken as a precise definition of the meaning of Δf and we shall call Δd the "gainlength" for laser emission. Now we may say that the 337 μm output of the pulsed HCN laser occurs as the effective length of its resonator is swept through the gainlength of a low-loss cavity mode.

Let us now consider the factors which determine the effective gainwidth in our 337 μm laser. We can make several simplifying assumptions in this case because at the instants of onset and extinction of its 337 μm output pulse the laser is at threshold. Since for our (high pressure) laser the spontaneous emission line is essentially homogeneously broadened (Appendix 2) the *unsaturated* intensity gain per unit length may be written as (Bennett, 1962),

$$g(\omega) = g_o \left[\frac{\Delta\omega^2}{(\omega - \omega_o)^2 + \Delta\omega^2} \right] \qquad 5.2$$

where g_o is determined by the degree of excitation of the laser, ω_o is the angular frequency at line centre and $\Delta\omega$ is the half-width at half power of the spontaneous emission line. Now suppose that the total loss per pass of the

laser cavity (length d) is α. Then if the unsaturated gain per pass at line centre is a constant k times the loss we have,

$$e^{g_o \cdot L} - 1 = k\alpha \qquad 5.3$$

where L is the length of amplifying medium. Thus the gain per unit length may be written as

$$g(\omega) = \frac{\ell n(1 + k\alpha)}{L} \cdot \left[\frac{\Delta\omega^2}{(\omega - \omega_o)^2 + \Delta\omega^2}\right] . \qquad 5.4$$

Now, when the resonant frequency of the laser cavity is being swept (e.g. by plasma effects) through the spontaneous emission line, threshold is reached at a frequency corresponding to the solution of

$$e^{g(\omega)L} - 1 = \alpha \ , \qquad 5.5$$

or

$$g(\omega) = \frac{\ell n(1 + \alpha)}{L} .$$

Equating eqs. 5.4 and 5.5 we find the threshold operating frequency to be given by

$$\omega = \omega_o \pm \sqrt{\frac{\ell n(1 + k\alpha)}{\ell n(1 + \alpha)} - 1} \cdot \Delta\omega . \qquad 5.6$$

Thus the full gainwidth (radians/sec) for laser emission is

$$2\sqrt{\frac{\ell n(1 + k\alpha)}{\ell n(1 + \alpha)} - 1} \cdot \Delta\omega \equiv 2\sqrt{k' - 1} \cdot \Delta\omega \qquad 5.7$$

where k' is defined by eq. 5.7 ($k' \leq k$ for all α and $k' \simeq k$ when $\alpha << 1$). We can see that eq. 5.7 gives exactly the gainwidth which we expect when $\alpha << 1$ (and $g_o L << 1$). For instance, if the unsaturated gain per pass at line-centre is twice the cavity loss ($k = 2$), we would expect threshold to be reached at the half power points on the spontaneous emission profile; when $\alpha << 1$ eq. 5.7 does predict this. At higher gain levels however, there is the normal spectral narrowing of the effective gain profile, as indicated by the fact that $k' \leq k$.

We now calculate the passive cavity resonant frequency corresponding to the threshold operating frequency ω. Because of the "anomalous dispersion" (Sinclair and Bell, 1969) of the amplifying medium the cavity must be tuned off resonance just sufficiently to balance the phaseshift due to the active medium. That is, if $\psi(\omega)$ is the phaseshift per unit length due to anomalous dispersion the (passive) cavity resonant frequency ω_c is determined by

$$\frac{L}{c}(\omega_c - \omega) = -\psi(\omega) \cdot L \quad ,$$

or

$$\omega_c = \omega - \frac{cL}{d} \cdot \psi(\omega) \quad . \qquad 5.8$$

Here ω_c accounts for the effects of the bulk refractive index of the laser medium and the refractive index of the laser plasma electrons and d is the length of the laser resonator. Now $\psi(\omega)$ is given by (Bennett, 1962),

$$\psi(\omega) = -g(\omega) \cdot \frac{(\omega_o - \omega)}{2\Delta\omega} \qquad 5.9$$

so on combining eqs. 5.5 to 5.9 we find that the cavity frequency at threshold is,

$$\omega_c = \omega_o \pm \sqrt{k' - 1} \cdot \Delta\omega \pm \sqrt{k' - 1} \cdot \frac{c\ell n(1+\alpha)}{2d} \quad . \qquad 5.10$$

Now the passive Q of the laser resonator is given by

$$Q = 2\pi \cdot \frac{1}{\alpha} \cdot \frac{d}{\lambda} \qquad 5.11$$

$$\simeq \frac{\omega_o d}{c\alpha} \quad .$$

Thus eq. 5.10 may be written as

$$\omega_c = \omega_o \pm \sqrt{k' - 1} \cdot \Delta\omega \pm \sqrt{k' - 1} \cdot \frac{\ell n(1+\alpha)}{\alpha} \cdot \frac{\omega_o}{2Q} \quad . \qquad 5.12$$

For an axial mode in our laser resonator $\alpha \simeq 0.2$ (Sec. 2.2.3) and we introduce an error of only about 10% by writing $\ell n(1 + \alpha) \doteqdot \alpha$. In this approximation eq. 5.12 becomes

$$\omega_c \simeq \omega_o \pm \sqrt{k' - 1}\ (\Delta\omega + \Delta\omega_c) \quad . \qquad 5.13$$

where $\Delta\omega_c$ is the half-width at half power of the laser (passive) cavity resonance.

Thus there is significant frequency pulling when the laser is swept through its threshold operating frequency. In general this frequency is at the $1/k'$ power point of the spontaneous emission line and eq. 5.13 shows that the cavity resonance must be sufficiently further away from line centre so that the operating frequency is (approximately) at the $1/k'$ power point of the cavity response curve also. In the limit of low loss ($\alpha << 1$; $k' = k$) and low gain ($g_o L << 1$) this statement is exact. It follows that the effective gainwidth Δf (defined by eq. 5.1) is given by

$$\Delta f = 2 \cdot \sqrt{k' - 1} \left(\frac{\Delta\omega + \frac{\ell n(1 + \alpha)}{\alpha} \cdot \Delta\omega_c}{2\pi} \right) \quad , \qquad 5.14$$

or if $\alpha \lesssim 0.2$ Δf is given approximately by

$$\Delta f = 2 \cdot \sqrt{k' - 1} \cdot \left(\frac{\Delta\omega + \Delta\omega_c}{2\pi} \right) . \qquad 5.15$$

This approximation is useful for the TEM_{00} mode of our resonator (22% loss per pass; see Sec. 2.2.3) as it introduces an error of less than 10%. For the TEM_{01} mode (60% loss per pass) the full form eq. 5.14 must be used. Thus in our cavity mode sweeping observations we may regard the cavity resonance as being very sharp (as we have done in Ch. 4) provided we add $\sqrt{\ell n(1 + \alpha)}/\alpha$ times the passive cavity linewidth ($\Delta\omega_c/\pi$) to the spontaneous emission linewidth ($\Delta\omega/\pi$) to obtain an effective linewidth. The effective gainwidth is then $\sqrt{k' - 1}$ times the effective linewidth where $k'(> 1)$ is determined by the degree of excitation of the laser.

Let us now consider the expected value of the effective gainwidth in our laser. It is shown in Appendix 2 that the linewidth (full width at half power) of the 337 μm transition in our pulsed HCN laser is of the order of but probably somewhat less than 10 MHz. For the cavity used so far (Sec. 2.2.3) the Q is 2×10^5 (for the TEM_{00} mode) implying a cavity linewidth of 4.5 MHz. Thus the effective linewidth is of the order of 10 MHz. The largest unsaturated gain which has been reported for a 337 μm laser is 0.7 per metre (Jones et al, 1969) which

corresponds to an unsaturated gain per pass of 1.86 for our laser. In this case k (the ratio of the unsaturated gain per pass to the loss per pass) would be 8.5 and k' (eq. 5.7) would be 5.3. Then using eq. 5.15 (assuming $(\Delta\omega + \Delta\omega_c)/\pi \simeq 10$ MHz) we find the corresponding gainwidth for the TEM_{00} mode is about 21 MHz. This is an estimate of the upper limit for our laser because we do not expect the gain to be as high as 0.7 m^{-1}. In general therefore we expect the gainwidth to lie somewhere between 10 and 20 MHz; we now compare this prediction with our observations in Ch. 4.

The cavity mode sweeping observations presented in Sec. 4.2.1 indicated a gainwidth slightly larger than 10 MHz while under the high gain conditions studied in Sec. 4.3 we observed an apparent gainwidth of 21 MHz. In the latter case we suggested that the gainlengths of the TEM_{00} and TEM_{10} modes, whose resonant lengths differ by only 29 μm (equivalent to about 12 MHz), may have overlapped to give the large apparent gainlength. It may be shown using eq. 5.14 that if the gain of the laser were 0.4 m^{-1} the effective gainwidths of the TEM_{00} and TEM_{01} modes would be about 14 MHz and 8 MHz respectively. Thus the two modes would overlap long before the effective gainwidth of the TEM_{00} mode reached 21 MHz. We conclude that the TEM_{00} and TEM_{01} modes must have overlapped when

we observed an apparent gainwidth of 21 MHz. Thus the results in Chapter 4 indicate that the effective gainwidth for an axial mode in our laser lies between 10 and 20 MHz.

In the following sections of this chapter we describe our observations of plasma tuning of successive cavity resonances through the 337 μm emission line. This causes the laser to produce spiking output pulses. The essential requirement for this to occur is that the gain-lengths of successive (low loss) cavity modes be less than the difference in their resonant lengths. It is well known that this situation generally exists in HCN lasers; it is the basis of laser resonator interferometry (Steffen and Kneubühl, 1968) which has been used extensively with 337 μm lasers (Sec. 5.4.2). Laser resonator interferometry allows the mode structure of a submillimetre resonator to be studied simply by monitoring the laser output power as a function of cavity length. As the cavity length is changed monotonically a series of peaks in output intensity is recorded and the laser generally extinguishes between peaks; each peak corresponds to excitation of a different cavity mode (but see Sec. 5.4.2). That is, the gainlengths of successive low loss cavity modes do not generally overlap. We have seen that in our laser we do not expect the effective gainwidth to exceed about 20 MHz which corres-

ponds to a gainlength of 50 μm. But the resonant lengths of the nearest pairs of low-loss resonator modes for the resonators used in this chapter differ by 47 μm (Sec. 5.2.1). Thus under very high gain conditions our spikes may just overlap.

Table 5.1

Parameter	Optimum Operating Conditions	Spiking Output Conditions	Units
Discharge Capacitor	0.3	0.3	μF
Series Inductance	4 (≃0)	180	μH
Discharge Voltage	6.5	7.5	kV
Peak Discharge Current	800	120	A
Current Pulse Duration	∿ 4	∿ 22	μsec
Pulse Repetition Frequency	10	10	p.p.s
Electrode Separation	1.5	1.8	m
Mirror Radii	Plane/8	Plane/3.7	m
Mirror Apertures	3.8/5.1	5.1/7.6	cm
Output Coupling	Annular	13 mm dia. central hole in plane mirror	-
Mirror Separation	2.2	2.2	m
Gas : Pressure	0.7	0.7	torr
Flowrate	0.5	0.4	ℓ/s
Nitrogen/Methane ratio	1:2	1:2	-

ponds to a gainlength of 50 μm. But the resonant lengths of the nearest pairs of low-loss resonator modes for the resonators used in this chapter differ by 47 μm (Sec. 5.2.1). Thus under very high gain conditions our spikes may just overlap.

Table 5.1

Parameter	Optimum Operating Conditions	Spiking Output Conditions	Units
Discharge Capacitor	0.3	0.3	μF
Series Inductance	4 (≃0)	180	μH
Discharge Voltage	6.5	7.5	kV
Peak Discharge Current	800	120	A
Current Pulse Duration	∿ 4	∿ 22	μsec
Pulse Repetition Frequency	10	10	p.p.s
Electrode Separation	1.5	1.8	m
Mirror Radii	Plane/8	Plane/3.7	m
Mirror Apertures	3.8/5.1	5.1/7.6	cm
Output Coupling	Annular	13 mm dia. central hole in plane mirror	-
Mirror Separation	2.2	2.2	m
Gas : Pressure	0.7	0.7	torr
Flowrate	0.5	0.4	ℓ/s
Nitrogen/Methane ratio	1:2	1:2	-

5.2 Observations of Spiking Pulses

The pulsed laser, as described in Ch. 2 does not produce spiking output. However a few alterations in resonator and discharge conditions cause it to produce the spiking output shown in Fig. 5.1. These operating conditions are summarized in Table 5.1. For comparison, we have included the set of optimum operating conditions evolved in Ch. 2. The latter conditions are quite similar to those which were used for the observations of plasma effects which were described in Ch. 4.

There are two essential changes which cause our laser to produce spiking output. Firstly, the use of a low-amplitude long-duration (see Table 5.1 for comparison with previous conditions) current pulse (Fig. 5.1(a)) ensures that a state of population inversion exists during the period of excitation. At these times the electron density in the laser resonator is high enough to cause multiple mode sweeping. Secondly, we have used a more stable resonator configuration which allows stable resonator modes at higher electron densities. Under these circumstances laser action occurs during the period of excitation. We observe two spikes during the discharge current pulse as well as the normal delayed pulse in the

afterglow.

Figures 5.1(b), (c) and (d) show the laser output for successive reductions of 0, 13 and 25 μm in laser cavity length. It is clear that the delay of each pulse increases as the cavity length decreases. The duration of the last pulse is greater than that of the spikes, and increases as its delay is increased, simply because the rate of plasma tuning is slower later in its decay. The appearance of the pulse pattern shown in Fig. 5.1 varies quite markedly as the length of the resonator is further decreased (Fig. 5.2) but a half-wavelength (168 μm) decrease in cavity length always causes the pulse pattern to reproduce itself. At the same time the delay and duration of pulse 1 increase continuously to the values originally corresponding to pulse 3. Similarly, a decrease of about 50 μm in cavity length causes the delay of pulse 1 to increase to the value initially measured for pulse 2. These trends, which continue for many wavelengths of mirror displacement, clearly suggest that pulses are observed when different modes of the laser resonator are excited.

We now compare these observations with the predictions of our cavity mode sweeping theory. Details of the electron density measurement for the discharge conditions corresponding to Fig. 5.1 were presented in

Sec. 3.3.3. The time-varying electron density along the axis of the laser resonator under these conditions is shown in Fig. 3.11. Referring to Fig. 5.1 (d) we see that the peaks of pulses 1, 2 and 3 occur at about 18 μsec, 20 μsec and 30 μsec respectively. Figure 3.11 (p. 3.29) shows that the time intervals between pulse 1 and pulses 2 and 3 respectively, correspond to electron density changes of about 4×10^{11} cm^{-3} and 2×10^{12} cm^{-3}. These densities imply changes in the effective length of the laser resonator (eq. 4.2) of 40 μm between pulses 1 and 2 and 180 μm between pulses 1 and 3. The transverse modes of the laser resonator (details in Table 5.1) are separated by multiples of about 44 μm (Appendix 3; Table A3.1) and every mode is repeated after 168 μm ($\lambda/2$). Thus the effective length changes above are in satisfactory agreement with the mode separations of the laser.

In the next section we present a detailed comparison of theory and experiment. This is based on careful observations of the spiking output shown in Fig. 5.1 for a total reduction of six wavelengths (2000 μm) of cavity length in 13 μm steps. The operating conditions were identical to those described in the second column of Table 5.1

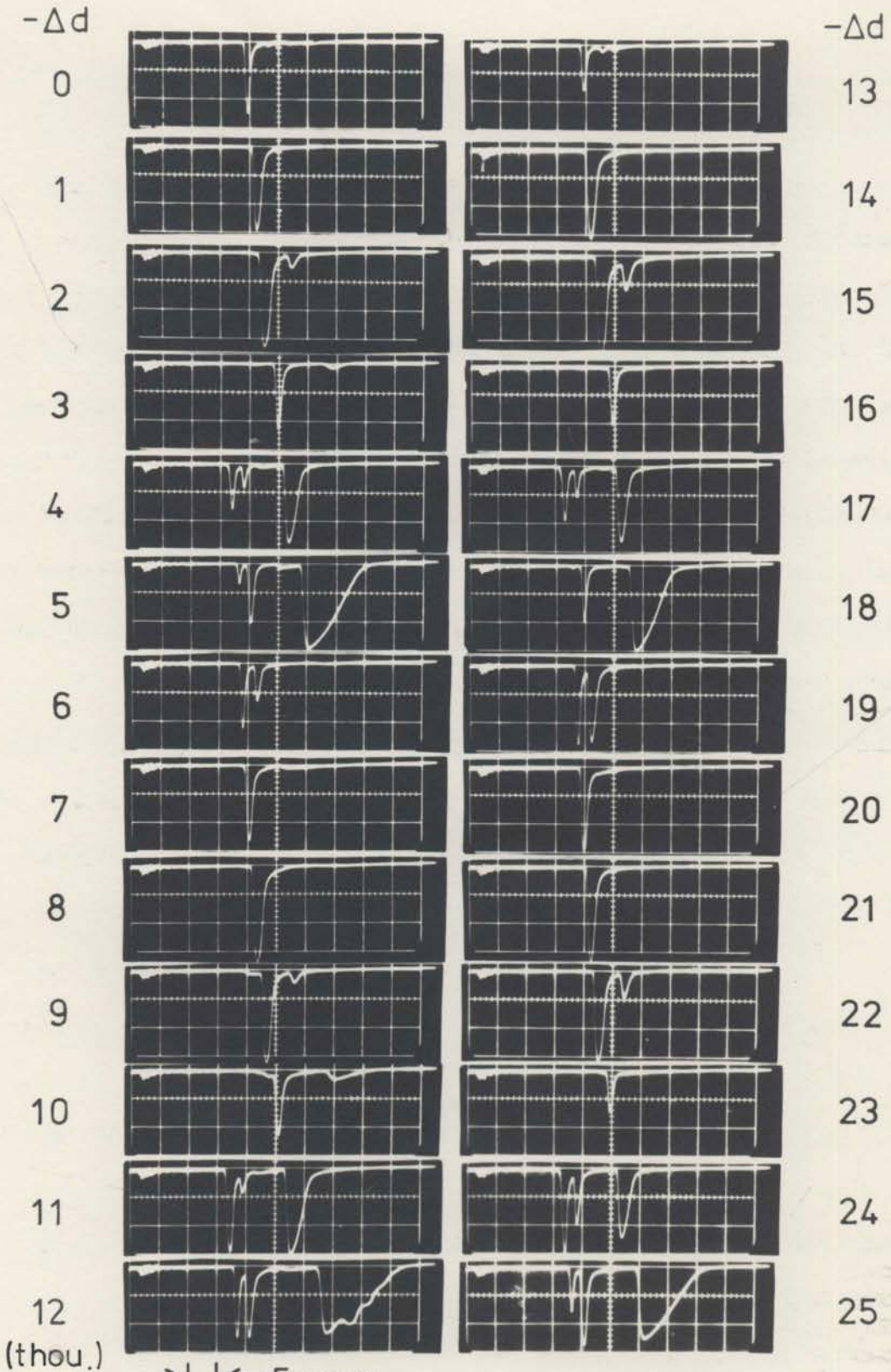
-Δd
0
1
2
3
4
5
6
7
8
9
10
11
12
(thou.)
-Δd
13
14
15
16
17
18
19
20
21
22
23
24
25
→| |← 5 μsec

5.2.1 Comparison of Theory and Experiment

Figure 5.2 shows a sequence of pictures of the laser output corresponding to two wavelengths of plane mirror displacement. As mentioned earlier, the appearance of the laser output varies considerably with cavity length but the pulse pattern reproduces itself after each half-wavelength of length change. The former point will be discussed later; the latter guarantees that all three pulses are of the same wavelength. Independent measurement with a Fabry-Perot interferometer verified that the wavelength of each pulse was 337 μm.

Experimental records which include those shown in Fig. 5.2 allow us to plot delay time as a function of laser cavity length for each of the three laser output pulses. This is shown in Fig. 5.3, which is based on the results of twelve half-wavelengths of plane mirror displacement. The error bars represent the spread of times at which each pulse was observed for a particular cavity length. Suitable multiples of $\lambda/2$ have been subtracted

---

Fig. 5.2 (opposite). Variation of laser output pulse pattern with the length of its resonator for the operating conditions described in Table 5.1. The photos of laser output correspond to successive reductions of 10^{-3} inch (25.4 μm) in cavity length. Adjacent pairs of photos correspond to a difference of 13 thou. (330 μm) in cavity length which is close to one wavelength (337 μm). [All photos show 10 mV per large scale division, vertically.]

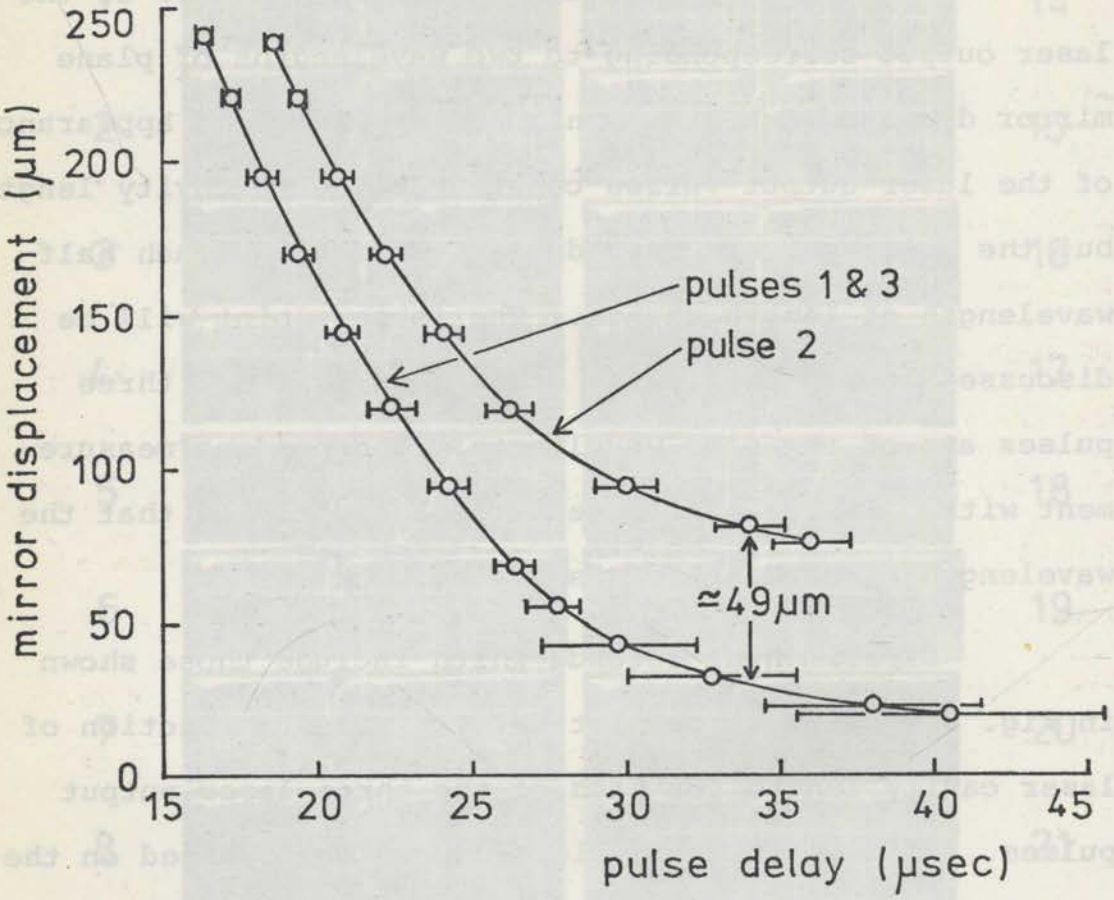

Fig. 5.3. Variation of pulse delay with laser mirror displacement (+ve in direction of increasing cavity length) for each of pulses 1, 2 and 3 (Fig. 5.1). The horizontal error bars represent the spread in times at which a pulse was observed for a given cavity length. The data was obtained from twelve successive halfwavelengths of mirror displacement.

where necessary, and hence the curves for the first and third pulses (pulses 1 and 3 in Fig. 5.1) coincide.

At this point it is appropriate to explain our definition of "pulse delay" used in Fig. 5.3. First of all, we are interested in comparing the observed cavity mode sweeping with the prediction of our measured electron density decay. Thus we should try to identify a feature of each pulse which corresponds to a fixed frequency on the spontaneous emission profile. The time of occurrence of this feature should then be defined as the pulse delay. Let us consider some possible definitions. The time of onset of laser action is unsuitable because the corresponding position on the 337 μm emission profile changes with the gain of the laser and the losses of different modes. The time of extinction of the laser pulses is unsuitable for the same reason. Another possible definition is the time of peak laser output for each pulse. However reference to Fig. 5.2 shows that the risetime of laser pulses is, to a large extent, independent of the length of the pulse. For the long delayed pulses peak laser output follows relatively soon after the onset of laser action, but for the "spikes" the peak lies near the centre of the pulse.

The definition of pulse delay which we have chosen is the mean of the switch-on and switch-off times of the laser pulses. The meaning of the switch-on time is obvious but Fig. 5.2 shows that many of the laser pulses have a small amplitude slowly decaying "tail" which complicates the measurement of switch-off time. The beginning of this slow decay (or tail) has been taken as the switch-off time. This definition of pulse delay is an estimate of when the laser cavity resonance is swept through line centre. Depletion of the population inversion during laser action (by stimulated and/or spontaneous emission) would be expected to cause laser emission to cease slightly higher on the 337 μm emission profile than where it starts. Thus our definition of pulse delay is weighted towards a time which is earlier than the arrival of the cavity resonance at line centre. However this is partly compensated by the faster rate of plasma tuning at earlier times (Fig. 3.11, p.3.29). In view of the foregoing considerations we believe that our definition of pulse delay is the most appropriate choice.

Figure 5.3 allows two important comparisons. Firstly, the curves for the first and second of the three output pulses are separated by a constant distance of 48.5 ± 2 μm. The expected separation of the resonant

lengths of the TEM_{00q} and $TEM_{p\ell q}$ modes for the resonator used in this experiment (eqs. A3.2 and A3.3; d = 2.19 ± 0.02 m), R_1 = 3.68 ± 0.05 m) is $(2p+\ell).(47.4 \pm 0.6)$ μm. Thus we conclude that if pulse 1 (Fig. 5.1) is due to oscillation of the $TEM_{p\ell q}$ mode of the laser resonator then pulses 2 and 3 are oscillations of the $TEM_{p(\ell+1)q}$ and $TEM_{p\ell(q+1)}$ modes respectively. We expect these to be the two lowest loss modes of the resonator. Although the Fresnel number N_o (Appendix 2) of our output coupling hole is only 0.9×10^{-3}, McCumber (1969) has shown that a confocal resonator with the same Fresnel number N as ours (n = 1.3, see Table A3.1) has the order of losses of its $TEM_{p\ell q}$ modes significantly altered by a single hole with Fresnel number of 10^{-3}. Thus we are unable to determine the values of p, ℓ and q for the two lowest loss modes of our resonator.

Let us now make the second comparison allowed by Fig. 5.3, that is; does the observed dependence of laser pulse delay on cavity length agree with that predicted by the electron density decay shown in Fig. 3.11? Since the plasma electron density, n, is always much less than the 337 μm cutoff density ($n_c = 9.8 \times 10^{15}$ cm^{-3}) the resulting change in effective cavity length is given by eq. 4.2,

$$\Delta L_{plasma} = - \frac{Ln}{2n_c}$$

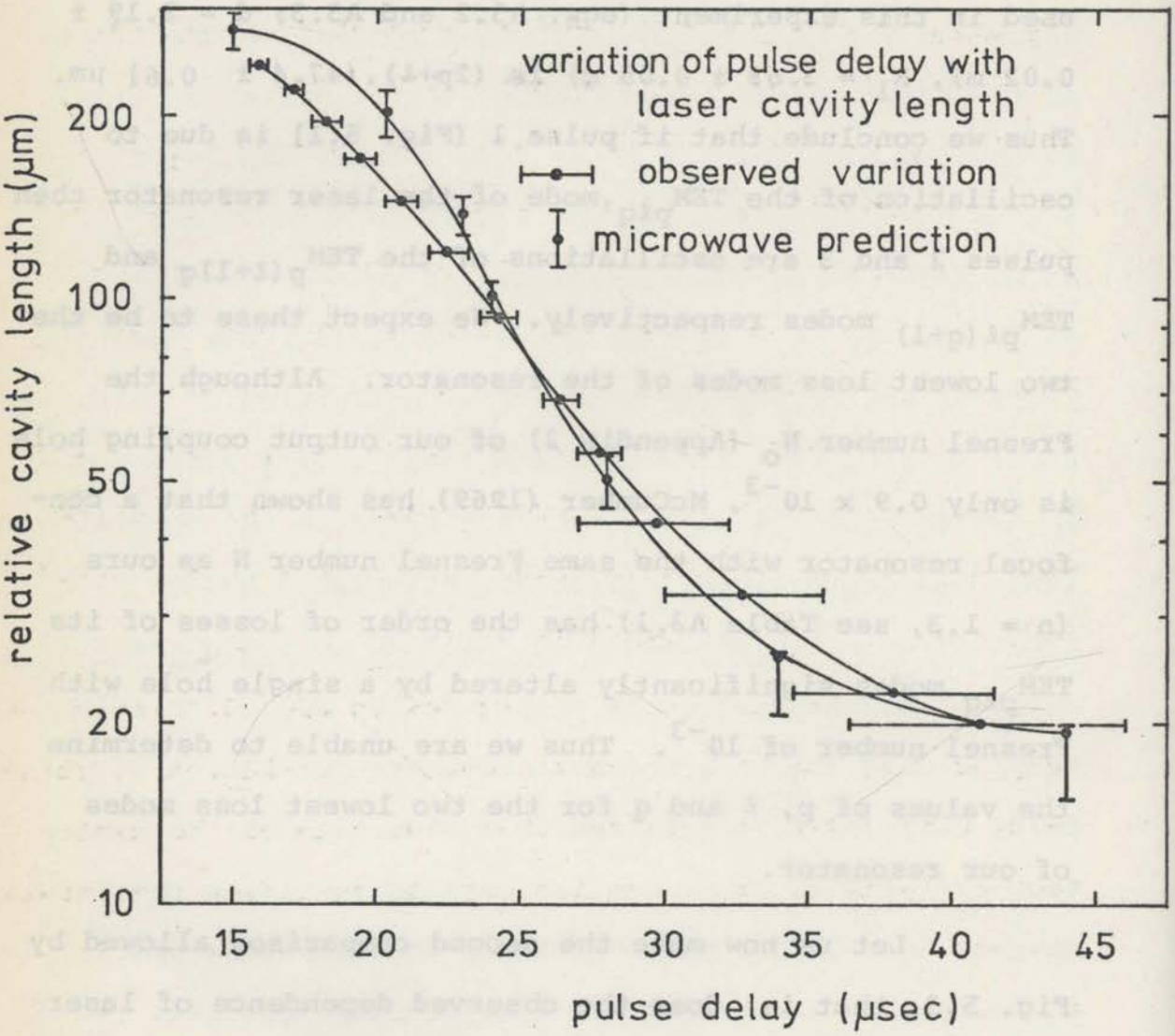

Fig. 5.4. Comparison of the observed variation of laser pulse delay with plane mirror displacement (horizontal error bars) with the prediction of the cavity mode sweeping theory, based on the electron density decay shown in Fig. 3.11 (vertical error bars). A constant has been added to the ordinate of the former curve to match the two curves at 41 μsec.

where L is the length of the plasma column (1.8 m). ΔL_{plasma} is plotted as a function of time in Fig. 5.4. To compare this with the observed dependence of pulse delay on cavity length (Fig. 5.3), we necessarily have to add an arbitrary constant, because we do not know the free-space length of the laser resonator to a fraction of a wavelength. Figure 5.3 already includes this constant which was chosen to match the two curves at a time of 41 μsec. However, for the present comparison (Fig. 5.4) a logarithmic scale is more appropriate. Thus the curve with horizontal error bars (Fig. 5.4) is merely replotted from Fig. 5.3 on a logarithmic scale.

Comparison of the two curves in Fig. 5.4 indicates very good agreement between the observed variation of pulse delay with cavity length and the prediction of the cavity mode sweeping theory. The two sets of results agree within the experimental errors at late times, while the small difference at early times could be easily accounted for by a small amount of axial non-uniformity of the laser discharge. It was suggested in Sec. 3.3.1.2 that the assumption of a uniform axial distribution of electron density might lead to an overestimate of plasma effects. The small difference at early times is indeed in the direction of such an overestimate. Nevertheless, these

results leave no doubt about the validity of the cavity mode sweeping theory.

Finally, we return to a point which was raised earlier. Figure 5.2 shows that although for some cavity lengths the laser output consists of two spikes during excitation and a delayed pulse in the afterglow of the discharge, for other cavity lengths there is only one output pulse, sometimes two. The variations in form of the laser output are of two kinds. Firstly, there appears to be a definite pattern of behaviour shown by our observations of the output for four halfwavelengths of mirror displacement (Fig. 5.2). Secondly, there are minor variations in the appearance of the pulse pattern observed from one halfwavelength of mirror translation to the next. We deal with these variations in order.

Whenever three pulses appear we know from our observations over six wavelengths of mirror displacement (Fig. 5.3) that the first and third are due to excitation of modes with the same transverse quantum numbers; $TEM_{p\ell}$ say. Then the second pulse is due to excitation of the $TEM_{p(\ell+1)}$ mode. We infer that the losses of the $TEM_{p(\ell+1)}$ mode are higher than those of the $TEM_{p\ell}$ mode because the former is excited for a smaller range of times in the lifetime of the laser plasma than the latter. Thus, all

other factors being equal, excitation of the $TEM_{p(\ell+1)}$ mode is less likely than excitation of the $TEM_{p\ell}$ mode. Now we must consider the gain of the discharge. The population inversion at any instant depends on the pumping rate history of the upper level, the rate of spontaneous emission from that level, and the number of molecules which have been de-excited by stimulated emission in the production of earlier laser pulses. [For simplicity, we are assuming that the lower laser level empties very quickly.] Thus the gain of our laser discharge varies with time, in a manner depending on the laser cavity length. It is probably true to say that the gain is high during the discharge current pulse and falls later on (laser action is never observed after $\simeq$ 45 μsec). We have no guarantee that the gain falls monotonically. Thus there will be times when the $TEM_{p\ell}$ mode may be excited but the higher loss $TEM_{p(\ell+1)}$ mode may not. This could explain the disappearance of the second spike for some cavity lengths. The disappearance of the third pulse is easy to understand. If the cavity length is adjusted so that the $TEM_{p\ell}$ mode is not swept for the first time until quite late, it will not be swept again until after 45 μsec. In fact the electron density in the laser is so low at 45 μsec that very little mode sweeping will occur after that time

(Fig. 3.11, p. 3.29). But after 45 μsec we never see laser emission, presumably because there is no population inversion; thus the $TEM_{p\ell}$ mode is not excited for a second time. This argument seems to explain how the systematic variation in the form of the pulse pattern with mirror displacement could come about. It is implicit that the population inversion in the HCN laser is not long lived but this is quite a reasonable assumption (Sec. 5.4.3).

We now return to the mirror variations in the appearance of the output pulse pattern mentioned above. Undoubtedly, the relative losses of different modes of the laser resonator are affected by mirror tilt. Since the axial displacement of the laser mirror was produced by adjusting its three tilt adjustments simultaneously, second order variations in mirror tilt must have occurred. This could readily cause the appearance or disappearance of marginal modes. In addition, small shot-to-shot variations in the laser discharge could have the same effect.

It should be remembered however that the detailed explanation of the experimental records shown in Fig. 5.2 is of secondary importance in the present study. We have shown in this section that the spiking output observed from our laser is of a form which can be explained by

cavity mode sweeping. We have made a careful comparison of the observed dependence of laser pulse delay on cavity length with the prediction of our plasma electron density measurements. Very good agreement was obtained. We now proceed to describe observations of multiple mode sweeping which further support the cavity mode sweeping theory.

Table 5.2

Parameter	Value	Units
Discharge Capacitor	0.3	μF
Series Inductance	180	μH
Discharge Voltage	7.3	kV
Pulse Repetition Frequency	10	p.p.s.
Electrode Separation	1.5	m
Mirror Radii	Plane/3.7	m
Mirror Apertures	3.8/7.6	cm
Output Coupling	Annular	-
Mirror Separation	2.2	m
Gas : Pressure	0.7	torr
Flowrate	0.4	ℓ/s
Nitrogen/Methane Ratio	1:2	-

5.3 Observations of Multiple Spiking

Under only slightly different conditions from those described in the previous section our pulsed HCN laser produces up to four spikes as well as a delayed pulse in the afterglow of the discharge. The operating conditions are set out in Table 5.2 (opposite). The discharge voltage and electrode separation are both less than for the observations presented in Sec. 5.2 (Table 5.1) but the peak current is approximately the same. The 8.8 mm microwave interferogram obtained under these conditions is similar to that shown in Fig. 3.9 for the previous set of spiking conditions so it is reasonable to assume that the time-varying electron density for the previous discharge conditions (Fig. 3.11, p. 3.29) is roughly applicable here too.

The essential change which causes the appearance of more spikes is the replacement of the output mirror with the large 13 mm diameter hole by the annular-output mirror described in Sec. 2.2.3. Apparently this resonator system has more low-loss modes than the one with hole-output. We will see later, that the two lowest loss modes of the new resonator do have lower losses than the corresponding modes of the resonator with hole-output.

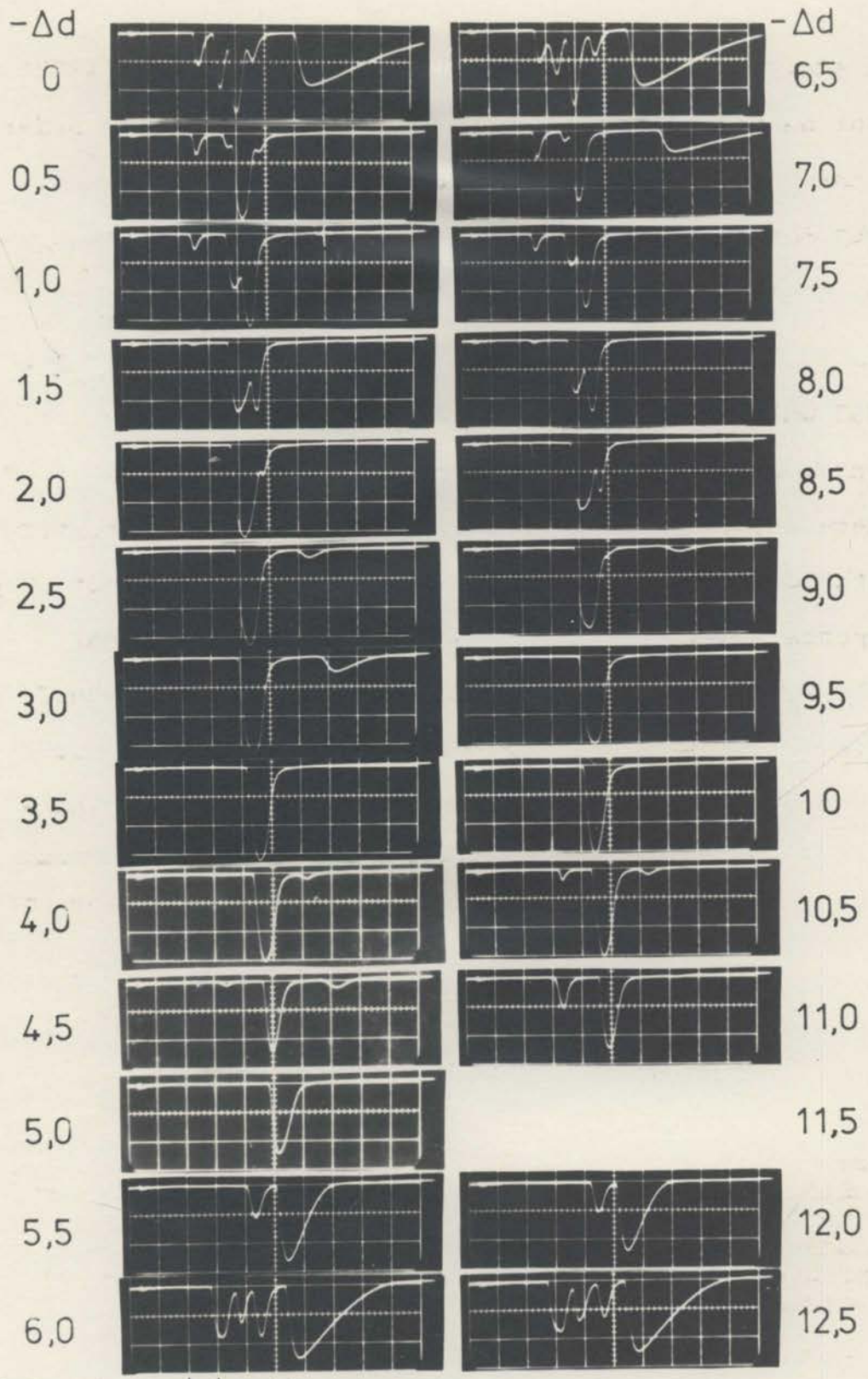
-Δd
0
0,5
1,0
1,5
2,0
2,5
3,0
3,5
4,0
4,5
5,0
5,5
6,0
-Δd
6,5
7,0
7,5
8,0
8,5
9,0
9,5
10
10,5
11,0
11,5
12,0
12,5
(thou.)
5 µsec

In addition, it is known (Steffen and Kneubühl, 1968) that annular-output *couples* output from the high order transverse modes more effectively than a central hole. Thus the resonator with annular-output is also expected to couple out more low-loss modes.

Figure 5.5 shows a sequence of pictures of the (337 μm) laser output corresponding to 10^{-3} inch (25.4 μm) decreases in laser cavity length. As before (Fig. 5.2) there are very large variations in the pulse structure with cavity length but again the form of the laser output repeats itself after each halfwavelength of mirror displacement. This suggests that the appearance and disappearance of some spikes (modes) at various cavity lengths depends on a systematic change in the balance

---

Fig. 5.5 (opposite). Multiple Spiking Output from the Pulsed HCN Laser

The series of oscilloscope records shows the variation of the laser output pulse pattern with the length of its resonator for the operating conditions of Table 5.2. It will be seen that there are up to four spikes during the discharge current pulse instead of the two shown in Figs. 5.1 and 5.2 (operating conditions in Table 5.1). The essential change causing this is the replacement of hole-output coupling with annular output coupling. Each photo corresponds to a successive reduction of 10^{-3} inch (25.4 μm) in cavity length. The adjacent pairs of photos correspond to a difference of approximately 1 wavelength (13×10^{-3} inch ≈ 330 μm) of cavity length.

between the time-varying gain of the laser and the relative losses of different modes. It does not appear to be due to variations of mirror tilt with axial displacement.

A striking feature of the laser output when four spikes appear is their strong tendency towards overlapping. Even when only two spikes appear (these will later be identified with excitation of the two lowest loss modes of the resonator) they overlap strongly. This indicates that the effective gainwidth is larger when the resonator incorporates annular output than with hole-output (Sec. 5.2). In view of the fact that the active medium was only 1.5 m long when annular output was used and 1.8 m long when hole-output was used, this can only be the result of the latter resonator having higher losses for its two lowest loss modes than the former.

Study of Fig. 5.5 reveals an effect which has not been reported in the literature. When the first spike occurs at early times its delay *decreases* with decreasing cavity length. This is clearly visible for the first pulse in the photos corresponding to total mirror displacements of 0, 0.5, 1 and 6.5, 7, 7.5, 8 thousandths of an inch (thou.). In both of these

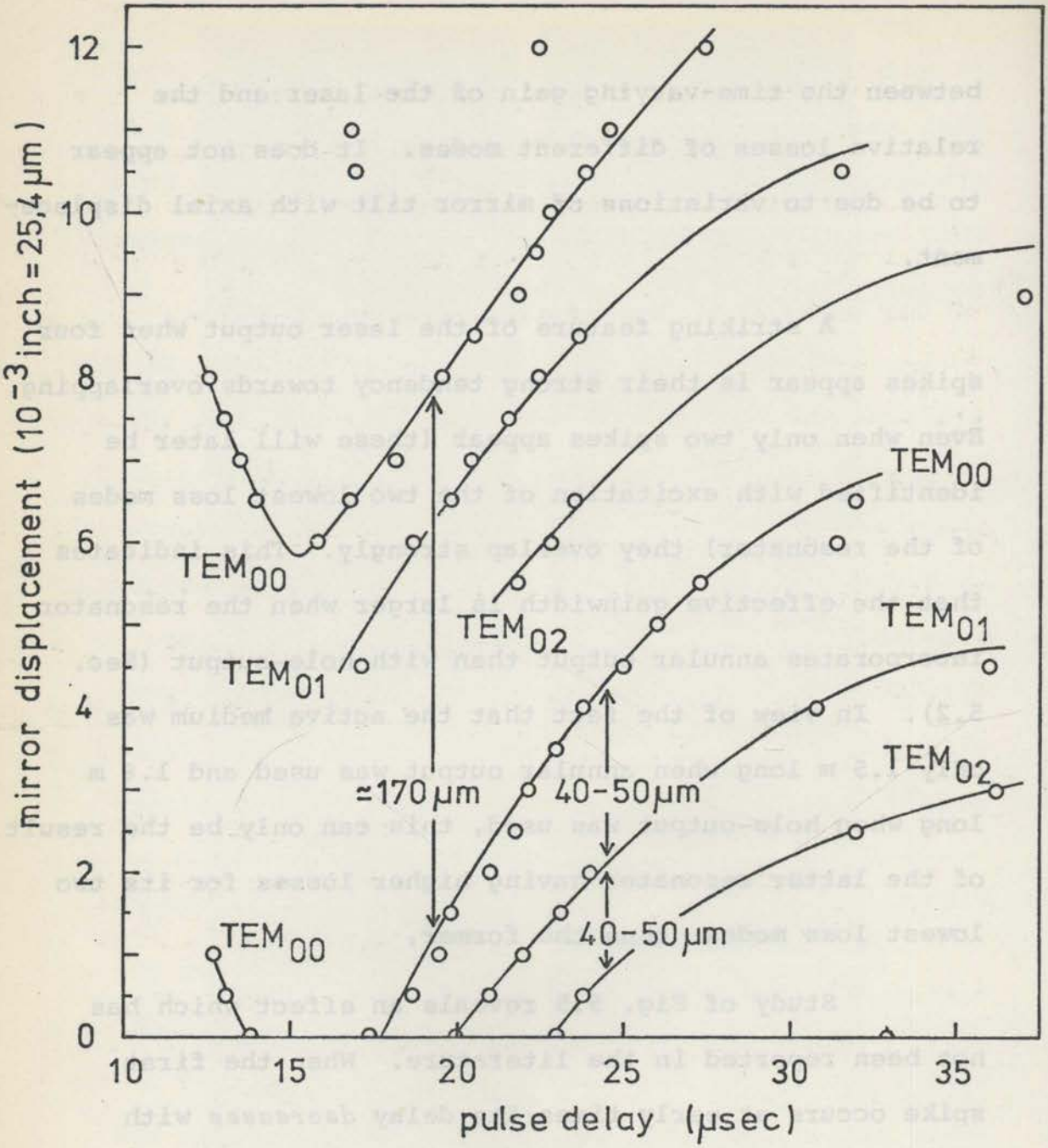

Fig. 5.6. Time of occurrence of laser output pulses as a function of cavity length for the experimental records shown in Fig. 5.5. The dominant pulse has been identified with excitation of the TEM_{00} mode which has the lowest losses when annular output coupling is used. The separations of the next two modes indicate that they are the next two lowest loss modes for the resonator used; TEM_{01} and TEM_{02}.

sequences the rising edge of the first pulse moves to the left as the cavity length decreases. This can only be consistent with the cavity mode sweeping theory if these pulses occur while the electron density along the axis of the laser discharge is still rising. Reference to the 8.8 mm microwave interferogram in Fig. 3.9 shows that the electron density reaches its maximum at approximately 15 μsec. The peaks of all the pulses mentioned above occur no later than 14 μsec. These pulses do indeed occur while the electron density is still rising and it follows that the same mode should oscillate again as the electron density decays away. It will be shown shortly, that this does happen.

The pattern of behaviour evident in Fig. 5.5 can be better studied by plotting the time of occurrence of the peak of each spike (or pulse) against laser cavity length as shown in Fig. 5.6. This graph shows very clearly that the varying number of pulses observed is a systematic (and periodic) function of cavity length. We observe the familiar increase in pulse delay with decreasing cavity length for pulses occurring during the electron density decay. It should be noted that although identification of the delay time of each pulse with that of its peak is undesirable for reasons discussed in

Sec. 5.2, the overlapping of spikes gives us little choice. For this reason the information in Fig. 5.6 is not compared with the prediction of an electron density measurement. It should be noted however, that Fig. 5.6 gives exactly the information required for the purpose of estimating changes in effective cavity length between the peaks of successive laser output pulses.

We suggested earlier that under some circumstances the same mode should oscillate twice (giving rise to two spikes); once when its resonant frequency is swept through the HCN emission line during the rise in electron density and again in the subsequent decay. Figure 5.6 shows very clearly how a spike which occurs when the electron density is near its maximum, divides into two as the laser resonator is further shortened. In Fig. 5.5 the first pulse in the photo corresponding to 6 thou. of mirror displacement divides into two in the photo for 6.5 thou. These two pulses spread further apart when the mirror displacement goes to 7 thou. and 7.5 thou. They occur as the effective length of the laser resonator is swept through the resonant length of the same mode twice, first from above and then from below. It follows that the first of these pulses is chirped (i.e. swept in frequency) from low frequency to high and the second from high

frequency to low. From Fig. 5.6 it is evident that the second of these pulses becomes the delayed pulse in the afterglow of the discharge after half a wavelength (≃ 6.5 thou.) of mirror displacement. Because this pulse is the dominant one, we identify it as an excitation of the TEM_{00} mode of the laser resonator, which has the lowest losses when annular output coupling is used. Inspection of Fig. 5.6 shows that when five pulses are observed (four spikes, one delayed) three of them (the first two, and the last) are due to excitation of an axial mode. The remaining two are spaced at successive intervals of 40-50 μm (1½-2 thou.) greater than the resonant length of an axial mode. This is consistent with the 47 μm mode spacing (Sec. 5.2.1) of the resonator. Accordingly we identify the third spike as the TEM_{01} mode. Reference to Table A3.1 (Appendix 3) shows that this is the next (after TEM_{00}) lowest loss mode of our resonator. Thus our identification of the TEM_{01} mode is consistent with the observation (Fig. 5.6) that it is second in order of dominance. The separation of the third spike is consistent with either the TEM_{02} mode or the TEM_{10} mode. However the former has lower losses (Table A3.1) so we identify the third spike with the TEM_{02} mode of our resonator.

Let us summarize the results of this section briefly. Under conditions when the pulsed HCN laser produces multiple spiking output we have shown that :

1. The variation of pulse delay with laser cavity length of all the pulses is qualitatively consistent with the cavity mode sweeping theory. As usual the delay of pulses which occur in the electron density decay of the plasma increases with decreasing cavity length.

2. In addition we have observed the phenomenon of *decreasing* pulse delay with decreasing cavity length for pulses which occur while the electron density in the laser resonator is still rising. This observation has not been reported anywhere in the literature.

3. The observed mode separations are consistent with the calculated separations for our resonator. We can readily identify the various laser output pulses with modes of the laser resonator in a manner which is simultaneously consistent with the calculated mode separations and the relative losses of the modes.

5.4 Conclusions

In this chapter we have described observations of spiking output from our pulsed 337 μm HCN gas laser. Two sets of experimental conditions were studied. In the first instance (Sec. 5.2) our resonator and discharge conditions were adjusted to give two essentially non-overlapping spikes during active excitation followed by the normal pulse in the afterglow of the laser discharge. This situation was ideal for comparing the observed dependence of pulse delay on laser cavity length with the prediction of our cavity mode sweeping theory; the latter was based on our measurements of the time varying electron density in the laser discharge. Very good agreement was obtained. In the second instance (Sec. 5.3) our resonator and discharge conditions were changed to allow multiple spiking during the laser current pulse. The normal delayed pulse was still observed in the afterglow. In this case we were able to make a detailed comparison of the qualitative features of the spiking output with the behaviour which the cavity mode sweeping theory leads us to expect. In every aspect of its behaviour the multiple spiking agrees with our theory.

These results leave no doubt that under circumstances when our pulsed HCN laser produces spiking output their origin is due to plasma effects. The spikes arise as the time-varying plasma refractive index of the laser discharge sweeps the effective length of the laser resonator through the resonant lengths of successive low-loss modes.

5.4.1 Comments on Other Spiking Observations

On the basis of experience with our pulsed HCN laser we believe the spiking output observed by other groups also has its origin in plasma effects. With longer lasers than ours, the increased gain makes oscillation of more transverse modes possible but the axial mode separation is still the same. Thus the density of available modes is higher. In addition the effect of a given electron density and the gainlength for laser emission are both proportional to the length of the laser resonator. Thus longer lasers should produce many more spikes with a greater tendency towards overlapping of adjacent spikes. They should also show a stronger tendency towards multiple mode sweeping when output occurs in the afterglow of the discharge. We discuss these two predictions in turn.

Firstly, Kon et al (1967) have observed many overlapping spikes produced by their 3.9 metre long laser when excited by a 140 A current pulse 8 μsec long (fig. 13 of their paper). This may be compared with the excitation used for our spiking observations where our 120 A current pulse lasted about 22 μsec. Thus the rate of plasma sweeping in the laser of Kon et al should be about three times the rate in our laser. Since our spikes have durations of the order of 3 μsec (Fig. 5.1) we would expect the spikes observed by Kon et al to have durations of the order of 1 μsec. The spiking pulses recorded by the Japanese do in fact have durations very close to 1 μsec.

We now return to our second prediction, that long lasers should show a tendency towards multiple mode sweeping in the afterglow of the discharge current pulse. Using a 6.47 metre laser resonator Steffen and Kneubühl (1968) have observed long (up to 200 μsec) 337 μm output pulses which clearly show the effects of overlapping of two adjacent cavity modes. These pulses were observed in the afterglow of a 2 μsec discharge current pulse. By observing the time resolved output of their laser while simultaneously producing a laser resonator interferogram (see Sec. 5.4.2) they were able to identify various peaks

in the laser output pulses as being due to excitation of different resonator modes. Examination of their records (fig. 11 of their paper) indicates that they are in accordance with our predictions for long lasers. In fact Steffen and Kneubühl did observe the increasing pulse delay with decreasing cavity length discussed in Sec. 4.2 and they proposed a time-varying plasma refractive index to explain it. However they did not seem to be aware of the possibility of plasma sweeping of successive, overlapping cavity modes as the cause of the peaks in their laser output.

We have shown that the form of the spiking output and the delayed pulse in the afterglow of the current pulse in HCN lasers is dictated by plasma effects. These are the most common forms in which 337 μm pulses are observed but there is one other form which we have not discussed. Under some circumstances multiple pulse emission in the afterglow of a short discharge current pulse is observed (Turner et al, 1968; Jones et al, 1969; Turner and Poehler, 1971). These pulses do not seem to have their origin in multiple mode sweeping but it is possible that more complicated plasma effects play a role in their production (Turner and Poehler, 1971).

5.4.2 Comments on Laser Resonator Interferometry

We have made several references to laser resonator interferometry which is the process of measuring the output power of a submillimetre laser as a function of cavity length. Because the net mode spacing of submillimetre resonators is generally greater than the gainlength for laser emission this procedure yields a series of peaks - each due to oscillation of a distinct mode of the laser resonator. If only one wavelength of laser emission is observed the pattern repeats after each half wavelength of axial displacement of one of the laser mirrors. In the case of a CW laser, this procedure yields very valuable information about the mode structure of its resonator and has been used successfully by several groups (Muller and Flesher, 1966; Kon et al, 1967; Staffsud et al, 1967; Frayne, 1969).

However, laser resonator interferometry has been used even more extensively with pulsed submillimetre lasers, where the integrated laser output pulses are plotted as a function of laser cavity length (Steffen et al, 1966; Kon et al, 1967 ; Schwaller et al, 1967; Steffen et al, 1967a, 1967b; Kneubühl and Steffen, 1967; Steffen

and Kneubühl, 1968). In view of the plasma effects observed in Chapters 4 and 5 the interpretation of these interferograms is quite complicated. We have seen that it is possible for several modes to lase in quick succession as a result of each discharge current pulse and so the interpretation of each peak in the laser resonator interferogram as being due to the excitation of a single mode of the laser resonator is a gross over-simplification. Even if a submillimetre laser excites only one resonator mode per discharge current pulse, the self tuning which results from the time-varying effective length of the decaying laser plasma will cause complications. It will "smear out" the range of cavity length over which each mode is observed and increase the tendency towards overlapping of the peaks representing adjacent cavity modes. Comparison of the laser resonator interferograms presented by Kon et al (1967) for pulsed (fig. 7) and CW (fig. 17) operation with only slightly different resonator configurations illustrates these points very clearly. [The difference between the two resonators is not significant in the context of this discussion (Schwaller et al, 1967).] The interferogram for CW operation (fig. 7) shows four transverse modes between successive axial modes and the laser output

falling almost to zero between adjacent pairs of modes. In sharp contrast, the interferogram obtained under pulsed operation shows only two transverse modes between successive axial modes and very strong overlapping. In fact more modes should oscillate in pulsed than in CW operation because of the higher gain of a pulsed discharge.

Despite these difficulties the groups using laser resonator interferometry of pulsed submillimetre lasers have been able to assign modes to the peaks in their interferograms; presumably in agreement with the predictions of resonator theory (Schwaller et al, 1967; Kneubühl and Steffen, 1967). Steffen et al (1967a) suspected plasma effects in HCN lasers as early as 1967. As mentioned in Section 5.4.1 their published laser output pulse shapes (Steffen and Kneubühl, 1968; fig. 11) show the effects of cavity mode sweeping quite clearly. By studying their laser resonator interferogram in conjunction with the time resolved pulse shapes corresponding to different cavity lengths they were able to identify various peaks in their laser output as being due to excitation of different modes of their resonator. They concluded correctly that laser resonator interferograms for pulsed lasers must be studied in conjunction with the time resolved laser output pulses. However none of the

other groups which have used laser resonator interferometry with pulsed HCN lasers appear to be aware of this, or any of the complications arising from plasma effects. Even Steffen and Kneubühl (1968) seem unaware of the full implications of their results (Sec. V, p.1002 of their paper).

5.4.3 Comments on Plasma-Q-Switching in the Pulsed HCN Laser

In view of the foregoing it appears that most pulsed HCN lasers are self Q-switched by plasma tuning effects in the laser resonator. This was proposed by McCaul (1970), in the form of a diverging lens of plasma electrons which prevents stable resonator modes until some time in the decay of the laser plasma. McCaul's results do not seem to confirm this theory (Sec. 4.4.2) for his laser but it could well apply to other pulsed lasers. However the results presented in Chapters 4 and 5 do indicate that our pulsed HCN laser is Q-switched by the more direct effect of the laser plasma electrons on the effective length of its resonator. Steffen and Kneubühl (1968) have applied the Q-switch theory of Garret (1967) in order to draw qualitative conclusions about the pulsed HCN laser. Although they treated the case of a Doppler broadened emission line (which is

possibly appropriate for their low pressure gas discharges; see Appendix 2) their conclusions are of interest in the present context. They were :

(a) That since the decay time of 337 μm laser output pulses is much longer than the decay time of photons in their laser resonator then pumping must continue throughout the period of laser emission. This conclusion is not necessarily correct for a Doppler broadened (inhomogeneous) transition because as the cavity resonance is swept through the spontaneous emission line different elements of the velocity distribution of emissive molecules are forced into stimulated emission. In this case a long lifetime of the upper laser level ($\gtrsim$ 200 μsec for Steffen and Kneubühl's laser) is sufficient to account for the observed pulse durations. However Steffen and Kneubühl's conclusion is correct if the transition is homogeneously (pressure) broadened (as in our laser) because all elements of the spontaneous emission line contribute to the gain of the laser as long as the cavity resonance lies somewhere within the effective gainwidth.

Referring now to our pulsed HCN laser, it is shown in Appendix 2 that pressure broadening should dominate. The decay time of pulses occurring in the afterglow of the gas discharge is of the order of 10 μsec

(Figs. 4.1, 4.2, 5.5) while the decay time of photons in the laser resonator (Sec. 2.2.3) is less than 0.1 μsec. Certainly in our laser, pumping must take place throughout the period of laser emission.

(b) Assuming that the lower level of the 337 μm transition is very short lived Steffen and Kneubühl concluded that the shape of the laser output reflects the pumping rate of the upper level. This would be true if the laser were Q-switched *on* and then the cavity resonance kept at or near the centre of the emission line. However as the cavity resonance is swept through the emission line by plasma effects the laser output must fall to zero even if the upper level is still being strongly pumped. Steffen and Kneubühl's conclusion certainly does not apply to the laser pulses which they observed (fig. 11 of Steffen and Kneubühl, 1968) because these pulses show signs of multiple mode sweeping (see Sec. 5.4.2). But in cases where laser action occurs very late in the afterglow of the gas discharge when the electron density does not change the effective length of the laser resonator significantly *during* the period of laser emission the decay of the laser pulse should reflect the pumping rate of the upper level. This should apply to either homogeneously or inhomogeneously broadened transitions.

We now turn our attention to external Q-switching of HCN lasers. An important parameter in the discussion of Q-switching of a laser is the lifetime of the upper level of the laser transition. We shall assume that the lower level empties very quickly. The essential requirement for obtaining enhanced power output through Q-switching is that the upper state lifetime be greater than the decay time of photons in the laser resonator (Garrett, 1967; p. 122) and that the Q-switch time be shorter than, or of the order of, the latter.

By Q-switching a CW 337 μm HCN discharge with a rotating mirror Jones et al (1969) obtained an enhancement of two to three times the continuous output power of their laser. By using the approximate relationship

$$P_Q = \frac{\tau P_{CW}}{\tau_c} , \qquad 5.16$$

they estimated the lifetime τ of the upper level to be 6 μsec, perhaps a little longer. Here P_Q and P_{CW} are the Q-switched and CW powers respectively and τ_c is the decay time of photons in the laser resonator. Jones et al estimated τ_c from the decay rate of the Q-switched laser pulse.

Frayne (1969) obtained a factor of five enhancement in laser output power (at 337 μm) by

Q-switching a CW HCN discharge with a rotating mirror. He states that the minimum Q-switch time which he could practically use was 5 μsec, whereas he estimated the decay time of photons in his resonator to be 0.1 μsec. Thus in the approximate formula of Jones et al (eq. 5.16) τ_c should be taken as 5 μsec indicating an upper state lifetime of the order of 25 μsec. Using a more detailed analysis however, based on the results of Q-switching the laser twice in quick succession, Frayne inferred lifetimes of the order of several milliseconds. He appears to have made an error in his theory but does not give sufficient information to allow the analysis which follows to be checked. For instance, Frayne's eq. (4) implies that in the case when the spontaneous transition probability from the upper to the lower laser level is zero ($\lambda_a = 0$) the rate of equilibration of the population inversion immediately after a Q-switch pulse is independent of the spontaneous transition probability out of the lower laser level (λ_B). This is clearly incorrect. As most of Frayne's conclusions are based on his eq. (4) they may well be incorrect.

Yamanaka et al (1971) have estimated the upper level lifetime in a pulsed 337 μm HCN laser by using an appropriately phased rotating mirror to Q-switch it.

They observed no increase in laser output power and concluded that the lifetime of the upper level could not be much greater than the Q-switch time, suggesting that it might be as short as a few microseconds. They did not recognise that their laser is probably self Q-switched in normal pulsed operation, in which case the mechanical Q-switch should cause no enhancement in output power - even if the upper state lifetime is quite long. Thus we cannot place much faith in their lifetime estimate of a few microseconds.

It is clear that more experiments to determine the upper level lifetime of the 337 μm HCN transition are required. A new approach to the measurement of this parameter is presented in Ch. 6. At present it seems that although the lifetime is not as long as milliseconds, which might be expected for a vibration-rotation level, it is probably not much shorter than 10 μsec. It is therefore much longer than the decay time of photons in the laser resonator (less than 0.1 μsec, see Sec. 2.2.3) a condition which is known to be responsible for the spiking phenomena associated with pulsed solid state lasers (Smith and Sorokin, 1966; p.86) and should have its analogy in HCN lasers (see Ch. 6). In solid state lasers such spiking can be averted by Q-switching and the

same should be true for the pulsed HCN laser. Thus HCN lasers would be expected to produce spiking output from this origin unless they were self Q-switched by plasma mode sweeping effects. In fact, when they do produce spiking output, we have shown that this is due to a succession of Q-switch events.

We conclude that since spiking output is generally observed under discharge conditions similar to ours (e.g. Kon et al, 1967; see Sec. 5.4.1) that its origin lies in plasma effects. The fact that spiking is never observed when the output appears in the afterglow of the laser discharge indicates that HCN lasers are generally self-Q-switched by the plasma cavity mode sweeping mechanism which we have observed in our laser.

Chapter 6

A 337 μm HCN LASER INTERFEROMETER FOR PLASMA DIAGNOSTICS

6.1 Introduction

In Chapter 2 of this thesis we described a pulsed and a continuous HCN laser. Since then, in Chapters 3, 4 and 5, we have studied plasma effects in the pulsed HCN laser; these were based on microwave interferometric measurements of electron densities in the laser discharge plasma. However, for measuring very high electron densities in laboratory plasmas the 337 μm wavelength of the HCN laser itself has considerable promise. We now consider ways in which our CW HCN laser may be used for interferometric electron density measurements. In particular we study the possibility of using a self-modulating laser interferometer configuration.

We first describe a simple theory of loss modulation of a laser with particular emphasis on the CW HCN laser. This leads to several practical predictions in regard to fringe size, fringe shape and frequency response of a loss modulated laser. We then describe self modulating laser interferometer configurations which we have tried.

Evaluation of the performance of these configurations allows us to make several comparisons of theory and experiment and to choose a configuration which is suitable for our plasma diagnostic application in the study of a decaying helium plasma (Ch. 7).

6.2 Advantages of the 337 μm Laser Interferometer

Interferometry at 337 μm permits measurement of transient electron densities in pulsed laboratory plasmas up to the 337 μm cutoff density of 9.8×10^{15} cm^{-3}, while the lower limit depends on the plasma path length and the minimum detectable phase change (e.g. 3.1×10^{12} cm^{-3} for π phase change over a 1 m path length). Although other techniques can be used to measure electron densities in this range, interferometry using the 337 μm HCN laser line offers a number of advantages. For example, while conventional 2 mm microwave methods can be used to measure densities up to cutoff at 3×10^{14} cm^{-3}, diffraction effects limit operation to short path lengths. Decreasing the wavelength to 337 μm can provide acceptable spatial resolution over longer path lengths without seriously reducing sensitivity. Even better spatial resolution may be achieved by using multipass techniques in conjunction with visible and near-infrared lasers (Gerardo and Verdeyen, 1963; Hooper and Bekefi, 1966; Heckenberg and Smith, 1971). However for comparable sensitivity, the effects of vibration and misalignment are very much worse than at 337 μm and interpretation of the results may be complicated by the contribution of atomic species to the refractive index of the plasma. The most common alternatives to interferometry

for measuring electron densities in transient plasmas (not in LTE) are Stark broadening of hydrogen (or hydrogen impurity) lines and Thomson scattering. Even in relatively cold (less than 1 eV) plasmas, Stark broadening is useful only above about 3×10^{14} cm^{-3}. Thomson scattering, which is in any case much more complicated than interferometry, can only be extended below 10^{14} cm^{-3} with extreme difficulty.

In this chapter, we focus our attention on self-modulating laser interferometer (hereafter abbreviated to "laser interferometer") configurations, in which the output beam is passed through the plasma under study and reflected back on itself into the laser (Fig. 6.1). The phase and amplitude of this return beam control the amplitude of the laser output, which is monitored by a detector. The plasma electron density can be deduced from the phase shift thus measured. A number of workers (Gerardo and Verdeyen, 1963; Hooper and Bekefi, 1966; Ashby et al, 1965) have operated such systems incorporating CW He-Ne lasers operating in the visible and near-infrared regions and one system using a 10.6 μm CO_2 laser has been described (Herold and Jahoda, 1969). More recently Peterson and Jahoda (1971) demonstrated the feasibility of using the 337 μm HCN laser in a self-modulating configura-

tion, in contrast to previous applications (Olsen, 1971; Parkinson et al, 1968; Turner and Poehler, 1968; Chamberlain et al, 1969) in which this laser has simply been used as a source in a conventional interferometer. The greatly increased sensitivity of plasma interferometry at 337 μm makes a laser interferometer based on a far-infrared HCN laser an attractive proposition, particularly in view of the simplicity and ease of operation of laser interferometers.

It is possible to describe the laser interferometer on the basis of a simple theory which leads to some interesting conclusions. It is shown in Sec. 6.34 that under certain circumstances the laser interferometer can have a peaked frequency response. The factors affecting the shape and size of the laser interferometer fringes are also discussed. The fringe shape is of importance in the interpretation of fractional fringe measurements (Hooper and Bekefi, 1966) while the possibility of a nonlinear dependence of fringe size on return beam amplitude limits the use of laser interferograms for determination of the plasma temperature from the magnitude of the attenuation. In practice, however, attenuation measurements may well be rendered worthless by the refractive effects of plasma density gradients (Ch. 7) so this is not considered a serious disadvantage.

6.3 The Theory of the Laser Interferometer

To understand the behaviour of the laser interferometer, we consider first the factors which determine the operating point of the laser itself. The effect of returning part of the output beam into the laser cavity can then be treated as a modulation of the cavity loss.

The active medium of the laser is characterized by a gain per unit length, g, resulting from stimulated emission. That is

$$\frac{dI}{dx} = gI \quad , \qquad 6.1$$

where I is the radiation intensity in the cavity. The gain falls off with increasing intensity because of reduction of the population inversion (saturation). The steady state intensity is determined by the condition that the energy gained per pass is just equal to the energy lost. Considering one round-trip of the cavity, this implies

$$A \exp(2g\ell) - 1 = 0 \quad , \qquad 6.2$$

where A is the (intensity) attenuation factor for a round trip and ℓ is the length of the active medium.

The functional form of the saturation characteristic depends on a number of factors, but there is strong justification for writing it as (Sinclair and Bell, 1969)

$$g(I) = \frac{\alpha}{(1 + \beta I)^r} \quad . \qquad 6.3$$

The unsaturated gain per unit length, α, and the saturation parameter, β, are determined by the excitation and de-excitation rates of the energy levels involved in the laser transition. The gain, g, is of course a function of the wave frequency also. Equation 6.3 is sometimes taken to represent the line-centre gain and should then be multiplied by the line-shape function. Here g is used to represent the gain at the frequency of oscillation. The value taken by the exponent, r, depends on the processes which broaden the corresponding spontaneous emission line (Sinclair and Bell, 1969; White et al, 1963; Smith, 1966). Since pressure broadening dominates in our CW HCN laser (Sec. 2.4.3), we employ the form of eq. 6.3 appropriate to homogeneous broadening (Sinclair and Bell, 1969), that is r is taken as unity in subsequent discussion. The results obtained are readily extended to the general case of arbitrary r.

6.3.1 Loss Modulation by Return Beam

In what follows, it is convenient to write the attenuation factor in the form

$$A = (1 - L)\ (1 - T) \quad , \qquad 6.4$$

where T is the fraction of stored energy lost per round trip of the cavity as output (i.e. T is the (intensity) transmissivity of the laser output mirror) and L represents all other losses. From eqs. 6.2 to 6.4, the quiescent cavity intensity, I_o, is given by

$$(1 - L)\ (1 - T)\ \exp\left(\frac{2\alpha\ell}{1 + \beta I_o}\right) - 1 = 0 \quad . \qquad 6.5$$

To simplify analysis and avoid some complications discussed below, we now assume that the losses are small (say $L + T \lesssim 20\%$). This assumption is valid for the 633 nm and 1.15 μm He-Ne laser transitions which have been used extensively for laser interferometry but not for the very high gain 3.39 μm line. It is also valid for the 337 μm HCN laser used in our experiments. When the losses are small, the exponential term in eq. 6.5 must be close to unity and so we can write

$$\frac{2\alpha\ell}{1 + \beta I_o} = L + T \quad . \qquad 6.6$$

When part of the output beam is returned into the laser, the losses represented by T are modified according to the phase and amplitude of the return beam. For the interferometer shown in Fig. 6.1, the laser output intensity is TI. The intensity of the return beam incident on the output mirror of the laser is $\varepsilon^2 TI$, where ε^2 represents the attenuation of the return beam *intensity* due to diffraction, reflection and transmission losses etc., in the *external* path. Thus the intensity returned into the cavity after passing through the output mirror is $\varepsilon^2 T^2 I$. In the absence of the return beam, the amplitude of the wave reflected by the output mirror (amplitude reflectance r) is $r\sqrt{I}$. If the return beam undergoes a total phase change ϕ, the effective reflected amplitude becomes (coherent sum)

$$A = r\sqrt{I} + \varepsilon T\sqrt{I}\, e^{j\phi} \quad , \qquad 6.7$$

where we have redefined ε to include the effect of mismatching of the reflected and return wavefronts at the output mirror, which results in reduced modulation of the reflected amplitude. The corresponding intensity is

$$|A|^2 = r^2 I\ (1 + 2\varepsilon T \cos \phi) \quad , \qquad 6.8$$

where the term in T^2 has been neglected and r has been taken as unity in the term containing T. We now discuss

the implications of eqs. 6.7 and 6.8.

The phase variation of the reflected amplitude, A, is usually ignored in discussions on laser interferometry. It has the effect of varying the apparent length of the cavity by a fraction of a wavelength, thereby pulling the laser operating frequency. This has two consequences. Firstly, the phase shift in the external path is in turn changed, requiring that the equations above be reconstructed, allowing for pulling, to produce a closed system for solution. As this procedure is algebraically involved it will not be attempted here. It suffices to establish conditions under which pulling can be ignored. From eq. 6.7, the maximum phase change in the effective reflected amplitude is approximately εT radians in which case the frequency is pulled by an amount

$$\delta\omega = \frac{c}{2\ell}\,\varepsilon T \quad , \qquad 6.9$$

where $\delta\omega$ is the shift in the laser wave angular frequency ω, and $2\ell/c$ is the transit time for radiation around the cavity (for convenience, the cavity length is taken to be the same as the length, ℓ, of the active medium). The phase of the return beam will then be changed by

$$\delta\phi = \delta\omega\,\frac{2L}{c} \quad , \qquad 6.10$$

where L is length of the external return path. Clearly from eqs. 6.9 and 6.10, $\delta\phi$ will be insignificant if $\varepsilon TL/\ell$ is small, as is the case for the HCN laser interferometers described in Sec. 6.4. Note that although such pulling can alter the fringe shape, the positions of maxima and minima remain unchanged since there is no pulling for $\phi = 0$ or π.

The other effect of pulling is to shift the laser operating frequency on the gain profile. In the case of optical lasers where there are normally several longitudinal cavity modes within the gainwidth this is of little significance. In contrast, the gainwidth of the HCN laser is less than the spacing between low loss modes, as demonstrated by the fact that the laser can be extinguished by manipulation of the cavity length (Steffen and Kneubühl, 1968). However, from eq. 6.9, if εT were as large as 0.1, the pulling would only be ± 1.3 MHz for our laser (ℓ = 1.8 m), compared with a gainwidth of about 13 MHz (see Sec. 2.4.3). We conclude that the effects of phase variation of the reflected amplitude are small in the case of our system and can be neglected. [Nevertheless, if the laser were deliberately tuned near the edge of the gain profile, frequency pulling could be significant.]

However, a small change in the *magnitude* of the effective reflected amplitude results in a relatively

large change in the total loss of the laser cavity and will cause significant variation of the laser output level. It is clear from eq. 6.8 that to account for this effect the attenuation factor, A (given by eq. 6.4) must be replaced by

$$A' = (1 - L)\ (1 - T)\ (1 + 2\varepsilon T \cos \phi). \qquad 6.11$$

Using the same arguments as led to eq. 6.6, we obtain

$$\frac{2\alpha \ell}{1 + \beta I} = (L + T) \left(1 - \frac{2\varepsilon T}{L + T} \cos \phi\right) . \qquad 6.12$$

Equation 6.12 establishes the dependence of cavity intensity on return beam phase and amplitude. We now discuss in detail the shape of the laser interferometer fringes and the way in which their size depends on the amplitude of the return beam. Comparison of eqs. 6.6 and 6.12 yields

$$\frac{I}{I_o} = 1 + \frac{1 + \beta I_o}{\beta I_o} \frac{\frac{2\varepsilon T}{L + T} \cos \phi}{1 - \frac{2\varepsilon T}{L + T} \cos \phi} . \qquad 6.13$$

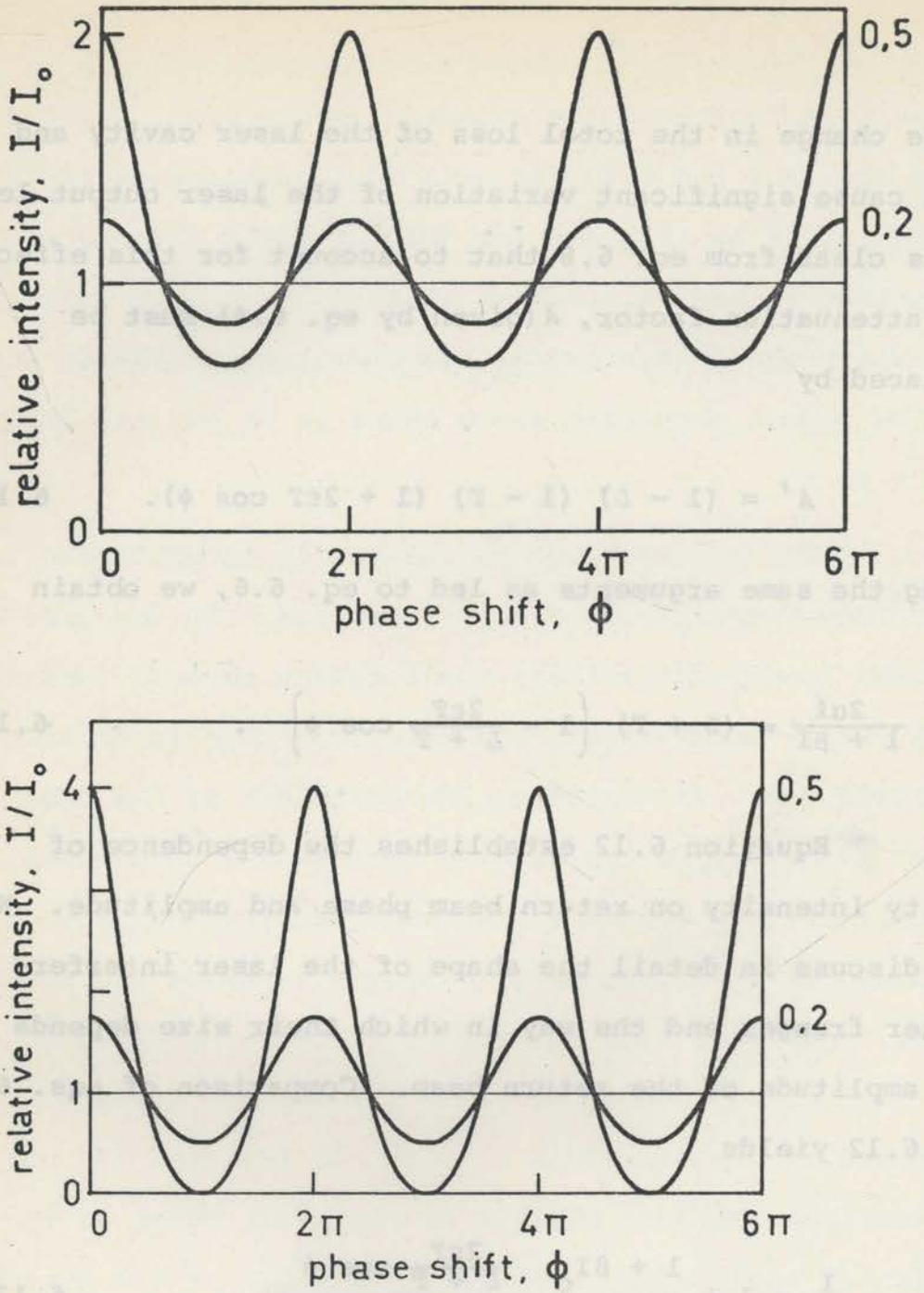

Fig. 6.2. Laser interferometer output as a function of phase shift in the return path (eq. 6.13) for two values, 0.2 and 0.5, of the parameter $2\varepsilon T/(L + T)$. This parameter is a measure of the depth of loss modulation (eq. 6.12).

(a) Highly saturated laser: $(1 + \beta I_o)/\beta I_o = 1$.

(b) Laser operating closer to threshold: $(1 + \beta I_o)/\beta I_o = 3$.

6.3.2 Laser Interferometer Fringe Shape

It is clear from eq. 6.13 that unless

$$\frac{2\varepsilon T}{L + T} \ll 1 \quad , \qquad 6.14$$

that is, unless the depth of modulation of the losses is small, the fringes will have a non-sinusoidal shape (Figs. 6.2 (a) and (b)). Note however that eq. 6.13 is not strictly correct for values of ε approaching unity (i.e. when losses in the return system are small). In this case the laser output mirror acts with the return mirror to form a Fabry-Perot cavity and beams which make more than one pass of this cavity must then be taken into account. Such an arrangement will of itself produce non-sinusoidal fringes. By performing a standard Fabry-Perot calculation assuming plane wavefronts in a plane parallel resonator it can be shown that the effective reflected intensity at the output end of the laser now varies as

$$|A|^2 = r^2 I \left[1 + \frac{2\varepsilon T}{r} \left(\frac{\varepsilon r + \frac{\varepsilon T}{2r} + \cos \phi}{1 + \varepsilon^2 r^2 + 2\varepsilon r \cos \phi} \right) \right] . \qquad 6.15$$

Although one would expect this result to be modified by considerations of mode structure and resonator geometry, it is in fact equivalent to the result obtained by Hooper

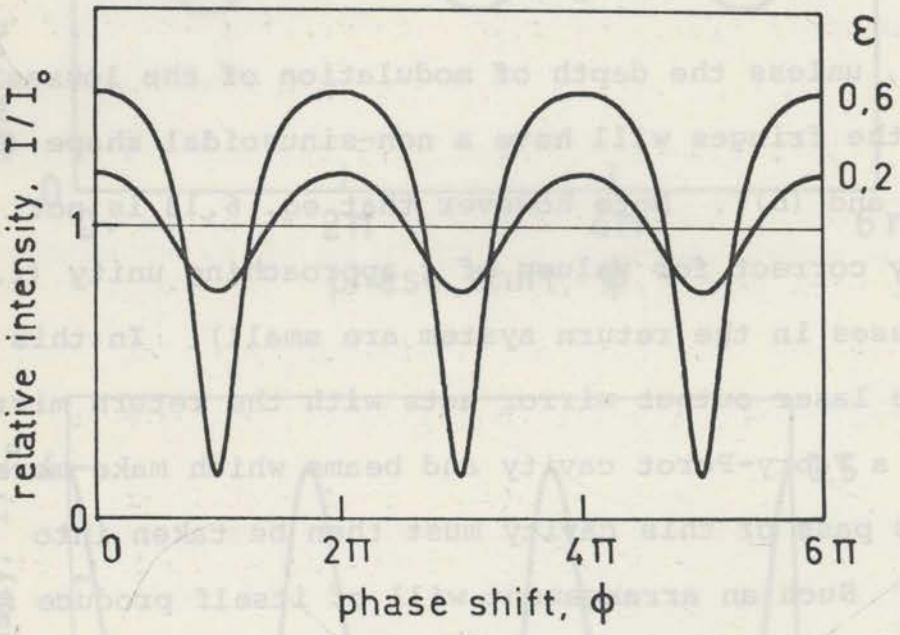

Fig. 6.3. Fabry-Perot interferometer fringes (eq. 6.16) for two values of the return system attenuation, ε. ϕ is the phase shift due to a single (back and forth) pass of the return system. The following parameter values which are appropriate to the case of a 633 nm He-Ne laser have been used: $(1 + \beta I_o)/\beta I_o = 2$, $T = 0.01$, $L = 0.03$, $r = 0.99$.

and Bekefi (1966) taking these factors into account. Their calculation assumes that the laser excites only a single mode of the external cavity and also that frequency pulling may be neglected. [This latter condition may well be violated in practice, since the sensitivity of return beam phase to frequency in the region of Fabry-Perot resonance of the external cavity is greatly enhanced (by a factor of the order of the Q of the external cavity) compared with the corresponding single pass situation. The qualitative features of the fringe shape will still correspond to those predicted by eq. 6.15, however.]

The following equation results when eq. 6.15 replaces eq. 6.8 in a derivation analogous to that of eq. 6.13.

$$\frac{I}{I_o} = 1 + \frac{1 + \beta I_o}{\beta I_o} \frac{k}{1 - k} ,$$

where

$$k = \frac{2\varepsilon T}{L + T} \cdot \frac{1}{r} \cdot \frac{\varepsilon r + \frac{\varepsilon T}{2r} + \cos \phi}{1 + \varepsilon^2 r^2 + 2\varepsilon r \cos \phi} . \qquad 6.16$$

Figure 6.3 shows the shape of fringes obtained from eq. 6.16 when values appropriate to a 633 nm He-Ne laser are assumed. The flattened tops and sharp troughs contrast markedly with the fringe shape associated with the non-

linearity of the laser itself. In fact in the case of the 633 nm He-Ne laser interferometer, the non-sinusoidal fringes often observed are due to the Fabry-Perot effect which invariably dominates the effect of intrinsic laser nonlinearity.

It is possible however, with a laser employing hole-output coupling (Sec. 6.4) to return a large part of the output back into the laser after only one pass and to suppress any reflection from the external surface of the output mirror, thus preventing Fabry-Perot action. The equations derived above should at least qualitatively describe the behaviour of a laser interferometer using hole coupling and indeed non-sinusoidal fringes such as predicted by eq. 6.13 have been observed (see Sec. 6.4).

Far from being an inconvenience, multiple reflections between the laser output and return mirrors may be utilized to increase the sensitivity of the interferometer. One approach is to construct the return system as a Fabry-Perot cavity coupled to the laser cavity. Greatly increased sensitivity is possible, but only for fractional fringe shifts (Hooper and Bekefi, 1966). Alternatively, techniques exist for isolating a beam which has made a prescribed number of passes through the plasma under study for return into the laser (Heckenberg and

Smith, 1971). However at the long 337 μm wavelength, diffraction prevents complete suppression of the unwanted beams. Equation 6.12 is easily modified as follows to take into account the presence of multipass beams :

$$\frac{2\alpha\ell}{1 + \beta I} = (L + T)\left(1 - \frac{2T}{L + T}\sum_{n=1}^{\infty} \varepsilon_n \cos(n\phi + \phi_n)\right) . \quad 6.17$$

Here ε_n represents the relative amplitude of the beam returning to the laser after n complete passes of the return system, with relative phase ϕ_n. The feasibility of such multipass operation with a 337 μm HCN laser is demonstrated in Sec. 6.4.

6.3.3 Laser Interferometer Fringe Size

In connection with the size of laser interferometer fringes there are two main points of interest: firstly, the functional relation between fringe height and return beam attenuation and, secondly, the size of fringes produced by the laser interferometer in comparison with those produced by conventional interferometers. This latter point does not appear to have been discussed in the literature, but is of considerable practical interest.

From eq. 6.13, which is appropriate to single pass operation, the peak-to-peak fringe height is given by

$$\frac{I_{max} - I_{min}}{I_o} = \frac{1 + \beta I_o}{\beta I_o} \left(\frac{2 \frac{2\varepsilon T}{L + T}}{1 - \left(\frac{2\varepsilon T}{L + T} \right)^2} \right) \qquad 6.18$$

This equation shows the relationship between fringe height and return beam amplitude (proportional to ε) to be linear only while eq. 6.14 is satisfied. As noted above, unless hole-output coupling is used, Fabry-Perot action of the return system will occur for ε large and will provide a second source of non-linearity.

Equation 6.18 can also be used to compare the size of the fringes produced by a laser interferometer with those produced by conventional interferometers, such as the Michelson and Mach-Zehnder types. This point is of considerable practical interest in plasma diagnostic work because of the high losses in the optical systems used and the noisy electrical environment. An appropriate figure of merit, S, for the interferometers is the ratio of peak-to-peak intensity height of the fringes at the detector to the quiescent output power of the laser, TI_o.

Firstly, we consider a laser interferometer with beam-splitter output (Fig. 6.6) as such a system seems the most suitable for operation at 337 μm (Sec. 6.4). The beam leaving the laser is divided between the detector and

the probing path. Part of the beam returning to the laser after passing through the plasma is lost by reflection off the beamsplitter. In the case of small modulation, which is where fringe height is important, the figure of merit S for such a system is given by

$$S_{\text{Laser Interferometer}} = \frac{T}{L + T} \cdot \frac{1 + \beta I_o}{\beta I_o} \cdot \varepsilon \qquad 6.19$$

where the use of a 50% beamsplitter (which maximizes S) is assumed. As before, $T/(L + T)$ is the output expressed as a fraction of the total laser losses and ε^2 is the fractional intensity of the radiation returning from the lossy optical system incorporating the plasma under study.

In the case of the Michelson interferometer the reference arm losses can be made small and will be neglected. The same factor ε will be appropriate to describe the relative amplitude of the beam returning from the plasma since the losses there are just the same as in the laser interferometer. It is easy to show (again assuming a 50% beam-splitter) that for the Michelson interferometer

$$S_{\text{Michelson}} = \varepsilon \quad . \qquad 6.20$$

It is more difficult to make a valid comparison with a Mach-Zehnder type interferometer where the probing

beam passes only once through the plasma. In this case it is more difficult to keep losses in the long reference arm much lower than those in the probing arm. We assume therefore that the intensity of each of these beams is reduced by a factor ε in its passage. Once more assuming 50% beam-splitters leads to

$$S_{\text{Mach-Zehnder}} = \varepsilon \, . \qquad 6.21$$

Equation 6.19 shows that under typical operating conditions the fringes produced by the laser interferometer are about the same size as those produced by conventional interferometers. On the other hand in the case of a laser which operates close to threshold (βI_o small) the laser interferometer can produce fringes considerably larger than a conventional interferometer using the same laser as source. Note, however, that in this case, the frequency response of the laser interferometer will be limited. (See below).

It should be mentioned here that a conventionally arranged Michelson interferometer will, unless special precautions are taken, return enough power into the laser to cause laser modulation. If sinusoidal fringes are required this problem must be overcome either by use of a polarizing isolator or by tilting the beams in the system.

6.3.4 Laser Interferometer Frequency Response

The frequency response of the laser interferometer is limited not only by the response time of the detector used but also by the fact that the output of the laser cannot change extremely rapidly (Hooper and Bekefi, 1966; Uchida, 1967). We discuss two factors which affect the frequency response, limiting discussion to the low loss, small modulation case. Firstly, a fundamental limitation results from the fact that the high Q laser resonator does not allow the trapped radiation intensity to change rapidly. If the laser is operated close to threshold, the cut-off frequency is even further depressed by the presence of the active medium. In deriving an expression to describe these effects, we assume that the laser gain can saturate much faster than the radiation intensity can change so that the gain is related at any moment of time to the radiation intensity by the equilibrium expression eq. 6.3. [It is implicit that the width of the sideband spectrum associated with amplitude modulation of the laser output is small compared with the gainwidth.] If the laser intensity changes at a rate comparable with the rates of excitation and de-excitation of the laser levels this assumption is invalid. This second case will be discussed later.

Provided that the period of modulation of the laser interferometer is large compared with the transit time, $2\ell/c$, for radiation around the cavity, the gain and losses of the laser may be treated as lumped parameters. The time rate of change of cavity intensity is then given by

$$\frac{dI}{dt} = \frac{c}{2\ell} I \left(e^{2g\ell} A' - 1 \right) . \qquad 6.22$$

Substituting into this equation the forms used previously for g and A' (eqs. 6.3 and 6.11), and approximating for small losses (as in eq. 6.12) yields

$$\frac{dI}{dt} = \frac{c}{2\ell} I \left(\frac{2\alpha\ell}{1 + \beta I} - L - T + 2\varepsilon T \cos \phi \right) . \qquad 6.23$$

Assuming that the depth of modulation is small as it will be in most experimental situations, we can treat the modulation as a small perturbation, i.e.

$$I = I_o + i , \quad |i| << I_o . \qquad 6.24$$

The saturation characteristic may then be approximated by

$$\frac{2\alpha\ell}{1 + \beta I} = \frac{2\alpha\ell}{1 + \beta I_o} - \frac{2\alpha\ell}{(1 + \beta I_o)^2} \beta i . \qquad 6.25$$

Combining eqs. 6.23 - 6.25, we obtain

$$\frac{di}{dt} = \frac{c}{2\ell} I_o \left(\frac{-2\alpha\ell}{(1 + \beta I_o)^2} \beta i + 2\varepsilon T \cos \phi \right) . \qquad 6.26$$

If ϕ increases linearly with time to give a modulation angular frequency p, the solution of eq. 6.26 (using a phasor representation for i) is,

$$i = 2\varepsilon I_o \left(\frac{T}{L + T} \right) \left(\frac{1 + \beta I_o}{\beta I_o} \right) \Big/ (1 + j\, p/p_o) , \qquad 6.27$$

where

$$p_o = \frac{c}{2\ell} (L + T) \frac{\beta I_o}{1 + \beta I_o} . \qquad 6.28$$

Equation 6.27 indicates that the laser interferometer has a flat response up to cut-off at p_o, above which the fringe amplitude is inversely proportional to frequency. The physical significance of the cut-off frequency is better seen when it is expressed as

$$p_o = \frac{\omega}{Q_c} \frac{\beta I_o}{1 + \beta I_o} , \qquad 6.29$$

where ω is the laser wave angular frequency and Q_c is the cavity "Q" given by

$$Q_c = \frac{2\ell}{c} \frac{1}{L + T} \omega . \qquad 6.30$$

Q_c determines the bandwidth of the cavity alone. In the presence of the active medium, the modulation bandwidth is reduced to a value corresponding to a "dynamic" Q,

$$Q_d = Q_c \frac{1 + \beta I_o}{\beta I_o} . \qquad 6.31$$

A laser operating near threshold ($\beta I_o << 1$) will then have a severely limited frequency response. It is this effect in conjunction with a high cavity Q which is responsible for the very slow response time often associated with the 633 nm He-Ne laser interferometer (Potter, 1969). In the case of the HCN laser described in Ch. 2, Q_c is of the order of 5×10^5 so that the modulation response cutoff frequency ($p_o/2\pi$) is of the order of 900 kHz, assuming a moderate degree of saturation ($\beta I_o \simeq 1$).

In determining the frequency response limitation imposed by cavity Q effects, we assumed that the rates of excitation and de-excitation of the laser levels were much greater than the rate of modulation of the laser intensity, so that the equilibrium gain saturation formula (eq. 6.3) would be applicable. This will indeed be true for atomic lasers, where the quantities of interest are atomic radiative and collisional lifetimes of order 10^{-6} to 10^{-8} sec, which are generally less than the time constant

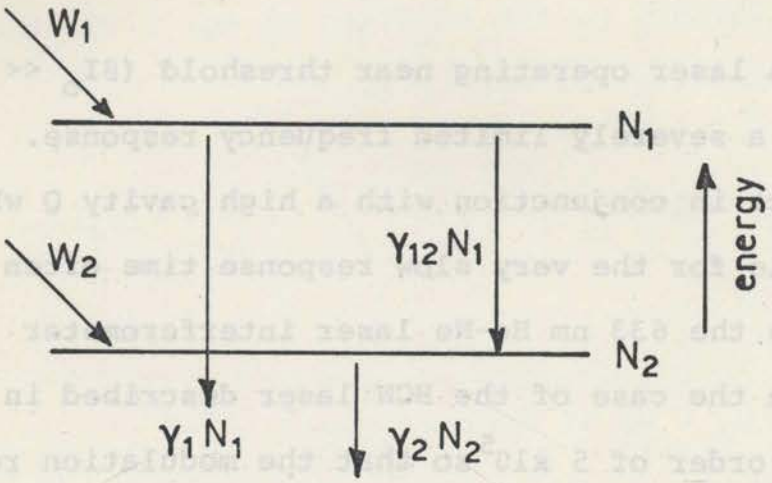

Fig. 6.4. Model of laser excitation and de-excitation processes used in the calculation of laser interferometer frequency response. The γ's are total effective decay rates (collisional plus radiative).

associated with the cavity Q. However, the lifetimes of vibration-rotation levels in molecular lasers can be much longer, of the order of milliseconds. To determine the effect of such slow rates on the frequency response of the laser interferometer, we consider the following simple model for the excitation and de-excitation mechanisms (Fig. 6.4).

The upper and lower laser levels, populations N_1 and N_2 respectively, are assumed to be pumped at rates W_1 and W_2, independent of N_1 and N_2. De-excitation (collisional and radiative) of the upper level occurs through two distinct routes: to the lower laser level with transition probability γ_{12}, and to all other levels, probability γ_1. The total probability for a transition out of the lower level is γ_2. This model leads to the following rate equations (for a homogeneously broadened transition) :

$$\frac{dN_1}{dt} = W_1 - (\gamma_1 + \gamma_{12})\, N_1 - \sigma(N_1 - N_2)I \quad , \tag{6.32}$$

$$\frac{dN_2}{dt} = W_2 + \gamma_{12}N_1 - \gamma_2 N_2 + \sigma(N_1 - N_2)I \quad ,$$

where σ represents the probability of stimulated emission. For the case of small modulation, N_1, N_2 and I may be expressed in terms of their quiescent (no return beam)

values plus a small perturbation :

$$N_1 = N_{10} + n_1 \quad ,$$

$$N_2 = N_{20} + n_2 \quad , \qquad 6.33$$

$$I = I_o + i \quad .$$

Noting that the gain has the form

$$2g\ell = B(N_1 - N_2) \quad , \qquad 6.34$$

where B is a constant, we obtain the following equation from eqs. 6.32 and the rate equation (6.22) for the cavity intensity :

$$\frac{dn_1}{dt} = -(\gamma_1 + \gamma_{12})n_1 - \sigma(n_1 - n_2)I_o - \sigma(N_{10} - N_{20})i \quad ,$$

$$\frac{dn_2}{dt} = \gamma_{12}n_1 - \gamma_2 n_2 + \sigma(n_1 - n_2)I_o + \sigma(N_{10} - N_{20})i \quad , \qquad 6.35$$

$$\frac{di}{dt} = \frac{c}{2\ell} I_o(B(n_1 - n_2) + 2\varepsilon T \cos pt) \quad .$$

The (steady state) solution of these equations for is (phasor representation)

$$i = 2\varepsilon I_o \frac{T}{L+T} \frac{1+\beta I_o}{\beta I_o} \Bigg/ \left(j\, {}^{p}/_{p_o} + \frac{1 + {}^{1}/_{\beta I_o}}{1 + \dfrac{(jp+\gamma_1+\gamma_{12})(jp+\gamma_2)}{\sigma I_o(2jp+\gamma_1+\gamma_2)}} \right) . \qquad 6.36$$

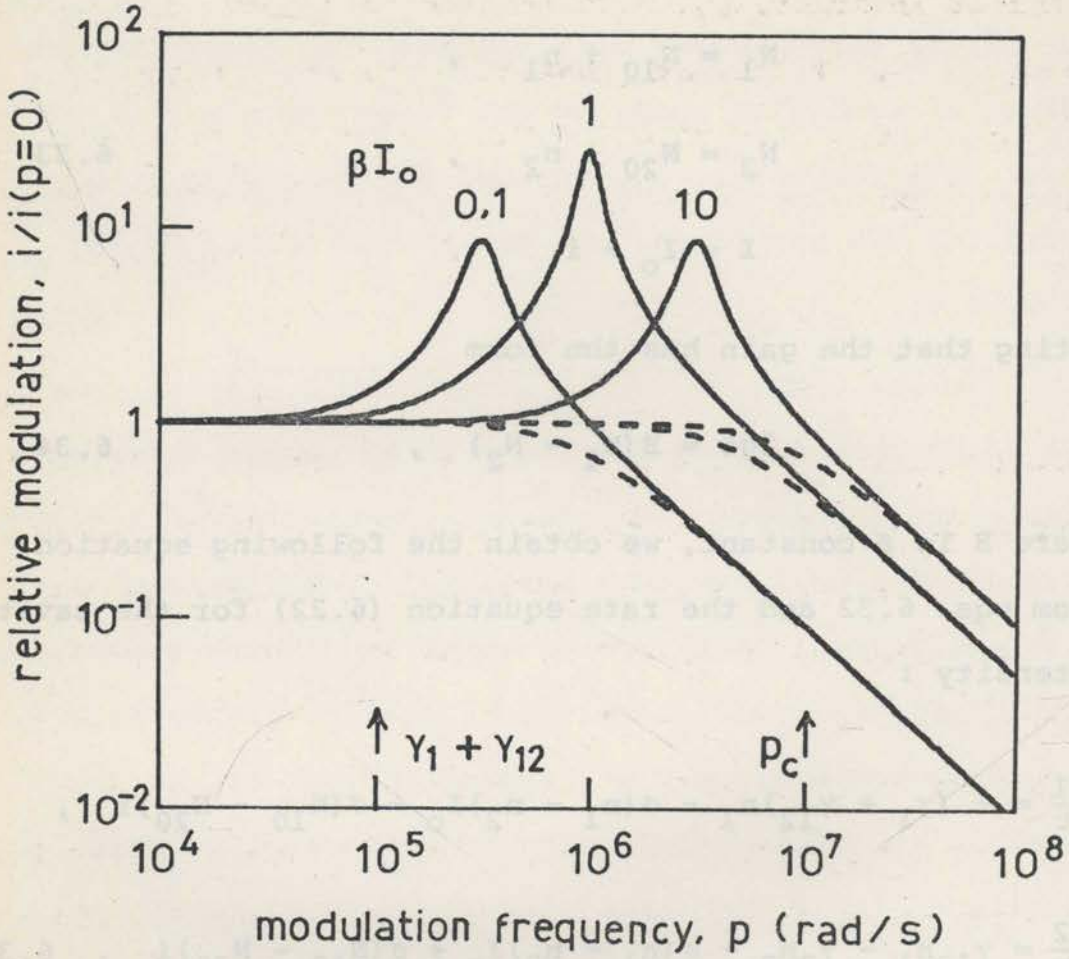

Fig. 6.5. Modulation response of a laser interferometer calculated from eq. 6.36. The values indicated for the total transition probability out of the upper level, $(\gamma_1 + \gamma_{12})$, and the passive cavity cutoff frequency, $p_c = (c/2\ell)\ (L + T)$, are appropriate to the case of a 337 μm HCN laser (see text). The transition probability out of the lower level, γ_2, is assumed to be very large ($\gamma_2 >> p_c$). The broken curves show the response due to cavity Q effects alone (all γ's $>> p_c$).

If the various lifetimes are short compared with times of interest, eq. 6.36 reduces to a form corresponding to eq. 6.27. It follows that the saturation paramater β may be expressed in terms of the excitation and de-excitation rates of our model:

$$\beta = \frac{\sigma}{\gamma_2} \frac{\gamma_1 + \gamma_2}{\gamma_1 + \gamma_{12}} . \qquad 6.37$$

When the level lifetimes are not short the response is more complicated. If the upper state transition probability $(\gamma_1 + \gamma_{12})$ is particularly small and γ_2 large compared with p_o, the response (Fig. 6.5) will be flat only up to a frequency of order $(1 + \beta I_o)(\gamma_1 + \gamma_{12})$, at which point it begins to rise. After passing through a resonance, the response ultimately falls below the low frequency level at the "cavity limit", $p = p_o$. Beyond this frequency the roll off is controlled by the cavity Q effect.

The essential characteristic leading to the peaked modulation response is an upper state lifetime appreciably greater than the decay time of photons in the laser cavity. Such a situation occurs in most molecular and solid state lasers, where it is responsible for several related effects. It is the basis for obtaining enhanced power output through Q-switching (Garrett, 1967; p.122). A more directly

related phenomenon is the "spiking" associated with free-running solid state lasers using pulsed excitation (Smith and Sorokin, 1966; p.86). The explanation of such spiking follows from the behaviour of solutions to the Statż- de Mars rate equations (Smith and Sorokin, 1966; p.69) used in the description of solid state lasers. A simple linearized perturbation analysis (Smith and Sorokin, 1966; p.86), while understandably failing to account for large signal behaviour, predicts a damped oscillatory response to disturbances. The ringing frequency and damping constant derived in this transient analysis correspond to the frequency and width of the resonant peak predicted by our analysis of the steady state modulation response of the laser interferometer. Indeed a peaked frequency response has been predicted for loss modulation of a solid state laser (McCumber, 1966).

Thus the prediction of a peaked response is not altogether unexpected. However, the experiment described in Sec. 6.4 indicates that our system had a flat response up to a fringing rate of at least 10 kHz, which was the limit of measurement. Furthermore Peterson and Jahoda (1971) have observed fringing rates up to 150 kHz ($p = 9 \times 10^5$ rad/s) with no apparent deviation from flat response. This is surprising in view of the fact that

vibration-rotation levels generally have lifetimes of the order of milliseconds. Unfortunately, we do not have reliable estimates for the lifetimes in the HCN laser. It is believed that the lower level is comparatively short lived (Chantry, 1971; p.241) ($\gamma_2 >> \gamma_1 + \gamma_{12}$), in which case the general shape of the response curve is not seriously affected by assuming the lower level lifetime to be negligibly short ($\gamma_2 >> p_c$). Other evidence (Jones et al, 1969; Yamanaka et al, 1971; see Sec. 5.4.3) suggests that the upper level may have a lifetime as short as a few μsec. A value of 10 μsec ($\gamma_1 + \gamma_{12} = 10^5$/sec) was used for the plots of Fig. 6.5. It is apparent that an extended flat response could be explained if the upper level lifetime was fairly short and the laser moderately saturated ($\beta I_o > 1$). A rising frequency response has been observed in the case of a CO_2 laser interferometer (Herold and Jahoda, 1969). Unfortunately the data presented is not sufficient to allow detailed comparison with our theory. To resolve the question of laser interferometer frequency response it is desirable that measurements be made using molecular lasers at much higher fringing rates than have been achieved to date.

Let us conclude this section by stating what has been achieved so far. We have developed a simple theory

of the laser interferometer principle with a bias towards its application to a 337 μm HCN laser. This has led to several practical conclusions in relation to laser interferometer fringe size, fringe shape, and frequency response. These are summarized at the end of the chapter. We now proceed to describe our experimental evaluation of the performance of several practical laser interferometer configurations based on the CW 337 μm HCN laser described in Ch. 2. This allows several comparisons of our theory with experimental observations and gives some measure of the success of our theory in predicting the performance of the HCN laser interferometer.

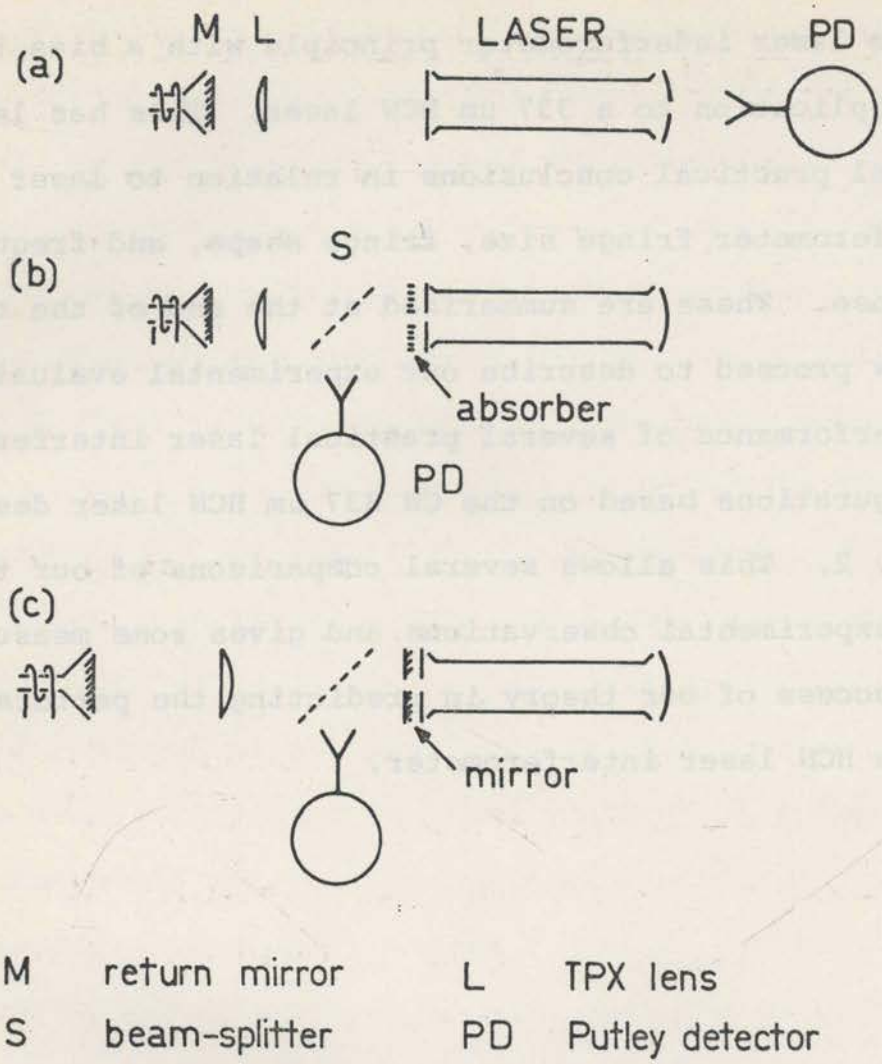

Fig. 6.6. Three configurations used to evaluate the performance of the HCN laser interferometer system. The loudspeaker was driven by a low frequency (5 to 50 Hz) audio oscillator at amplitudes of up to 1 cm peak to peak.

(a) Laser with double ended output. The lens was required to return a large part of the divergent (diffraction limited) laser output beam to the coupling hole.

(b) Single ended output with 50 μm mylar beam-splitter coupling output to the Putley detector. The absorber was used to prevent Fabry-Perot action of the return system.

(c) Multipass return system used to obtain high fringing rates. The optical system was designed for three pass operation.

6.4 Practical Laser Interferometer Configurations using a CW HCN Laser

In order to investigate the suitability of the CW HCN laser (Ch.2) for use in a laser interferometer, the arrangements of Fig. 6.6 were set up. Phase modulated laser output was returned to the laser resonator by a return mirror mounted on the cone of a dynamic loudspeaker, and the laser response was observed with a Putley detector (Putley, 1963) ($t_r \simeq 0.2$ μsec) operating at 4.2 K in a 25 kG magnetic field (Appendix 1). A T.P.X. (Chantry et al, 1969) lens was used to collimate the divergent (diffraction limited) laser output beam. T.P.X. is a plastic having very good transmission properties in the far-infrared. Because its refractive index (1.43) is the same for both optical and far-infrared wavelengths, far-infrared "optical" systems incorporating T.P.X. lenses may conveniently be aligned with the visible beam of a He-Ne laser (see Fig. 7.4).

The system shown in Fig. 6.6(a), analogous to that used by Ashby et al (1965) with a He-Ne laser, is desirable because it is simple and easy to align. However the results obtained were quite unsatisfactory, as the modulation of the output (at either end of the laser) was very weak and erratic. This is ascribed partly to poor

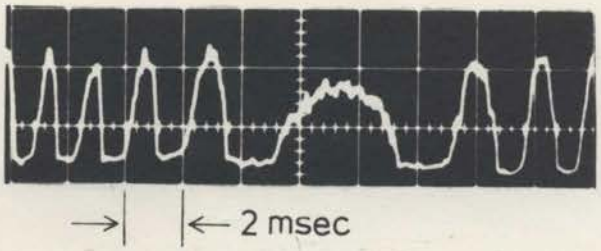

Fig. 6.7. Laser interferometer fringes obtained with the configuration of Fig. 6.6b showing extinction of the laser output. This effect is conclusive evidence that the interference fringes observed were genuine laser output modulation rather than simple interference of various beams of radiation.

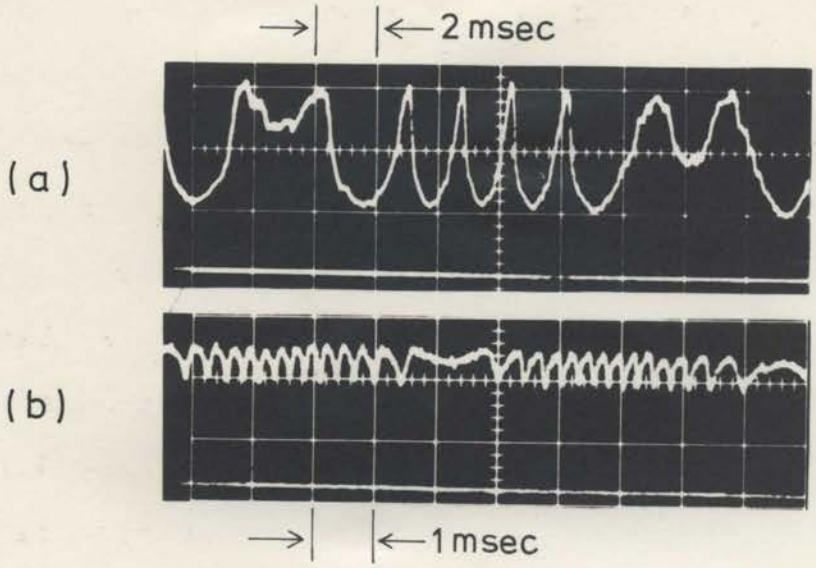

Fig. 6.8. Laser interferometer fringes showing the two types of fringe distortion discussed in the text. Each photograph shows a baseline corresponding to zero laser output.

(a) Fringes obtained with the test configuration of Fig. 6.6(b) when as much as possible of the output beam was coupled back into the laser, showing the effect of intrinsic laser nonlinearity (c.f. Fig. 6.2).

(b) Moving mirror fringes obtained with the configuration of Fig. 7.4. Only a small fraction of the laser output was coupled back into the laser, but the fringes still show distortion due to Fabry-Perot action arising from spurious reflections from surfaces in the return system (c.f. Fig. 6.3).

coupling between the return beam and the (necessarily off axis) laser operating mode (McCumber, 1965) and partly to the noisy, marginal operation of the laser when both mirrors have output holes (see Sec. 2.4.3).

The arrangement shown in Fig. 6.6(b) uses a laser with only one output hole, which operates far more stably and powerfully. Once again only poor modulation was observed when the laser was operated in the noisy modes. However, when operated in the quiet modes, strong modulation of the output was observed - so strong in fact that when the laser was deliberately operated near threshold it was able to oscillate only for a small range of return beam phase (Fig. 6.7). This effect is conclusive evidence that the interference fringes observed are genuine laser output modulation rather than simple interference of various beams of radiation. Figure 6.8 shows less deeply modulated fringes obtained in two different circumstances. The fringes shown in Fig. 6.8(a) were obtained by siting the return mirror as close to the laser as possible while covering the outside of the laser output mirror with absorbing material to suppress multiple reflections. In this case the laser losses were sufficiently strongly modulated that its inherent nonlinearity resulted in the sharp peaking of the fringes. Those in Fig. 6.8(b) were

obtained in the case where the oscillating return mirror was sited some 3 m from the laser at the other end of the SUPPER I plasma source described in Ch. 7 (Fig. 7.4). In this case the return beam amplitude was small and multiple reflections between plane surfaces (Fabry-Perot action) in the optical system are responsible for the sharpness of fringe troughs. Thus the two results depicted correspond to the two possible causes of fringe distortion discussed in Sec. 6.3.2. The shape of the typical fringes shown in Fig. 6.8(a) conforms well to the predictions of the simple theory of Sec. 6.3.2.

We saw in Sec. 6.3 that if the upper level lifetime of the HCN laser were as long as milliseconds that the laser interferometer should have a severely limited frequency response. But, as the projected plasma decay measurements (Ch. 7) required useful fringe amplitude at rates up to 20 kHz the frequency response of the HCN laser interferometer was of considerable importance. We now describe the results of our investigations of frequency response up to 10 kHz; they were made before we were aware of Peterson and Jahoda's 1971 measurements which show useful modulation response up to 150 kHz. However the present results allow us to make a useful comparison of the theory and experiment and demonstrate the practicability

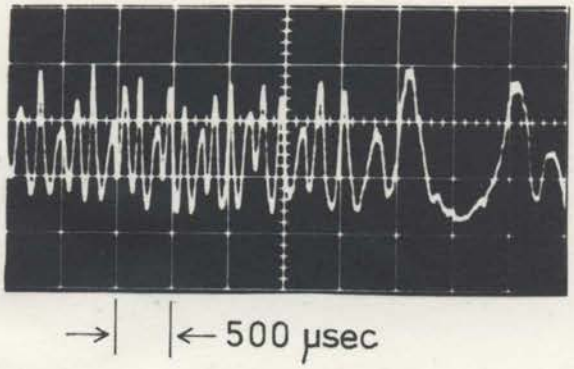

Fig. 6.9. Three pass laser interferometer fringes obtained with the configuration of Fig. 6.6c. The maximum fringing rate shown is of the order of 10 kHz. Although the design of the optical system should prevent all but the three pass beam from re-entering the laser, diffraction effects allow a small proportion of the unwanted beams to enter the laser causing the periodic nonuniformity in fringe height in the figure.

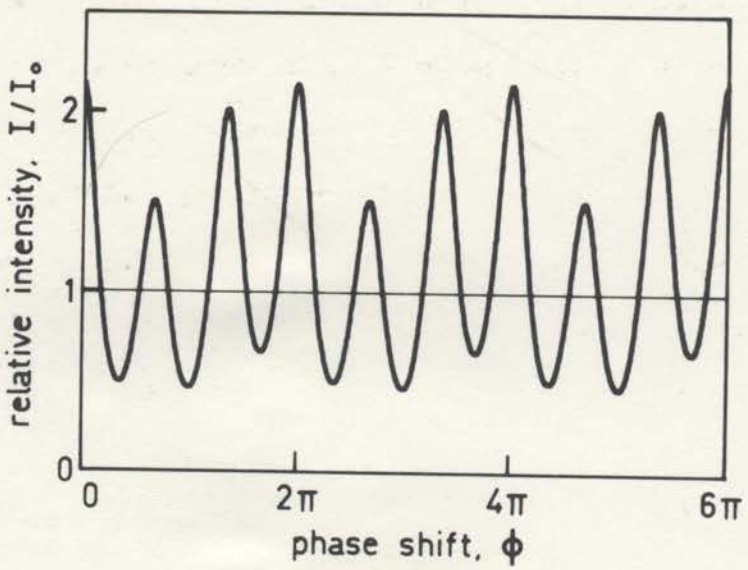

Fig. 6.10. For comparison with Fig. 6.9 this plot shows the expected fringe shape (eq. 6.17) when a small amount of single pass return beam is mixed with the three pass return beam of our multipass system. Note that ϕ is the phase shift of the return beam due to a single (back and forth) pass of the return system.
Parameter values: $(1 + \beta I_o)/\beta I_o = 2$, $T/(L + T) = 0.5$, $\varepsilon_1 = 0.1$, $\varepsilon_3 = 0.3$, $\phi_1 = 50^o, \phi_3 = 0$.

of using multipass techniques with the HCN laser interferometer to obtain increased sensitivity. This would be particularly useful for measuring low electron densities especially when probing over short pathlengths.

With the arrangement of Fig. 6.6(b) it was readily established that the frequency response of the HCN laser interferometer was flat up to a fringing rate of 3.5 kHz, a limit imposed by unsteady motion of the loudspeaker cone at higher frequencies. However, by using the multipass system of Fig. 6.6(c), in which the 337 μm beam was reflected back and forth three times in the external cavity, fringing rates up to 10 kHz were obtained with the same moving mirror. The design of such multipass systems has been described elsewhere (Heckenberg and Smith, 1971). Figure 6.9 shows fringes generated in one half cycle of mirror motion in such a system operating at its limit. These measurements indicate a flat response up to 10 kHz. The variation in the sizes of successive fringes results from the fact that the technique used to isolate the beam returning after three passes of the optical system from those which had made only one or two is not completely effective at this long wavelength because of diffraction. The fringe shape expected when the signal returned to the laser has a single pass component one third the amplitude

of the triple pass component has been calculated from eq. 6.17 and is shown in Fig. 6.10. For this combination of single pass and triple pass components the theory predicts fringe shapes which are similar to the experimental record of Fig. 6.9. Thus the operation of this three-pass system is well described by our simple theory.

6.5 Summary

In this chapter we have described a simple theory of loss-modulation of a laser and an experimental evaluation of several laser interferometer configurations based on our CW 337 μm HCN laser (Ch. 2). We have been able to test some of the predictions of the theory experimentally. The most important results of this work are summarized below:

(a) Laser Interferometer Fringe Shape

Our theory predicts two major sources of fringe distortion in laser interferometers - that due to the intrinsic non-linearity of the laser itself and more commonly, that resulting from multiple reflections in the return system. Using our HCN laser interferometer we have observed fringe shapes which are in good agreement with the predictions of the theory. When the non-linearity of loss-modulation of the laser dominates the fringes are peaked upwards (i.e. in direction of increasing laser output power; see Fig. 6.2) but when Fabry-Perot action in the external cavity is dominant the fringes are peaked downwards.

(b) Laser Interferometer Fringe Size

Our theory indicates that under most circumstances the size of laser interferometer fringes is comparable with

those produced by conventional interferometers using the same laser as source.

(c) Laser Interferometer Frequency Response

The frequency response of the laser interferometer is fundamentally limited by the high Q of the laser resonator. The presence of the active medium lowers the cutoff frequency, the effect being particularly severe for a laser operating near threshold. In the case of molecular lasers such as the HCN laser the lifetimes of the laser levels appreciably exceed the decay time of photons in the laser cavity. This leads to the prediction of a strongly peaked frequency response.

Experiments on an HCN laser interferometer reported elsewhere show no apparent deviation from a flat modulation response up to a fringing rate of 150 kHz. This is somewhat higher than the frequency at which the response is predicted to begin rising, assuming a lifetime of 10^{-5} sec for the upper laser level. It is desirable that further measurements be made at higher fringing rates to resolve this question. In any case, the observed response is adequate for most plasma afterglow measurements.

We have found that our HCN laser interferometer has a flat frequency response up to 10 kHz, which was the

limit of measurement.

(d) Practical Laser Interferometer Configurations

We have investigated the performance of two basic HCN laser interferometer configurations and a multipass version of one of these. We have found that a laser interferometer using hole-output coupling at one end of the laser and an external beamsplitter to monitor the laser output level (Fig. 6.6(b)) should be a practical proposition for plasma diagnostics. This basic configuration is readily modified for multipass operation (Fig. 6.6(c)) which can be used to obtain a worthwhile improvement in sensitivity. An HCN laser using output coupling holes in both mirrors is unsuitable for use in a laser interferometer configuration.

We now proceed (Ch. 7) to describe the use of a 337 μm laser interferometer for measuring electron densities in a decaying helium plasma. We shall see that in addition to the advantages predicted in Sec. 6.2 the HCN laser interferometer configuration has unexpected advantages in its immunity to unwanted plasma effects on the probing beam.

Chapter 7

APPLICATION OF 337 μm DIAGNOSTICS TO A DECAYING HELIUM PLASMA

7.1 Introduction

In this chapter we describe the use of the 337 μm laser interferometer system (Ch. 6) for measuring electron densities in a decaying helium plasma, in the range from 2×10^{12} cm^{-3} to 10^{14} cm^{-3} for an effective path length of 150 cm. The plasma was prepared in the Wills Plasma Physics Department's SUPPER I source ("Sydney University Plasma Physics Experimental Rig" - No. 1).

Although in principle 337 μm interferometry allows measurements up to the cutoff density of 9.8×10^{15} cm^{-3} we will see that the refractive effects of the plasma (beam bending and focusing) are complicating factors at high densities, especially when probing over a long path-length. The SUPPER I plasma demonstrates these difficulties admirably, as well as allowing comparison of the performance of the laser interferometer with that of conventional interferometers using the 337 μm laser as source, and the observation of Faraday rotation of the 337 μm beam when propagating parallel to a strong (9 kG) magnetic field.

Because of its importance in the present chapter, and because the decay of the SUPPER I helium plasma is studied in detail in Ch. 8, we begin with a brief description of the plasma source and the method of plasma preparation.

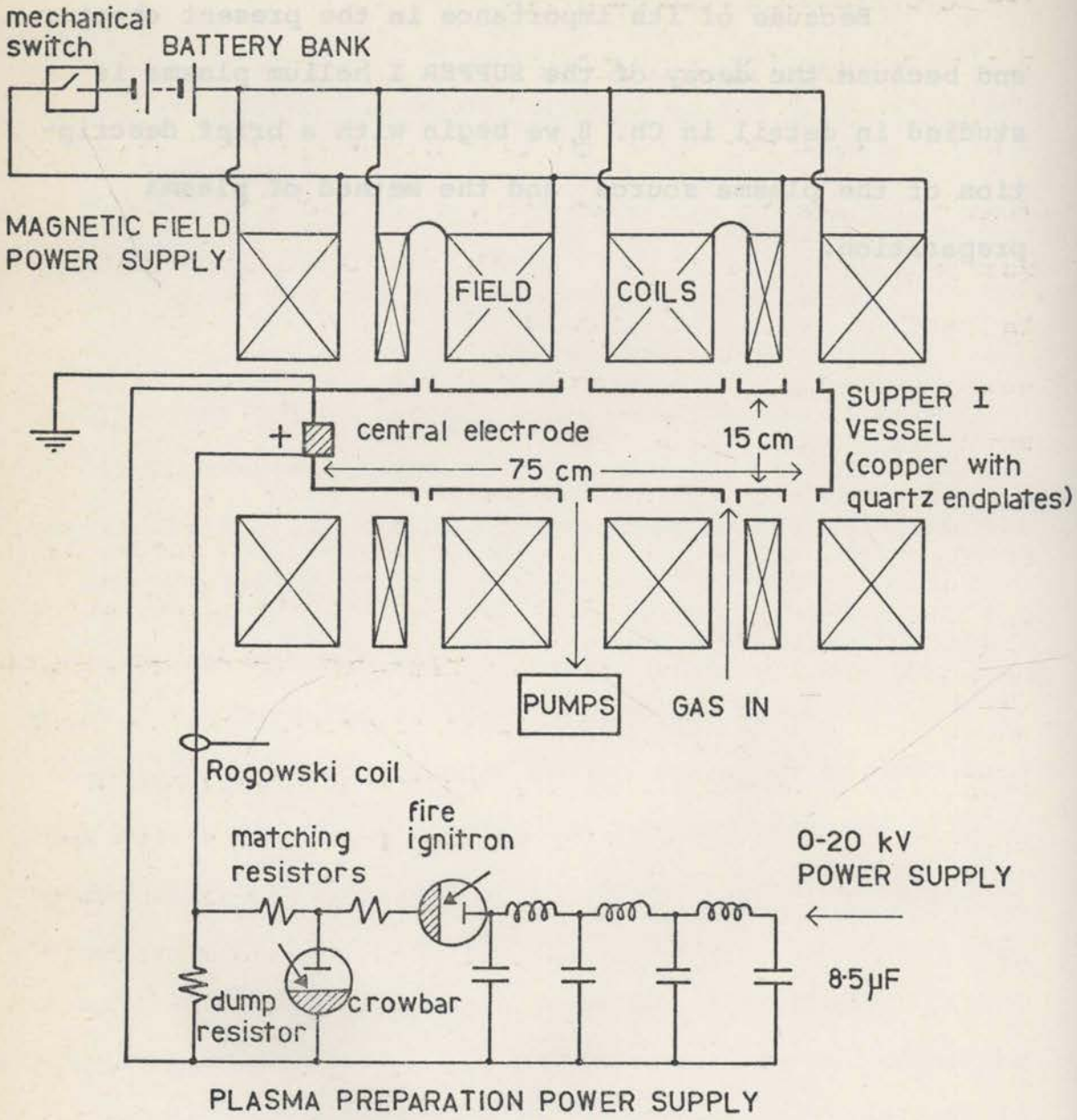

Fig. 7.1. Schematic diagram of the SUPPER I plasma source showing the magnetic field solenoid and supply, the copper vessel with portholes and the plasma preparation power supply.

7.2 The SUPPER I Plasma Source

7.2.1 Description of Machine

The SUPPER I vessel is a copper cylinder 15 cm in (inside) diameter and 75 cm long, sealed at both ends by quartz plates (Fig. 7.1). A number of portholes are included to allow observations of the plasma inside and to enable connections to be made with the pumping, gas inlet and pressure gauging systems. All seals are made with neoprene O-rings. A more detailed description (Brennan et al, 1963) has been published elsewhere. The vessel is evacuated through a 4 cm diameter port at its axial centre by a pair of 5 cm diameter oil diffusion pumps operated in parallel via a freon cooled baffle to prevent silicone oil entering the vessel. A rotary mechanical pump backs the diffusion pumps and can also be used for roughing out the system at high pressures. This pumping system is capable of maintaining a base pressure of 2×10^{-2} mtorr which is a factor of 5000 below the gas pressures typically used for plasma preparation. Helium gas is admitted to the plasma vessel continuously, its flowrate (about 1 ℓ-torr/sec) being adjusted to balance the pumping rate at the operating pressure (100 mtorr). As the machine is fired only about once per minute each plasma is produced from a completely *new charge of gas*. Commercial grade helium is used but

measurements of plasma decay rates (Heckenberg, 1972) indicate that passing the helium through liquid air traps makes no detectable difference. However plasma preparation does liberate impurities from the vessel walls, including hydrogen which is useful for diagnostic purposes. The gas pressure is monitored by three Pirani gauges, an ionization gauge and an Alphatron gauge, all of which are calibrated periodically against a McCleod gauge. In the intervening periods their agreement indicates that their calibrations have not drifted more than a few percent.

The vacuum vessel is surrounded by a water cooled solenoid which provides a uniform (± 4%) magnetic field of up to 10 kG for a period of about a second while the plasma is prepared and decays away. The solenoid is energized by a bank of 120 diesel engine starting batteries which can supply up to 5000 A for a few seconds at a time. The first step in the plasma preparation sequence is the closing of a mechanical circuit breaker which completes the field circuit. The inductance of the field solenoid causes a delay of about 1 sec before the field reaches its steady value. At this point the plasma preparation power supply is triggered ("fire" ignitron) and a shock front propagates along the vessel forming the plasma. Just before the shock front reaches the end of the vessel the "crowbar" ignitron is triggered and after a further 0.5 sec the magnetic field

circuit is opened.

7.2.2 Plasma Preparation

The plasma described in this thesis was prepared by the so-called "$\underset{\sim}{J} \times \underset{\sim}{B}$" process (Brennan et al, 1963) which is a particularly suitable preparation method when a large magnetic field is available. In this method a constant current source consisting of a bank of 8.5 μF capacitors connected as an artificial line (Fig. 7.1) is discharged between the central electrode and the SUPPER I vessel wall. The ensuing radial current of about 10 kA reacts with the strong (9 kG) axial magnetic field to produce a rotating plasma. At the same time an ionizing shock front travels down the vessel at a velocity of a few centimetres per microsecond. Although the total energy input (430J) exceeds the product (number of atoms x second ionization potential), much of the energy input goes into plasma rotational energy (Alfvén and Wilcox, 1962; Irons, 1965) so that significant second ionization of helium is probably not achieved. The energy required for complete single ionization is 170 J.

The plasma rotational energy is subsequently removed by short circuiting ("crowbarring") the supply just before the shock front reaches the end of the vessel. The plasma turbulence caused by this is seen in framing

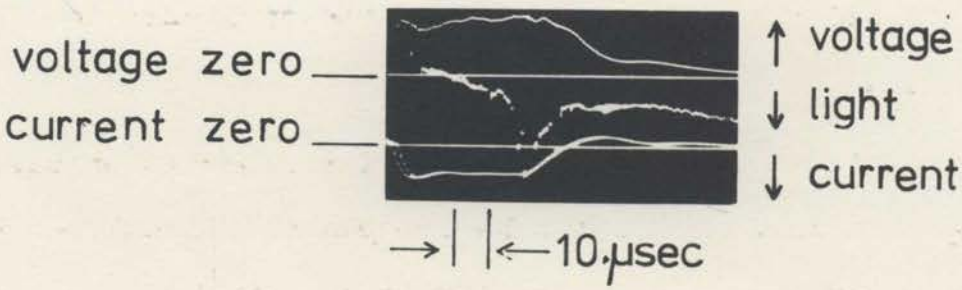

Fig. 7.2. Records of the J x B preparation of the helium plasma; filling pressure 100 mtorr, in a 9 kG magnetic field. The oscilloscope was triggered at the same time as the fire ignitron. The voltage (1000 V/large scale division) was measured with a 1000:1 divider connected between the firing electrode and ground, and the current record (7.4 kA/large scale division) is the integrated output of a Rogowski coil. The effect of crowbarring at 40 μsec is clearly visible.

Also shown is the light signal observed at a side port 68 cm from the electrode end of the vessel. The passage of the shock front (shock velocity 1.7 cm/ μsec) is clearly visible.

camera photographs (e.g., Irons and Millar, 1965) to die away within 100 μsec leaving a quiescent plasma uniformly distributed along the length of the vessel. Crowbarring the preparation capacitor bank before the front reaches the end of the vessel also serves to reduce erosion of the endplate and the consequent liberation of impurities into the plasma.

Figure 7.2 shows records of the plasma preparation voltage and current for the helium plasma. Breakdown occurs within a few microseconds of the triggering of the fire ignitron (Fig. 7.1). The voltage on the electrode drops rapidly to a value of a few thousand volts (the "burning voltage") which remains constant while the shock front is propagating and which represents the back EMF of the rotating plasma. A resistor is included in the preparation circuit so that the total impedance seen by the pulse line is equal to its characteristic impedance. The voltage and current waveforms show the effect of firing the crowbar ignitron quite clearly. The electrode-wall voltage falls away as the plasma rotational velocity decreases, the plasma dumping its rotational energy by feeding current to the crowbar load. If the plasma is not crowbarred the curren decreases rapidly at the end of the preparation line pulse, without reversing direction, and the voltage decays slowly as the plasma rotation runs down because of viscous losses.

Since, while the plasma is rotating, it tends to be "centrifuged" towards the vessel walls uncrowbarred plasmas tend to exhibit a pronounced central hollow. The turbulence introduced by crowbarring tends to distribute the plasma more uniformly across the diameter of the vessel. The light received by a photodiode 68 cm from the electrode end of the vessel is also shown in Fig. 7.2. The passage of the ionizing shock front is clearly visible.

Study of such records together with those of a microwave interferometer measuring the late decay of the plasma allowed the shot-to-shot and experiment-to-experiment reproducibility of the plasma to be checked. Perturbations of the plasma preparation due to holes drilled in the end-plate supporting the firing electrode were soon discovered this way (Sec. 7.3.1).

7.2.3 Properties of the Helium Plasma

Electron density measurements made in the SUPPER I helium plasma prepared under the conditions described in Sec. 7.2.2 (Heckenberg, 1972) indicate an initial electron density in much of the plasma nearly equal to the pre-discharge gas atom number density. This leads to two conclusions. Firstly, since the energy required for second ionization ($\simeq$ 54 eV) is much larger than that required to form a singly charged helium ion ($\simeq$ 25 eV),

and since much of the plasma preparation energy goes into rotational energy which is subsequently lost, we conclude that the plasma consists of electrons, singly charged He^+ ions, and neutral helium atoms. Secondly, since the electron temperature (see Ch. 8) at times of interest is never greater than 10^4 K we know that collisional attenuation of a 337 μm probing beam will never be significant (see Sec. 3.2.1 and Table 3.1). Thus the only property of interest in our 337 μm wave propagation experiments is the electron density of the helium plasma.

Measurements made by Heckenberg (1972) indicate that the SUPPER I helium plasma is very nearly uniform along its axis for times as early as 100 μsec and as late as 2000 μsec after plasma preparation. Because of this uniformity, interferometric measurements made along lines parallel to the vessel axis (which give average densities along these lines) may be used as plasma density measurements without correction. By using 3.39 μm multipass (He-Ne) laser interferometry, and Stark broadening of the Hβ line emitted by hydrogen present as an impurity, Heckenberg was able to measure electron densities from 3×10^{15} cm^{-3} down to 10^{14} cm^{-3}. These measurements suggested the existence of a central electron density "hollow" at early times without being able to provide a clear picture of the plasma on axis. Use of the 337 μm

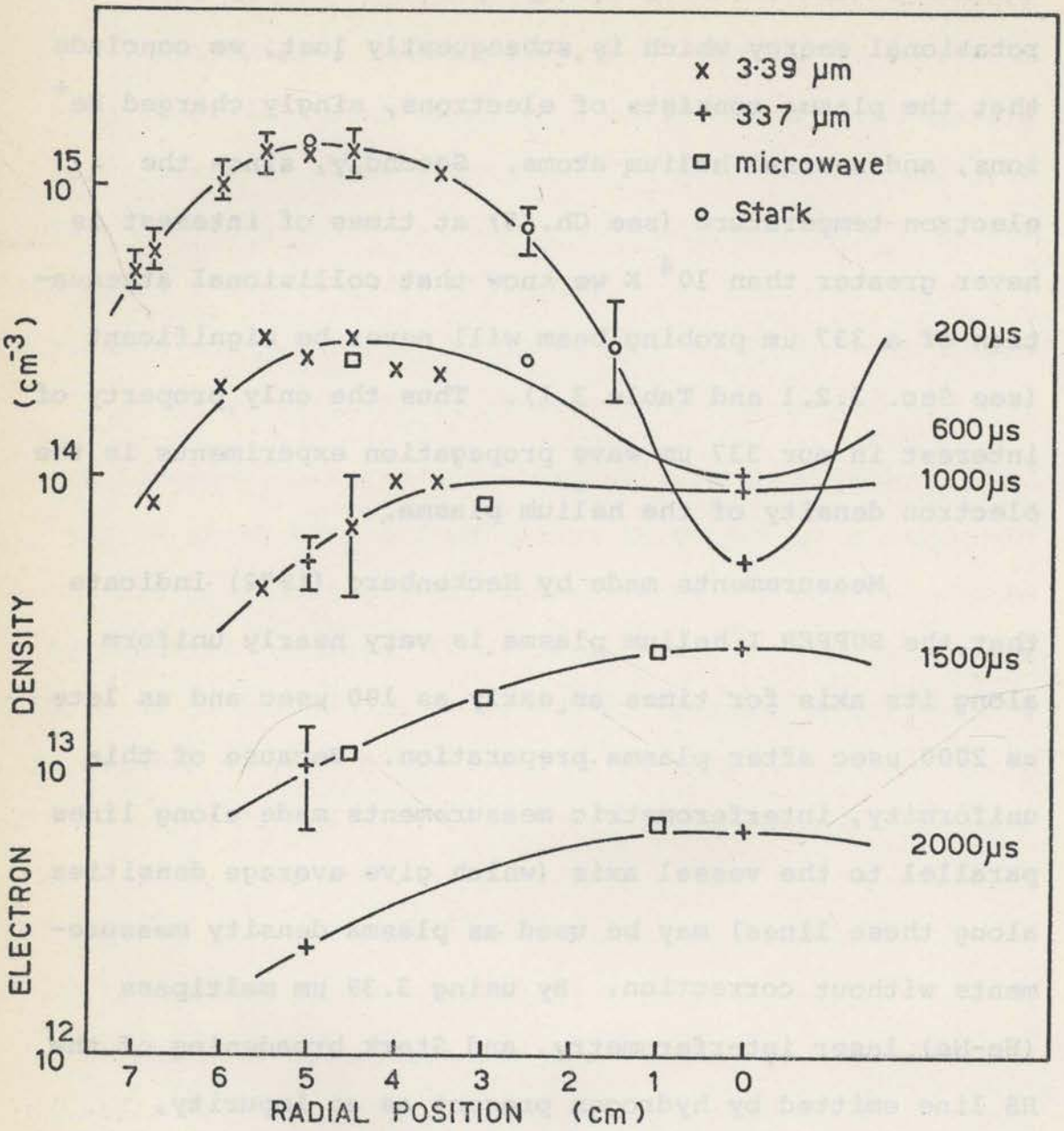

Fig. 7.3. Electron density profiles of the decaying Helium plasma (after Heckenberg, 1972). It is evident that without the information provided by 337 μm interferometry the detailed form of these profiles would be unclear.

laser interferometer described in Sec. 7.3.1 and some microwave reflection techniques (Heckenberg, 1972) provided electron density measurements in the range from 10^{14} cm^{-3} down to 10^{12} cm^{-3}. These measurements allowed the radial electron density profiles shown in Fig. 7.3 to be built up. All the measurements were made at positions spaced along a horizontal radius of the plasma vessel.

Measurements of the intensity of light emitted by the plasma (Heckenberg, 1972) show that the plasma is symmetric about its axis. Thus Fig. 7.3 shows that immediately after preparation the plasma exhibits a pronounced hollow near the axis where the electron density is over an order of magnitude smaller than it is nearer the vessel wall. The diameter of the hollow corresponds to that of the firing electrode. One is thus led to conjecture that the current flowing to the shock front flows from the sharp edges of the electrode, parallel to the magnetic field so that little heating or ionization occurs near the vessel axis. As time passes however, the density on axis rises slowly while the bulk of the plasma is decaying, until at about 1100 μsec after breakdown a fairly uniform radial distribution results. After that time the central density falls away at a rate comparable with that of the rest of the plasma so that the shape of the distribution does not change markedly.

With this background information we now proceed to describe the 337 μm diagnostics and the propagation of 337 μm radiation through the SUPPER I helium plasma in some detail. We shall study the decay of the helium plasma in Chapter 8.

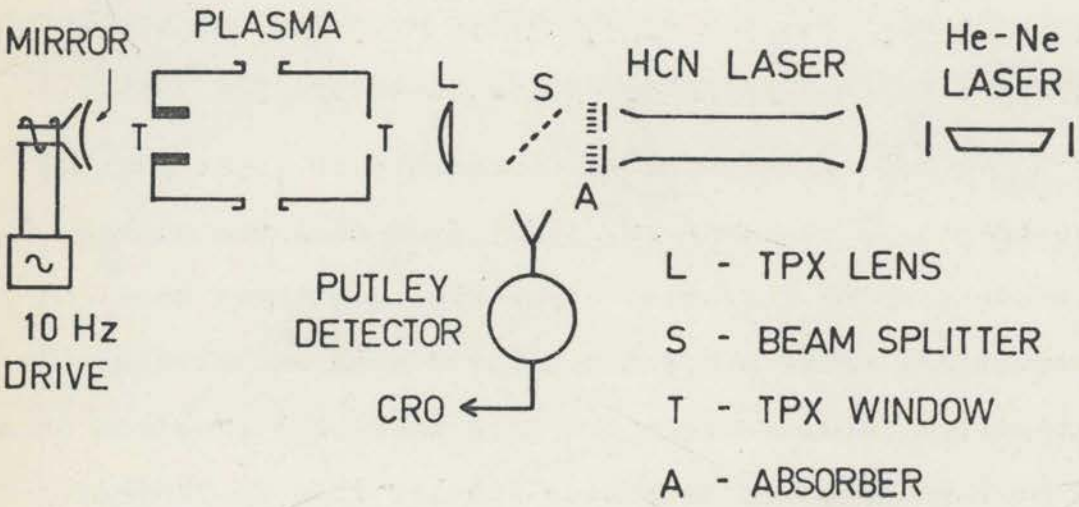

Fig. 7.4. Schematic diagram of the 337 μm HCN laser interferometer used to measure the electron density on and 5 cm from the axis of the SUPPER I plasma source. The optical system was aligned with a He-Ne laser beam shining through a pinhole in the aluminized surface of the right-hand HCN laser mirror.

7.3 Electron Density Measurements with the 337 μm Laser Interferometer

7.3.1 Experimental Setup

The interferometer configuration (Fig. 7.4) used in our measurements on the SUPPER I helium plasma was an extension of the bench setup of Fig. 6.6(b) described in Chapter 6. The moving mirror was retained to allow rapid optimization of the optical system before a plasma shot, the frequency of the fringes generated being sufficiently low that it was not necessary to stop the return mirror prior to plasma preparation. The HCN laser and its associated optical system (Fig. 7.4) were rigidly mounted on an aluminium girder frame resting on partially inflated scooter inner tubes which effectively isolated the system from vibration emanating from the pumping systems. A TPX collimating lens coupled the divergent (diffraction limited) output beam of the laser through the plasma vessel to be reflected from the return mirror back through the plasma and optical system to the laser, where its re-entry caused modulation of the output level. A 50 μm thick mylar beamsplitter coupled part of the laser output into the Putley detector. Since the TPX lenses and windows used are transparent to visible light and, furthermore, since the lenses have the same focal length in the visible as in the far-infrared it was possible to use a 633 nm He-Ne

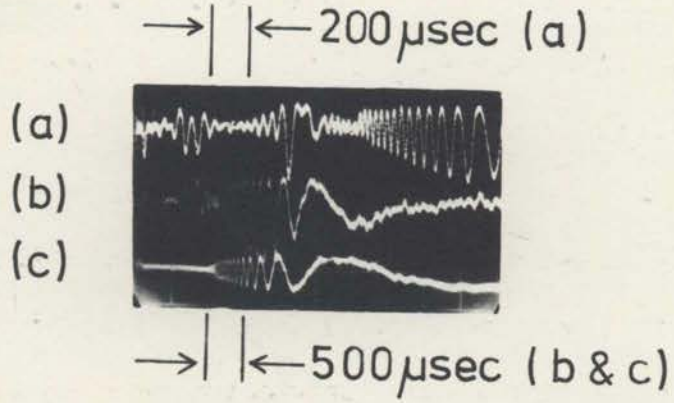

Fig. 7.5. HCN laser interferogram obtained when probing along the axis of the SUPPER I helium plasma. Plasma preparation occurs in the first 50 μsec. Traces (a) and (b) (different timebases) show the Putley detector response to the 337 μm laser interferometer output. Trace (b) was triggered one small division (100 μsec) before the graticule zero. Trace (c) is the output of a 2.5 mm microwave interferometer operating across the SUPPER I vessel (Fig. 7.7).

laser beam passing through a pinhole in the aluminized surface of the far laser mirror for preliminary alignment.

Measurements were made at two radial positions: on the axis of the vessel, and 5 cm from the axis. Holes drilled in the vessel endplates were fitted with TPX windows to allow passage of the 337 μm beam, while the tubular central electrode was itself fitted with a 2 cm diameter TPX window to allow measurements to be made in the central density hollow which had been indicated by earlier measurements (Sec. 7.2.3). The hole drilled at r = 5 cm in the endplate supporting the electrode was restricted to a diameter of 1.25 cm to avoid perturbing the plasma preparation. When a larger hole was tried, severe erosion of the TPX window occurred, the resulting liberation of impurities affecting the plasma preparation. However, 4 cm diameter holes were used in the other endplate without any adverse effects on the plasma being observed.

7.3.2 Electron Density Measurements

Figure 7.5 shows a typical experimental record made on the axis of the vessel. Traces (a) and (b) (different time scales) are the Putley detector response to the output of the laser interferometer. The fringes indicate the varying phase of the 337 μm probing beam as the plasma decays. Trace (c) is the output of a 2.5 mm

microwave interferometer (operating across a diameter of the vessel) which was used throughout all the measurements described, to monitor the reproducibility of the plasma. The 337 μm fringes show a marked variation in amplitude with time. We have already ascertained (Sec. 7.2.3) that attenuation of the 337 μm beam will always be negligible but there are two other effects which could account for this type of behaviour. These are plasma focusing by the strong radial electron density gradient at the axis of the vessel (Fig. 7.3), and Faraday rotation of the probing beam which is propagating parallel to a 9 kG magnetic field. In fact we will see in Sec. 7.4.3 that the laser is effectively modulated even when the return beam polarization is at right angles to the laser output polarization. Thus the time-variation in fringe amplitude apparent in Fig. 7.5 is not caused by Faraday rotation. In Sec. 7.3.3 we shall show that it results from plasma focusing of the 337 μm beam probing the plasma.

Since the electron density is always much less than the cutoff density ($n_c = 9.8 \times 10^{15}$ cm^{-3}) for 337 μm radiation the phase shift due to a double passage through the plasma (d = 150 cm) varies linearly with the electron density. Thus we have (from eq. 3.21),

$$n_e = 2.2 \times 10^{12} \frac{\Delta\Phi}{\pi} \text{ cm}^{-3} \qquad 7.1$$

3,39μm
337μm
2,5mm
average electron density (cm^{-3})
10^{14}
10^{13}
10^{12}
0
1
2
3
time (ms)

where Φ is the plasma phase-shift at any instant of time. Use of this relation allows the variation of electron density with time to be plotted as in Fig. 7.6. The interferogram (Fig. 7.5) indicates that at a time of 900 μsec after breakdown the density versus time curve passes through a stationary value and the sense of change before that time is not uniquely determined. This problem is resolved by the observation that when the phase is changing monotonically each fringe will simply represent a 2π change. However, should the phase change rise to a maximum value $2n\pi + \phi$ and then decrease again there will result n fringes during the rise, a small fringe of relative amplitude cos ϕ, and then a further n fringes during the fall. Such a small fringe is often observed in the experimental record, shot-to-shot variations in the peak density causing its appear-

---

Fig. 7.6 (Opposite). Average electron density on the axis of the SUPPER I helium plasma as a function of time. The 337 μm laser interferometer results are represented by circles. At late times each successive point corresponds to a phase change of π (half a fringe) while at earlier times many of the available points have been omitted to avoid cluttering the figure. Horizontal error bars denote the experimental uncertainty in the time at which a particular phase shift occurred : this uncertainty is mainly the result of shot-to-shot variation. The vertical error bars on the 337 μm results indicate an uncertainty of up to $\pm \pi/2$ which results from the difficulty involved in estimating the phase shift in the return path when the plasma has completely decayed. Measurements made by three pass 3.39 μm interferometry and 2.5 mm microwave reflection interferometry (Heckenberg, 1972) are also shown.

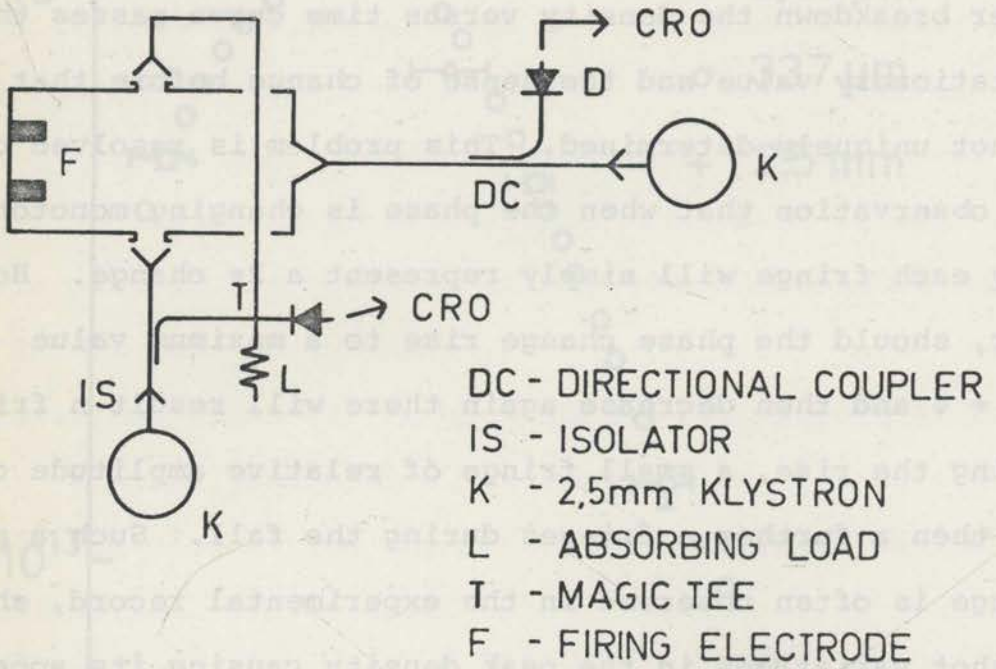

Fig. 7.7. 2.5 mm microwave diagnostics used to measure electron densities in the SUPPER I helium plasma. A conventional interferometer operating radially across the vessel was used to monitor the reproducibility of the plasma. Estimates of electron density on axis (2.5 mm points of Fig. 7.6) were obtained using the configuration operating along the vessel axis. Here signal reflected from the firing electrode interfered with a reference wave reflected at the horn-endplate mismatch.

ance to vary somewhat.

Regarding the accuracy of these measurements, apart from an uncertainty of up to $\pm 10^{12}$ cm^{-3} (one quarter fringe) resulting from the difficulty in estimating the phase shift in the return path when the plasma has completely decayed the shot-to-shot variation of the plasma itself was the limiting factor. Of course since the exact form of the axial distribution of plasma density cannot be determined to such accuracy the density at any point in the plasma is not so well determined.

Figure 7.6 also shows estimates of the electron density on the axis of SUPPER I made previously (Heckenberg, 1972) by 3.39 μm multipass interferometry and 2.5 mm microwave reflection interferometry. Although both methods gave results in good agreement with those obtained with the 337 μm interferometer, the three pass 3.39 μm interferometer was working at the limit of its sensitivity and the microwave measurements suffered from uncertainty as to precisely what region of plasma was being probed because of the pronounced diffraction of the long wavelength radiation. The 2.5 mm results were obtained by measuring the phase shift of radiation reflected by the electrode back to a transmitting horn at the other end of the vessel by means of the microwave circuit of Fig. 7.7. The reference wave required for operation as an interferometer

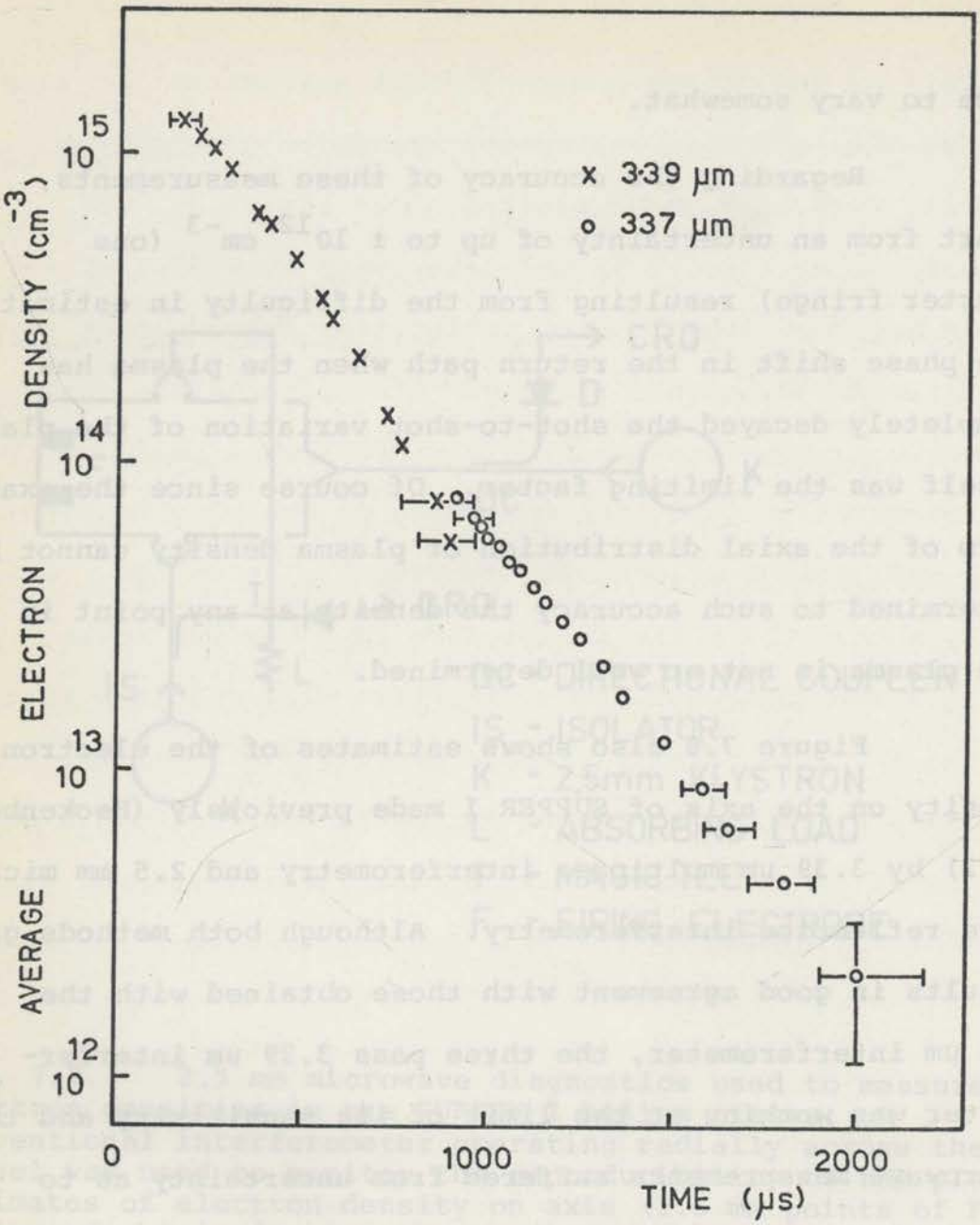

Fig. 7.9. Electron density versus time at a position 5 cm from the axis of the $\tilde{J} \times \tilde{B}$ prepared helium plasma. Multipass 3.39 μm interferometer results (Heckenberg, 1972) are shown together with measurements made with the HCN laser interferometer.

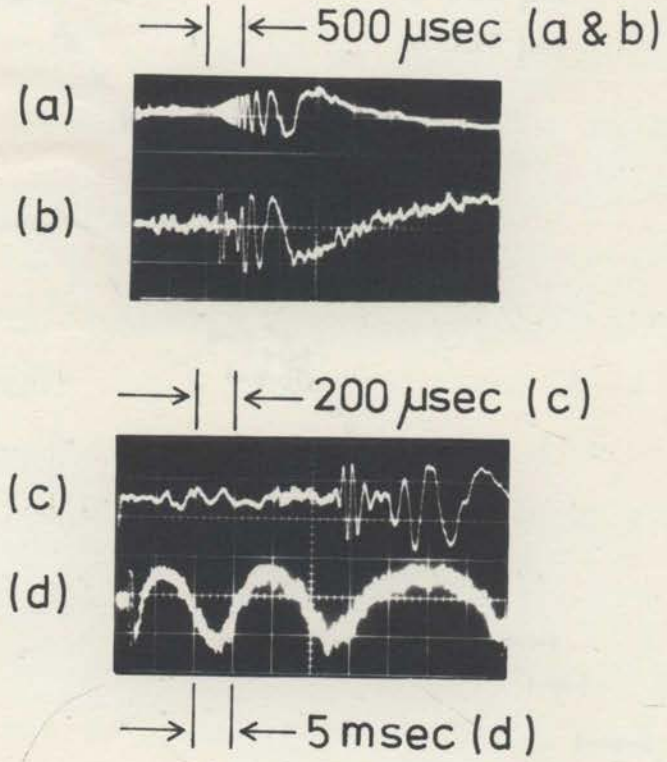

Fig. 7.8. HCN laser interferogram obtained when probing 5 cm from the axis of the SUPPER I helium plasma. The four records are for the same plasma shot. Trace (a) is the 2.5 mm microwave interferometer output. Traces (b), (c) and (d) are the HCN laser interferometer output displayed on different timebases. In (d) the phase variation resulting from the motion of the return mirror is visible. The plasma fringes occur in the first half division of this trace.

was provided by the power reflected at the horn/endplate mismatch. Note that the microwave interferogram shown in Fig. 7.5(c) was not the output of such an instrument but rather that of a conventional 2.5 mm interferometer (Fig. 7.7) operating radially half way along the length of the vessel.

Figure 7.8 shows interferograms obtained 5 cm from the vessel axis in the same helium plasma. The signal from the Putley detector is shown on a number of different timebases and on the slowest (5 ms/large scale division) the fringes generated by the moving return mirror are visible. Electron densities derived from these results are shown in Fig. 7.9, together with the results of earlier 3.39 μm laser interferometer measurements (Heckenberg, 1972). Quite good agreement is obtained. Examination of the interferogram of Fig. 7.8 raises an interesting point. We have already pointed out (Sec. 7.2.3) that absorption of the 337 μm beam by the SUPPER I helium plasma will always be negligible so that it is not immediately obvious why no 337 μm fringes are observed before about 900 μsec after breakdown at this radius. Since such fringes would have appeared at a high frequency it was necessary to establish whether this absence of observable fringes was due to laser interferometer bandwidth limitations or were the result of some plasma effect.

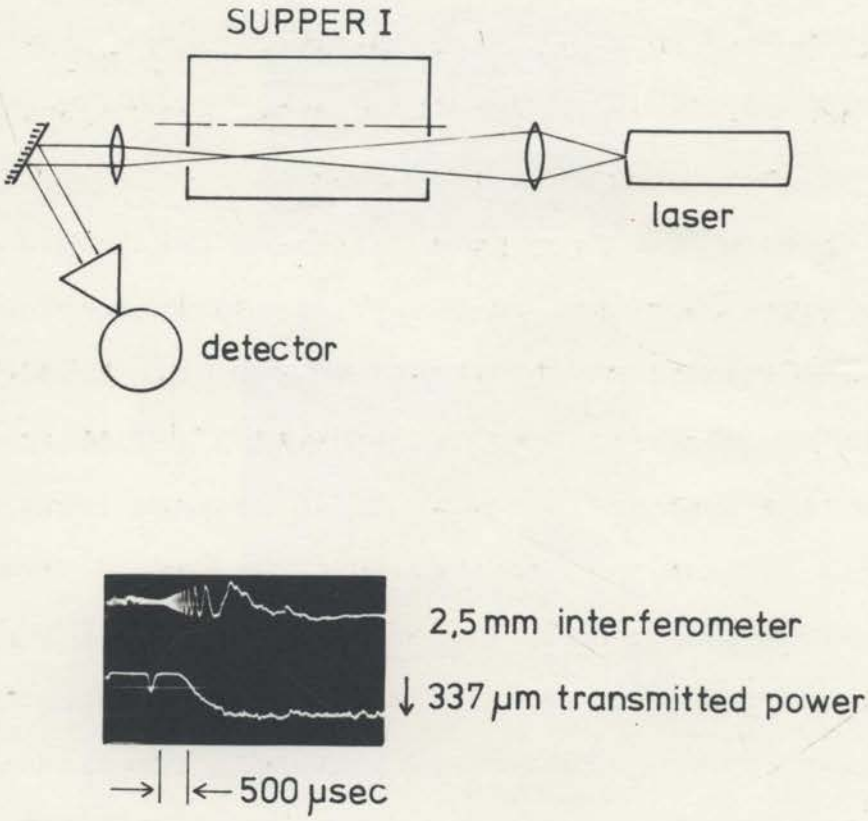

Fig. 7.10. Schematic diagram of the optical system used to measure the transmission of 337 μm radiation propagating 5 cm from the vessel axis. The laser output is focused as a spot falling on the vessel exit window. Plasma electron density gradients deflect the spot, varying the power reaching the detector. An experimental record is shown below. The upper trace is the output of the 2.5 mm interferometer monitoring plasma reproducibility. The lower trace is the time-varying 337 μm power reaching the detector.

To ascertain whether the plasma affects the intensity of the signal returned into the laser it is desirable to measure directly the amount of power returned after passing twice through the plasma. However, because of diffraction, it is difficult to avoid return beam modulation of the laser while making such a measurement. To avoid such effects the power reaching the return mirror after a single pass through the plasma was measured by siting the detector at the return mirror end of SUPPER I (Fig. 7.10). The mirror was re-positioned so as to reflect the transmitted beam into the detector horn and so no 337 μm power was returned into the laser. The results obtained (Fig. 7.10 (lower)) show that the presence of the plasma has a very strong effect on the amplitude of the return beam. Thus the variations observed in fringe size with time cannot simply be attributed to laser frequency response effects. Rather, they result from bending effects of the radial electron density gradients known to be present. We now consider these effects in detail.

7.3.3 Plasma Beam Bending and Focusing

It was shown in Sec. 4.4.1 that in the paraxial approximation, which is appropriate here, a light ray propagating in the z direction through a medium with

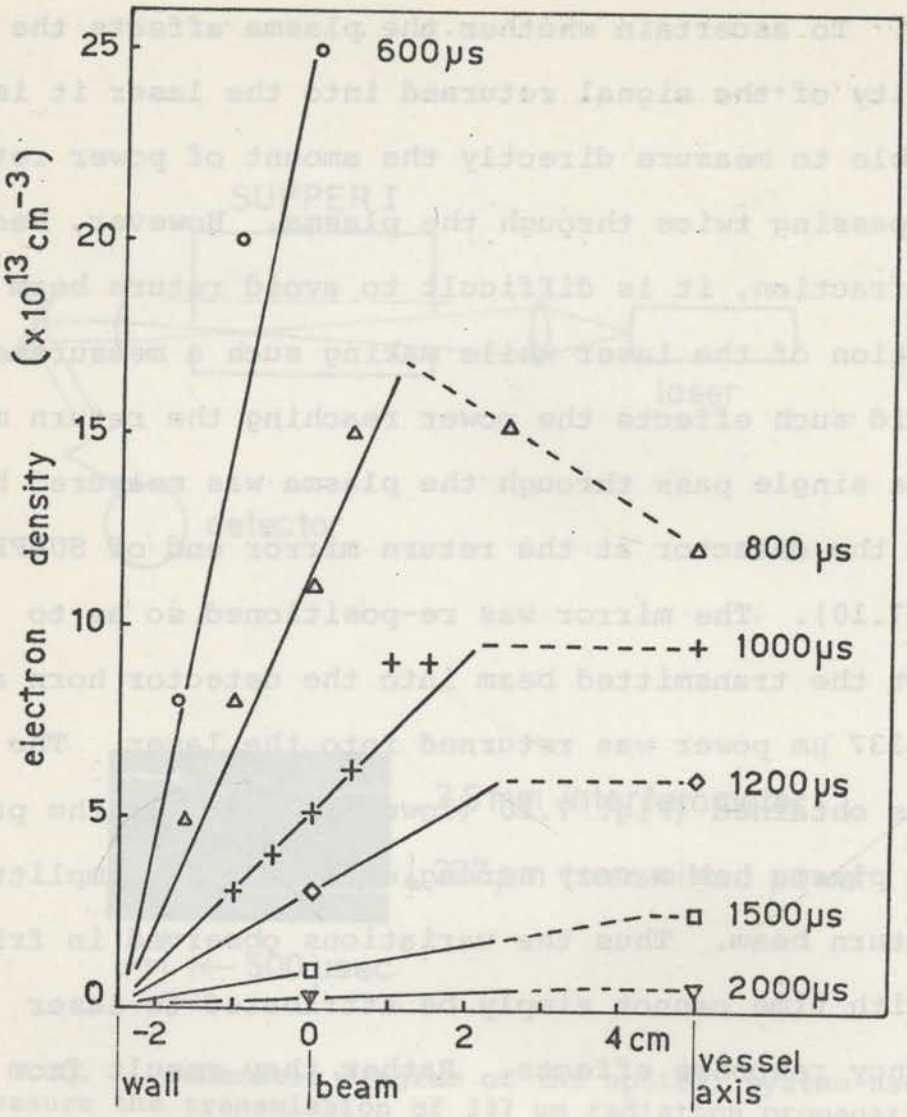

Fig. 7.11. Measurements of the radial distribution of electron density in the SUPPER I vessel (Heckenberg, 1972) which show that it is reasonable to approximate the radial variation in the vicinity of r = 5 cm by a linear relationship (eq. 7.3).

transverse electron density gradient dn/dx is described by the differential equation (eq. 4.5)

$$\frac{d^2x}{dz^2} = -\frac{1}{2n_c}\frac{dn}{dx} , \qquad 7.2$$

as long as the electron density n is much less than the cutoff density n_c. At the r = 5 cm position (and times of interest) in the SUPPER I helium plasma n is never greater than 5×10^{14} cm^{-3} (Fig. 7.3) whereas for 337 μm radiation n_c is 9.8×10^{15} cm^{-3}. Thus eq. 7.2 is applicable. Since the plasma refractive index (eq. 3.18) is quite close to unity the bending of a ray as it enters or leaves the plasma is negligibly small.

Two cases have to be considered corresponding to the two radial positions at which electron density measurements were made with the 337 μm laser interferometer. The simpler case which is treated first is at a position 5 cm from the axis of SUPPER I. Figure 7.11 shows electron density measurements at various radii plotted on a linear scale to demonstrate that near 5 cm from the vessel axis the electron density may be approximated by the linear relationship

$$n = n_o (1 + \beta x) \qquad 7.3$$

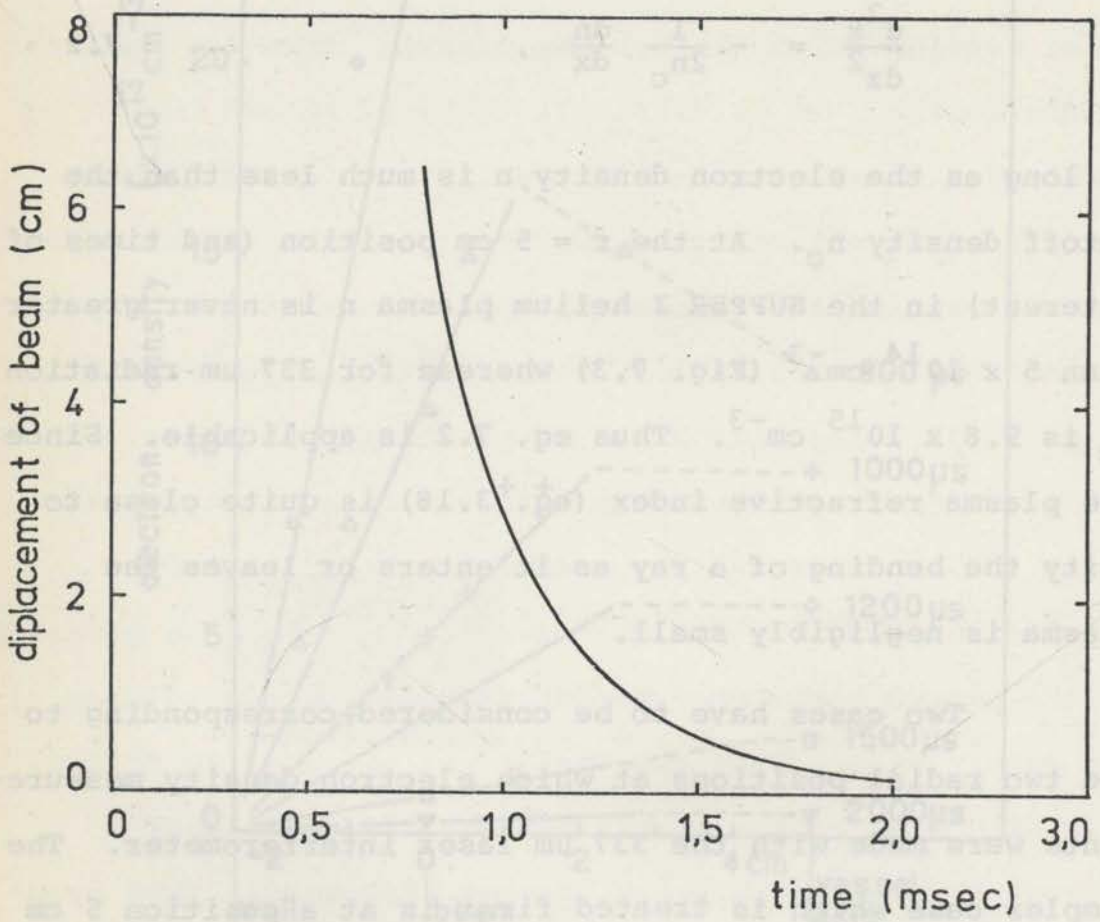

Fig. 7.12. Deflection of the 337 μm probing beam towards the vessel wall by the linear electron density gradients of Fig. 7.11. A displacement of more than 2.5 cm means that the beam is bent to strike the vessel wall.

where x is the distance from the r = 5 cm position (positive towards the vessel axis), n_o is the electron density at r = 5 cm, and β has the value 0.4.

Combining eqs. 7.2 and 7.3 gives the differential equation

$$\frac{d^2x}{dz^2} = -\frac{1}{2}\frac{n_o}{n_c}\beta$$

for the path of the probing beam. This has the solution

$$x = -0.1\frac{n_o}{n_c}z^2 \qquad 7.4$$

for a ray entering at x = 0 parallel to the vessel axis. This equation shows that the ray is bent towards the vessel wall by an amount depending on the density gradient (entering the equation here through the value of n_o). The extent of this deflection at the other end of SUPPER I (z = 75 cm) is of critical importance because of the limited area of the TPX beam exit window (only 1.25 cm in diameter).

The density-gradient/time relation depicted in Fig. 7.11 leads to the deflection/time graph of Fig. 7.12, which shows that the deflection of the beam will be quite severe early in the decay of the plasma. Thus, it is clear why the 337 μm interferometer gave no fringes until quite late in the decay when it was set up at this radial

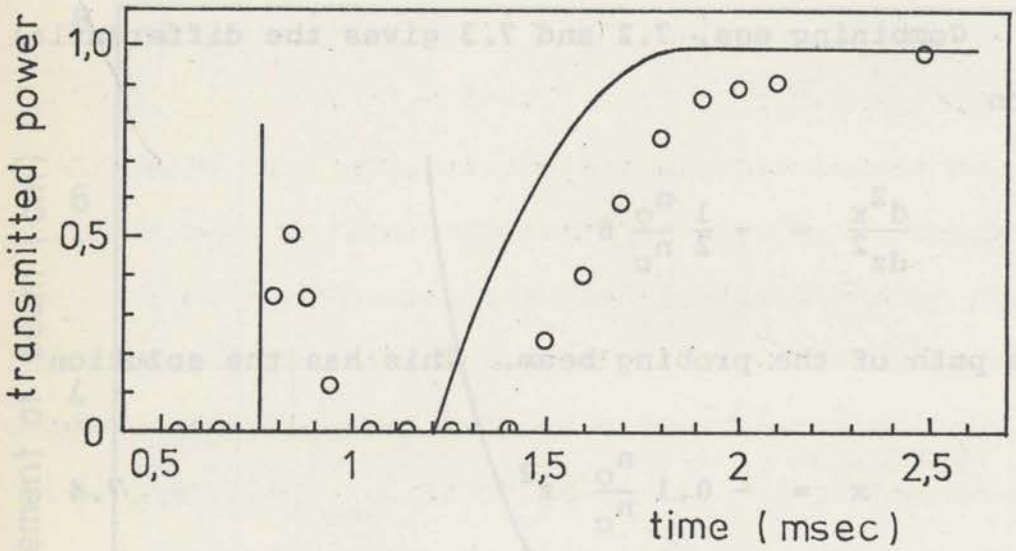

Fig. 7.13. The circles represent the experimental variation of 337 μm power transmitted through the SUPPER I helium plasma at a distance of 5 cm from the vessel axis (Fig. 7.10). The smooth curve shows variation of transmitted power predicted by our simple model. The vertical line indicates the predicted time of transmission of a pulse of 337 μm radiation due to reflection off the SUPPER I vessel wall.

position. This interpretation is confirmed by the results of the transmission experiment already mentioned above. The Putley detector was set up (Fig. 7.10) so as to directly monitor the amount of 337 μm radiation transmitted on a single pass through the plasma vessel. The lenses were adjusted for maximum transmission before the plasma was produced, thus ensuring that the image of the laser output hole (a spot of 1.7 cm diameter) covered the SUPPER I beam exit hole (1.25 cm diameter). When the plasma was prepared, the amount of radiation transmitted dropped to zero for a considerable time, rose to a peak, fell back to zero, and then rose more gradually to its former value before preparation. A typical experimental record is shown in Fig. 7.10.

The spot of radiation falling on the exit hole of SUPPER I will have a considerable spread of intensity at the edges because of diffraction, but this effect is neglected to simplify the analysis. In this case a circular spot of 1.7 cm diameter is displaced from the centre of a 1.25 cm diameter hole by the distance plotted in Fig. 7.12 as a function of time. The transmitted intensity can be taken as proportional to the common area. This results in the smooth curve plotted in Fig. 7.13. The shape of the transition from no transmission to full transmission is well accounted for but the time at which

it occurs is seen to be wrong. The assumption that the 1.7 cm diameter spot was not centred on the small exit hole before the plasma was fired is sufficient to move the theoretical curve up to 150 μsec to the right, into close agreement with the experimental results.

The transmission peak which occurs at about 800 μsec can be explained in the following way. The agreement obtained at late times allows little doubt that the beam is being strongly deflected at the time when the peak appears. This leads to the hypothesis that the beam is so strongly deflected as to hit the copper vessel wall, where it is reflected in such a way as to pass through the exit hole. This would require that the beam strike the wall halfway along its length which from eq. 7.4 requires $n_o = 1.74 \times 10^{14}$ cm^{-3} which from Fig. 7.9 occurs at 750 ± 100 μsec. The fact that the peak actually occurs somewhat later than this is not surprising. The effect of the initial misalignment postulated above would be to cause it to appear later. Besides, the bending of the beam in this case is so extreme as to strain the validity of the approximations used in the analysis.

Having seen that plasma beam bending can account for the observed variation of 337 μm transmitted power at the r = 5 cm position we now turn our attention to the

time-varying amplitude of laser interferometer fringes which was observed when probing the SUPPER I vessel along its axis (Fig. 7.5). It will be shown in Sec. 7.4 that this variation is not caused in any way by Faraday rotation of the probing beam. In fact we find that the behaviour on axis results from the focusing effect of the central density hollow of the plasma. As the detailed shape of this hollow is not well known we assume, for the purpose of estimating focusing effects, that it is parabolic. That is,

$$n = n_o (1 + \alpha r^2) \qquad 7.5$$

where n_o is the electron density on axis and $\alpha (> 0)$ can be estimated from the electron density profiles in Fig. 7.3. (In practice α was estimated from the knowledge of the densities at $r = 0$ and $r = 2$ cm.) Substituting eq. 7.5 into eq. 7.2 we obtain the ray differential equation,

$$\frac{d^2 r}{dz^2} = - \alpha \frac{n_o}{n_c} r$$

which has as solution

$$r = r_o \, \mathrm{Cos} \, (\sqrt{\alpha \, n_o / n_c} \, z + \phi) \, , \qquad 7.6$$

meaning that a ray entering the plasma parallel to the axis

is bent to cross the axis after travelling a "focal length" f given by

$$f = \frac{\pi}{2\sqrt{\alpha\ n_o/n_c}} \quad , \qquad 7.7$$

and crosses again each 2f thereafter. Figure 7.14 shows f plotted as a function of time for the decaying helium plasma under study. Early in the decay while the central hollow is still deep the focal length is considerably shorter than the length of the vessel. It increases continuously, becoming longer than the vessel at about 1000 μsec after plasma preparation.

At very late times the electron density hollow disappears entirely, the profile then having its maximum at the vessel axis. This corresponds to a negative value of α in eq. 7.5 and the solution becomes

$$r = r_o \text{ Cosh } (\sqrt{|\alpha|\ n_o/n_c}\ z + \phi) \quad , \qquad 7.8$$

the ray diverging continuously from the axis. Since the peak density n_o is by this time quite small, the effect at late times is small enough to be neglected.

In order to observe the effects of plasma focusing by the central density hollow a transmission measurement similar to that described above (Fig. 7.10) for

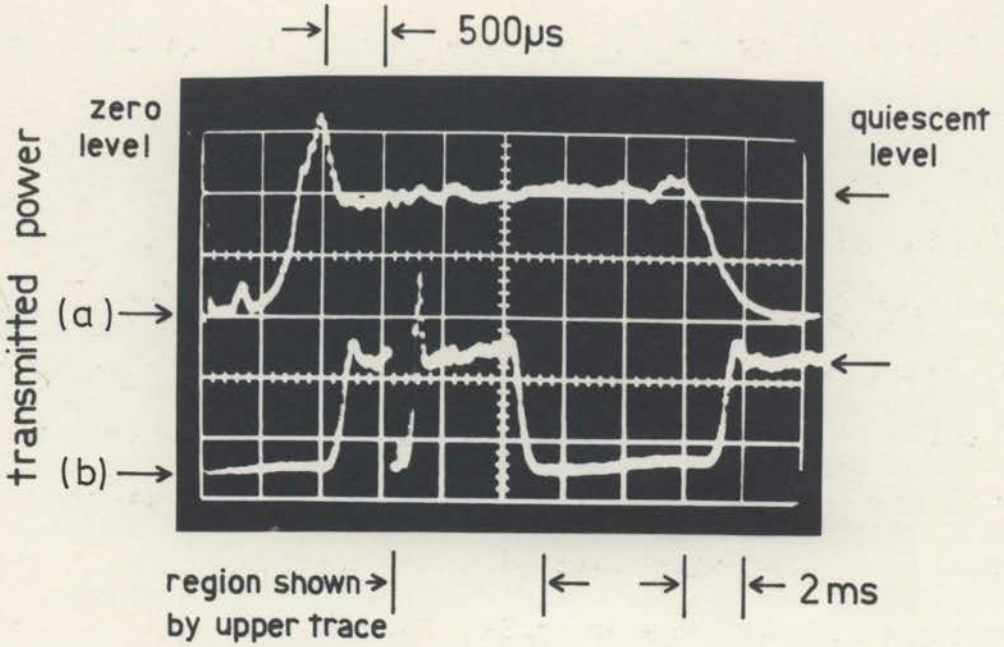
500μs
zero level
quiescent level
transmitted power
(a)
(b)
region shown by upper trace
2ms

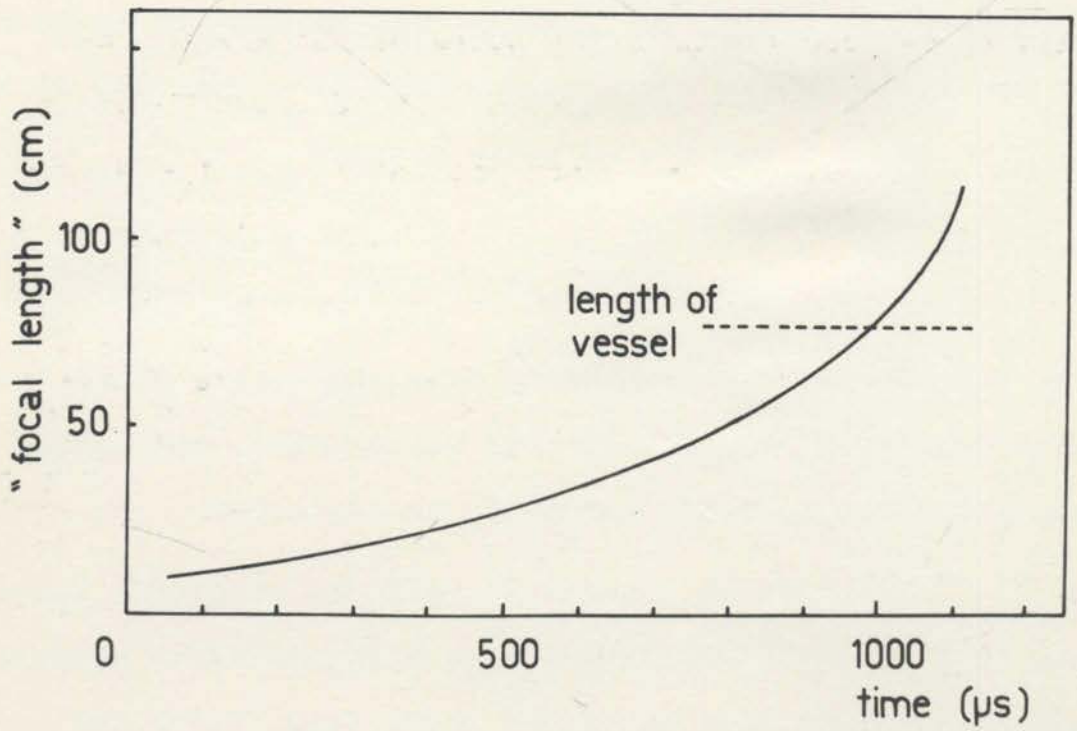
"focal length" (cm)
100
50
0
500
1000
time (μs)
length of vessel

r = 5 cm was made on the axis of SUPPER I. In this case the laser output was focused on the SUPPER I *entrance* window. Two transmission peaks were observed (Fig. 7.14), the major one corresponding in time to a plasma focal length equal to the vessel length. A more variable subsidiary peak corresponded to a plasma focal length of one third the vessel length. That is, in each case maximum signal was detected when the beam leaving the plasma was parallel. A detailed analysis, taking into account the divergence of the beam entering SUPPER I and the limited acceptances of the exit window and detector optical system was unable, however, to satisfactorily account for the fact that virtually no power was detected before 800 μsec. This is because the detector subtended at the SUPPER I exit window an angle greater than the divergence angle of the entering beam. Under our present theory the divergence of the exit beam cannot exceed this value and hence

---

Fig. 7.14 (Opposite). The experimental record shows the 337 μm power transmitted along the axis of the SUPPER I plasma as a function of time (trace (a)). As the detection system was AC coupled the laser beam was chopped (at about 80 Hz - trace (b)) to establish the zero level. The plasma was prepared early in the "on" part of the chopping cycle and decayed before the beam was chopped off. Trace (a) shows the time-varying transmission, beginning at the instant of plasma preparation. The curve plotted below is the time-variation of the "focal length" (eq. 7.7) associated with the electron density hollow on the axis of the SUPPER I plasma.

all the power entering SUPPER I should have been detected. However, this theory does not take into account any error in the direction of the beam entering SUPPER I. Measurements have shown that the laser output beam direction may not be along the laser tube axis (Sec. 2.4.3) and the positions of the optical components in the interferometer are adjusted by trial and error to optimise the fringes generated by moving the return mirror with no plasma present. This alignment is much less critical than is required to ensure that a beam focused near the exit window by the plasma leaves at a sufficiently small angle to the axis to reach the detector.

Since the beam has a crossover near the window where it enters, it will leave the vessel parallel to the axis, independent of its initial tilt, when the plasma focal length is equal to the length of the vessel. When this happens, a large part of the transmitted power can reach the detector. On the other hand, when the plasma focal length is equal to half the length of the vessel, the exit beam will be inclined to the axis at an angle just equal to that with which it entered the vessel and may well miss the detector altogether. In view of the likelihood of misalignment of the beam, it is considered that this effect is responsible for the fact that no power was detected at early times.

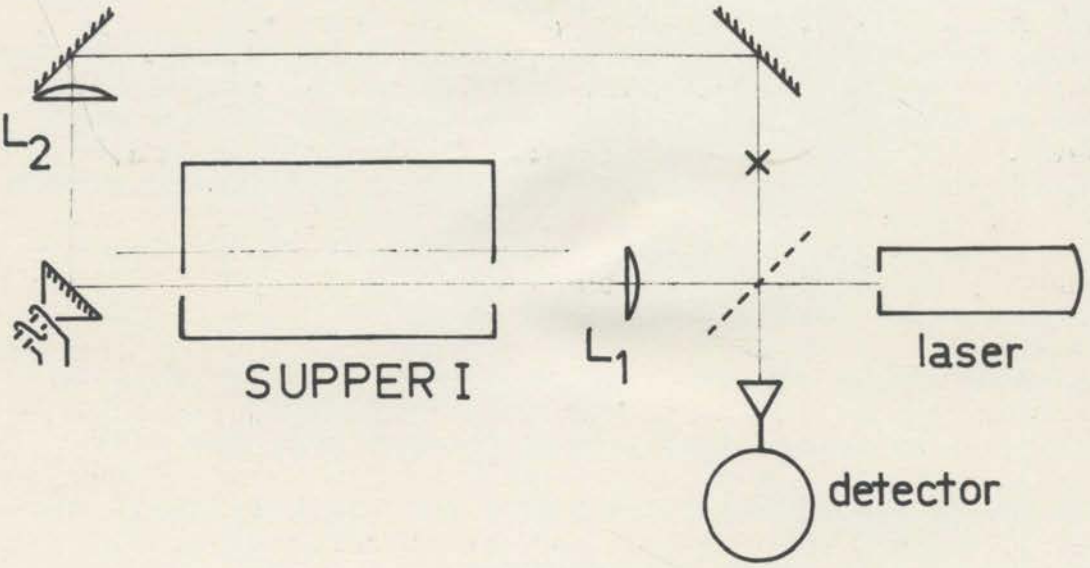
L2
SUPPER I
L1
laser
detector

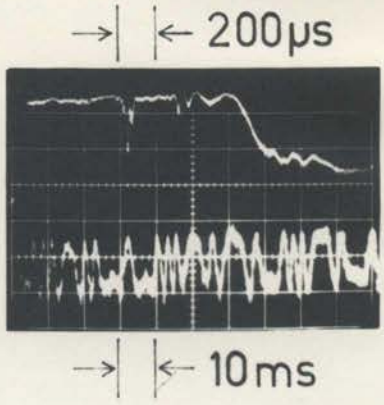
200μs
10ms

7.3.4 Comparison of the Laser Interferometer with Conventional Interferometers

In order to evaluate the degree of superiority of the HCN laser interferometer over conventional interferometers the interferometer depicted in Fig. 7.15 was set up. The long coherence length of the laser radiation allows the use of unequal probing and reference paths. A lens L_1 images the laser output hole at the SUPPER I exit hole which is in turn imaged by a second lens L_2 to a point X chosen to be the same distance from the detector as is the laser output hole. This ensures that the two interfering beams have the same wavefront curvature. A 633 nm He-Ne laser beam passing through a pinhole in the aluminized coating of the right-hand HCN laser mirror allowed the optical system to be aligned. This was found particularly easy to do and in preliminary alignment and testing large amplitude moving mirror fringes were observed.

Figure 7.15 (lower) shows the result of preparing a plasma. The lower trace shows on a slow timebase, moving mirror fringes interrupted at the beginning of the trace

---

Fig. 7.15 (Opposite). A conventional interferometer using a HCN laser as source set up 5 cm from the vessel axis. A typical experimental record is shown. The presence of the plasma tilts the probing beam so that it does not interfere effectively with the reference beam.

by the presence of the plasma. The upper trace (200 μsec/large scale division) shows instead of the expected fringes only the fact that power is transmitted along the probing path after 1200 μsec in the same way as shown by the direct transmission measurements at this radial position (Fig. 7.10). The fringes at about 1000 μsec are spurious, resulting from modulation of the laser by power reflected from the firing end of the vessel. Reference to laser interferometer density measurements made earlier shows that the last fringe should occur at about 1700 μsec. The fact that no plasma fringes appear in spite of the fact that power is clearly being transmitted along the probing path (and even causing moving mirror fringes while no plasma is present) can be explained in terms of the bending of the HCN laser beam in the plasma. The optical system of the interferometer is designed so as to return efficiently any radiation leaving the exit hole of SUPPER I to the point X. However it does not remove the tilt of the beam with respect to the vessel axis caused by the plasma density gradient although it does reduce it by a factor of three. If the directions of the two beams reaching the receiving horn of the Putley detector are such that there is one half wavelength disagreement in the wavefronts over the horn diameter the two beams will simply add incoherently. Calculation of

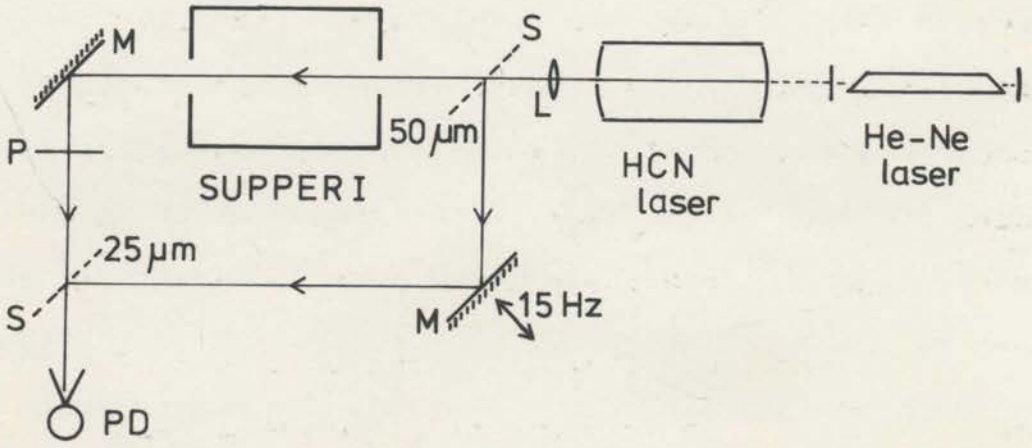

M mirror
S beamsplitter
P polarizer
L lens (T.P.X.)
PD Putley detector

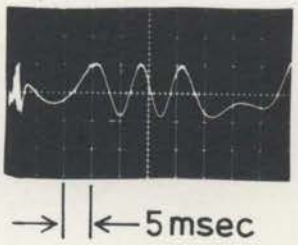

Fig. 7.16. Mach-Zehnder interferometer configuration which was used to measure electron densities on axis of the SUPPER I helium plasma. The trace below shows moving mirror fringes corresponding to one half cycle of mirror oscillation. Near the beginning of the trace there is a group of fast fringes caused by preparation and decay of the plasma. On an expanded time scale these fringes are similar to those shown in Fig. 7.17.

the tilt of the probing beam in this case shows that the plasma density gradient introduces just sufficient tilt to cause this problem. In this respect the laser interferometer (or a Michelson interferometer) is superior because the reciprocal nature of the bending process ensures that the deflection of the probing beam after its first passage through the plasma is cancelled on its return.

We have seen that in at least one set of circumstances the laser interferometer can make meaningful electron density measurements where a conventional interferometer will not work at all. In order to make a more realistic comparison of the performance of a conventional interferometer with that of the laser interferometer a Mach-Zehnder interferometer (Fig. 7.16) was set up to measure electron densities on axis of the SUPPER I vessel. At this position plasma beam bending should not prevent the conventional interferometer from operating. However we were interested in seeing what other disadvantages (or qualities) it might demonstrate. In this interferometer the HCN laser was polarized vertically (i.e. in a plane perpendicular to the page) by means of a thin horizontal wire inserted diametrically across the discharge tube about 10 cm in front of one of the laser mirrors. The 50 μm and 25 μm beamsplitters have reflection coefficients

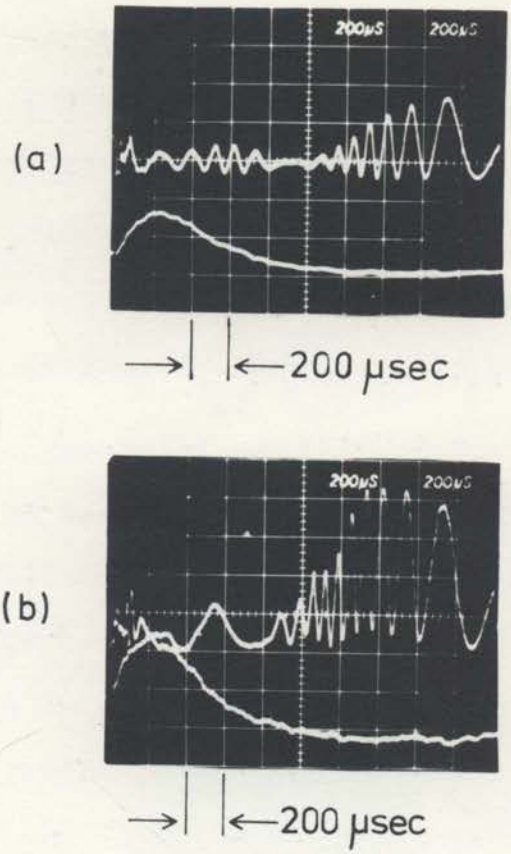

Fig. 7.17. Plasma fringes obtained with the Mach-Zehnder interferometer (Fig. 7.16). In each photo the lower trace is a continuation of the upper trace, on the same timebase. The upper trace is triggered at the instant of plasma preparation 40 μsec before the graticule zero. About 1 μsec is lost between upper and lower traces.

(a) Shows an interferogram obtained when the polarizer (Fig. 7.16) was adjusted for maximum transmission in the absence of a plasma. There is a pinchoff due to Faraday rotation at approximately 900 μsec, followed by 8 fringes in the plasma decay.

(b) Shows an interferogram obtained under the same conditions of plasma preparation as (a) but the polarizer has been adjusted to allow more fringes to be observed.

of about 50% and 25% respectively for the laser polarization. The thinner beamsplitter was used to recombine the probing and reference beams to compensate for losses in the probing arm of the interferometer.

Preliminary alignment of the Mach-Zehnder interferometer with a He-Ne laser beam was somewhat easier than for the laser interferometer and quite deep moving mirror fringes (Fig. 7.16) were readily obtained. Figure 7.17(a) shows the result of preparing a plasma. Very clear fringes are obtained late in the afterglow of the plasma but their amplitude pinches to zero at about the time when the density along the vessel axis goes through its turning point (Fig. 7.6). As a result the fringes which appear before the "pinchoff" (zero in fringe amplitude) cannot be interpreted. However, even in the absence of this difficulty the early fringes are of little diagnostic use as their form exhibits considerable shot-to-shot variation. This is probably due to shot-to-shot variations in plasma focusing on the vessel axis and the non-reciprocal nature of the Mach-Zehnder optical system.

The pinchoff, which is followed by about 8 fringes in the subsequent decay of the plasma is caused by Faraday rotation of the linearly polarized probing beam. It will be shown in Sec. 7.4.2 that for propagation parallel to a

9 kG magnetic field, the angle of polarization of the 337 μm beam should be rotated 90° when the electron density is sufficient to cause a phaseshift of $8\frac{3}{4} \times 2\pi$ radians. Thus the pinchoff should be followed by $8\frac{3}{4}$ fringes. The observation in Fig. 7.17(a) of 8 fringes after pinchoff is in reasonable agreement with this prediction.

The problem of counting plasma fringes near the Faraday rotation pinchoff can be partially overcome by putting a suitably oriented polarizer in the interferometer probing arm as shown in Fig. 7.16. By adjusting the polarizer to pass the component of radiation polarized at 45° to the angle of polarization of the laser output, in the direction of Faraday rotation, we can ensure that the beams being recombined at the detector do not have their polarizations at right angles until 135° of Faraday rotation has taken place. Since for a given magnetic field the angle of Faraday rotation and the plasma phaseshift are both proportional to the electron density (Secs. 7.4.1 and 7.4.2) the addition of the polarizer should allow us to observe about 13 fringes after pinchoff. Figure 7.17(b) shows a Mach-Zehnder interferogram produced by the SUPPER I helium plasma under these circumstances. About 11 fringes are visible in the decay of the plasma (equivalent to 22 laser interferometer fringes), but plasma focusing prevents

the appearance of fringes at earlier times. Nevertheless the insertion of the polarizer in the interferometer probing arm does extend the range of measurement.

Analysis of the interferograms (Figs. 7.17 (a) and (b)) allowing for the fact that the Mach-Zehnder interferometer has only half the sensitivity of the laser interferometer, gives electron densities in agreement with Fig. 7.6 in the range from 4×10^{12} cm^{-3} to 10^{14} cm^{-3}. However these interferograms give no information about the rising electron density at early times or the electron density turnover (Fig. 7.6). We conclude that because of the non-reciprocal nature of the Mach-Zehnder optical system, it is not as immune to plasma focusing as the laser interferometer.

7.4 Faraday Rotation of 337 μm Radiation in SUPPER I

In our analysis so far, of the propagation of 337 μm radiation along the axis of the SUPPER I helium plasma, we have used the refractive index appropriate to a plasma with no magnetic field (eq. 3.18). We shall see that in the present circumstances this is quite valid for the purpose of estimating electron densities and plasma beam bending and focusing effects. However the presence of the strong (9 kG) axial magnetic field in SUPPER I does cause an additional effect, that of Faraday rotation of the linearly polarized probing beam. In order to discuss this effect we need to introduce the theory of propagation of an electromagnetic wave in a plasma parallel to a magnetic field.

In this section we first present this theory before discussing some of its implications in the context of laser interferometry. It will be seen that although Faraday rotation is a small effect at shorter wavelengths (Dellis et al, 1965) it can cause several radians of rotation of a 337 μm probing beam in our plasma. In this respect it promises to be a useful diagnostic tool in its own right.

Following the theory we describe experimental observations of the effects of Faraday rotation of 337 μm

radiation in the SUPPER I helium plasma. The laser interferometer exhibits an interesting immunity to polarization effects. As far as we know this is the first observation of Faraday rotation of 337 μm radiation in a laboratory plasma. However, Faraday rotation of far-infrared radiation propagating through a laboratory plasma was reported by Dellis et al in 1965. In their experiments the far-infrared source was a pulsed 27.9 μm water vapour laser.

7.4.1 Propagation of Electromagnetic Waves in Plasmas Parallel to a Magnetic Field

A description of the propagation of electromagnetic waves in plasmas is considerably complicated by the presence of a magnetic field (Heald and Wharton, 1965, p.12). However the simplest case to consider is that of propagation parallel to the magnetic field, which is our present interest. A linearly polarized wave entering a plasma parallel to a magnetic field is best considered as two counter-rotating circularly polarized components. The component which is rotating in the direction of electron cyclotron rotation in the magnetic field is called the right hand circularly polarized wave; the other is called the left hand circularly polarized wave. The left and right hand circularly polarized waves interact differently with the plasma electrons when they are

immersed in a large magnetic field, with the result that they have separate refractive indices μ_ℓ and μ_r respectively. When the collision frequency for momentum transfer for electrons is sufficiently small, as is the case in the SUPPER I helium plasma (Table 3.1) μ_ℓ and μ_r are given by (Heald and Wharton, 1965, p.18)

$$\mu_{\ell,r} = \left[1 - \frac{\frac{\omega_p^2}{\omega^2}}{1 \pm \frac{\omega_b}{\omega}} \right]^{\frac{1}{2}} , \qquad 7.9$$

where ω_p is the electron plasma frequency (eq. 3.1) and the plus sign applies to the left hand circularly polarized wave, ω is the wave angular frequency and,

$$\omega_b = \frac{eB}{m} \qquad 7.10$$

is the electron cyclotron frequency. B is the value of the axial magnetic field and e and m are respectively the charge and mass of an electron. When B = 0 eq. 7.9 reduces to eq. 3.15 which we obtained before for propagation in a plasma without a magnetic field. For propagation of 337 μm radiation ($\omega = 2\pi \times 890 \times 10^9$ sec^{-1}) in a 9 kG magnetic field ω_b/ω is about 0.03 and for the range of densities encountered in the SUPPER I helium plasma $\omega_p^2 << \omega^2$ (Table 3.1). Thus, using the binomial expansion twice we

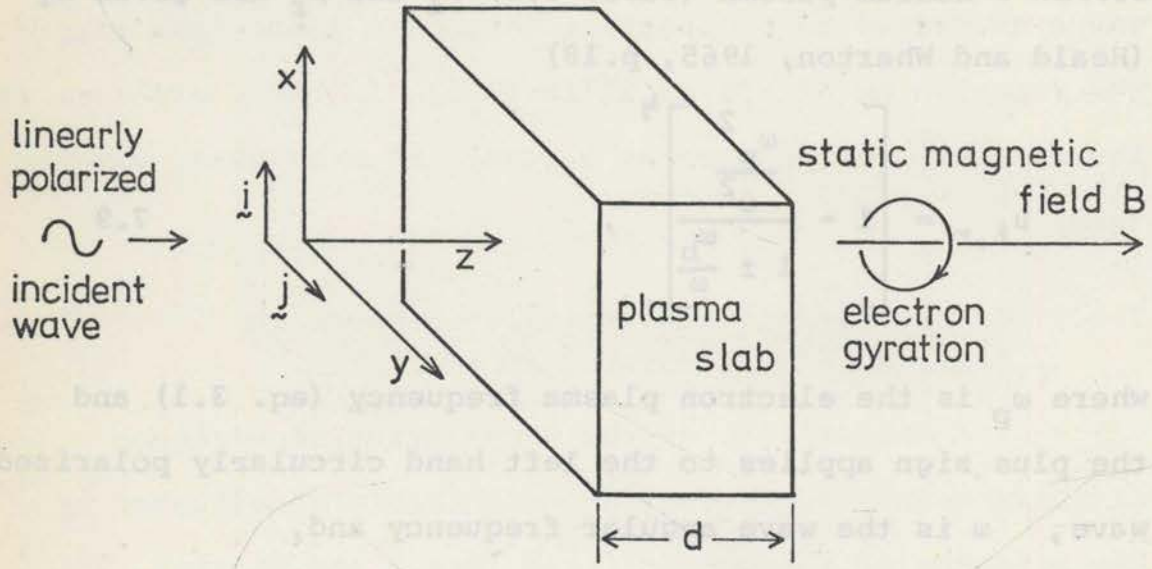

Fig. 7.18. Schematic representation of a linearly polarized wave incident on a plasma slab. We are considering the case of propagation parallel to a large static magnetic field.

find that eq. 7.9 is well approximated for our plasma by the expression

$$\mu_{\ell,r} = 1 - \frac{\omega_p^2}{2\omega^2} \cdot \left(1 \mp \frac{\omega_b}{\omega}\right) \quad , \qquad 7.11$$

where the minus sign applies to the left hand circularly polarized wave. In what follows it will be more convenient to express eq. 7.11 (using eqs. 3.1 and 3.17) as

$$\mu_{\ell,r} = 1 - \frac{n}{2n_c} \left(1 \mp \frac{\omega_b}{\omega}\right) \quad , \qquad 7.12$$

where n is the plasma electron density and n_c is the cutoff density for 337 μm radiation.

Let us now consider the propagation of a linearly polarized plane-wave which is incident on a plasma slab (in the z direction) parallel to a superimposed magnetic field. The situation is shown in Fig. 7.18. Suppose the wave is initially polarized in the x direction (unit vector $\underset{\sim}{i}$). The time-varying electric field $\underset{\sim}{E}_i(t)$ incident on the plasma slab is

$$\underset{\sim}{E}_i(t) = E_o \, \underset{\sim}{i} \, \text{Cos } \omega t \qquad 7.13$$

which can be expressed as the sum of left and right hand circularly polarized waves $\underset{\sim}{E}_\ell(t)$ and $\underset{\sim}{E}_r(t)$ where

$$\underset{\sim}{E}_{\ell}(t) = \frac{E_o}{2} (\underset{\sim}{i} \text{ Cos } \omega t - \underset{\sim}{j} \text{ Sin } \omega t) ,$$

and 7.14

$$\underset{\sim}{E}_{r}(t) = \frac{E_o}{2} (\underset{\sim}{i} \text{ Cos } \omega t + \underset{\sim}{j} \text{ Sin } \omega t) .$$

Here $\underset{\sim}{j}$ is a unit vector in the y direction. After propagation through a length d of plasma the corresponding time-dependent electric fields of the circularly polarized waves $\underset{\sim}{E}'_{\ell}(t)$ and $\underset{\sim}{E}'_{r}(t)$ are,

$$\underset{\sim}{E}'_{\ell}(t) = \frac{E_o}{2} (\underset{\sim}{i} \text{ Cos}(\omega t + \phi_{\ell}) - \underset{\sim}{j} \text{ Sin}(\omega t + \phi_{\ell}))$$

and 7.15

$$\underset{\sim}{E}'_{r}(t) = \frac{E_o}{2}(\underset{\sim}{i} \text{ Cos}(\omega t + \phi_{r}) + \underset{\sim}{j} \text{ Sin}(\omega t + \phi_{r})) ,$$

and the resultant time-varying field $\underset{\sim}{E}'(t)$ is the sum of these two. ϕ_{ℓ} and ϕ_{r} are the phase shifts experienced by the left and right hand waves respectively. These phase-shifts are given by,

$$\phi_{\ell,r} = \frac{2\pi d}{\lambda} \cdot \mu_{\ell,r} \qquad 7.16$$

where μ_{ℓ} and μ_{r} are given by eq. 7.12 and λ is the free-space wavelength of the probing beam. ϕ_{ℓ} is slightly greater than ϕ_{r}. If we add the components given by eqs.

7.15 we find that the time-variation of the electric field of the wave emerging from the plasma is given by,

$$\underset{\sim}{E}'(t) = E_o \cos\left(\omega t + \frac{\phi_\ell + \phi_r}{2}\right) \cdot \left[\underset{\sim}{i} \cos\frac{\phi_r - \phi_\ell}{2} + \underset{\sim}{j} \sin\frac{\phi_r - \phi_\ell}{2}\right]$$

$$= E_o \underset{\sim}{p} \cos\left(\omega t + \frac{\phi_\ell + \phi_r}{2}\right) \qquad 7.17$$

where $\underset{\sim}{p}$ is a unit vector (defined by eq. 7.17) at angle $(\phi_r - \phi_\ell)/2$ to the unit vector $\underset{\sim}{i}$. Thus the linearly polarized probing beam leaves the plasma with its plane of polarization rotated $(\phi_\ell - \phi_r)/2$ radians (which is positive) *in the opposite sense* to that of electron gyration in the magnetic field. In addition it experiences a total phaseshift $\Phi = (\phi_\ell + \phi_r)/2$ radians which (from eqs. 7.12 and 7.16) is given by

$$\Phi = \frac{2\pi d}{\lambda}\left(1 + \frac{n}{2n_c}\right) . \qquad 7.18$$

The phaseshift with respect to free-space propagation, $\Delta\Phi$, is then given by

$$\Delta\Phi = \frac{2\pi}{\lambda} \cdot \frac{nd}{2n_c} . \qquad 7.19$$

This is exactly the same as the result for zero magnetic field (eq. 3.21). Thus we may ignore the magnetic field

(parallel to the direction of propagation) when using plasma phaseshift measurements to infer time dependent electron densities. The only effect of the magnetic field is to rotate the plane of polarization of the probing beam. However this rotation will have important consequences when this beam is recombined with an unrotated reference beam in an interferometer. In the next section we turn our attention to the effects of Faraday rotation in practical interferometry.

7.4.2 Effect of Faraday Rotation on Interferometer Performance

In this section we investigate the effect which Faraday rotation should have on conventional and laser interferometers. We start by analysing the performances of the Mach-Zehnder (the simplest case) and Michelson interferometer configurations. We then use the results for the Michelson interferometer as a basis for discussing the possible performance of a laser interferometer.

7.4.2.1 Conventional Interferometers

Let us consider the Mach-Zehnder interferometer shown in Fig. 7.16 (polarizer omitted). If the time-varying electric field of the reference beam arriving at the detector is $E_o \underset{\sim}{i} \cos \omega t$ then comparison of eqs. 7.13, 7.17 and 7.19 tells us that the time-variation of the

probing beam when it arrives at the detector is

$$k\, E_o\, \underset{\sim}{p}\, \mathrm{Cos}\ (\omega t + \Delta\Phi)\ ,$$

where $\underset{\sim}{p}$ is a unit vector defined by eq. 7.17, $\Delta\Phi$ is given by eq. 7.19 and k is a constant ($\simeq$ 1) which allows for attenuation of the probing beam. Thus the time-varying electric field arriving at the detector is

$$\underset{\sim}{E}_d(t) = E_o\, \underset{\sim}{i}\left[\mathrm{Cos}\ \omega t + k\ \mathrm{Cos}(\omega t + \Delta\Phi) \cdot \mathrm{Cos}\left(\frac{\phi_r - \phi_\ell}{2}\right)\right]$$

$$+ k\, E_o\, \underset{\sim}{j}\ \mathrm{Cos}(\omega t + \Delta\Phi) \cdot \mathrm{Sin}\left(\frac{\phi_r - \phi_\ell}{2}\right)\ . \qquad 7.20$$

There are two cases to consider; the detector may "see" only one polarization or it may be unpolarized. In the first case it is sensible to set up the detector to see the component of radiation polarized in the direction of the unit vector $\underset{\sim}{i}$. Then the time-varying power detected (assuming a square law detector) is proportional to,

$$P_x(t) = E_o^{\,2}\overline{\left[\mathrm{Cos}\ \omega t + k\ \mathrm{Cos}(\omega t + \Delta\Phi)\ \mathrm{Cos}\left(\frac{\phi_r - \phi_\ell}{2}\right)\right]^2} \qquad 7.21$$

where the bar indicates a time average over the radiation period $T = 2\pi/\omega$. Evaluating the time average we obtain,

$$P_x(t) = \frac{E_o^2}{2} + \frac{k^2 E_o^2}{2} \cos^2 \left(\frac{\phi_r - \phi_\ell}{2} \right)$$

$$+ kE_o^2 \cos \Delta\Phi \cdot \cos \left(\frac{\phi_r - \phi_\ell}{2} \right) . \qquad 7.22$$

The third term in eq. 7.22 represents the plasma fringes ($\propto \cos \Delta\Phi$) which are amplitude modulated by the slowly varying Faraday rotation "envelope" $\cos(\phi_r - \phi_\ell)/2$. $(\phi_r - \phi_\ell)/2$ is related to the plasma electron density at any instant by (eqs. 7.12 and 7.16),

$$\frac{\phi_r - \phi_\ell}{2} = - \frac{2\pi d}{\lambda} \cdot \frac{n}{2n_c} \cdot \frac{\omega_b}{\omega} . \qquad 7.23$$

Thus the electron density change Δn, between successive Faraday rotation "pinchoffs" (zeros in fringe amplitude), is given by

$$\pi = \frac{2\pi d}{\lambda} \cdot \frac{\Delta n}{2n_c} \cdot \frac{\omega_b}{\omega} ,$$

which implies a plasma phase shift $\Delta\Phi$ (eq. 7.19) between Faraday rotation pinchoffs of

$$\Delta\Phi = \frac{\pi\omega}{\omega_b} .$$

Thus the number of plasma fringes between successive pinchoffs is $\omega/2\omega_b$ which is close to 17.5 for 337 μm radiation and a 9 kG magnetic field. There should be $8\frac{3}{4}$ fringes after the last pinchoff in the decay of the plasma. This was approximately verified by our observation of 8 fringes after pinchoff in the Mach-Zehnder interferogram shown in Fig. 7.17(a). Equation 7.22 shows that in addition to the plasma fringes the detector will see a time-varying power proportional to $kE_o^2/2 \cdot \mathrm{Cos}^2(\phi_r - \phi_\ell)/2$. This power is not necessarily small as k is of the order of unity. It will have the effect of raising the troughs of the envelope of the interferogram as in Fig. 7.17(a). This is as it should be, because a polarizer was inserted in the interferometer optical system (Fig. 7.16) so that the detector could only see the component of polarization parallel to the laser output polarization.

We now turn to the second case when the detector is unpolarized. This is perfectly relevant in far-infrared (as distinct from microwave) contexts because most detectors (e.g. the Putley detector) are unpolarized. In this case the detector sees a time-varying power (obtained from eq. 7.20 in a manner analogous to the derivation of eq. 7.22) proportional to,

$$P(t) = \frac{E_o^2}{2} + \frac{k^2 E_o^2}{2} + kE_o^2 \,\mathrm{Cos}\,\Delta\Phi \cdot \mathrm{Cos}\left(\frac{\phi_r - \phi_\ell}{2}\right). \qquad 7.24$$

Thus the form of the plasma fringes is unchanged (c.f. eq. 7.22) by using an unpolarized detector. The one difference is that the fringe envelope is no longer distorted by an added time-varying power, except to the extent caused by a possible variation of k (e.g. due to plasma focusing) with time.

Before discussing the effect of Faraday rotation on the laser interferometer let us briefly consider the case of a Michelson interferometer. Here the probing beam is reflected back through the plasma under study before being recombined with a reference beam at the detector. Since the handedness of each of the circularly polarized components of the linearly polarized probing beam is defined with respect to the direction of gyration of the plasma electrons it is not reversed by the reflection back through the plasma. Accordingly the Faraday rotation for two passes through the plasma is twice that for a single pass. Of course, the plasma phaseshift is doubled by the second pass also. Thus with a Michelson interferometer we expect to see the same number of plasma fringes between successive Faraday rotation pinchoffs as with a Mach-Zehnder interferometer. The one distinguishing difference is that since the sensitivity of the Michelson is double that of the Mach-Zehnder interferometer there will be twice as many pinchoffs and the last pinchoff will

occur later in the decay of a given plasma. However our reason for discussing the Michelson interferometer is that it is similar to the laser interferometer in that the probing beam makes a double pass through the plasma. Apart from the non-linearity of the laser interferometer we expect its behaviour to be the same as that of the Michelson interferometer. In the next section we shall consider the effect of the Faraday rotation on the laser interferometer in more detail.

7.4.2.2 The Laser Interferometer

In our analysis of the laser interferometer (Ch. 6) we treated the effect of the return beam on the laser by coherently adding its amplitude to the field amplitude in the laser resonator. In this respect the interaction was treated like simple interference; non-linearity arose from the gain saturation of the amplifying medium. We ignored polarization effects as it was implicit that the direction of polarization of the return beam was the same as that of the (linearly polarized) laser output. However, we would expect the effect of rotating the plane of polarization of the return beam in a laser interferometer to be similar to the effect in the case of a Michelson interferometer, which was discussed in the previous section. In particular we would expect to observe maximum modulation of the laser

output when the return beam polarization is parallel to the laser output and no modulation when the two are at 90° to each other. The non-linearity of the laser interferometer should merely distort the shape of the Faraday rotation modulation-envelope. Thus in our studies of the SUPPER I helium plasma (Sec. 7.3) we would expect that the interferograms obtained by probing the plasma along its axis (e.g. Fig. 7.5) should pinch off in amplitude every 17½ fringes (Sec. 7.4.2.1); the last $8\frac{3}{4}$ fringes in the interferogram should be preceded by such a pinchoff. In fact, with the experimental setup described in Sec. 7.3.1 no such effect was observed; the interferogram shown in Fig. 7.5 has no sign of a pinchoff at the appropriate time, and as we have already seen, the variations in fringe amplitude with time which do appear can be explained in terms of plasma focusing of the 337 μm beam by electron density gradients. Thus it appears that our laser interferometer configuration is immune to the possible effects of Faraday rotation of the return beam. We shall see in Sec. 7.4.3 that this immunity possibly results from the fact that the laser operating mode is not a simple transverse electromagnetic mode. In this case the interaction between the return beam and the laser cavity field will be quite complex and the effect of rotating the plane of polarization of the return beam will no longer be simple

to calculate. Before proceeding to Sec. 7.4.3 however, we shall consider a possible complication due to one other effect, and show that it may be neglected in the present context.

Since the laser interferometer incorporates a beamsplitter in its probing arm, and the beamsplitter has different reflection coefficients for beams polarized perpendicular to and in the plane of incidence then it is apparent that the beamsplitter may cause some rotation of the plane of polarization of the laser output beam and the return beam. We shall estimate the magnitude of this effect. Our beamsplitter consisted of Mylar film up to 50 μm thick. The reflection coefficients for 337 μm radiation incident at 45^{o} on two thicknesses of Mylar film are tabulated below (Hadni, 1969; p.32).

Film thickness	$R_{\parallel}$	$R_{\perp}$
6 μm	2%	5%
50 μm	16%	57%

Table 7.1

Here, $R_{\parallel}$ and $R_{\perp}$ are the reflection coefficients for radiation polarized parallel to and perpendicular to the plane

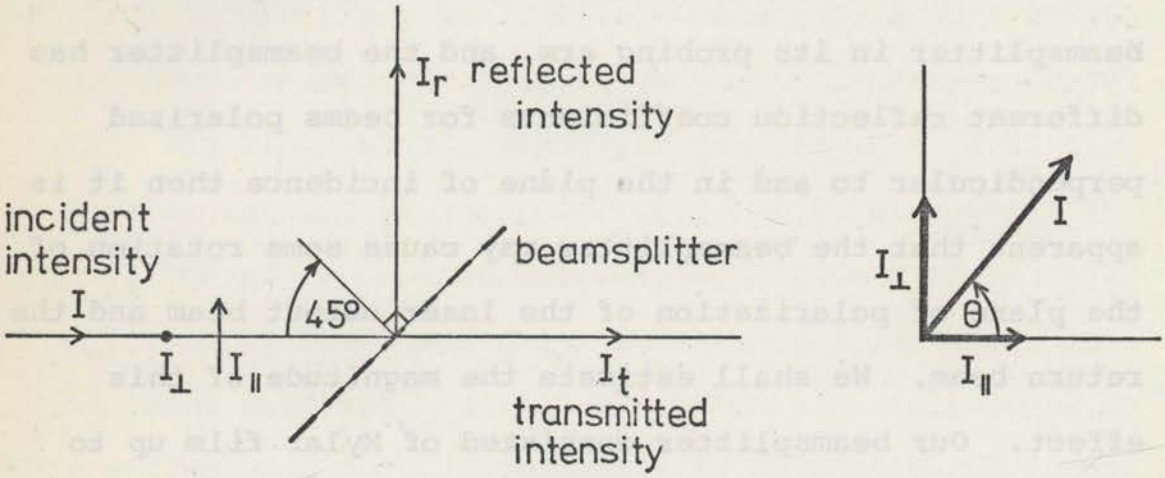

Fig. 7.19. Schematic diagram showing the reflection and transmission of a linearly polarized plane wave by a Mylar beamsplitter at 45° to the direction of incidence. The plane of polarization of the wave is at an arbitrary angle θ to the plane of incidence.

Also, from our definition of reflection coefficients in the previous paragraph the components of the reflected intensity I_r are given by,

$$I_{r\parallel} = I_{\parallel} \cdot R/3$$

and 7.27

$$I_{r\perp} = I_{\perp} \cdot R \quad .$$

Similarly the components of the transmitted intensity I_t are given by,

$$I_{t\parallel} = I_{\parallel} \cdot (1 - R/3)$$

and 7.28

$$I_{t\perp} = I_{\perp} \cdot (1 - R) \quad .$$

It is implicit in eqs. 7.27 and 7.28 that absorption in the thin film is negligible. Using eqs. 7.26 to 7.28 we may easily show that

$$\theta_r = \mathrm{Tan}^{-1} (\sqrt{3}\ \mathrm{Tan}\ \theta)$$

and 7.29

$$\theta_t = \mathrm{Tan}^{-1} \left(\sqrt{\frac{1 - R}{1 - R/3}}\ \mathrm{Tan}\ \theta \right),$$

where θ_r and θ_t refer to the angles of polarization, defined in the same way as θ, of the reflected and transmitted beams respectively. It is evident that unless $\theta = 0$ or 90^o there is a net rotation of both the transmitted and reflected beams. The rotation effect on the reflected beam is independent of the film thickness, but is unimportant anyway as in our laser interferometer (Fig. 7.4) the reflected beam is merely used to monitor the laser output level and the plane of polarization of the laser output does not rotate (Sec. 7.4.3).

The effect of the beamsplitter on the transmitted beam is more interesting. We can see immediately (eq. 7.29) that the rotation caused by the beamsplitter may be minimised by using a very thin film (R small, Table 7.1). However, regardless of the thickness of the film, it is obvious that the positions of maxima and minima of the Faraday rotation envelope are unaltered if the laser is polarized vertically or horizontally. The rotation due to the beamsplitter will merely distort the shape of the Faraday rotation envelope but the non-linearity of loss modulation of the laser causes this to happen anyway. Thus in this case the beamsplitter has no discernible effect.

If however, the laser is not polarized horizontally or vertically, which is often the case when it is not

deliberately polarized, then we would expect the effect of the beamsplitter to be more important. Suppose the laser output is polarized at an angle θ_ℓ to the horizontal. Looking at eq. 7.29 we see that the linearly polarized wave which enters the plasma after passing once through the beamsplitter will then be at an angle,

$$\text{Tan}^{-1}\left(\sqrt{\frac{1-R}{1-R/3}}\,\text{Tan}\,\theta_\ell\right)$$

to the horizontal. After a double pass through the plasma its angle is rotated $\pm\,\theta_p$ where θ_p is the Faraday rotation angle for the plasma and the plus and minus signs refer to the two possible directions of rotation depending on the direction of the magnetic field. Then the wave approaching the beamsplitter for the second time is at an angle

$$\text{Tan}^{-1}\left(\sqrt{\frac{1-R}{1-R/3}}\cdot\text{Tan}\,\theta_\ell\right)\pm\theta_p$$

to the horizontal. Applying eq. 7.29 again we find that the wave re-entering the laser is polarized at a total angle of

$$\theta'_\ell = \text{Tan}^{-1}\left[\sqrt{\frac{1-R}{1-R/3}}\cdot\text{Tan}\left[\text{Tan}^{-1}\left(\sqrt{\frac{1-R}{1-R/3}}\cdot\text{Tan}\,\theta_\ell\right)\pm\theta_p\right]\right] \qquad 7.30$$

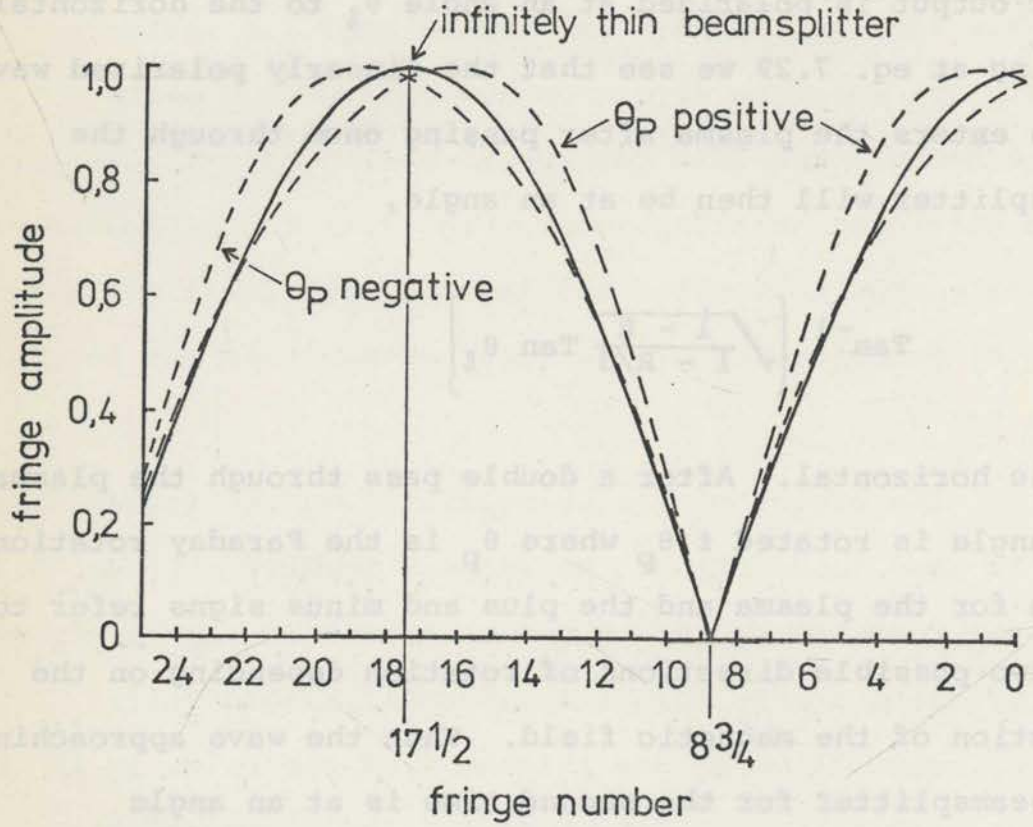

Fig. 7.20. Form of the Faraday rotation fringe envelope for a conventional interferometer. The solid curve shows the appearance of the envelope when there is no beamsplitter in the probing path. The two dotted curves (corresponding to the two possible senses of Faraday rotation) show the distortion which is introduced by a 50 μm beamsplitter when the laser output is polarized at 30° to the horizontal.

to the horizontal. When $\theta_p = 90^o$, that is when we should observe a minimum in the Faraday rotation envelope in the absence of a beamsplitter, we have

$$\text{Tan } \theta'_\ell = \sqrt{\frac{1 - R}{1 - R/3}} \text{ Tan} \left[\text{Tan}^{-1} \left(\sqrt{\frac{1 - R}{1 - R/3}} \cdot \text{Tan } \theta_\ell \right) + 90 \right]$$

$$\equiv \text{Tan } (\theta_\ell + 90) \quad ,$$

or

$$\theta'_\ell = 90 + \theta_\ell \quad .$$

Thus the beamsplitter has no net effect at this particular angle; the position (in the interferogram) of the Faraday rotation pinchoff is unaltered. This is not the case at the maximum of the fringe envelope which is moved by the presence of the beamsplitter. Rather than calculate the effect at this one point however we show, in Fig. 7.20, the full form of the Faraday rotation envelope predicted by eq. 7.30 when R = 0.5 (corresponding to a 50 μm beamsplitter) and $\theta_\ell = 30^o$ (a common value for our laser) and compare this form (for positive and negative θ_p) with the envelope corresponding to an infinitely thin beamsplitter. The ordinate for the curves in Fig. 7.20 is the equivalent fringe number for 337 μm radiation in a 9 kG magnetic field ($\theta_p = 90^o$ x fringe number/$8\frac{3}{4}$). The amplitude

as a function of fringe number which results corresponds to what we expect in our laser interferometer results (see Figs. 7.21(b) and 7.22) ignoring the additional distortion due to non-linearity of the instrument. However, the non-linearity of the laser interferometer cannot move the positions of the envelope maxima and minima. The curves plotted in Fig. 7.20 show that the distortion caused by the beamsplitter is quite noticeable, but the non-linearity of the laser interferometer would add to this anyway. The only feature which we might observe in principle is a slight shift in the positions of the peaks of the Faraday rotation envelope. However, even this effect is quite small and as we shall see in the next section, too small to observe in practice. We conclude that in our subsequent discussion we may ignore the rotation effect of the beamsplitter.

7.4.3 Observations of the Effect of Faraday Rotation on Laser Interferometer Performance

Our measurements with the Mach-Zehnder interferometer (Sec. 7.3.4) indicated that the linearly polarized laser output beam does indeed experience Faraday rotation of its plane of polarization when propagating axially through the SUPPER I helium plasma. We saw that the plane of polarization is rotated 90° for every 8 (or so) plasma fringes and that this is consistent with the known axial

No polarizer

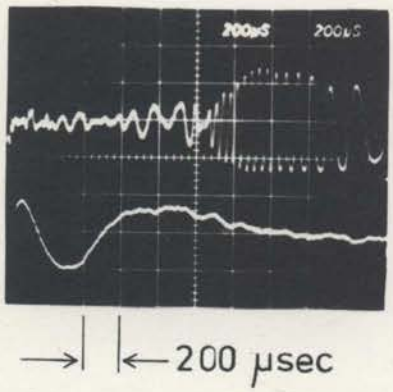

(a)

→| |← 200 μsec

Polarizer in front of laser output hole

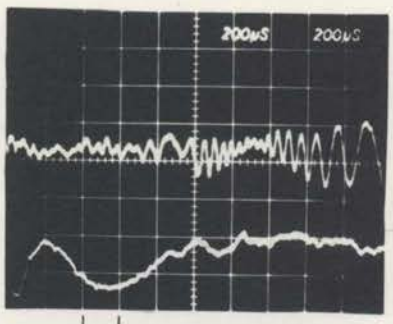

(b)

→| |← 200 μsec

Fig. 7.21. Interferograms obtained with the HCN laser interferometer probing the SUPPER I helium plasma along its axis. In both photos the lower trace is a continuation of the upper trace, on the same timebase. About 1 μsec is lost between the two traces. The upper photo corresponds to normal laser interferometer operation, while the lower photo shows a pinchoff due to Faraday rotation when a polarizer is placed in front of the laser output hole. The pinchoff is followed by about nine fringes in the subsequent decay of the plasma.

magnetic field strength of 9 kG. This has the effect that the last 8 fringes of the Mach-Zehnder interferograms (Fig. 7.17(a)) are preceded by a pinchoff due to Faraday rotation. We stated in Sec. 7.4.2 that we expected the same effect on laser interferometer records but the interferogram shown in Fig. 7.5 shows no sign of the effect of Faraday rotation whatever. We now return to discuss this anomally.

Figure 7.21 shows two interferograms obtained with the laser interferometer configuration (Fig. 7.4) for plasma conditions slightly different from those described in Sec. 7.2. The interferometer optical system was also altered, the net result being that plasma focusing had a different effect on laser interferograms than that shown in Fig. 7.5. However the important consideration is that apart from minor shot-to-shot variations in the plasma the interferograms in Fig. 7.21 were obtained under identical conditions *except* for one specific difference. The lower interferogram was obtained with a polarizer at the laser output hole. This polarizer was oriented to allow maximum transmission of the 337 μm output beam. It is evident that the polarizer forces the laser interferometer to be affected by Faraday rotation in the manner which we originally expected (Sec. 7.4.2). As predicted in Sec. 7.4.2.1 there is a pinchoff in fringe amplitude about 9 fringes before the final decay

of the plasma. Thus there is no doubt that the linearly polarized probing beam experiences the amount of Faraday rotation which we expected. However, we are now faced with the problem of explaining why the laser interferometer without a polarizer inserted is quite insensitive to the direction of polarization of the return beam. Reference to the upper photo in Fig. 7.21 shows that the laser is strongly modulated when the return beam is known to be at 90° to the laser output (i.e. about 9 fringes before the final decay of the plasma).

In order to shed more light on this behaviour the following experiment was performed. Although the laser is normally linearly polarized (see discussion below) a thin ($< \lambda/2$) wire was inserted horizontally across a diameter of the laser resonator about 10 cm from one of the laser mirrors. This introduces sufficient loss to components of radiation which are polarized horizontally to force the laser to produce vertically polarized output. This had the immediate effect that the laser was much less reliably modulated by the return beam. Subsequent investigations indicated that this was due to the stronger coupling betwee the Putley detector horn (Fig. 7.4) and the laser output via the 50 μm beamsplitter which has a reflection coefficie of about 50% for vertically polarized radiation. Previousl the laser output was more nearly horizontally polarized.

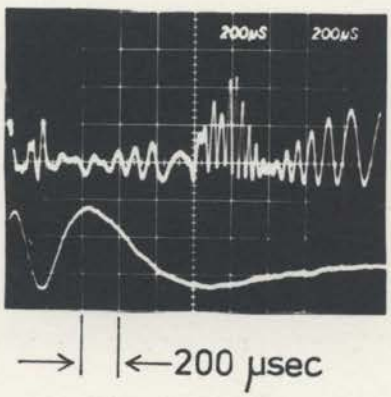

Fig. 7.22. Interferogram obtained with the modified HCN laser interferometer probing the SUPPER I helium plasma along its axis. The interferometer optical system and the plasma preparation conditions were approximately the same as those for Fig. 7.21 but the laser was polarized vertically by a horizontal wire in its resonator. It is clear that the wire makes the laser behave in the same manner as placing a polarizer in front of the laser output (c.f. Fig. 7.21(b)).

The situation was improved by using a thinner (25 μm) beamsplitter but even more so by reversing the 25 μm beamsplitter so that the Putley detector monitored the return beam rather than the laser output. Figure 7.22 shows an interferogram obtained under the same conditions as Fig. 7.21(a) but with the modifications described above. Clearly there is a pinchoff due to Faraday rotation about 8 fringes before the final decay of the plasma. Thus the insertion of a wire in the laser cavity has essentially the same effect as placing a polarizer at the laser output; it makes the laser interferometer respond to a polarization rotated return beam in a manner which simple interference arguments would lead us to expect.

Although we are not in a position to fully understand the immunity of the HCN laser interferometer to the effects of rotating the plane of polarization of the return beam it is sufficiently interesting to warrant some further discussion. Our measurements indicate that even in the absence of any attempt to polarize the HCN laser its output is always strongly linearly polarized. The direction of polarization is presumably determined by mirror imperfections or discharge inhomogeneities; it varies from day to day but it does not exhibit any short term variations. This direction must represent a direction for which the losses of the laser resonator are least. However the

variability of the direction of polarization suggests that it is only by a small margin that the losses for one direction are greater than those for all other directions. It is reasonable therefore,to expect the component of the laser interferometer return beam which is polarized at right angles to the laser output polarization to be able to excite the laser resonator. It should be possible for this radiation to be amplified by the laser medium and compete with the existing radiation field for gain. We might expect this process to cause a net rotation of the plane of polarization of the laser output. However observations of the interferometer output beam made with a polarizer in front of the Putley detector horn (Fig. 7.4) indicated that no such rotation takes place. Thus it is hard to see how the time-varying *phase* of the return beam could effectively modulate the losses of the laser resonator. A possible explanation is that the laser generally operates in tube-modes (Sec. 2.4.3) which are not simple transverse electromagnetic wave modes. The interaction between the return beam and the laser cavity field would then be somewhat more complex than we have envisaged. Nevertheless, it is clear that the insertion of a thin horizontal wire in the laser resonator damps the horizontally polarized component of the return beam quite severely. This component is then no longer

able to excite the laser resonator and the laser interferometer behaves as we originally expected (Sec. 7.4.2).

Without further experimental data it is not possible to go any further towards explaining the polarization insensitivity of the laser interferometer. However it is important to note that it can be a useful advantage, as each Faraday rotation pinchoff does cause difficulties in counting fringes. Nevertheless, we have demonstrated ways of making the laser interferometer polarization sensitive if so desired. For measuring higher electron densities when probing over long pathlengths it is possible that counting Faraday rotation envelopes could be a useful diagnostic method. A hydrogen plasma prepared in the SUPPER I source under similar conditions to our helium plasma (Brand et al, 1969) has an axial electron density exceeding 10^{15} cm^{-3} at early times. This would give about 200 337 μm fringes and more than 10 Faraday rotation pinchoffs. In this situation the Faraday rotation envelope could be used to measure the high electron densities directly.

7.4.4 Direct Transmission Observations of Faraday Rotation

Our results so far have definitely verified that Faraday rotation of the 337 μm probing beam does occur in the SUPPER I helium plasma. We saw that observa-

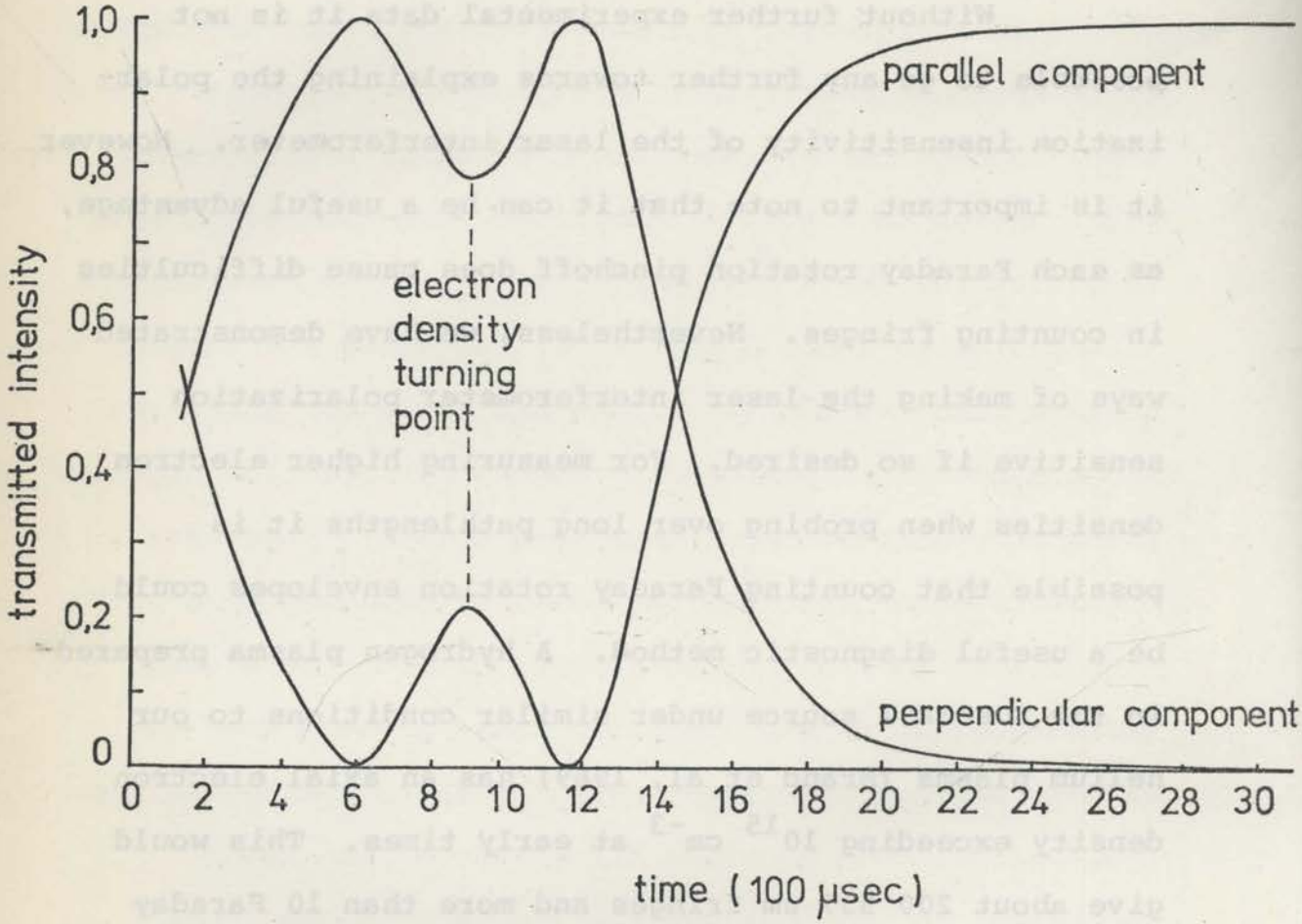

Fig. 7.23. Expected transmission as a function of time for the parallel and perpendicular components of a linearly polarized 337 μm beam propagating axially through the SUPPER I helium plasma. These curves are based on the time dependent electron density implied by the interferogram shown in Fig. 7.5 assuming that the total power transmitted is constant (i.e. plasma focusing is ignored).

tion of this effect was complicated by the behaviour of the laser interferometer. In this section we shall present the results of direct transmission experiments designed to reveal the presence of Faraday rotation. However, we will see that plasma focusing complicates these results even more than the behaviour of the laser interferometer complicated the previous results.

In a direct transmission experiment (Fig. 7.10, upper) we are interested in observing the time-varying horizontally and vertically polarized power components of the 337 μm beam transmitted through the plasma. This is easily achieved by inserting a suitably oriented polarizer in the configuration of Fig. 7.10 (upper) in front of the detector aperture. Assuming that the total power transmitted by the plasma is constant the expected time dependence of the power transmitted as vertically and horizontally polarized components is easily calculated. The interferogram (for an axial probing beam) shown in Fig. 7.5 and the fact that we expect 45^{o} of Faraday rotation (for a single pass) for each $8\frac{3}{4}$ fringes (Sec. 7.4.2) allows us to plot the curves shown in Fig. 7.23. However we expect the actual time-variation of transmitted components to be more complicated than the curves of Fig. 7.23 because they should be multiplied by the observed time-varying transmission of total power due to plasma

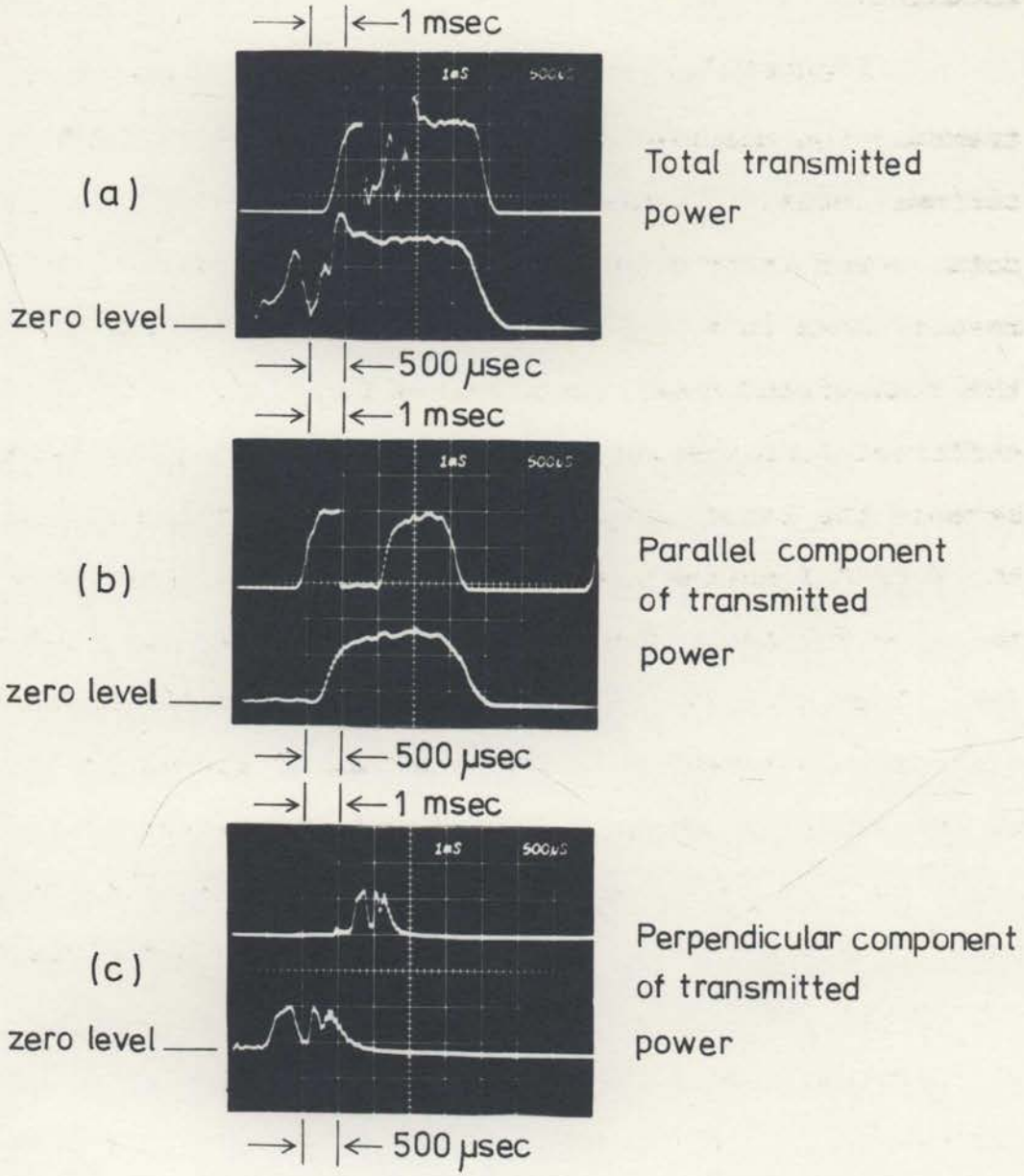

Fig. 7.24. Time varying 337 μm power transmitted axially by the SUPPER I helium plasma. As the detection system was AC coupled the 337 μm beam was chopped at about 120 Hz (upper traces) to establish a zero level. The plasma was prepared early in the "on" period of a chopping cycle, which lasted until well after the plasma had decayed away. The lower trace in each photo shows the time-varying transmission, beginning at the instant of plasma preparation.

focusing.

Figures 7.24 (a), (b) and (c) show records of transmission measurements obtained under three different circumstances. Figure 7.24(a) shows the result of a total power transmission experiment analogous to the result shown in Fig. 7.14. However the detailed form of the transmitted power as a function of time is quite different from the result shown in Fig. 7.14. This is because the laser output beam was no longer focused on the SUPPER I entrance window, but the optical system was the same for each of the traces in Fig. 7.24 (a), (b) and (c). Figures 7.24 (b) and (c) show the results of transmission measurements when a polarizer is placed in front of the detector aperture. In (b) the polarizer was adjusted to transmit the component of polarization of the beam which was parallel to the laser output polarization (which was vertical), and (c) shows the transmission of the perpendicular component. The small wiggles on these traces are due to laser modulation by spurious reflections off the SUPPER I firing electrode or end window. The result shown in Fig. 7.24(c) is quite complicated and varied significantly from shot to shot as did the form of (a) at early times. As the three traces (a), (b) and (c) apply to different plasma shots we cannot expect (b) and (c) to add to give exactly the result in (a). These

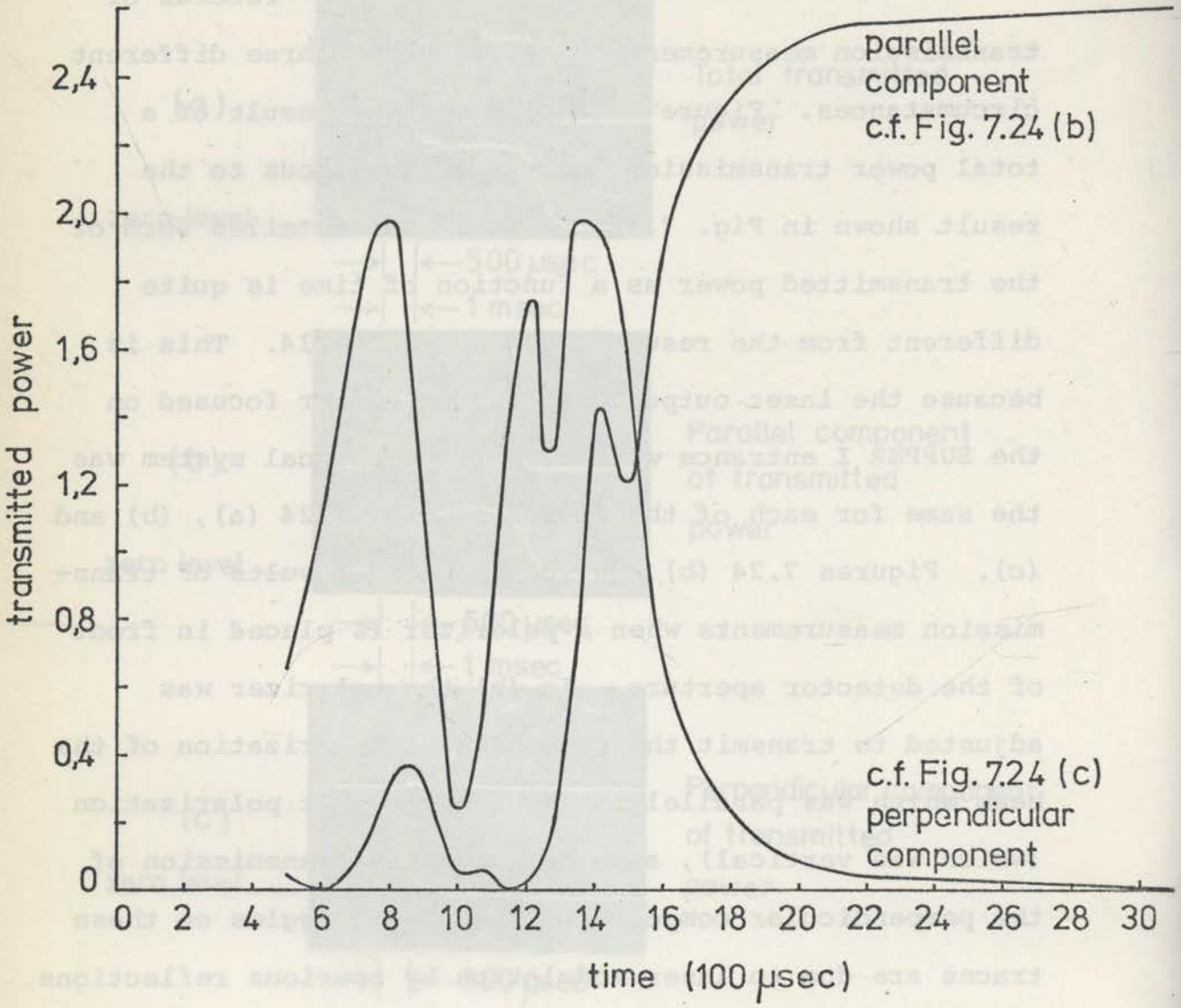

Fig. 7.25. Curves showing the expected time-varying transmission of parallel and perpendicular components of the linearly polarized 337 μm beam propagating axially through the SUPPER I helium plasma. These curves compare satisfactorily with the experimental records shown in Fig. 7.24.

three traces were chosen so that they corresponded as nearly as possible however. To check whether the form of the traces in (b) and (c) agrees with the expected transmission, we have multiplied the known time-varying total power (trace (a)) by the curves in Fig. 7.23. This yields the curves plotted in Fig. 7.25. It is clear that the general form of these curves agrees with the observed transmission of the horizontally and vertically polarized power components shown in Figs. 7.24 (b) and (c). In view of the shot-to-shot variations in transmitted intensity at early times this agreement is quite satisfactory.

Thus we may conclude that although the effects of Faraday rotation are clearly observable in direct transmission records their form is considerably complicated by plasma focusing. Particularly because of shot-to-shot variations in the plasma focusing effect they do not lend themselves to a detailed quantitative analysis. It is evident that the pinchoffs in laser interferometer records (Figs. 7.21 and 7.22) give a better quantitative measure of the amount of Faraday rotation.

7.5 Summary

The important results of the work described in this chapter are summarized below.

1. We have described the SUPPER I plasma source and a method of preparing a helium plasma which is suitable for studying the diagnostic value of the 337 μm HCN laser interferometer. The description of this plasma is also useful as an introduction to our study of the decay of the helium plasma in Chapter 8.

2. The HCN laser interferometer has proven useful for making electron density measurements in the range from 2×10^{12} cm^{-3} to 10^{14} cm^{-3} under circumstances which make other techniques (microwave methods, 3.39 μm laser interferometry and Stark broadening) difficult or impossible to apply. In our particular plasma the refractive effects of transverse electron density gradients caused some complications in the interpretation of interferograms.

3. We have compared the performance of the laser interferometer configuration with two conventional interferometers. It was found to be less sensitive to plasma beam bending and focusing effects than a Mach-Zehnder interferometer because of the reciprocal nature of its optical system. In one case (Sec. 7.3.4) the laser interferometer

was able to measure electron densities where plasma beam bending prevented a conventional (single pass) interferometer from working at all. An additional advantage is that the laser interferometer sensitivity is doubled by the second pass of the probing beam through the plasma under study. In principle all these advantages could be realized using a Michelson interferometer. However the laser interferometer exhibited one quality which is not shared by the Michelson interferometer configuration. Unless deliberate steps are taken to make it otherwise, the HCN laser interferometer is immune to the effects of Faraday rotation of the plane of polarization of the beam returned to the laser resonator. This can be quite useful as each Faraday rotation pinchoff complicates the counting of plasma fringes.

4. We have observed Faraday rotation of the plane of polarization of the linearly polarized 337 μm beam probing the SUPPER I helium plasma. With our strong (9 kG) magnetic field and the 150 cm effective pathlength used in our experiments an electron density of 10^{14} cm^{-3} causes about 180^{o} of Faraday rotation. For measuring electron densities up to 10^{16} cm^{-3} therefore, counting of Faraday rotation "fringes" could prove to be a useful method.

Chapter 8

THE DECAY OF A HELIUM PLASMA

8.1 Introduction

At this point our interest turns away from the HCN laser and its applications, towards the processes responsible for the decay of a highly ionized helium plasma. Initially the author's interest in this plasma was the application of HCN laser diagnostics to it, in order to measure electron densities in a range and situation inaccessible to other techniques. This diagnostic work, together with a description of the SUPPER I plasma source and some properties of the helium plasma under study, was described in Ch. 7. Inevitably, the author became interested in the plasma itself and joined N.R. Heckenberg in a collaborative study of the plasma decay. The results of that study are presented in this chapter.

We shall start by summarizing the present experimental and theoretical status of the subject of plasma decay. We then describe those properties of our helium plasma which were not described in Ch. 7 before studying the decay process and thermal economy of our helium plasma.

8.1.1 Background Theory

We expect, for the large 9 kG axial magnetic field in which our helium plasma is immersed, that the process of plasma diffusion will play a very minor role in the plasma decay. The problem of decay of a magnetically confined plasma has been the subject of considerable theoretical and experimental investigation. In early studies of transient plasmas, particularly hydrogen plasmas, the process first thought to be responsible for plasma decay was two-body recombination,

$$H^+ + e^- \rightarrow H + h\nu$$

which is also known as radiative recombination. However theoretical calculations of the decay rate based on this reaction made by Zanastra (1946) were found to give rates considerably smaller than those observed experimentally, for example, by Craggs and Meek (1945) and Fowler and Atkinson (1959).

Decay dominated by three body recombination, which is the inverse of collisional ionization

$$H^+ + e^- + e^- \rightarrow H^* + e^-$$

was suggested by Giovanelli (1948a,b) in connection with stellar atmospheres. The decay rate expected for this

process was first calculated by D'Angelo in 1961. D'Angelo considered radiative transitions between bound levels and electron collisional ionization as well as three body recombination but neglected collision-induced transitions between bound states. Although the decay rates predicted by this theory were more than an order of magnitude higher than the two-body rate they were still smaller than observed values (Hinnov and Hirschberg, 1962). Hinnov and Hirschberg pointed out the importance of inelastic and superelastic electron collisions in determining the populations of the bound states of the recombining atoms. Their approximate theory gave larger decay rates than did D'Angelo's and agreed well with their experimental results with low electron density ($< 5 \times 10^{13}$ cm^{-3}), low temperature (< 3000 K) hydrogen and helium plasmas.

A more general treatment of three body recombination for a hydrogen plasma was given by Bates, Kingston and McWhirter (1962 a). They solved a set of rate equations for the population and depopulation of the atomic energy levels taking account of recombination events, which produce excited neutrals, and subsequent inelastic and superelastic collisions of electrons with these excited states. Their calculations yielded a "collisional-radiative decay coefficient" α which described the decay of the plasma through the equation

$$\frac{dn_e}{dt} = -\alpha n_e n_i \quad , \qquad 8.1$$

where n_e and n_i are the densities of electrons and ions respectively. If the process were a two body one α would not depend on n_e; in fact it depends on both temperature and density. The results of Bates and his co-workers yielded the quantitative dependence of α on these parameters as well as the distribution of electrons in the excited states (Bates and Kingston, 1963; Bates et al, 1967). Their values for the decay coefficient agreed well with the experimental results of Hinnov and Hirschberg.

More recently Drawin (1969a) has recalculated collisional-radiative recombination coefficients using basically the same method as Bates, Kingston and McWhirter but more recent data for the cross sections involved, finding as a result, reductions in the recombination coefficient of up to a factor four as compared with the earlier results. However, it is difficult to distinguish experimentally between the two sets of results. Drawin (1969b,c) has also calculated the effect of neutral atom collisions on the decay rate, finding that they are negligible when the percentage ionization is higher than a fraction of one per cent.

Within the accuracy which may be achieved experimentally the collisional radiative recombination theory accounts well for the results of experiments with decaying hydrogen plasmas (Cooper and Kunkel, 1965; Irons and Millar, 1965; Quinn, 1965; Litvak and Edwards, 1966; Barrault and Hughes, 1967; Brand et al, 1969; Newton and Sexton, 1969). However, although most of the theoretical calculations discussed above pertain only to hydrogen plasmas their results also agree reasonably well with experimental decay rates for helium plasmas (Robben et al, 1963; Gusinow et al, 1966; Mosburg, 1966; Newton and Sexton, 1968). The reasons for this agreement, and the conditions under which the hydrogen theory can be expected to describe the helium decay, are discussed later.

The theoretical problem of three-body recombination decay may be treated in a simpler but more physical manner than the full collisional-radiative recombination theory however. We now describe such an alternative approach, which was developed for hydrogen by Byron, Stabler and Bortz (1962) but has since been applied to helium by Chen (1967). The arguments apply equally well to both gases.

When electrons recombine by the three-body process they do so mainly to the upper states. Because the probability of collisional deexcitation to an adjacent level is an order of magnitude larger than that to any

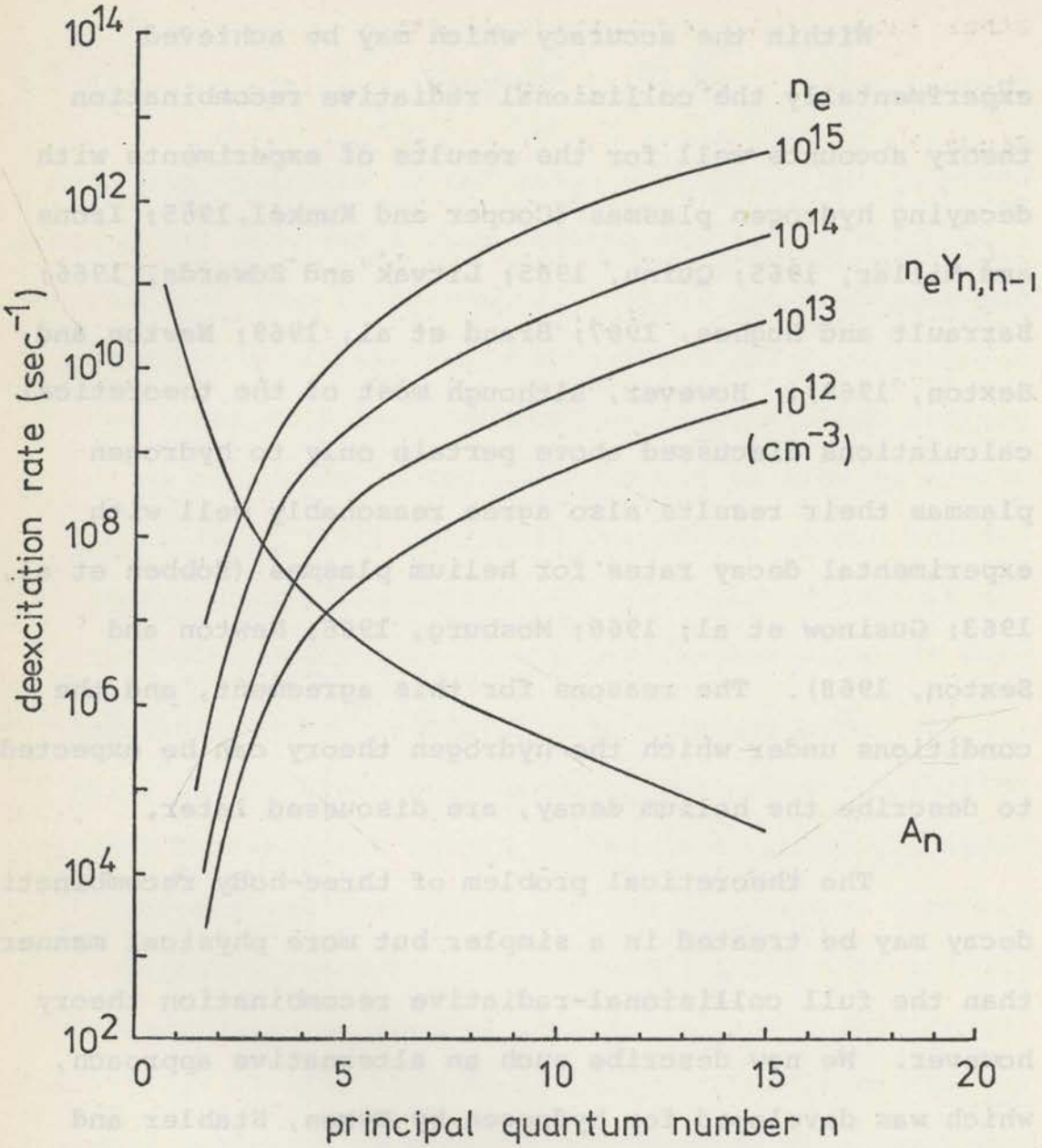

Fig. 8.1. Electron collisional deexcitation rate $n_e Y_{n,n-1}$ and spontaneous decay rate A_n as a function of principal quantum number n for the excited states of helium. It is clear that for any value of electron density there is a level for which the total (i.e. collisional plus radiative) deexcitation rate is a minimum. This is the "bottleneck" level discussed in the text.

other level, most recombining electrons must cascade through the excited states to reach the ground state. Since the collisional transition probability decreases rapidly as lower levels are reached there is a minimum in total deexcitation probability (collisional plus radiative) before the rate of radiative deexcitation becomes large at low levels. These points are illustrated in Fig. 8.1 where the deexcitation probabilities for helium atoms due to radiative and collisional processes (as calculated by Chen, 1967) are shown as a function of the principal quantum number of the excited electron. Thus a "bottleneck" occurs which limits the effective deexcitation rates of the upper levels and thus the recombination rate.

Above this bottleneck the levels have populations which are maintained close to the equilibrium populations given by the Saha-Boltzmann equation, by collisions with the free electrons. Below it, radiative deexcitation empties the levels into the ground state level so that the populations of the lower excited states are lower than the equilibrium values. The recombination rate can be taken to be equal to the net rate of deexcitation (i.e. transition probability x population) of the level with the lowest deexcitation rate plus the contribution from radiative transitions bypassing it.

This simple theory gives results in quite good agreement with those of the collisional-radiative recombination theory of Bates, Kingston and McWhirter (1962a) for hydrogen and with the experimental decay of helium (Chen, 1967).

We mentioned earlier that the collisional-radiative recombination theory for hydrogen has been applied successfully to both hydrogen and helium plasmas. This is reasonable because, except for the lowest states, the level structure of neutral helium is very similar to that of hydrogen (Bates and Kingston, 1964). However the theory of Byron et al makes it clear that this will be valid only when the bottleneck level is one which is similar in both atoms. Thus the hydrogen theory would be inapplicable to hot dense helium plasmas where the bottleneck level is low. On the other hand, for conditions where the level with the smallest deexcitation rate is 3 or above, both hydrogen and helium plasmas should behave similarly.

Drawin and Emard (1971) and Drawin et al (1971) have calculated collisional-radiative recombination coefficients specifically for helium considering the singlet and triplet systems as two individual systems coupled to each other by collisional processes. Although

these results respond differently to the effects of radiation trapping, the values of the decay coefficient for recombining plasmas are within a factor of two of those for hydrogen under most conditions. In our studies of a decaying helium plasma in this chapter we shall compare our experimental results with the theory of Drawin and Emard.

8.2 Plasma Electron Temperature Profiles

We described the preparation of, and the electron density profiles in, the SUPPER I helium plasma in Sec. 7.2. As this plasma is to be the subject of our study of recombination-decay its radial electron temperature profiles as a function of time are also required.

Temperature measurements in the decaying helium plasma were made by Heckenberg (1972) using two methods. A series of line-ratio (or Boltzmann-plot; Cooper, 1966) measurements were made at a position 5 cm from the vessel axis which is where the plasma is densest early in the decay. This method is applicable if the plasma is in local thermodynamic equilibrium, which our plasma is not, or if the upper levels of the transitions concerned have populations determined by the Saha-Boltzmann distribution (Cooper, 1966) for collisions with free electrons. Fortunately the decay process of our plasma is such that for all of the atomic energy levels above a certain level (the bottleneck level discussed in Sec. 8.1.1) electron collisional excitation and deexcitation dominate over radiative deexcitation and the populations closely follow the Saha-Boltzmann distribution. The transitions used for the present line-ratio measurements were chosen so that their upper levels were well above the bottleneck level.

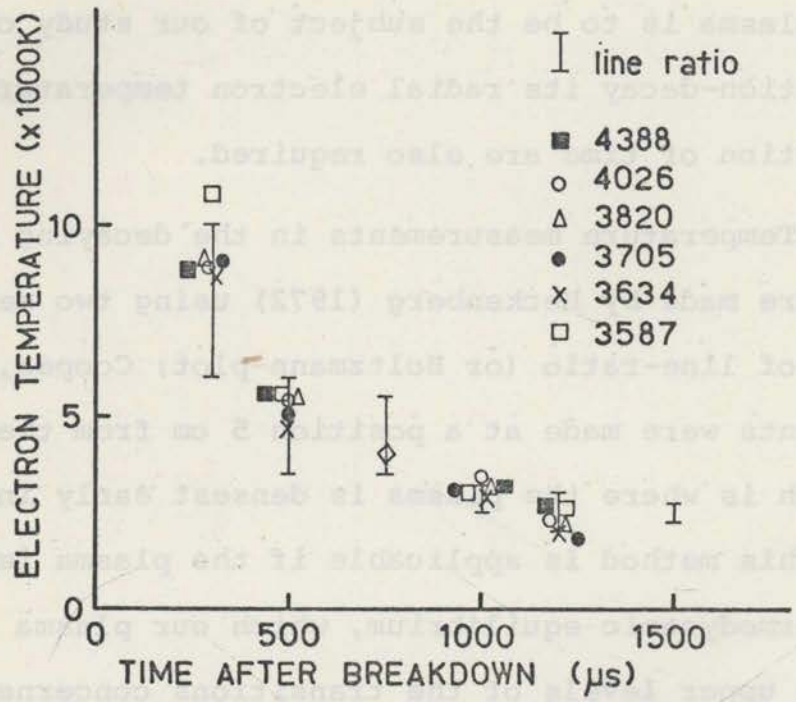

Fig. 8.2. Estimates of the electron temperature of the helium plasma 5 cm from the vessel axis (Heckenberg 1972). The results of applying the Boltzmann-plot method to measurements of the intensities of six lines are shown. Also shown are the results of applying to each line in turn the single line intensity method taking T_e = 3800 K 800 μsec after breakdown.

Even at r = 5 cm however the results were not entirely satisfactory, the scatter in the points on the logarithmic plot being such that precise estimates of the temperature could not be obtained. Further, the temperature estimates obtained were not reproducible from run-to-run to better than 20%.

Alternatively the variation of electron temperature may be estimated from the intensity of a single line if the electron density is known (Cooper, 1966). Again, the population of the upper level of the associated transition must have its population determined by the Saha-Boltzmann distribution, but this condition was readily satisfied by choosing transitions from levels with sufficiently high quantum numbers.

Figure 8.2 shows the correspondence between the single line intensity method and the line ratio method. Estimates of the electron temperature 5 cm from the vessel axis made by the line-ratio method using six neutral helium spectral lines are shown. Also shown are six separate estimates, each based on the intensity of a single one of the spectral lines used for the ratio estimate, the known electron density as a function of time at this radius (Fig. 7.3; p.7.9), and the assumption of a temperature of 3800 K 800 μsec after breakdown. The

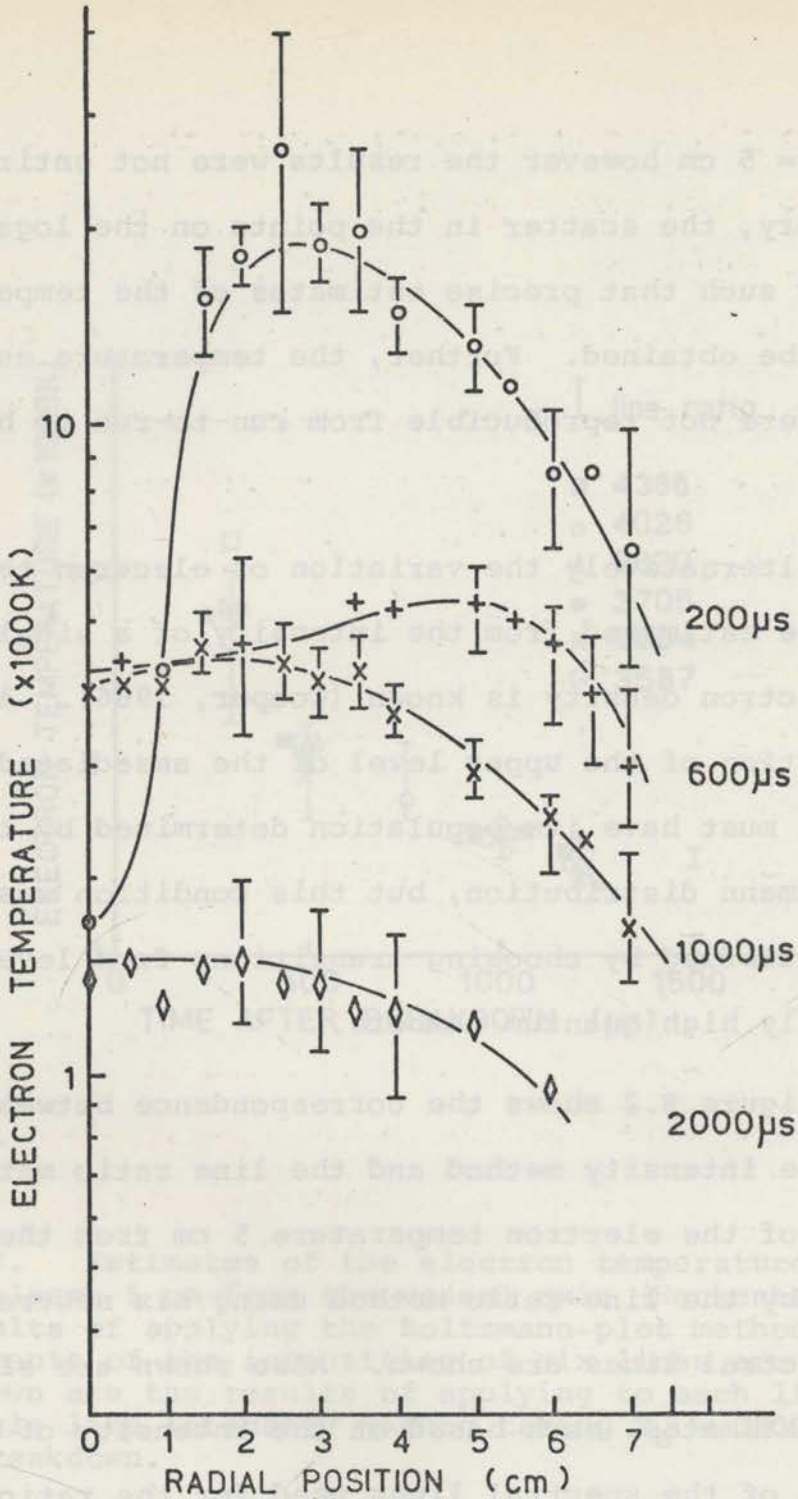

Fig. 8.3. Radial electron temperature profiles for the decaying helium plasma determined by the single line intensity method applied to the 3820 and 3634 Å lines, based on a datum of T_e = 3800 K at r = 5 cm, 800 μsec after breakdown.

satisfactory agreement obtained between the two methods allowed the much more convenient single line method to be used (in conjunction with the known electron density profiles) to estimate the radial temperature profile.

Electron temperature profiles for the plasma were built up by measuring the radial distribution of intensity of the 3820 and 3634 Å lines. Combining this information with the known electron density profiles (Fig. 7.3, p.7.9) yields the temperature profiles shown in Fig. 8.3. They exhibit the same sort of structure as the density profiles of Fig. 7.3, that is, they indicate that the central region is comparatively undisturbed by plasma preparation. Unfortunately it was not feasible to make the electron density and light intensity measurements simultaneously, so that high accuracy cannot be expected for these results. Together with the scatter in the measurements of the light intensity, the uncertainty in the values of electron density results in an uncertainty of up to 50% in the relative temperature values obtained. Since the absolute value of the temperature at the datum point, on which all these relative measurements are based, cannot be determined to better than about 30%, the absolute temperature values could be in error by as much as 80%.

8.3 Decay Processes in the Helium Plasma

As suggested in Sec. 8.1.1, the presence of the large (9 kG) magnetic field and the 75 cm length of the SUPPER I plasma vessel will ensure that the rate of loss of plasma by diffusion to the vessel walls will be smaller than the recombination rate. Although we will see later that the effects of radial plasma diffusion are not entirely negligible we will begin this discussion by examining whether collisional-radiative recombination can account for the observed decay rate. Throughout this section we will be concerned with the behaviour of the plasma at two radial positions; on axis, and 5 cm from the axis, chosen because extensive measurements are available at these positions and they correspond to the regions of maximum plasma density late and early respectively in the decay (Fig. 7.3; p.7.9).

In the course of this study questions relating to the optical thickness of our plasma and the extent to which plasma diffusion occurs will assume considerable importance. However the length of discussion required to resolve these points when they arise would disrupt the presentation of the more essential physics of the plasma decay. Accordingly the calculations and discussions relating to these topics are left until the end of this section, where they are

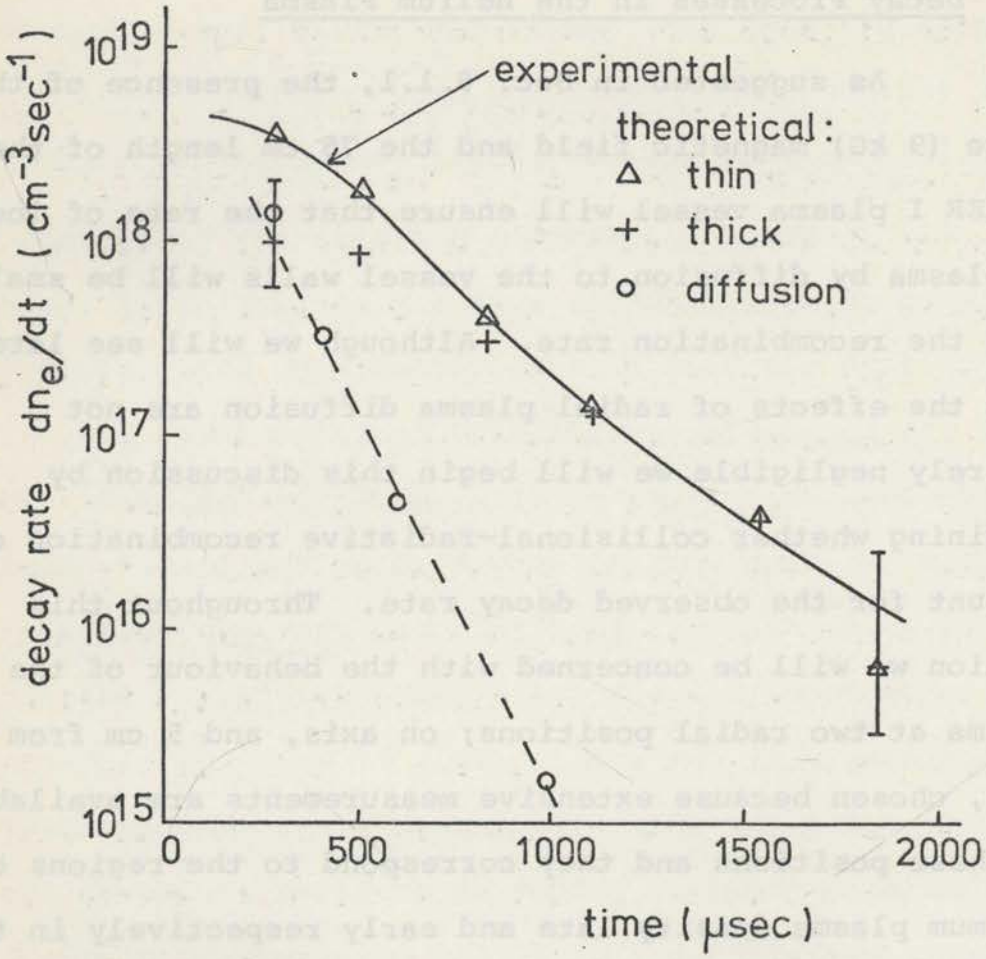

Fig. 8.4. Rate of decay of the SUPPER I helium plasma at the r = 5 cm position. The experimental points are derived from the measurements of the electron density while the theoretical estimates of the recombination rate are based on the measured electron density and temperature at this position. The typical error bars shown on the theoretical estimates correspond to the uncertainty in the electron temperature.

The estimates of the diffusion loss rate are based on the measured electron density gradients.

presented in Secs. 8.3.1 and 8.3.2. In the meantime the results of these sections are quoted as required.

Let us now consider the decay at the r = 5 cm position in our plasma. Since the electron density and temperature at this point are known as a function of time, reference to the calculations of Drawin and Emard (1971) of the collisional-radiative recombination coefficient for helium plasmas provides theoretical values for the rate of decay of electron density. Early in the decay the theoretical rate depends quite markedly on the transparency of the plasma to line radiation, particularly the ultraviolet lines resulting from transitions to the helium ground state. It is shown in Sec. 8.3.1 that the helium plasma is always "thin" (transparent) to visible line radiation but we cannot predict with certainty whether it is "thick" (opaque) or thin to its ultraviolet lines. In fact we estimate that the plasma loses between 30% and 90% of its ultraviolet photons. Thus we have plotted as points in Fig. 8.4 the expected collisional radiative recombination rates for two limiting cases. The upper set of points is the decay rate expected for a plasma which is thin to all radiation; the lower set corresponds to a plasma which is thin to visible line radiation but thick to the ultraviolet (or "Lyman") radiation. We expect the decay rate

of our plasma to lie somewhere between these two sets of points. Figure 8.4 also shows the observed decay rate, as obtained from plasma electron density measurements (Fig. 7.3; p.7.9). It is evident that the theoretical and experimental results agree well at late times, when the occurrence or otherwise of radiative trapping is unimportant. However at early times the observed decay rate follows closely the theoretical estimate for a plasma thin to all radiation. Thus we must conclude that either the plasma is thin to all radiation or it is partially thick to the ultraviolet lines and some diffusion away from the r = 5 cm position occurs at early times.

We therefore considered whether radial plasma diffusion may contribute to the decay at r = 5 cm at early times. The method of calculation of the expected diffusion rate is described in Sec. 8.3.2 and the results are shown as the dotted curve in Fig. 8.4. Except in the first 600 μsec of the decay the effect of diffusion can be seen to be negligible compared with recombination. However early in time when there are steep radial density gradients both towards the centre and towards the wall ($\partial^2 n/\partial r^2$ is large) the calculated diffusion rate represents up to one quarter of the observed decay rate. Although this is quite a substantial fraction it is not sufficient to make the

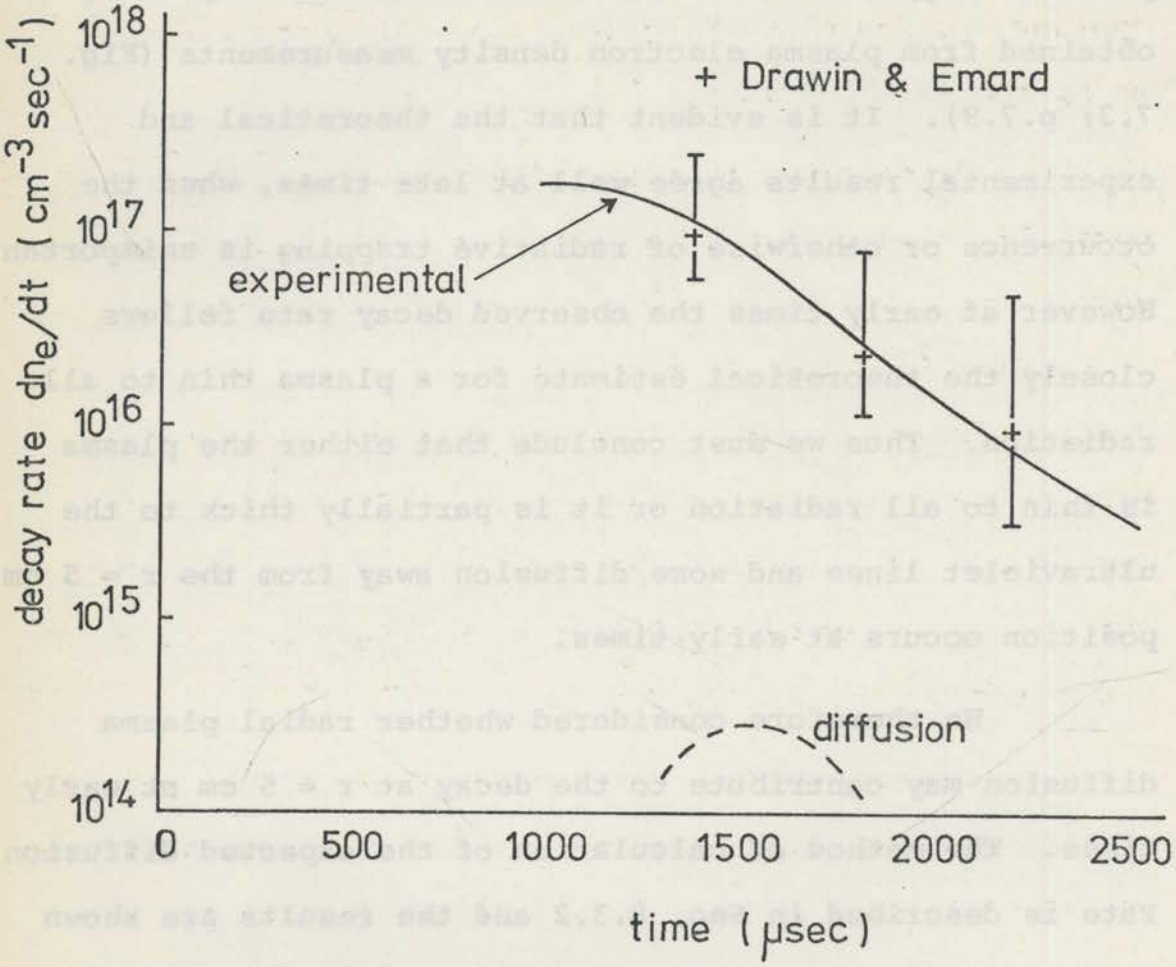

Fig. 8.5. Decay rate of the central part of the helium plasma. Theoretical values (Drawin and Emard, 1971) of the recombination rate based on the measured electron density and temperature show good agreement with the observed rate. The uncertainty in the theoretical value results from uncertainties in the temperature and density.

Estimates of the loss rate by radial diffusion are also shown (Sec. 8.3.2.).

collisional-radiative model for a plasma which is optically thick to ultraviolet line radiation (Fig. 8.4) look more appropriate for describing our plasma than the model for an optically thin plasma.

We conclude that our plasma must be essentially optically thin to all line radiation. In this case the decay of the plasma at the r = 5 cm position is well accounted for by collisional-radiative recombination theory, although plasma diffusion must contribute at early times. In view of the uncertainties in electron temperature measurements the agreement is very satisfactory but cannot really be considered as strong verification of the theory of Drawin and Emard.

Let us now consider the behaviour of the plasma on the vessel axis, firstly at times after about 1000 μsec when the electron density is definitely falling and the plasma has adopted a simple radial density profile with a central maximum. Evaluation of the diffusion loss rate late in the decay (Sec. 8.3.2) shows that, compared with the observed decay rate, there is negligible flow of plasma from the central position as shown in Fig. 8.5. Thus it is appropriate to compare the observed decay rate with that predicted by the theory of Drawin and Emard (1971). At the low densities and temperatures encountered

after 1000 μsec, the collisional-radiative recombination rate is not dependent on the optical thickness of the plasma. Figure 8.5 shows the predictions of the theory (corresponding to Drawin and Emard's figs. 2 and 3 for thin and thick plasmas respectively) plotted for comparison. It is clear that at these late times collisional-radiative recombination theory accounts well for the observed decay rate.

Having seen that collisional-radiative recombination adequately describes the on-axis behaviour of the plasma at late times we shall now consider early times when the electron density and temperature both rise steadily until about 800 μsec while the surrounding regions rapidly decay. At about 800 μsec the profiles become fairly flat, and thereafter the central density and temperature drop away at a rate comparable to that at greater radii. This behaviour suggests that at early times diffusion into the central region from the surrounding high density regions outweighs the loss of ions and electrons due to volume recombination there. Although the detailed shapes of the electron density profiles near the vessel axis are not known, reference to the profiles which were obtained (some of which appear in Fig. 7.3; p.7.9) has allowed estimates of diffusion rates into the central hollow to be made. The diffusion calculations are described in Sec. 8.3.2.

t	n_e	T_e	$\left(\frac{\partial n}{\partial t}\right)_D$	$\left(\frac{\partial n}{\partial t}\right)_R$	$\left(\frac{\partial n}{\partial t}\right)'_R$	$\left(\frac{\partial n}{\partial t}\right)_O$
200	5^{13}	1800	$+0.9^{17}$	-1.5^{18}	-1.5^{17}	$+1.6^{17}$
400	8^{13}	2500	$+0.7^{17}$	-1.3^{18}	-2.6^{17}	$+1.4^{17}$
600	1.0^{14}	4200	$+0.2^{17}$	-3^{17}	-7^{16}	$+0.7^{17}$
800	1.2^{14}	4000	$+0.15^{17}$	-3^{17}	-7^{16}	0
1000	9.5^{13}	4000	$+0.1^{17}$	-3^{17}	-7^{16}	-2.3^{17}
μsec	cm^{-3}	K	$cm^{-3}sec^{-1}$	$cm^{-3}sec^{-1}$	$cm^{-3}sec^{-1}$	$cm^{-3}sec^{-1}$

In this table numbers like 5^{13} should be read as 5×10^{13}.

t = Time after plasma preparation.

n_e = Electron density.

T_e = Electron temperature.

$\left(\frac{\partial n}{\partial t}\right)_D$ = Calculated diffusion rate into centre of plasma.

$\left(\frac{\partial n}{\partial t}\right)_R$ = Calculated collisional-radiative recombination rate (thin).

$\left(\frac{\partial n}{\partial t}\right)'_R$ = As above but with all temperatures 50% higher than those shown in the table.

$\left(\frac{\partial n}{\partial t}\right)_O$ = Observed rate of change of electron density.

Table 8.1. Observed rate of change of electron density on axis of the SUPPER I helium plasma at early times compared with the calculated contributions from plasma diffusion and collisional-radiative recombination.

The results, which are presented in Table 8.1 must be regarded as very approximate estimates however, because the diffusion rate at the centre of the plasma depends strongly on the shape of the electron density profile there. Table 8.1 also shows the measured rate of rise of electron density on axis and the calculated collisional-radiative recombination rate based on the known electron density and temperature.

At times up to 600 μsec the calculated diffusion rate into the central density hollow is only about one third to one half the observed rate of rise, which is an order of magnitude smaller than the calculated collisional-radiative recombination rate. By 1000 μsec however, the electron density is falling at about the rate predicted for recombination, and diffusion is negligible. As we saw in Fig. 8.5 this situation prevails throughout the subsequent decay.

Now in view of the agreement obtained at late times it is unlikely that our temperature estimates (which determine the theoretical recombination rate) are far from being correct but they *could* be in error by 50% (see Sec. 8.2). Raising the temperature estimates by this amount at early times does significantly reduce the expected recombination rate as shown in Table 8.1. However, our

calculated diffusion rate (which is proportional to $T^{-\frac{1}{2}}$ and would be reduced by 20%) is still smaller than the difference between the observed rate of rise and the new recombination rate by a factor of four or more. We must therefore enquire into the possibility of other processes causing the density to rise at early times.

There are several other processes apart from diffusion which could lead under some circumstances to density increases in part of a decaying plasma. Electron collisional ionization can be ruled out on the basis of the calculations of Drawin and Emard (1971) because of the low temperature of the electrons in the present plasma. Photoionization due to irradiation of the central plasma region by photons emitted in radiative recombination events in the surrounding high density regions can be shown to have a negligible effect (Appendix 4). Similarly it can be shown that ionization, by Penning or other processes, of metastables diffusing into the central region could not account for the observed rate of rise (Appendix 4). Thus we are faced with the problem of explaining the discrepancies between the figures in Table 8.1.

Since no other process can explain the rising density at early times we are forced to conclude that plasma diffusion causes this rise. However, even if we

suppose that our on-axis temperatures are in error by 50% at early times the calculated recombination rate is still much too large to be made up by the calculated diffusion rate less the observed rate of rise. Thus it must be that diffusion into the central density hollow occurs faster than we have calculated. One possible explanation is that the turbulence introduced by crow-barring the plasma (at ≃ 40 μsec) may persist on-axis until quite late times giving rise to enhanced ("anomalous") diffusion rates.

We can summarize the results of this section as follows: Comparison of the observed decay rates at two radial positions in the plasma with collisional-radiative recombination theory indicates that the plasma decays mainly by three-body recombination. At early times, when severe electron density and temperature gradients exist however, the effects of radial plasma diffusion are important.

In the two subsections which follow we present our calculations regarding optical thickness of, and diffusion in, the helium plasma. The results of these calculations have considerable bearing on the conclusions of this present section.

8.3 Optical Thickness of the Helium Plasma

As we have already seen, the predictions of the collisional-radiative recombination theory can depend strongly on the optical thickness of the plasma (e.g. Fig. 8.4). In this section we shall examine the optical thickness of our helium plasma, our principal interest being in the range of temperatures and densities encountered at the r = 5 cm position.

A suitable parameter for characterizing the optical thickness of a plasma to line radiation of wavelength λ_{pq} is its optical depth at line centre τ_{pq} which is given by the expression (Bates et al, 1962b),

$$\tau_{pq} = \frac{\pi e^2}{2mc(2k\ \ell n2)^{\frac{1}{2}}} \cdot \left(\frac{M}{T}\right)^{\frac{1}{2}} \cdot \lambda_{pq}\ f_{pq}\ n(p)L \ . \qquad 8.2$$

Here e(e.s.u.) and m are the charge and mass of an electron, k is Boltzmann's constant and c is the velocity of light in vacuum. M and T are the mass and temperature of atoms in the plasma, f_{pq} is the absorption oscillator strength of the transition between atomic energy levels p and q and n(p) is the density of atoms in the lower level p. L is a characteristic length of the plasma. Numerically τ_{pq} is given by

$$\tau_{pq} = 2.5\text{x}10^{-6}\ (T[K])^{-\frac{1}{2}}\ n(p)[cm^{-3}]\lambda_{pq}[cm]\ f_{pq}L[cm] \ . \qquad 8.3$$

The significance of τ_{pq}, for a line which is dominantly Doppler broadened - a situation which prevails in our present plasma (Hearn, 1963), is as follows. Suppose that monochromatic radiation of wavelength λ_{pq} is incident in direction x on a semi-infinite plasma slab with intensity I_o per unit solid angle. Then after travelling a distance L through the plasma, the intensity I per unit solid angle in direction x is given by

$$I = I_o e^{-\tau_{pq}} . \qquad 8.4$$

Evidently if $\tau_{pq} << 1$ we may say that a plasma of characteristic dimension L is optically "thin"; all the line radiation due to transitions between levels p and q will escape from it. The situation is not as clear when $\tau > 1$ or even $\tau >> 1$. It is quite possible for a plasma to scatter radiation very effectively (τ large) but if there are *no* inelastic collisions between excited atoms in level q with other species, each photon absorbed is merely re-emitted to eventually escape from the plasma. Thus a plasma may be deep (τ large) but not "thick" (no radiation escapes from the plasma); we shall see such a situation in due course.

Let us now consider the depth of our helium plasma to visible line radiation. A representative line

is the 5876 $\mathring{A}$ 1s3p to 1s2p transition which has an absorption oscillator strength of 0.61 (Wiese et al, 1966) which is far larger than the strength for any of the other visible lines. An upper limit to the number density of atoms in the 2^1P_1 level at any time may be obtained by supposing that each recombination event produces an excited 2^1P_1 neutral (which is a singlet level) and ignoring the fact that about $^3/4$ of the excited helium atoms are actually trapped in the triplet system. Thus we may write

$$A_{21}\, n(2^1P_1) = -\frac{dn_e}{dt}\,, \qquad 8.5$$

where A_{21} (equal to 2×10^9 sec^{-1}; Wiese et al, 1966) is the spontaneous emission probability of the 2^1P_1 level (collisional deexcitation will always be negligible - see Fig. 8.1) and dn_e/dt is the observed electron density decay rate at any instant of time. This equation is valid so long as the plasma is not optically thick to the ultraviolet photons emitted spontaneously by the 2^1P_1 helium atoms - we saw earlier in Sec. 8.3 that this is the case. Using the largest decay rate which is ever observed ($dn_e/dt \simeq 5 \times 10^{18}$ cm^{-3} sec^{-1} at r = 5 cm, 200 μsec; Fig. 8.4) we obtain from eq. 8.5: $n(2^1P_1) = 2.5 \times 10^9$ cm^{-3}. If we substitute this value into eq. 8.3 with T = 300 K which is a lower limit, and L = 8 cm which is an upper

limit, we obtain $\tau_{32} = 0.1$. Thus even taking these extreme values, all of which tend to make the optical depth large, we find that the plasma is optically thin to the 5876 Å line. We conclude that the plasma is definitely optically thin to all its visible lines at all times.

Now let us consider the thickness of the plasma to the ultraviolet lines of helium, all of which result from transitions to the ground state. The best line to consider is the 584 Å $1s2p - 1s^2$ transition which has an absorption oscillator strength of .28 (Wiese et al, 1966) which is substantially greater than the strength for any of the other ultraviolet lines. From the point of view of plasma energy loss, this line is the most important. Reference to Fig. 8.4 shows that the time in the plasma decay when optical thickness is most important is at very early times. Let us consider the instant 200 μsec after plasma preparation, when the electron density (at r = 5 cm) is about 10^{15} cm^{-3} and the electron temperature is about 10^4 K. Estimates of the electron-ion and ion-atom transfer rates for these conditions (see Sec. 8.4) indicate that the atom temperature will not be very much less than 10^4 K. Now anticipating that the plasma will be optically deep, because of the high density of absorbers (ground state

atoms) for the ultraviolet lines, we estimate an upper limit for τ_{12}. If we substitute $n(1) = 2 \times 10^{15}$ cm^{-3} (equal to the neutral filling density less the ion density) and T = 300 K (a gross underestimate) in eq. 8.3 we obtain $\tau_{12} = 860$. The plasma could not be any deeper than this. But it does not necessarily follow that the plasma is optically thick. Reference to Fig. 8.1 indicates that when $n_e = 10^{15}$ cm^{-3} the electron collisional deexcitation rate of helium in the 1s2p state is only about 10^6 sec^{-1} while the spontaneous decay rate of this level is 2×10^9 sec^{-1}. Thus, roughly speaking, when an atom absorbs a 584 Å photon there is only a 1/2000 chance that its energy will be lost to the electron gas as the result of an electron superelastic collision before the atom spontaneously re-emits a 584 Å photon. Hearn (1963) has solved this problem accurately and shown that the fraction of photons lost by the plasma depends on the optical depth τ_{12} as well as a parameter F_o given by,

$$F_o = \frac{n_e Y_{21}}{A_{21} + n_e Y_{21}} \quad . \qquad 8.6$$

Y_{21} is the rate coefficient for deexcitation by electron collision, defined so that $n(2) n_e Y_{21}$ is the total number of deexcitations per cm^3-sec. A_{21} is the spontaneous transition probability for the 2^1P_1 level of helium. Fig.

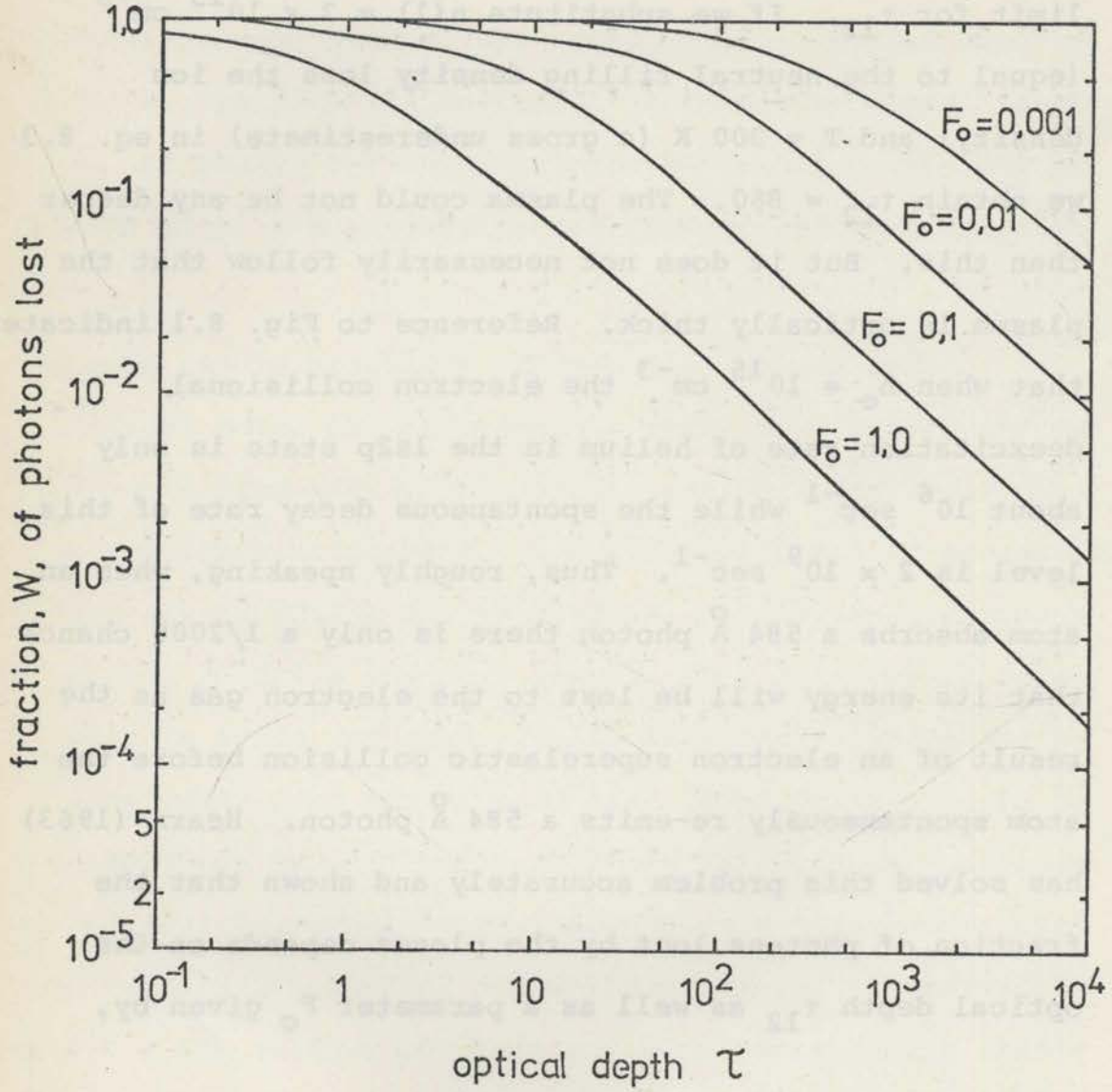

Fig. 8.6. Fraction of photons lost by a plasma as a function of optical depth for a range of values of F_o. If F_o is of the order of unity the plasma is collision dominated and a photon absorbed by an atom is unlikely to be re-emitted. If $F_o \ll 1$ the excited atoms re-emit photons at a much greater rate than they suffer inelastic collisions with electrons; the plasma can then be optically thin even though it is optically deep.

8.6 shows the result computed by Hearn for the fraction W of photons lost by an infinite plasma slab as a function of its optical depth τ for several values of F_o. For F_o of the order of 0.001 and τ_{12} of the order of 900 about 30% of photons emitted are lost; when $n_e < 10^{15}$ cm^{-3} this fraction will increase. But our estimate of τ_{12} was an upper limit. If we allow for the fact that the neutral temperature at the centre of the plasma is actually near to 10,000 K and as a result pressure balance dictates that the neutral density should be somewhat less than 3.3×10^{15} cm^{-3}, perhaps as low as 5×10^{14} cm^{-3}, then τ is only about 40. In this case reference to Fig. 8.6 indicates that 90% of photons emitted would eventually escape from the plasma.

Since these estimates depend rather strongly on the value of F_o we should make the following clarifying comments. The value of the spontaneous emission probability (A_{21} in eq. 8.6) for helium is known accurately to be 2×10^9 sec^{-1} (Wiese et al, 1966). The collisional deexcitation probability Y_{21} is harder to estimate. The value of $n_e Y_{21}$ taken from Fig. 8.1 is based on the calculations of Chen (1967) who used the classical formulation of Gryzinski (1959) to estimate Y_{21}. [Figure 8.1 does not readily allow a precise estimate; calculation using Chen's eq. (5) gives a value of 8×10^{-10} cm^{3}sec^{-1} for Y_{21}.]

Although there is no direct experimental verification of this estimate it has been widely used for calculating collisional-radiative recombination rates, in fairly good agreement with experimentally measured decay rates (e.g. see Robben et al, 1963, and the comments of Bates et al, 1967). It appears that our estimate of $n_e Y_{21}$ could not be in error by as much as an order of magnitude in which case the conclusion that our plasma is at least partly optically thin (to 584 Å radiation) is not affected. In support of this, we note that the helium plasma studied by Chen exhibited partial optical thinness for conditions similar to ours (see also Newton and Sexton, 1968).

The purpose of these calculations was to find out which collisional-radiative recombination rate should describe the decay of our plasma. We now see that the experimental decay rate should lie between that calculated by Drawin and Emard for a plasma optically thin to all lines (Drawin and Emard, 1971; fig. 2) and the value for a plasma which is thin to visible lines and thick to resonance (ultraviolet) lines (Drawin and Emard; fig. 3). The present calculations show that the plasma should be nearer to being thin than thick, in agreement with experimental observations in Sec. 8.3 (Fig. 8.4).

8.3.2 Plasma Diffusion

The reader will recall that we commenced Sec. 8.3 by assuming that plasma diffusion across our large (9 kG) magnetic field is negligible. However, some experimental results indicated that plasma diffusion may be taking place. The results of calculated diffusion rates were then presented.

In this section we show how these diffusion results were obtained.

The diffusion of charged particles through a plasma is governed by Fick's law (McDaniel, 1964; p.495),

$$\frac{\partial n}{\partial t} = \underset{\sim}{\nabla} \cdot (D \underset{\sim}{\nabla} n) \qquad 8.7$$

where n is the number density of charged particles at a point and D is an appropriate diffusion coefficient. D is a property of the particles themselves and the background through which they are diffusing. The diffusion coefficient which is appropriate for our helium plasma is that for a highly ionized gas in a large magnetic field. In this case Golant (1963) has shown that the coefficients for diffusion parallel to and perpendicular to the magnetic field are given by :

$$D_{\parallel} = \frac{k(T_i + T_e)}{m_i \nu_{in}} \qquad 8.8$$

and

$$D_{\perp} = \frac{k(T_e + T_i)}{m_i \nu_{in} \left[1 + \frac{\omega_{ce}\omega_{ci}}{\nu_{in}(\nu_{ei} + \nu_{en})}\right]} . \qquad 8.9$$

In these equations the subscripts e, i and n stand for electrons, ions and neutrals respectively; k is Boltzmann's constant and m and T are mass and temperature respectively. ν_{ab} is the collision frequency for momentum transfer between species a and b and ω_{ci} and ω_{ce} are the ion and electron cyclotron frequencies. It is implicit in eqs. 8.8 and 8.9 that

$$m_i \nu_{in} >> m_e \nu_{en} . \qquad 8.10$$

The justification for this assumption will appear below (Table 8.2).

In order to calculate the effects of diffusion in our helium plasma we need to estimate the collision frequencies for the range of temperatures and densities of interest.

The electron-ion collision frequency is given (to an accuracy of 10%; Banks, 1966a) by

$$\nu_{ei} = \frac{3.6\ n_e[cm^{-3}]\ \ell n\ \Lambda}{(T_e\ [K])^{3/2}}\ , \qquad 8.11$$

where n_e and T_e are the electron temperature and density respectively and Λ is the ratio of the cutoff radii in the integral for the total Coulomb scattering cross-section. $\ell n\ \Lambda$ is a slowly varying function of n_e and T_e and for our plasma it is appropriate to let $\ell n\ \Lambda = 6$ (Spitzer, 1962).

Electron-neutral collisions may be treated as hard-sphere collisions and accordingly their collision frequency is given by

$$\nu_{en} = n_n v_t \sigma \qquad 8.12$$

where n_n is the neutral density, v_t is the average thermal speed of electrons and σ is the cross-section for momentum transfer. For electrons in Helium the appropriate value of σ is $7.5 \pm .8 \times 10^{-16}$ cm^2 for electron temperatures up to about 1 eV (Banks, 1966a).

Ion-neutral collisions in helium are dominated by charge exchange processes at all temperatures of interest (Banks, 1966b) and the collision frequency for momentum transfer is (Banks, 1966b)

$$\nu_{in} = 8.7 \times 10^{-13}\ n_n (T_i+T_n)^{\frac{1}{2}} \left[11.6-1.04\ \log_{10}(T_i+T_n)\right]^2 . \qquad 8.13$$

Helium: p = 100 mtorr, $n_n = 3.3 \times 10^{15}$ cm^{-3}, $B_o = 9$ kG.

n_e	T_e	ν_{ei}	ν_{en}	ν_{in}
10^{15}	10,000	2.2×10^{10}	4.7×10^{9}	2.0×10^{7}
4×10^{14}	6000	1.9×10^{10}	4.5×10^{9}	1.7×10^{7}
10^{14}	4000	8.5×10^{9}	2.9×10^{8}	1.4×10^{7}
4×10^{13}	3000	5.3×10^{9}	1.0×10^{8}	1.3×10^{7}
10^{13}	1500	3.7×10^{9}	1.8×10^{7}	1.0×10^{7}
4×10^{12}	1000	2.8×10^{9}	5.9×10^{6}	0.9×10^{7}
cm^{-3}	K	sec^{-1}	sec^{-1}	sec^{-1}

$$\omega_{ce} = 1.6 \times 10^{11} \text{ sec}^{-1}$$
$$\omega_{ci} = 2.2 \times 10^{7} \text{ sec}^{-1}$$

Table 8.2. Collision frequencies for representative densities and temperatures in the decay (at r = 5 cm) of the SUPPER I helium plasma.

Here n_n (cm^{-3}) is the neutral density and T_i and T_n (K) are the ion and neutral temperatures respectively.

Equations 8.11, 8.12 and 8.13 allow us to calculate the collision frequencies of interest for a range of temperatures and densities corresponding (approximately) to the decay of the helium plasma at r = 5 cm. These data are presented in Table 8.2. We have, for the purpose of making these estimates, assumed that $T_i = T_n = T_e$ which is reasonable for our plasma (see Sec. 8.4).

We are now in a position to estimate the radial and longitudinal diffusion rates of our plasma. We consider axial diffusion first. In this case the time constant τ for axial diffusion (in the fundamental mode) is given approximately by (McDaniel, 1964; p.506)

$$\tau = \frac{L^2}{D_{||}\pi^2} \qquad 8.14$$

where L is the length of the plasma. Using Table 8.2 and eqs. 8.8 and 8.14 we find that at early times τ is about 30 msec and increases by a factor of about five at later times. Since the observed decay time-constant of the plasma is about 1 msec we conclude that axial diffusion is unimportant.

Let us consider the more interesting case of radial diffusion. Referring to Table 8.2 we see that

$$\frac{\omega_{ce}\omega_{ci}}{\nu_{in}(\nu_{ei} + \nu_{in})} >> 1$$

so that the radial isothermal diffusion coefficient $D_\perp$ (eq. 8.9) may be written as

$$D_\perp = \frac{k(T_e + T_i)\ (\nu_{ei} + \nu_{en})}{m_i \omega_{ce}\omega_{ci}} \quad . \qquad 8.15$$

Further, reference to Table 8.2 indicates that we will introduce an error of only 20% at early times and considerably less at later times by neglecting ν_{en} in eq. 8.15; thus electron-ion collisions determine the radial diffusion rate in our plasma. In this approximation $D_\perp$ is the same as the value given by Golant (1963) and Spitzer (1962; p.43) for a fully ionized gas. Numerically $D_\perp$ is now given by

$$D_\perp = \frac{2.6 \times 10^{-10}\ n_e[cm^{-3}]}{(T_e[K])^{\frac{1}{2}}}\ cm^2 sec^{-1} \qquad 8.16$$

where we have substituted for ν_{ei} from eq. 8.11 (with $\ell n\ \Lambda = 6$).

At this stage a few comments on this approach are appropriate as the treatment of Golant (1963) has several shortcomings. Firstly, Golant considers only an isothermal situation wherein diffusion results from a

number density gradient $\underset{\sim}{\nabla}n$ only. However the strong temperature gradients in our plasma (Fig. 8.3) will surely cause some thermal diffusion. Within the framework of Golant's analysis temperature gradients may easily be included by replacing the number density gradient $\underset{\sim}{\nabla}n$ in eq. 8.7 by $\underset{\sim}{\nabla}\overline{n\ T}/T$ and diffusion may be considered to be driven by the partial pressure gradient

$$\underset{\sim}{\nabla}p = kT\underset{\sim}{\nabla}n + nk\underset{\sim}{\nabla}T \quad , \qquad 8.17$$

in agreement with Spitzer (1962; p.43) for a fully ionized gas.

A second shortcoming of Golant's analysis is that it is based on the equations of motion of electrons and ions, treating collisions with all particles as simple binary encounters in terms of phenomenological collision frequencies. A more precise analysis for a fully ionized gas (Shkarofsky et al, 1966), which uses the Fokker-Planck equation to treat electron-ion interactions more realistically, shows that the situation is not nearly as simple as eq. 8.17 indicates. Using Shkarofsky et al's eqs. (8 - 109c) and (8-112d) we may show that if we use Golant's diffusion constant the total pressure gradient driving the diffusion must be modified to

$$\underset{\sim}{\nabla}p)_{\text{effective}} = g_\sigma \underset{\sim}{\nabla}(nkT) - \frac{5}{4}\left[\frac{h_\mu g_\sigma - h_\sigma g_\mu}{\left(\frac{\nu_{ei}}{\omega_{ce}}\right) g_\mu^2 + h_\mu^2}\right] nk\underset{\sim}{\nabla}T \qquad 8.18$$

where the g's and h's are numerical functions of ω_{ce}/ν_{ei} of the order of unity. For our plasma conditions we obtain from Shkarofsky et al (1966) (or more conveniently from Shkarofsky et al, 1963),

$$g_\mu \simeq 0.4 \qquad h_\mu \simeq 1$$
$$g_\sigma \simeq 0.8 \qquad h_\sigma \simeq 1 \qquad 8.19$$

so that eq. 8.18 becomes

$$\underset{\sim}{\nabla}p)_{\text{effective}} \simeq 0.8\ kT\underset{\sim}{\nabla}n + 0.3\ nk\underset{\sim}{\nabla}T \quad . \qquad 8.20$$

Thus the full analysis indicates that the diffusion due to number density gradients is not quite as great as the simple theory predicts and the thermal diffusion is only about one third as large as predicted (c.f. eq. 8.17). Calculations for our plasma indicate that $\underset{\sim}{\nabla}T/T$ is generally of the same order as $\underset{\sim}{\nabla}n/n$ so eq. 8.20 indicates an error of only 10% if we assume that diffusion is driven by the pressure gradient

$$\underset{\sim}{\nabla}p)_{\text{effective}} = kT\underset{\sim}{\nabla}n \qquad 8.21$$

and ignore thermal diffusion altogether. This is the method which will be adopted in our subsequent calculations. Since it is not altogether clear how applicable the results of Shkarofsky et al will be for our not-fully ionized plasma a more accurate approach is not justified.

The method of evaluating diffusion rates was as follows: Equation 8.16 was substituted into eq. 8.7 and the derivatives were evaluated (in cylindrical coordinates) to give

$$\frac{\partial n}{\partial t} = \frac{2.6\times10^{-10}}{T^{\frac{1}{2}}} \left[\frac{n}{r}\frac{\partial n}{\partial r} + \left(\frac{\partial n}{\partial r}\right)^2 - \frac{n}{2T}\frac{\partial T}{\partial r}\frac{\partial n}{\partial r} + n\frac{\partial^2 n}{\partial r^2} \right] \text{cm}^{-3}\text{sec}^{-1} \qquad 8.22$$

where n is in cm^{-3} and T is in K.

At the r = 5 cm position in the plasma the various terms in eq. 8.22 were estimated from the electron density (Fig. 7.3; p.7.9) and electron temperature (Fig. 8.3) profiles, for a number of times in the decay of the plasma. The results are plotted in Fig. 8.4 and were discussed in Sec. 8.3.

At the r = 0 cm position eq. 8.22 takes the simple form,

$$\frac{\partial n}{\partial t} = 2.6 \times 10^{-10} \frac{n}{T^{\frac{1}{2}}} \frac{\partial^2 n}{\partial r^2} \text{ cm}^{-3} \text{ sec}^{-1} \qquad 8.23$$

This equation was used to estimate the diffusion rates at the centre of the plasma at both early (Table 8.1) and late (Fig. 8.5) times in the decay of the plasma. The method adopted was to match the experimental profile with a simple analytic function near the centre of the plasma in order to obtain its second derivative. Since the second derivative depends sensitively on the shape of the function at $r = 0$ this method can only be considered to give very approximate estimates of the diffusion rate.

This concludes our calculations of diffusion rates in the SUPPER I helium plasma. The results of these calculations were used in the analysis of the decay process of the plasma which was presented earlier in Sec. 8.3 and were discussed then.

Having completed our discussion of the decay process of the plasma we turn our attention in the next section to the ways in which it may lose its energy.

8.4 Thermal Economy of the Helium Plasma

We now wish to examine the thermal economy of the decaying helium plasma. This is a rather complex problem, partly because of the nature of the electron temperature and density distribution of the plasma, partly because of the complexities of the atomic structure of helium, and partly because of our limited knowledge of the plasma characteristics. We are in a position, however, to distinguish some salient points. For these reasons we shall restrict our attention to the late decay of the plasma, that is, the period after 1000 μsec, when the plasma has adopted a fairly simple radial structure with a central electron density of less than 10^{14} cm^{-3} and central temperature of less than 4000 K. We shall simply consider the behaviour of the plasma on the vessel axis.

The rate of internal energy loss of the plasma per unit volume is given by,

$$\frac{dE}{dt} = \frac{d}{dt}\left(\frac{3}{2} n_n k T_n\right) + \frac{d}{dt}\left(\frac{3}{2} n_i k T_i\right) + \frac{d}{dt}\left(\frac{3}{2} n_e k T_e\right) + I \frac{dn_e}{dt} . \qquad 8.24$$

Since n_e and n_i are less than about 10^{14} cm^{-3} and n_n is of the order of 10^{15} cm^{-3} the second and third terms of the right hand side of eq. 8.24 are negligible. The liberation

of ionization energy, I, which occurs at recombination is an important term in eq. 8.24 and is one which presents several problems.

The three-body recombination process, which is far more important than radiative recombination, forms highly excited neutrals which give up an amount of energy I in relaxing to the ground state. These neutrals are de-excited partly by electron collisions, partly by spontaneous radiative transitions and partly by deexcitation at the vessel walls. Thus part of the ionization energy is lost as radiation, part goes towards heating the remaining electrons and part is lost to the walls. We can say roughly that the downward transitions will be collision induced down to the bottleneck level (Sec. 8.1.1) then mainly radiative down to the n = 2 state. One quarter of them will be in the singlet system and three quarters in the triplet system. Now since the energy of these n = 2 states is more than 80% of the ionization energy of helium we can in the present analysis neglect radiation losses by visible line radiation, but it is important to determine the fate of the excited atoms in the n = 2 state. We have seen that the plasma is essentially optically thin to the ultraviolet lines resulting from transitions to the 1^1S_0 ground state in the singlet system, the principal line being the 584 $\mathring{A}$ 2^1P_1 to 1^1S_0 transition. Thus we can

estimate that the radiative energy loss of the singlet system is about equal to the rate of populating the n = 2 singlet levels multiplied by their energy which is 0.87 I.

Since these levels are populated by radiative transitions down from the bottleneck level they will be populated at the rate that this level is depopulated which is about ¼ dn_e/dt (Byron et al, 1962; Chen, 1967; Bates et al, 1967). Thus we can estimate that the rate of radiative loss from the singlet system is ¼ x 0.87 I dn_e/dt. For our present purposes it is sufficiently accurate to suppose that the total radiation loss-rate is ¼ Idn_e/dt. The other three quarters of the recombination energy is trapped in the triplet system, principally in the 2^3S_1 metastables. The energy of these metastables may be lost by superelastic collisions with electrons, diffusion to the vessel walls or by electron collisional excitation into the nearest level which may make an allowed transition to the ground state. Since this state (2^1P_1) is 1.4 eV above the 2^3S_1 state, an energy difference much greater than the average electron energy, the major metastable removal processes will be electron collisional deexcitation and diffusion.

Let us evaluate the importance of metastable diffusion by comparing the probability of electron

t	n_e	T_e	$n_e K(2,1)$	$1/\tau$
1000	10^{14}	4000	1.4×10^5	3.4×10^3
1355	4×10^{13}	2720	5.6×10^4	2.8×10^3
1815	10^3	1520	1.3×10^4	2.1×10^3
2220	4×10^{12}	1210	5.2×10^3	1.9×10^3
μsec	cm^{-3}	K	sec^{-1}	sec^{-1}

t = Time.
n_e = Electron density.
T_e = Electron temperature.

Table 8.3. Comparison of the collisional deexcitation rate ($n_e K(2,1)$) of helium 2^3S_1 metastables with the diffusion loss rate ($1/\tau$) for representative times in the late decay of the plasma.

collisional deexcitation with the diffusion decay rate. Now, the form of our density (Fig. 7.3; p.7.9) and temperature (Fig. 8.3) profiles after 1000 μsec is not unlike the Bessel function $J_o\left(\frac{2.4r}{R}\right)$ (where r is the radial coordinate and R is the vessel radius) which is the fundamental diffusion mode for our vessel geometry (McDaniel, 1964; p.503). Thus a suitable decay rate is the reciprocal of the time constant τ of this mode. McDaniel shows that τ is given by

$$\tau = \frac{1}{D}\left(\frac{R}{2.4}\right)^2 \qquad 8.25$$

where D here is the metastable diffusion constant.

Phelps (1955) has measured the diffusion coefficient for 2^3S_1 metastables at room temperature, and since it should scale as $T^{\frac{1}{2}}$ (McDaniel, 1964; p.50) we can easily obtain estimates for temperatures of interest. Table 8.3 compares the probabilities of deexcitation and loss by diffusion for representative times late in the decay of the plasma. The collisional deexcitation rate was calculated from the coefficient K(2,1) given by Bates et al (1967) which is based on measurements of the excitation cross section. It can be seen that metastable diffusion can be neglected except very late in the decay when the number of electrons is very small. The effect

of metastable diffusion is that each metastable lost carries with it most of the ionization energy I which would otherwise have found its way to the electrons. Thus we see that during most of the decay about three quarters of the ionization energy from each three-body recombination event is eventually given up to the plasma electrons. We now examine how the electrons may lose this energy which must ultimately reach the vessel walls.

Because of the large superimposed magnetic field we expect that thermal conduction by the ions and electrons in our plasma will be negligible. Calculation of the thermal conductivity for a fully ionized gas (Spitzer, 1962; p.145) does indeed yield values much smaller than the known thermal conductivity of neutral helium gas (Saxena and Saxena, 1968). Therefore, we are led to suspect thermal conduction by the background neutral gas as the major energy removal process. Before calculating the expected thermal conduction rate however, it is pertinent to ask how the electrons may lose their energy to the neutral helium atoms. It is shown by Banks (1962a) that in general the rate of energy loss of species 1 by elastic collisions with species 2 is given by

$$-\frac{dU_1}{dt} = 3n_1 \cdot \frac{m_1 m_2}{(m_1 + m_2)^2} \cdot k(T_1 - T_2)\nu_{12} \qquad 8.26$$

t	n_e	T_e	ν_{ei}	ν_{en}	ν_{in}	ν_{ni}	ν_{nn}
1000	10^{14}	4000	8.5^9	2.9^8	1.4^7	4.2^5	2.7^6
1355	4^{13}	2700	5.8^9	9.5^7	1.3^7	1.6^5	2.2^6
1815	10^{13}	1500	3.4^9	1.8^7	1.0^7	3.0^4	1.6^6
2220	4^{12}	1200	2.4^9	6.2^6	0.9^7	1.1^4	1.5^6
μsec	cm^{-3}	K	sec^{-1}	sec^{-1}	sec^{-1}	sec^{-1}	sec^{-1}

In this table numbers like 8.5^9 should be read as 8.5×10^9.

t	T_e	ΔT_{ei}	ΔT_{in}	indirect ΔT_{en}	direct ΔT_{en}
1000	4000	100	30	130	2800
1355	2700	280	70	350	1700
1815	1500	470	90	560	9000
2220	1200	560	80	640	2.2×10^5
μsec	K	K	K	K	K

t = Time after plasma preparation.
n_e = Electron Density.
T_e = Electron Temperature.
ΔT_{12} = Temperature difference between species 1 and 2 required to transfer energy at the rate $3/4$ I dn_e/dt.
ν_{12} = Number of collisions per second experienced by a particle of species 1 with particles of species 2.

Table 8.4. Collision frequencies and interparticle temperature differences on axis of the SUPPER I helium plasma for representative times in the late decay. The upper table shows all of the collision frequencies of interest. The lower table shows the interparticle temperature differences which would be required to transfer energy between the respective particle species at the rate $3/4$ I dn_e/dt.

where m_1 and m_2 are the masses of the two species, T_1 and T_2 are their temperatures and ν_{12} is the collision frequency for momentum transfer. n_1 is the number density of particle species 1 and k is Boltzmann's constant. Now the two major routes whereby the electrons may lose energy to the atoms are by direct collisions or by collisions with ions which then pass their energy on to the atoms. It is clear (from eq. 8.26) that electron-ion and electron-neutral collisions are equally efficient for energy transfer but we expect the electron-ion collisions to be much more frequent than electron-neutral collisions. In the first instance therefore, the electrons are more likely to lose their thermal energy to the ions than to the atoms. Since charge exchange processes lead to quite a large ion-neutral collision rate the ions may readily pass this energy on to the neutrals. These points are illustrated by the figures in Table 8.4. This table shows, for a representative set of times in the late decay of the plasma, the collision frequencies of interest and the temperature differences which must exist between the different particle species in order to transfer energy at the rate $^3/4\ I\ dn_e/dt$ where I is the ionization energy of helium. Evidently the energy must pass from the electrons to the ions and then from the ions to the atoms. At the earlier times all three particle species are at about the same temperature,

but at very late times when the electron (and the ion) density is low the interparticle temperature differences become large compared with the electron temperature.

Let us now consider thermal conduction in more detail. The thermal conductivity of helium in thermodynamic equilibrium has been measured by Saxena and Saxena (1968) for temperatures up to 1,350 K, less accurately by Blais and Mann (1960) for temperatures up to 2,000 K and estimated theoretically by Lick and Emmons (1965) for temperatures up to 50,000 K. For temperatures up to 10,000 K these values all fit the curve,

$$\kappa = \kappa_o T^{3/4} \qquad 8.27$$

where $\kappa_o = 2.3 \times 10^{-5}$ watt cm^{-1} $K^{-7/4}$, to an accuracy of about ± 20%. In our plasma the ion density is one to two orders of magnitude greater than the density in equilibrium helium (Lick and Emmons, 1965) so it is pertinent to enquire into the possibility of ion-neutral collisions changing the thermal conductivity from the value given by eq. 8.27. Because the charge-exchange cross-section for these collisions is considerably greater than the cross-section for neutral-neutral collisions (Banks, 1962b) the neutral-ion collision rate may approach the neutral-neutral collision rate even though the ion density is much less

than the neutral density. We compare these collision rates in Table 8.4, for representative times in the late decay of the plasma. The neutral-ion collision frequency is calculated from eq. 8.13 and the estimates of the neutral-neutral collision frequency were based on hard-sphere collisions between helium atoms (collision diameter 2 $\mathring{A}$; McDaniel, 1964; p.35). It will be seen that at the highest densities of interest here, the neutral-ion collision frequency is about one fifth of the neutral-neutral collision frequency. Now the thermal conductivity of a gas is given by

$$\kappa = \frac{1}{3} nc\lambda\bar{v} \quad , \qquad 8.28$$

where n, λ and $\bar{v}$ are the number density, mean free path and the average thermal speed of the gas molecules and c is the specific heat per molecule. The ion-neutral collisions reduce λ but do not affect any of the other quantities, thereby reducing the thermal conductivity. Thus we would expect that at the highest densities encountered in the late decay of the plasma the value of the thermal conductivity given by eq. 8.27 would be reduced by about 20% by ion-neutral collisions. An effect of this magnitude is inconsequential in the present analysis. However we should note that at the higher ion densities occurring earlier in the helium decay ν_{ni} is

up to three times as large as ν_{nn}. At these densities the thermal conductivity would be reduced by a factor of about four.

Having seen that we may, for our present purposes, write the thermal conductivity as in eq. 8.27 we shall consider the rate of conduction from the centre of the plasma from 1000 μsec onwards. Since the major energy source is from recombination, which is occurring throughout the plasma but principally near its centre we use the following simple model. We suppose that the plasma consists of a uniform rod, of radius r_c, of plasma liberating energy at a rate Q watts cm^{-3} throughout its volume and surrounded by unionized helium conducting heat to the vessel walls. The background neutral gas in the central region is responsible for heat conduction in that region. At any point in the vessel where the power dissipation density is P watts cm^{-3} we have,

$$P = - \underset{\sim}{\nabla} \cdot (\kappa \underset{\sim}{\nabla} T) \qquad 8.29$$

where P = Q or zero depending on position. Since the length of the vessel is much greater than its diameter we may neglect the effects of axial conduction. Therefore, integrating eq. 8.29 over a cylindrical volume of radius r and applying Green's theorem we find,

t	T_n	$\frac{3}{4} I\frac{dn_e}{dt}$	$\frac{d}{dt}(\frac{3}{2}n_n kT_n)$	Q_{exp}	Q_{cond}
1000	3870	0.45	0.06	0.51	2.2
1355	2370	0.36	0.08	0.44	0.94
1815	960	0.09	0.05	0.14	0.16
2220	560	0.03	0.01	0.04	0.06
sec	K	W cm^{-3}	W cm^{-3}	W cm^{-3}	W cm^{-3}

t = Time after plasma preparation.

T_n = Central atom temperature (from Table 8.4).

$Q_{exp} = \frac{3}{4} I\frac{dn_e}{dt} + \frac{d}{dt}\frac{3}{2}(n_n kT_n)$.

Q_{cond} = Theoretical conduction rate calculated from eq. 8.31 using T_n from Table 8.4 and T_w = 300 K.

Table 8.5. Comparison of the theoretical thermal conduction rate (Q_{cond}) with the rate of change of plasma internal energy (Q_{exp}) which is not accounted for by radiation. The conduction rate is based on central atom temperatures sufficiently below the electron temperature to allow indirect electron-atom energy transfer at a rate 3/4 Idn_e/dt (see Table 8.4).

$$T(r)^{7/4} - T(r_c)^{7/4} = \frac{7Qr_c^2}{8\kappa_o} \ell n \frac{r_c}{r} \quad ; \quad r \geq r_c$$

and, 8.30

$$T(r)^{7/4} - T(o)^{7/4} = - \frac{7Q}{16\kappa_o} r^2 \quad ; \quad r \leq r_c \ .$$

Combining these two equations we obtain,

$$Q = \frac{16\kappa_o (T_n^{7/4} - T_w^{7/4})}{7r_c^2 (1 + 2\ell n(R/r_c))} \qquad 8.31$$

where T_n is the central atom temperature, T_w is the temperature of the vessel wall and R is the vessel radius. Inspection of the electron density (Fig. 7.3, p.7.9) and temperature (Fig. 8.3) profiles indicates that a value of r_c of 5 cm should be appropriate.

We are now in a position to compare the expected thermal conduction rate, Q, at the centre of the plasma, with that part of the rate of change of internal energy which must be carried off by the electrons, $^3/4$ I dn_e/dt, plus the neutral cooling term $d/dt(^3/2\ n_n k T_n)$. Table 8.5 shows our estimates of these two terms compared with the rate Q for thermal conduction (eq. 8.31) based on central atom temperatures T_n obtained from Table 8.4. The values of dn_e/dt were simply obtained from the measured electron

density decay (Fig. 7.6, p.7.14) and the values of $d/dt(^3/2\ n_n kT_n)$ were obtained by plotting the temperatures T_n given in Table 8.4 to obtain the rate of change. Because the acoustic wave transit time for our vessel is somewhat less than the decay time, pressure balance dictates that the product $^3/2\ n_n kT_n$ should be constant throughout the vessel at any instant of time. By assuming a parabolic electron temperature profile (T_n at vessel centre, 300 K at vessel walls) we have allowed for this effect in calculating $d/dt(^3/2\ n_n kT_n)$.

Reference to Table 8.5 indicates that atom thermal conduction can easily account for the observed rate of energy loss of the plasma at all times. However the calculated conduction rate exceeds the observed rate by a factor of up to four at early times. This is probably due to the flat form of the electron temperature profile (Fig. 8.3) (and therefore the atom temperature profile) over a large central region of the plasma at these early times. This does not conform well with the shape predicted by our simple model (eqs. 8.30). Nevertheless, the figures in Table 8.5 indicate clearly that the plasma loses its energy to the vessel wall by thermal conduction through the background neutral gas.

8.5 Summary

We have found that the decay of the helium plasma prepared in a 9 kG magnetic field is dominated by the collisional-radiative recombination process, but that at early times some plasma diffusion results from steep electron temperature and density gradients set up in the preparation process. This diffusion is responsible for the filling in of the central hollow of the plasma. Later in the decay where diffusion can be shown theoretically to have a negligible effect good agreement is obtained with the numerical results of Drawin and Emard's collisional-radiative recombination theory for helium.

The escape of energy from the plasma was shown to be dominated by thermal conduction by the neutral atoms, even though the plasma was at least partly optically thin to the ultraviolet lines arising from transitions to the ground state. This was so because about three quarters of the three body recombination events lead to the formation of triplet metastable states, each carrying about 80% of the helium ionization energy, and these states have no allowed radiative transitions to the ground state.

Appendix 1

Far-Infrared Detectors

For the observations described in this thesis two far-infrared detectors were used. They were:

(1) a room-temperature Golay cell (Unicam Instruments, Cambridge, England) and,

(2) a liquid helium cooled Putley detector (Advanced Kinetics, Costa-Mesa, California, U.S.A. - Model IRD-4A).

We shall briefly summarize the properties of these detectors in the two sections which follow.

A1.1 The Golay Cell

The Golay cell (Golay, 1947) is a pneumatic thermal detector (Putley and Martin, 1967; p.127) which has the very important advantage of working at room temperature.

Since the Golay cell relies for its operation on the absorption of radiation by a small sample of gas it has a long response time - about 25 msec. It is essentially a broadband detector; the principal wavelength limitations are imposed by the transmission qualities of its entrance window and diffraction effects at long wave-

lengths. Our Golay cell is fitted with a 3 mm diameter diamond window and thus it is quite sensitive throughout the far-infrared.

The Golay cell has a nominal responsivity of 2×10^5 volts per watt and a noise equivalent power of about 10^{-10} watt in a bandwidth of 1 Hz. Golay cells are generally used with steady radiation, chopped at about 10 Hz. Under these conditions they are linear up to output voltages of the order of 1 volt - equivalent to about 10^{-5} watts, average.

When detecting far-infrared laser pulses our Golay cell generally received peak powers far greater than 10^{-5} W at its entrance window. However we were careful to ensure that the average power level was always limited to somewhat less than 10^{-5} W. Since the laser pulses last for only tens of microseconds (e.g. see Fig. 2.5(a), p.2.18), and the Golay cell response time is much longer than this, then its response to HCN laser pulses is just its "impulse-response" (Bracewell, 1965) which is equivalent to its frequency response. It follows that the integral of the Golay cell response to our HCN laser pulses must be its step response; integration of the experimental record shown in Fig. 2.5(b) (p.2.18) clearly indicates a rise-time of about 25 msec.

It is quite straightforward to show that the area under the response of the Golay cell to an HCN laser pulse, integrated along the time axis only as far as the point where it becomes negative (at about 25 msec in Fig. 2.5(b); p.2.18) is simply proportional to the laser pulse energy. The proportionality constant is just the reciprocal of the Golay cell responsivity.

Since we observed that the time-dependence of the Golay cell response was independent of its height for several orders of magnitude of laser pulse energy (an indication of good linearity) then its area was simply proportional to its height. Thus we were able to measure laser pulse energy (in arbitrary units) by simply measuring the height of the Golay cell response to the laser output.

A1.2 The Putley Detector

The Putley detector (Putley, 1963) is a free-carrier photoconductive device in which the active element is an n-type indium antimonide (InSb) crystal immersed in liquid helium. It relies for its operation on the fact that its carriers (electrons) have a very low thermal capacity (effective mass ≈ 0.013 x electron mass) and are very weakly coupled to the crystal lattice. Radiation incident on the crystal is absorbed by the carrier

electrons, they rapidly thermalize its energy among themselves, and their temperature rises well above that of the crystal lattice which remains at the temperature of the liquid helium in which it is immersed.

Since the electrical conductivity of such a crystal depends on the temperature of its carriers, radiation may be detected by biasing the crystal with a constant current and measuring the voltage which appears between its terminals. [Our detector uses bias currents between 100 μA and 500 μA.]

The combination of low thermal capacity of the carriers and their weak coupling to the crystal lattice gives the Putley detector a very short rise-time. In addition, the low operating temperature combined with the low resistance (e.g. 100 Ω in zero magnetic field) of typical samples leads to a low noise equivalent power. The response time and noise equivalent power of the Putley detector are of the order of 0.2 μsec and 10^{-11} Watt (in a bandwidth of 1 Hz) respectively.

Because the free-carrier photoconductivity mechanism has no energy threshold the Putley detector is essentially broadband in operation. The response diminishes at short wavelengths (< 100 μm, but it has useful response to ≃ 20 μm) due to reduced absorption by the

carrier electrons and at long wavelengths (several mm) due to the small size of practical far-infrared detector samples compared with the wavelength.

Large magnetic fields may be used to enhance the responsivity of the Putley detector in two different ways. For very high fields (e.g. 20 kG and larger) the cyclotron frequency of the free carriers (with their reduced mass) is in the far-infrared and gives rise to enhanced, narrow-band detection at the cyclotron frequency. However this tunable mode does not work for fields less than about 8 kG (Putley and Martin, 1967). Thus the tunable mode cannot be used for detection of the 337 μm wave frequency (890 GHz) which (for a carrier effective mass of 0.013 electron masses) corresponds to a magnetic field of only 6.5 kG.

In general however, a large magnetic field can be used to increase the responsivity of the Putley detector by "freezing-out" free-carriers (Putley and Martin, 1967) and raising the resistance of the InSb crystal. This effect is generally limited to fields below about 10 kG; above this, the tunable mode enhances the responsivity at the carrier cyclotron frequency but reduces it elsewhere. However the maximum field for broadband enhancement of responsivity depends on the particular crystal sample. With our detector, the responsivity at 337 μm increases

monotonically with magnetic field strength up to the maximum attainable value of 36 kG although there is not very much improvement from 25 kG to 36 kG.

For most of the observations described in this thesis the Putley detector was operated with a magnetic field of 25 kG. At this field strength the responsivity was of the order of a few hundred volts per watt.

The rise-time of the detector system was limited by the post-detector amplifier system but was less than 0.5 μsec.

Appendix 2

Line Broadening in HCN Lasers

The two processes which broaden the 337 μm HCN emission line are the Doppler effect and collision (or pressure) broadening. In this appendix (Sec. A2.1) we calculate the classical Doppler and collision linewidths for a HCN molecule in our pulsed HCN laser. We base the calculation on optimum operating conditions (Sec. 2.3.3.3). Since the classical Doppler and collision linewidths are comparable in magnitude in our lasers we then consider the possibility of collisional narrowing (Dicke, 1953) of the Doppler contribution to the total linewidth (Sec. A2.2). We conclude with a discussion concerning the validity of classical collision linewidth calculations (Sec. A2.3). The latter two sections allow us to view the present simple calculations (Sec. A2.1) in the correct perspective.

A2.1 Classical Calculation of Doppler and Collision Linewidths

The Doppler linewidth (full width at half power) for an emitter of mass m (molecular weight M) and absolute temperature T radiating at frequency f_o is (Townes and Schawlow, 1955),

$$\Delta f_D = \sqrt{\frac{8\ \ell n(2) kT}{mc^2}} \cdot f_o \qquad \text{A2.1}$$

$$= 7.2 \times 10^{-7} \sqrt{\frac{T}{M}} \cdot f_o$$

where k is Boltzmann's constant and c is the velocity of light in vacuum.

Pressure Broadening has linewidth,

$$\Delta f_P = \frac{1}{\pi \tau} \qquad \text{A2.2}$$

where τ is the time between dephasing collisions (Townes and Schawlow, 1955).

Equation A2.1 gives an accurate estimate of the Doppler linewidth in the absence of collisions while eq. A2.2 gives only a rough estimate of the collision linewidth (see Sec. A2.3). However eqs. A2.1 and A2.2 are good enough to allow us to calculate the relative magnitudes of the contributions from the two sources of broadening.

We estimate τ, the time between collisions of an HCN molecule (collision diameter $D_H \simeq 10$ Å; Townes and Schawlow, 1955) in a background of methane and nitrogen (collision diameters $D_C \simeq 3.8$ Å and $D_H \simeq 4.1$ Å respectively; McDaniel, 1964; p.35) as follows:

Assuming "hard-sphere" collisions the collision rate of an HCN molecule with N_2 molecules is,

$$Z_N = \pi\, n_N \left(\frac{D_H + D_N}{2}\right)^2 \bar{v} \qquad \text{A2.3}$$

where n_N is the nitrogen number density and,

$$\bar{v} = \sqrt{\frac{8\ kT}{\pi\mu}} \qquad \text{A2.4}$$

is the average relative thermal speed of nitrogen and hydrogen cyanide molecules. μ is the reduced mass of the two species. A similar expression gives the rate for collisions with CH_4 molecules. Then, combining eqs. A2.2 to A2.4 the total collision rate for nitrogen and methane in the ratio 1:2 becomes

$$Z \equiv \frac{1}{\tau} = Z_N + Z_C$$

$$= \pi \sqrt{2}\, n\, D_H^2 \sqrt{\frac{8\ kT}{\pi\ m_H}}$$

$$\times \left[\frac{1}{3} \cdot \left(\frac{D_N+D_H}{2D_H}\right)^2 \sqrt{\frac{m_H+m_N}{2m_N}} + \frac{2}{3} \cdot \left(\frac{D_C+D_H}{2D_H}\right)^2 \sqrt{\frac{m_H+m_C}{2m_C}}\right]$$

$$= 0.52\, \pi \sqrt{2}\, n\, D_H^2 \sqrt{\frac{8\ kT}{\pi\ m_H}}\ ; \qquad \text{A2.5}$$

where the subscripts H, N and C refer to HCN, N_2 and CH_4 respectively. n is the total number density of nitrogen and methane given by n = p/kT where p is tht total pressure. Equation A2.5 is 0.52 times the expression given by Steffen and Kneubühl (1968) which strictly only applies for self collisions in pure HCN gas.

For a 1:2 mixture of nitrogen and methane at 0.7 torr (optimum operating conditions in our pulsed HCN laser) eq. A2.5 becomes,

$$Z = 1.4\pi \times 10^{8} T^{-\frac{1}{2}}$$

which gives the linewidth,

$$\Delta f_P = 1.4 \times 10^{8} T^{-\frac{1}{2}} \text{ Hz.} \qquad \text{A2.6}$$

Using equations A2.1 and A2.6 we tabulate, in table A2.1, the Doppler and collision linewidths of HCN in the optimum gas mixture (Sec. 2.3.3.3) for a set of temperatures in the range of interest.

Table A2.1

HCN temperature	$\Delta\nu_p$	$\Delta\nu_D$
300	8.1	2.1
500	6.3	2.7
1000	4.4	3.9
1500	3.6	4.8
2000	3.1	5.5
2500	2.8	6.1
3000	2.6	6.7
3500	2.4	7.3
K	MHz	MHz

The total linewidth may be approximately estimated by taking the square root of the sum of the squares of the contributions from the two sources (Townes and Schawlow, 1955). However we will see (Secs. A2.2 and A2.3) that both contributions may be smaller than the figures in Table A2.1. For we have not considered collisional narrowing of the Doppler contribution (Sec. A2.2) or the possible departure of the collision linewidth from the classical $T^{-\frac{1}{2}}$ variation with temperature T. The collisional linewidth may vary as T^{-1} or $T^{-3/2}$ (Sec. A2.3).

In view of the foregoing comments and the data in Table A2.1 we infer that in our pulsed laser (at optimum operating conditions, $p \simeq 0.7$ torr) the total 337 μm linewidth is of the order of, but somewhat less than 10 MHz.

In our CW laser ($p \simeq 1.5$ torr; Sec. 2.4.3) the collision linewidth would be about twice as big as in the pulsed laser (Table A2.1). The total linewidth should be greater in the CW laser provided that collision broadening dominates; as it will do if the temperature is not too high. In Sec. 2.4.3 we argue that this is indeed the case; we show that the HCN temperature in the CW laser is less than 2600 K and that the total linewidth is about 13 MHz. Thus the 337 μm emission line in our CW laser is essentially homogeneously broadened. This is supported by the fact that no published laser resonator interferogram (Steffen and Kneubühl, 1968) for a CW laser shows the Lamb-dip (Sinclair and Bell, 1969). Yamanaka et al (1968) mention observing a Lamb-dip of 2% in a CW laser operating at 0.2 torr where the collision linewidth would be an order of magnitude less than in our laser.

Unfortunately we cannot use similar arguments in relation to laser resonator interferograms of pulsed lasers. Here plasma effects would be expected to mask the observation of a Lamb-dip anyway (see Sec. 5.4.2). However in our pulsed laser at optimum operating conditions

the pressure is quite high (0.7 torr). It seems likely that unless the HCN temperature is very high the line will be essentially homogeneously broadened.

A2.2 Collisional Narrowing of the Doppler Line-width

Recent publications (Berman and Lamb, 1970, 1971) indicate that collisional effects on line broadening in lasers cannot be treated properly on a classical basis and a quantum mechanical approach is required. Unfortunately, such a treatment does not lead simply to an expression for the total lineshape (and linewidth). However, Smith et al (1971) have shown that in the case where the perturbers are not more massive than the emitting species the classical "weak collision" approximation of Galatry (1961) is applicable. Galatry shows that if the emitter is radiating at wavelength λ and has mean free path d between collisions then the lineshape is readily calculated in two limits. These are conveniently expressed in terms of the parameter

$$\frac{2\pi d}{\lambda} \simeq \frac{\text{Standard Doppler Linewidth}}{\text{Classical Impact Linewidth}}$$

(i) Low pressure limit : $\frac{2\pi d}{\lambda} >> 1$.

In this case Doppler broadening dominates and the lineshape is obtained by "folding" the Gaussian Doppler and (relatively narrow) Lorentzian pressure profiles to obtain the familiar Voigt (Wiese, 1967) profile. The total linewidth is not significantly different from the Doppler linewidth calculated in the standard way.

(ii) High pressure limit : $\frac{2\pi d}{\lambda} << 1$.

Here pressure broadening dominates and the combined lineshape is Lorentzian with a full width at half power of the order of $\left[\frac{1}{\pi\tau} + \frac{2\pi d}{\lambda} \cdot \Delta f_D\right]$ where τ is the time between collisions and Δf_D is the standard Doppler linewidth (full width at half power). Here, there is significant "collisional narrowing" (Dicke, 1953) of the Doppler contribution to the total linewidth. It follows that in the limit $\frac{2\pi d}{\lambda} << 1$ the Doppler contribution to the total linewidth is negligible. [Nevertheless, the collision narrowed Doppler profile may be observed experimentally. Various transitions, for which the relevant energy levels are not appreciably perturbed by collisions (Dicke, 1953), exhibit Lorentzian profiles narrower than the Doppler profile appropriate to the temperature of the emitter (Cooper et al, 1968).]

In our CW 337 μm laser (Sec. 2.4.3) $\frac{2\pi d}{\lambda}$ is of the order of unity and consequently the expression for the lineshape must be integrated numerically. Galatry presents the results of such a numerical integration and shows that even in this region there is significant ($\times \frac{1}{2}$) collisional narrowing of the Doppler profile. Our previous upper limit of 6 MHz for the linewidth due to the Doppler effect (Sec. 2.4.3) is therefore an overestimate as it did not take the possibility of collisional narrowing into account.

A2.3 Classical Collision-Linewidth Calculations

In connection with line broadening two important points should be mentioned. Firstly, the cross section for momentum transfer (as derived from viscosity measurements) is not generally the same as the cross section for collisions which perturb the energy levels of the emitter (Townes and Schawlow, 1955). "Momentum transfer collisions" are responsible for establishing a Maxwellian velocity distribution and for producing collisional narrowing of the Doppler profile. Thus in the discussion above d is to be interpreted as the mean free path between momentum transfer collisions while τ is the mean time between perturbing collisions. Secondly, according to the "hard sphere" picture of kinetic theory the time between

collisions (and hence the collision linewidth) is inversely proportional to the square root of the temperature. Although this model gives satisfactory results as far as momentum transfer collisions are concerned experimental observations of collision linewidths often show deviations from this dependence on temperature (Gordy et al, 1953). This is because the relevant collision cross section is not temperature independent but tends to decrease with rising temperature (T) leading to collision linewidths which can vary as T^{-1} or even $T^{-3/2}$ (Gordy et al, 1953).

Appendix 3

Resonator Modes in Submillimetre Lasers

In Chapters 4 and 5 of this thesis we are concerned with plasma tuning of resonator modes through the "effective gainwidth" (Sec. 5.1.1) of the HCN line. Accordingly, the properties of modes in submillimetre laser resonators are of particular interest to us. In this appendix we calculate the mode separations of the HCN laser resonators described in this thesis and we discuss their relative losses.

A3.1 Mode Separations in Resonators Employing Spherical Mirrors

An important consideration in the design of a resonator is its diffraction loss. The most important parameter for characterizing a resonator in this regard is the Fresnel number,

$$N = \frac{a_1 a_2}{4\lambda d} \qquad \text{A3.1}$$

where a_1 and a_2 are the mirror apertures, d is the mirror separation and λ is the wavelength of interest. We can see the significance of N quite simply. If a circular aperture of diameter a_1 is illuminated with parallel coherent radiation of wavelength λ a diffraction pattern

results (at distances >> λ) with its first minimum at angular position 1.22 λ/a_1. At distance d therefore the central maximum has diameter 2d 1.22 λ/a_1. If at distance d we collect (or reflect) only the radiation falling onto an aperture of diameter a_2 (< 2d 1.22 λ/a_1) then a rough measure of the amount of diffraction loss is the square of $a_2/(2d\ 1.22\ \lambda/a_1) = a_1a_2/2.44\ \lambda d$. If $a_2 > 2d\ 1.22\ \lambda/a_1$ this quantity gives an indication of how effectively the second aperture intercepts the radiation emitted by the first. Thus $N = a_1a_2/4\lambda d$ gives an indication of the diffraction loss of a laser resonator. If N >> 1 we expect very little diffraction loss; if $N \lesssim 1$ we expect diffraction losses to be quite significant.

Because of the long wavelength, submillimetre resonators of reasonable dimensions usually have Fresnel numbers of the order of unity. To keep losses down to a reasonable level concave spherical mirrors are usually employed in preference to plane parallel mirrors. For infinite apertures such resonators may be shown to have a large number of transverse electromagnetic ($TEM_{p\ell q}$) modes whose resonant lengths are given by (Kogelnik and Li, 1966)

$$L_{p\ell q} = \frac{\lambda}{2}\left(q + \frac{2p + \ell + 1}{\pi}\,\mathrm{Cos}^{-1}\sqrt{g_1g_2}\right) , \qquad \text{A3.2}$$

where $$g_1 = 1 - \frac{d}{R_1} \quad ,$$

A3.3

and $$g_2 = 1 - \frac{d}{R_2} \quad .$$

Here R_1 and R_2 are the radii of curvature of the two mirrors; q is the longitudinal order number, p is the radial quantum number and ℓ is the azimuthal quantum number. p and ℓ give the number of radial and azimuthal nodes in the $TEM_{p\ell}$ mode pattern.

The mode separations of submillimetre resonators using plane-parallel mirrors are summarized in a paper by Schwaller et al (1967).

For N infinite eq. A3.2 is exact and it is an excellent approximation for $N >> 1$. Kneubühl and Steffen (1967) have shown that eq. A3.2 must be modified for resonators with low Fresnel numbers, and give an equation for determining the minimum Fresnel number N_{min} for which their modified version of eq. A3.2 can be expected to be correct. They have verified their results for sub-millimetre resonators. For any of the resonators described in this thesis, the Fresnel number is greater than Kneubühl and Steffen's N_{min} and their correction to eq. A3.2 amounts to less than or of the order of 0.01%

Table A3.1

Laser	Pulsed	Pulsed	Pulsed	C.W.	C.W.	Units
Section Reference	2.2, 2.3, 4.2, 4.3	5.2	5.3	2.4 6.4	2.4 6.4	
R_1	8	3.7	3.7	3.7	3.7	m
R_2	∞	∞	∞	3.8	∞	m
a_1	5.1	7.6	7.6	7.6	7.6	cm
a_2	3.8	5.1	3.8	7.6	7.6	cm
d	2.2	2.2	2.2	1.8	1.8	m
N	0.7	1.3	1.0	2.4	2.4	-
Output	diffraction	13 mm hole in mirror #2	diffraction	5 mm hole in mirror #1	5 mm hole in both	-
$L_{p\ell q}-L_{ooq}$	$29(2p+\ell)$	$47(2p+\ell)$	$47(2p+\ell)$	$61(2p+\ell)$	$50(2p+\ell)$	μm
Tube-modes?	Unlikely	Unlikely	Apparently not	Likely	Very Likely	-

for the first few transverse modes ($0 \leqslant 2p + \ell \leqslant 6$). Thus eq. A3.2 may confidently be used to calculate the mode separations of our resonators.

Table A3.1 shows the dimensions of the resonators described in this thesis, and the difference in resonant lengths of their $TEM_{p\ell q}$ and TEM_{00q} modes. It is apparent that the mode spacing of low loss modes is generally greater than the gainlength for laser emission ($\simeq$ 25 μm). Thus the gainlengths of successive modes will not overlap. An exception is the pulsed laser with a plane mirror and an 8 m radius spherical mirror. Under high gain conditions the TEM_{00} and TEM_{01} modes might overlap, a possibility which was suggested by observations described in Sec. 4.3.

It is important to note that these calculations are for open resonators and take no account of the possibility of reflection of laser radiation by the inside wall of the discharge tube. Reflections tend to reduce the losses of the TEM modes, and also allow other modes (e.g. TE and TM) to be excited (Steffen and Kneubühl, 1968). When reflections are important we speak of "tube-modes" - they have been studied in detail by Steffen and Kneubühl.

In our experiments with the pulsed HCN laser internal wall reflections were quite unlikely because the mirror apertures were somewhat smaller than the tube

diameter. In experiments with the CW laser however, the mirror apertures were equal to the tube diameter and central output coupling holes were always used. In this case the occurrence of tube-modes is quite likely. The abundance of operating modes and the noisy output which we observed from the CW laser (Sec. 2.4.3) suggest that tube-modes were dominant.

A3.2 Relative Losses of Resonator Modes

In our observations of multiple mode sweeping in our pulsed HCN laser (Ch. 5) the relative losses of the axial and low order transverse modes will determine the number of "spikes" which are observed. In general, we are not able to simply calculate the relative losses of the modes of our laser resonators. However we can make some comments about the order of increasing magnitude of the losses of different modes.

For resonators with Fresnel number near unity the losses of transverse modes increase quite rapidly with transverse order. For the first few transverse modes $TEM_{p\ell}$ the losses increase monotonically with $2p + \ell$. McCumber (1965) has computed the losses of transverse modes up to $2p + \ell = 9$ for confocal resonators without coupling apertures. We show in Table A3.2, the losses

of the first few transverse modes of such a resonator with N = 1.

Table A3.2

pℓ	% loss per pass	2p + ℓ
00	< .1%	0
01	.9%	1
02	7%	2
10	20%	2
03	28%	3
11	47%	3
04	60%	4
12	83%	4

It should be noted that McCumber writes his transverse quantum numbers in the order ℓp. We have reversed the order in the table above to agree with our notation and the notation of all of our other references. The losses shown in Table A3.2 are rather smaller than those in our laser resonators (e.g. the loss of the TEM_{00} mode of the resonator described in Sec. 2.2.3 is 23% per pass) because non-confocal systems were used. Although none of our resonators are confocal however, the order of

losses of the modes of those not using hole output-coupling would be expected to be the same as in Table A3.2. This is of importance in our discussions in Secs. 4.3 and 5.3.

Of course the inclusion of output coupling apertures in one or both laser mirrors may change the order of losses of the modes of a resonator. The order shown in Table A3.2 is unlikely to apply. In this case we cannot make any general comments about the new order of increasing losses (McCumber, 1965, 1969); each case must be considered on its own merits. We discuss cases of interest when they arise (e.g. Sec. 5.2.1).

Appendix 4

Photoionization, and Ionization of Metastables on-Axis in the SUPPER I Helium Plasma

In this appendix we show that neither photoionization of neutral helium atoms nor ionization of metastable helium atoms by other processes could be responsible for the rising electron density which is observed at early times.

A4.1 Photoionization

The central part of the plasma will be irradiated by continuum ultraviolet photons emitted in radiative recombination events in the rapidly decaying outer plasma regions. We will show however, that ionization resulting from the absorption of such photons could not account for the observed rise in density.

The flux of photons leaving each cubic centimetre of the recombining outer part of the plasma which would be able to photoionize a neutral is just the rate of radiative recombination into the ground state, which we can take (Allen, 1955) as being of the order of 5×10^{16} cm^{-3} sec^{-1} (the value for r = 5 cm 400 μsec after breakdown). Considering a small volume on the axis of the vessel surrounded by an annular volume of plasma extending from

an inner radius of 3 cm to the vessel wall, isotropically emitting such photons, we can estimate the flux through the small volume assuming that the plasma is optically thin to continuum ultraviolet radiation. Within our small volume will be a density of neutral atoms of the order of 3.3×10^{15} cm^{-3}, the pre-discharge density, with a photo-ionization cross section of 7×10^{-18} cm^{-2} (Ditchburn and Öpik, 1962). We find that the rate of production of ions and electrons would be less than 6×10^{15} cm^{-3} sec^{-1} which is an order of magnitude smaller than the observed rate of rise even though this estimate is conservatively large.

A4.2 Ionization of Inward Diffusing Metastables

Since three quarters of the highly excited atoms formed by three body recombination will be in triplet states and will tend to be deexcited into the lowest triplet state, the metastable 2^3S_1, the possibility exists of a considerable number of atoms in this state diffusing (fairly rapidly, since they are uncharged) into the central region of the vessel. Such atoms would be comparatively easily ionized, either by electron collision or by the Penning ionization reaction:

$$He\ (2^3S_1) + He\ (2^3S_1) \rightarrow He\ (1^1S_0) + He^+\ (1s) + e^-$$

However, the ionization rate cannot exceed the rate of influx of metastables from the outer plasma region. Since we can easily estimate the diffusion coefficient for these atoms (McDaniel, 1964, p.50; Phelps, 1955) to be less than 2×10^{14} cm^2 sec^{-1} it is only necessary to estimate the radial metastable density gradient to find the rate of influx. We can conservatively take the on-axis metastable density to be zero and estimate the peak metastable density in the following way.

In the region where 2^3S_1 metastables are being formed, the equilibrium density will be determined by the balance of the rates of formation (by recombination) and removal (by diffusion and electron collisional deexcitation). Now, the diffusion loss rate (see eq. 8.25)

$$R_{diff} = D \cdot \left(\frac{2.4}{R}\right)^2 \qquad \text{A4.1}$$

is considerably smaller than the electron collisional deexcitation rate

$$R_{coll} = K(2,1)n_e \qquad \text{A4.2}$$

where K(2,1) is a rate coefficient with a value of the order 10^{-9} cm^3 sec^{-1} (Bates et al, 1967). Thus we may write

$$\frac{3}{4}\frac{dn_e}{dt} \simeq K(2,1)n_e n_m \qquad \text{A4.3}$$

where n_m is the metastable density. Considering the plasma conditions at r = 5 cm at the typical time 400 μsec after breakdown when $n_e = 7 \times 10^{14}$ cm^{-3} we find that the metastable density will be less than 10^{12} cm^{-3}. Diffusion across the density gradient implied can only account for the appearance of metastables at the centre at a rate of less than a tenth of the rate at which ions actually appear even when we ignore the fact that most of the diffusing metastables will be deexcited before reaching the centre.

A4.3 Conclusion

We conclude that neither ionization of metastables diffusing to the centre nor photoionization could account for the rise in density observed at the centre of the plasma early in the decay.

References

H. Alfvén and J. Wilcox (1962), Astrophys. J. 136, p.1016.

C.W. Allen (1955), "Astrophysical Quantities", Athlone Press, London, p.91.

D.E.T.F. Ashby, D.F. Jephcott, A. Malein and F.A. Raynor (1965), J. Appl. Phys. 36, 1, p.29.

P. Banks (1966a), Planet. Space Sci. 14, p.1085.

P. Banks (1966b), Planet. Space Sci. 14, p.1105.

M.R. Barrault and P. Hughes (1967), Proc. 8th Int. Conf. on Phenomena in Ionized Gases, Vienna, p.4.

D.R. Bates, A.E. Kingston and R.W.P. McWhirter (1962a), Proc. Roy. Soc. A.267, p.297.

D.R. Bates, A.E. Kingston and R.W.P. McWhirter (1962b), Proc. Roy. Soc. A. 270, p.155.

D.R. Bates and A.E. Kingston (1963), Planet. Space Sci. 11, p.1.

D.R. Bates and A.E. Kingston (1964), Proc. Roy. Soc. 279, p.31.

D.R. Bates, K.R. Bell and A.E. Kingston (1967), Proc. Phys. Soc. 91, p.288.

W.R. Bennett, Jr. (1962), Phys. Rev. 126, 2, p.580.

P.R. Berman and W.E. Lamb, Jr. (1970), Phys. Rev. A2, p.2435.

P.R. Berman and W.E. Lamb, Jr. (1971), Phys. Rev. A4, p.319.

N.C. Blais and J.B. Mann (1960), J. Chem. Phys. 32, p.1459.

M. Born and E. Wolf (1965), "Principles of Optics", Pergamon Press, London, p.122.

R. Bracewell (1965), "The Fourier Transform and its Applications", McGraw-Hill, N.Y., p.179.

G.F. Brand, N.R. Heckenberg and C.N. Watson-Munro (1969), Aust. J. Phys. 22, p.337.

M.H. Brennan, J.A. Lehane, D.D. Millar and C.N. Watson-Munro (1963), Aust. J. Phys. 16, 3, p.340.

S.C. Brown (1959), "Basic Data of Plasma Physics", Wiley, N.Y.

S. Byron, R.C. Stabler and P.I. Bortz (1962), Phys. Rev. Lett. 8, p.376 (erratum p.497).

J. Chamberlain, H.A. Gebbie, A. George and J.D.E. Beynon (1969), J. Plasma Phys. 3, p.75.

G.W. Chantry, Helen M. Evans, J.W. Fleming and H.A. Gebbie (1969), Infrared Phys. 9, p.31.

G.W. Chantry (1971), "Submillimetre Spectroscopy", Academic Press, N.Y., p.244.

Che Jen Chen (1967), Phys. Rev. 163, 1, p.1.

W.S. Cooper and W.B. Kunkel (1965), Phys. Rev. 138A, p.1022.

J. Cooper (1966), Reports on Progress in Physics, XXIX, pt. 1, p.35.

V.G. Cooper, A.D. May, E.H. Hara and H.F.P. Knapp (1968), Can. J. Phys. 46, p.2019.

J.D. Craggs and J.M. Meek (1945), Nature, 156, p.21.

N. D'Angelo (1961), Phys. Rev. 121, p.505.

A.N. Dellis, W.H.F. Earl, A. Malein and S. Ward (1965), Nature, 207, 4992, p.56.

R.H. Dicke (1953), Phys. Rev. 89, p.472.

R.W. Ditchburn and U. Öpik (1962), "Atomic and Molecular Processes", D.R. Bates, ed., Academic Press, London.

H.W. Drawin (1969a), Z. Physik, 225, p.470.

H.W. Drawin (1969b), Z. Physik, 225, p.483.

H.W. Drawin (1969c), EUR-CEA-FC-515.

H.W. Drawin, F. Klan and H. Ringler (1971), Z. Naturforsch. 26a, p.186.

H.W. Drawin and F. Emard (1971), Z. Physik, 243, p.326.

R.G. Fowler and W.R. Atkinson (1959), Phys. Rev. 113, p.1268.

P.G. Frayne (1969), J. Phys. B. Ser. 2, 2, p.247.

L. Galatry (1961), Phys. Rev. 122, p.1218.

C.G.B. Garrett (1967), "Gas Lasers", McGraw-Hill, N.Y., p.122.

H.A. Gebbie, N.W.B. Stone and F.D. Findlay (1964), Nature, 202, p.685.

O. Gehre (1972), Max-Planck-Institut für Plasmaphysik, IPP IV/39.

J.B. Gerardo and J.T. Verdeyen (1963), Appl. Phys. Lett. 3, p.121.

R.G. Giovanelli (1948a), Aust. J. Scient. Res. A. 1, p.275.

R.G. Giovanelli (1948b), Aust. J. Scient. Res. A. 1, p.289.

V.E. Golant (1963), Sov. Phys. Uspekhi, 6, 2, p.161.

M.J.E. Golay (1947), Rev. Sci. Instr. 18, p.357.

J.P. Gordon and H. Kogelnik (1964), Bell Syst. Tech. J. 43, p.2873.

W. Gordy, W.V. Smith and R.P. Trambarulo (1953), "Microwave Spectroscopy", Wiley, N.Y., p.196.

M. Gryzinski (1959), Phys. Rev. 115, p.374.

M.A. Gusinow, J.B. Gerardo and J.T. Verdeyen (1966), Phys. Rev. 149, 1, p.91.

A. Hadni (1969), "L'Infrarouge Lointain", Presses Universitaires de France, Paris.

M.A. Heald and C.B. Wharton (1965), "Plasma Diagnostics with Microwaves", Wiley, N.Y.

A.G. Hearn (1963), Proc. Phys. Soc. 81, p.648.

N.R. Heckenberg and W.I.B. Smith (1971), Rev. Sci. Instr. 42, p.977.

N.R. Heckenberg (1972), Ph.D. Thesis, University of Sydney, Australia.

H. Herold and F.C. Jahoda (1969), Rev. Sci. Instr. 40, p.145.

E. Hinnov and J.G. Hirschberg (1962), Phys. Rev. 125, p.795.

L.O. Hocker and A. Javan (1967), Phys. Lett. 25A, 7, p.489.

L.O. Hocker, A. Javan, D. Ramachandra Rao, L. Frenkel and T. Sullivan (1967), Appl. Phys. Lett. 10, 5, p.147.

E.B. Hooper and G. Bekefi (1966), J. Appl. Phys. 37, p.4083.

F.E. Irons (1965), Ph.D. Thesis, University of Sydney, Australia.

F.E. Irons and D.D. Millar (1965), Aust. J. Phys. 18, p.23.

R.G. Jones, C.C. Bradley, J. Chamberlain, H.A. Gebbie, N.W.B. Stone and H. Sixsmith (1969), Appl. Opt. 8, 3, p.701.

F.K. Kneubühl and H. Steffen (1967), Phys. Lett. 25A, 8, p.639.

H. Kogelnik and T. Li (1966), Proc. IEEE, 54, 10, p.1312.

S. Kon, M. Yamanaka, J. Yamamoto and H. Yoshinaga (1967), Jap. J. Appl. Phys. 6, 5, p.612.

T. Li (1965), Bell Syst. Tech. J. 44, p.917.

W.J. Lick and H.W. Emmons (1965), "The Transport Properties of Helium from 200 to 50,000 K", Harvard University Press, Cambridge, U.S.A.

D.R. Lide and A.G. Maki (1967), Appl. Phys. Lett. 11, 2, p.62.

M.M. Litvak and D.F. Edwards (1966), J. Appl. Phys. 37, p.4462.

B.W. McCaul (1969), Ph.D. Thesis, Stanford University, California, U.S.A.

B.W. McCaul (1970), Appl. Opt. 9, 3, p.653.

B.W. McCaul and A.L. Schawlow (1970), Ann. N.Y. Acad. Sci. 168, p.697.

D.E. McCumber (1965), Bell. Syst. Tech. J. 44, 2, p.333.

D.E. McCumber (1966), Phys. Rev. 141, p.306.

D.E. McCumber (1969), Bell Syst. Tech. J. 48, 6, p.1919.

E.W. McDaniel (1964), "Collision Phenomena in Ionized Gases", Wiley, N.Y.

A.G. Maki (1968), Appl. Phys. Lett. 12, 4, p.122.

L.E.S. Mathias, A. Crocker and M.S. Wills (1968), IEEE J. Quant. Electron. QE-4, 4, p.205.

E.R. Mosburg (1966), Phys. Rev. 152, p.166.

W.M. Muller and G.T. Flesher (1966), Appl. Phys. Lett. 8, 9, p.217.

A. Murai (1969), Jap. J. Appl.Phys. 8, 2, p.250.

A.A. Newton and M.C. Sexton (1968), J. Phys. B, Ser. 2, 1, p.669.

A.A. Newton and M.C. Sexton (1969), J. Phys. B, Ser. 2, 2, p.1069.

J.N. Olsen (1971), Rev. Sci. Instr. 42, p.104.

G.J. Parkinson, A.E. Dangor and J. Chamberlain (1968), Appl. Phys. Lett. 13, p.233.

R.W. Peterson and F.C. Jahoda (1971), Appl. Phys. Lett. 18, p.440.

A.V. Phelps (1955), Phys. Rev. 99, 4, p.1307.

I.C. Potter (1969), J. Appl. Phys. 40, p.4770.

E.H. Putley (1963), Proc. IEEE, 51, p.1412.

E.H. Putley and D.H. Martin (1967), "Spectroscopic Techniques for Far-Infrared, Submillimetre and Millimetre Waves", D.H. Martin, ed., North Holland, Amsterdam.

J.M.P. Quinn (1965), Plasma Phys. (J. Nuc. Energy C), 7, p.113.

R. Robben, W.B. Kunkel and L. Talbot (1963), Phys. Rev. 132, p.2363.

L.C. Robinson (1964), Rev. Sci. Instr. 35, p.1239.

L.C. Robinson and L.B. Whitbourn (1971), Proc. IREE Aust. 32, p.355.

V.K. Saxena and S.C. Saxena (1968), J. Phys. D. Ser 2, 1, p.1341.

P. Schwaller, H. Steffen, J.F. Moser and F.K. Kneubühl (1967), Appl. Opt. 6, 5, p.827.

I.P. Shkarofsky, T.W. Johnston and M.P. Bachynski (1966), "The Particle Kinetics of Plasmas", Addison-Wesley, London, p.367.

I.P. Shkarofsky, Ira B. Bernstein and B.B. Robinson (1963), Phys. Fluids, 6, 1, p.40.

D.C. Sinclair and W.E. Bell (1969), "Gas Laser Technology", Holt, Rinehart and Winston, N.Y., P.33.

P.W. Smith (1966), IEEE J. Quant. Electron. QE-2, p.62.

W.V. Smith and P.P. Sorokin (1966), "The Laser", McGraw-Hill, N.Y.

E.W. Smith, J. Cooper, W.R. Chappell and T. Dillon (1971), J. Quant. Spectrosc. Radiat. Transfer, 11, p.1567.

L. Spitzer, Jr. (1962), "Physics of Fully Ionized Gases", Interscience, N.Y.

O.M. Staffsud, F.A. Haak, and K. Radisavljevic (1967), IEEE J. Quant. Electron. QE-3, 11, p.618.

H. Steffen, J. Steffen, J.F. Moser and F.K. Kneubühl (1966), Phys. Lett. 20, 1, p.20.

H. Steffen, B. Keller and F.K. Kneubühl (1967a), Electron. Lett. 3, 12, p.561.

H. Steffen, J.F. Moser and F.K. Kneubühl (1967b), J. Appl. Phys. 38, p.3410.

H. Steffen and F.K. Kneubühl (1968), IEEE J. Quant. Electron. QE-4, 12, p.992.

C.H. Townes and A.L. Schawlow (1955), "Microwave Spectroscopy", McGraw-Hill, N.Y.

R. Turner and T.O. Poehler (1968), J. Appl. Phys. 39, p.5726.

R. Turner, A.K. Hochberg, and T.O. Poehler (1968), Appl. Phys. Lett. 12, 3, p.104.

R. Turner and T.O. Poehler (1971), J. Appl. Phys. 42, 10, p.3819.

T. Uchida (1967), IEEE J. Quant. Electron. QE-3, p.7.

L.B. Whitbourn, L.C. Robinson and G.D. Tait (1972), Phys. Lett. 38A, p.315.

A.D. White, E.I. Gordon and J.D. Rigden (1963), Appl. Phys. Lett. 2, p.91.

W.L. Wiese, M.W. Smith and B.M. Glennon (1966), "Atomic Transition Probabilities", NSRDS-NBS 4, 1.

W.L. Wiese (1965), "Plasma Diagnostic Techniques", R.H. Huddlestone and S.L. Leonard, eds., Academic Press, N.Y., p.302.

M. Yamanaka, H. Yoshinaga and S. Kon (1968), Jap. J. Appl. Phys. 7, 3, p.250.

M. Yamanaka, T. Yamauchi and H. Yoshinaga (1971), Jap. J. Appl. Phys. 10, 11, p.1601.

H. Zanastra (1946), Proc. Roy. Soc. A. 186, p.236.